

**Numerical Investigation of Subsonic and Hypersonic
Rarefied Gas Flows over Different Geometries using
Direct Simulation Monte Carlo Approach**

THESIS

Submitted in partial fulfillment
of the requirements for the degree of
DOCTOR OF PHILOSOPHY

by

DEEPAK NABAPURE

ID No. 2015PH480056H

Under the Supervision of

Dr. RAM CHANDRA MURTHY KALLURI




BIRLA INSTITUTE OF TECHNOLOGY & SCIENCE, PILANI

2022

BIRLA INSTITUTE OF TECHNOLOGY AND SCIENCE, PILANI

CERTIFICATE

This is to certify that the thesis entitled, “**Numerical Investigation of Subsonic and Hypersonic Rarefied Gas Flows over Different Geometries using Direct Simulation Monte Carlo Approach**” submitted by **DEEPAK NABAPURE** ID No. **2015PH480056H** for award of Ph.D. of the Institute embodies original work done by him under my supervision.

Signature of the Supervisor: 

Name in capital letters : **Dr. RAM CHANDRA MURTHY KALLURI**

Designation: **Assistant Professor, Mechanical Engineering Department,
BITS-Pilani Hyderabad Campus**

Date: **January 21, 2022**

DECLARATION

I, DEEPAK NABAPURE, declare that this THESIS titled, '**Numerical Investigation of Subsonic and Hypersonic Rarefied Gas Flows over Different Geometries using Direct Simulation Monte Carlo Approach**' and the work presented in it are my own. I confirm that:

- The work contained in this thesis is original and has been done by myself under the general supervision of my supervisors.
- The work has not been submitted to any other Institute for any degree or diploma.
- I have conformed to the norms and guidelines given in the Ethical Code of Conduct of the Institute.
- I have followed the guidelines provided by the Institute in writing the thesis.
- Whenever I have used materials (data, theoretical analysis, and text) from other sources, I have given due credit to them by citing them in the text of the thesis and giving their details in the references.
- Whenever I have quoted written materials from other sources, I have put them under quotation marks and given due credit to the sources by citing them and giving required details in the references.

Name in capital letters : DEEPAK NABAPURE

Signed: 

Date: **January 21, 2022**

ACKNOWLEDGEMENTS

This thesis is the final destination of my journey in obtaining my doctoral degree. First of all, I praise and thank God for blessing me with an opportunity to undertake this research. I am highly indebted to my supervisor Dr. Ram Chandra Murthy K, for giving me an opportunity to work under him. His exceptional guidance and immense patience, helped me complete this research. I am sincerely grateful to Dr. Satish Kumar Dubey and Dr. Santanu Prasad Datta as my Doctoral Advisory Committee (DAC) members for their valuable comments and insightful suggestions at various stages of research work. My deep sense of regard to Prof. NSK Reddy current head, Prof. Amit Kumar Gupta, former head, Department of Mechanical Engineering, BITS-Pilani, Hyderabad campus, for providing an amiable ambiance leading to the successful completion of my research. Prof. G Sundar, current Director, and Prof. V Sambasiva Rao, former Director, BITS-Pilani, Hyderabad campus, deserve my sincere gratitude for providing me all resources and state-of-the-art facilities at the campus to carry out my research. My notable thanks to Prof. Souvik Bhattacharyya Vice-Chancellor, BITS-Pilani, for providing me an excellent platform for carrying my doctoral work at the institute. I heartily thank Prof. Vamsi Krishna Venuganti, Associate Dean, BITS-Pilani, Hyderabad campus, for his support throughout the research work. I extend my warm gratitude to all the Faculty Members, Ph.D. colleagues, Department of Mechanical Engineering, BITS-Pilani, Hyderabad campus for their support and encouragement to carry out my research work. Last but not least, I would like to pay high regards to my parents, sister and brother-in-law for their unconditional love, encouragement, and support throughout my tenure of my Ph.D. Besides this, I thank every individual who knowingly and unknowingly helped me complete my research.

Deepak Nabapure

January 21, 2022

ABSTRACT

One of the most researched problems in the space community is the study of highspeed re-entry vehicles entering the earth's atmosphere. This interest is mainly due to the design of new generation space vehicles that can improve the existing space shuttle designs. These vehicles fly at extremely high (often hypersonic) speeds for a significant part in the rarefied setting. Furthermore, the space vehicle passes through various rarefaction regimes, atmospheric temperatures, and they experience complex flow behaviors, which include shock interactions which are generally investigated using various computational methods. Although the vehicle's streamlined aerodynamic surface form is preferred, minor discontinuities such as protuberances, notches, steps, gaps, or cavities can prevail either during its manufacturing or during its operation. These discontinuities lead to flow separation, circulation, and re-attachment, which have significant implications on the flow and heat transfer performance of these surfaces.

In this thesis work, the flow behavior is explored for different flow configurations using the Direct Simulation Monte Carlo (DSMC) approach, an effective method for studying rarefied flows. The investigations are performed using the open-source *dsmcFoam* code, which is a part of OpenFOAM.

Initially the verification studies were performed to confirm the accuracy of the results. Then the *dsmcFoam* has been validated against the standard benchmark results from the previous literature. In the first part, the physics of the rarefied internal flows is investigated. The problem modeled belongs to internally confined flows where at least one boundary is moving, imparting fluid motion. The lid-driven square cavity is the configuration selected, and the studies have been performed for argon flow for both double-sided and four-sided lid-driven cavity for both parallel and anti-parallel wall motions. The effect of the direction of wall motion and the influence of Mach number on the flow physics are analyzed. Furthermore, the rarefaction effects are also thoroughly investigated for different Knudsen numbers. The analysis showed that flow and thermal properties are directly proportional to the Mach number. The variation in the flow and

thermal properties is found to be significant at the onset of the transition regime and much smaller in the free molecular regime.

In the second part, the rarefied flow behavior for external flows is discussed at length. The different discontinuities that are typically encountered on the surfaces of space vehicles are approximated as a simplified geometry for modeling the irregularities around such vehicles. The configurations include the flow over a backward-facing step, forward-facing step, open cavity, and wall-mounted cube. A comprehensive analysis of the effects of Mach number, wall temperature and Knudsen number on the flow-field properties, i.e., velocity, pressure, temperature, density, and surface properties, i.e., pressure coefficient, skin friction coefficient, and heat transfer coefficient were performed. Flow properties were found to increase with Mach number and wall temperature. The variation in flow properties is more sensitive to Mach number than the wall temperature. The surface properties were found to decrease with Mach number and increase with wall temperature. The flow properties and surface properties were found to increase with Knudsen number and are primarily affected by the interplay of compressibility and viscous dissipation effects. Also, some studies were performed by incorporating specific chemical reactions.

Thus, it is observed that the existence of discontinuity in the form of steps, gaps, cavities cannot be overlooked. For the conditions investigated, it is observed that the thermal and aerodynamic loads on the surfaces of discontinuities increased, thus demanding better aerodynamic thermal protection.

Keywords:

Backward-Facing Step, Cavity, DSMC, Forward-Facing Step, Mach Number, OpenFOAM, Knudsen Number, Rarefied Gas Flows, Wall-mounted cube.

Table of Contents

CERTIFICATE	i
DECLARATION	ii
ACKNOWLEDGEMENTS	iii
ABSTRACT	iv
Table of Contents	vi
List of Tables	ix
List of Figures	x
List of Abbreviations	xviii
List of Symbols	xix
1 Introduction	1
1.1 Background of rarefied gas flows	1
1.2 The Knudsen number	5
1.3 Classification of flow regimes	6
1.4 Macroscopic and Microscopic approaches	8
1.5 Overview of the DSMC method	9
1.6 Scope of the present work	10
1.7 Outline of the thesis	10
2 Review of the past work	13
2.1 Lid-driven cavity	13
2.2 Backward-facing step	16
2.3 Forward-facing step	18
2.4 Open cavity	19
2.5 Wall-mounted cube	21

2.6	Gaps identified in the literature	22
2.7	Objectives of the present work	24
3	Computational methodology adopted in the present work	26
3.1	Direct Simulation Monte Carlo (DSMC)	26
3.1.1	Background of DSMC	26
3.1.2	Choice of simulation parameters	28
3.1.3	DSMC Algorithm	28
3.1.4	Particle motion and wall collision	29
3.1.5	Modeling inter-molecular collisions	31
3.1.6	Sampling flow properties	33
3.1.7	Chemical reaction modeling	35
3.2	Limitations of DSMC	35
4	Validation studies	37
4.1	Grid, timestep and particles per cell independence	37
4.2	Validation of flow inside a lid-driven cavity	38
4.3	Validation of flow over a flat plate	40
4.4	Validation of flow over a backward-facing step	41
4.5	Validation of flow over an open cavity	43
4.6	Validation of chemically reacting flow over a cylinder	45
5	Modeling and investigation of the rarefied flow physics of internal flows	48
5.1	Introduction	48
5.2	Double-sided lid-driven cavity	52
5.2.1	Anti-parallel wall motion	52
5.2.1.1	Influence of Mach number	52
5.2.1.2	Influence of Knudsen number	54
5.2.2	Parallel wall motion	59
5.2.2.1	Influence of Mach number	59
5.2.2.2	Influence of Knudsen number	61
5.3	Four-sided lid-driven cavity	65
5.3.1	Anti-parallel wall motion	65
5.3.1.1	Influence of Mach number	65
5.3.1.2	Influence of Knudsen number	76
5.3.2	Parallel wall motion	82
5.3.2.1	Influence of Mach number	82
5.3.2.2	Influence of Knudsen number	92
5.4	Comparison with NSF equations	96
6	Modeling and investigation of the rarefied flow physics of external flows	101
6.1	Analysis of rarefied flow over backward facing step	101
6.1.1	Influence of Mach number	105
6.1.2	Influence of Wall temperature	123
6.1.3	Influence of Knudsen number	135

6.2	Analysis of rarefied flow over forward facing step	154
6.2.1	Influence of Mach number	157
6.2.2	Influence of Wall temperature	164
6.2.3	Influence of Knudsen number	170
6.3	Analysis of rarefied flow over open cavity	187
6.3.1	Influence of Mach number	188
6.3.2	Influence of Wall temperature	201
6.3.3	Influence of Knudsen number	215
6.4	Analysis of rarefied flow over wall-mounted cube	230
6.4.1	Influence of Mach number	231
6.4.2	Influence of Wall temperature	240
6.4.3	Influence of Knudsen number	245
6.5	Comparison with chemical reacting flows	254
7	Conclusion and future scope	261
7.1	Summary and primary conclusions	261
7.2	Specific contributions to research	269
7.3	The usefulness of the research	269
7.4	Limitations of the current study	270
7.5	Future scope of work	270
	Bibliography	272
	Scientific publications from the present research work	300
	Brief Biography of the Candidate	305
	Brief Biography of the Supervisor	306

List of Tables

3.1	List of chemical reactions employed.	36
4.1	Details of the chosen test case for flat plate validation with Becker <i>et al.</i>	41
4.2	Details of the chosen test case for BFS validation with Guo <i>et al.</i> [135]	42
4.3	Details of the chosen test case for open cavity validation with Guo. <i>et al.</i> [2].	44
4.4	Details of the chosen test case for cylinder validation with Scanlon <i>et al.</i>	46
5.1	Simulation parameters for studying the cavity problem.	51
6.1	Gas properties.	104
6.2	Flow and simulation parameters.	104
6.3	Recirculation lengths of BFS for different Ma	107
6.4	Recirculation lengths for of BFS different T_w	123
6.5	Boundary layer thickness (δ) for different Kn at $X = 59\text{mm}$	140
6.6	Recirculation lengths of BFS for different Kn	140
6.7	Geometric parameters of the 2D-FFS.	155
6.8	The implemented boundary conditions for the 2D-FFS.	157
6.9	Recirculation lengths of FFS for different Ma	158
6.10	Recirculation lengths of FFS for different T_w	165
6.11	Recirculation lengths of FFS for different Kn	176
6.12	Geometric parameters of the 2D open cavity.	187
6.13	Boundary conditions for the 2D open cavity.	187
6.14	Boundary layer thickness (δ) at $X = 59\text{mm}$ of open cavity for different Kn	217
6.15	Variation of the center of the primary vortex of open cavity for different Kn	218
6.16	Geometric parameters of the 2D wall-mounted cube.	230
6.17	Boundary conditions for the 2D wall-mounted cube.	230

List of Figures

1.1	Applications of rarefied gas flows (retrieved from https://en.wikipedia.org/wiki/)	3
1.2	Effects of temperature during re-entry. (adapted from https://core.ac.uk/download/pdf/11133242.pdf)	5
1.3	Flow regimes in terms of Knudsen number.(adapted from http://repository.ias.ac.in/115048/1/1759-3093.2.1.1.pdf)	8
2.1	Schematics of the studied configurations.	25
3.1	Flowchart of a standard DSMC simulation	30
4.1	Verification studies for open cavity in the transverse direction at $X = 59\text{mm}$ and $Kn = 21.10$	39
4.2	Validation study of lid-driven cavity.	40
4.3	Validation study of flow over a flat plate.	42
4.4	Comparison of velocity contour for the case of $H = 30\text{km}$ (a) published results [135] (b) simulation results.	43
4.5	Validation study of flow over a BFS.	43
4.6	Distribution of Mach number contours and streamlines for cavities with $L/D = 5$ (a) Published results [2], (b) Present study.	44
4.7	Validation study of flow over an open cavity.	45
4.8	Validation study of chemically reacting flow over an cylinder.	47
5.1	Configuration of the lid-driven cavity flow problem	50
5.2	Meshed Domain of lid-driven cavity	52
5.3	Contours of flow field for $Ma = 0.70$ at $Kn = 1$ for anti-parallel wall motion.	54
5.4	Velocity streamlines for $Ma = 0.70$ at $Kn = 1$ for anti-parallel wall motion.	55
5.5	Comparison of non-dimensional velocity at $Ma = 0.17$ for different Kn for anti-parallel wall motion.	56
5.6	Comparison of non-dimensional pressure at $Ma = 0.17$ for different Kn for anti-parallel wall motion.	56
5.7	Variation of temperature ratio plotted along the four walls of the driven cavity at $Ma = 0.17$ for different Kn for anti-parallel wall motion.	57
5.8	Variation of heat flux ratio plotted along the four walls of the driven cavity at $Ma = 0.17$ for different Kn for anti-parallel wall motion.	58
5.9	Contours of flow field for $Ma = 0.70$ at $Kn = 1$ for parallel wall motion.	60

5.10	Velocity streamlines for $Ma = 0.70$ at $Kn = 1$ for parallel wall motion.	61
5.11	Comparison of non-dimensional velocity at $Ma = 0.17$ for different Kn for parallel wall motion.	62
5.12	Comparison of non-dimensional pressure at $Ma = 0.17$ for different Kn for parallel wall motion.	63
5.13	Variation of temperature ratio plotted along the four walls of the driven cavity at $Ma = 0.17$ for different Kn for parallel wall motion.	64
5.14	Variation of heat flux ratio plotted along the four walls of the driven cavity at $Ma = 0.17$ for different Kn for parallel wall motion.	65
5.15	Velocity (m/s) contours at $Kn = 1$ for different Ma for anti-parallel wall motion.	67
5.16	Velocity streamlines for $Ma = 0.70$ at $Kn = 1$ for anti-parallel wall motion.	68
5.17	Comparison of non-dimensional velocity and slip velocity at $Kn = 1$ for different Ma for anti-parallel wall motion.	69
5.18	Pressure (Pa) contours at $Kn = 1$ for different Ma for anti-parallel wall motion.	71
5.19	Comparison of non-dimensional pressure at $Kn = 1$ for different Ma for anti-parallel wall motion.	72
5.20	Temperature (K) contours at $Kn = 1$ for different Ma for anti-parallel wall motion.	73
5.21	Comparison of non-dimensional temperature at $Kn = 1$ for different Ma for anti-parallel wall motion.	74
5.22	Contours of Heatlines at $Kn = 1$ for different $Ma = 0.70$ for anti-parallel wall motion.	77
5.23	Variation of heat flux ratio plotted along the four walls of the driven cavity at $Kn = 1$ for different Ma	78
5.24	Comparison of non-dimensional velocity and velocity slip velocity at $Ma = 0.17$ for different Kn for anti-parallel wall motion.	79
5.25	Variation of pressure ratio plotted along the four walls of the driven cavity at $Ma = 0.17$ for different Kn for anti-parallel wall motion.	80
5.26	Variation of temperature jump ratio plotted along the four walls of the driven cavity at $Ma = 0.17$ for different Kn for anti-parallel wall motion.	81
5.27	Variation of heat flux ratio plotted along the four walls of the driven cavity at $Ma = 0.17$ for different Kn for anti-parallel wall motion.	82
5.28	Velocity (m/s) contours at $Kn = 1$ for different Ma for parallel wall motion.	83
5.29	Velocity streamlines for $Ma = 0.70$ at $Kn = 1$ for parallel wall motion.	84
5.30	Comparison of non-dimensional velocity and slip at $Kn = 1$ for different Ma for parallel wall motion.	86
5.31	Pressure (Pa) contours at $Kn = 1$ for different Ma for parallel wall motion.	87
5.32	Comparison of non-dimensional pressure at $Kn = 1$ for different Ma for parallel wall motion.	88
5.33	Temperature (K) contours at $Kn = 1$ for different Ma for parallel wall motion.	89
5.34	Comparison of non-dimensional temperature at $Kn = 1$ for different Ma for parallel wall motion.	90

5.35	Contours of Heatlines at $Kn = 1$ for different $Ma = 0.70$ for parallel wall motion.	91
5.36	Variation of heat flux ratio plotted along the four walls of the driven cavity at $Kn = 1$ for different Ma for parallel wall motion.	92
5.37	Comparison of non-dimensional velocity and slip at $Ma = 0.17$ for different Kn for parallel wall motion.	94
5.38	Comparison of non-dimensional pressure at $Ma = 0.17$ for different Kn for parallel wall motion.	95
5.39	Variation of temperature ratio plotted along the four walls of the driven cavity at $Ma = 0.17$ for different Kn for parallel wall motion.	96
5.40	Variation of heat flux ratio plotted along the four walls of the driven cavity at $Ma = 0.17$ for different Kn for parallel wall motion.	97
5.41	Comparison of non-dimensional flow-field properties computed by the DSMC and NSF for parallel wall motion.	99
5.42	Comparison of non-dimensional flow-field properties computed by the DSMC and NSF for anti-parallel wall motion.	100
6.1	Schematic of the 2D BFS.	102
6.2	Meshed domain of the BFS.	103
6.3	Influence of the top surface of BFS for various various flow-field properties at $X = 120\text{mm}$	106
6.4	Variation of the non-dimensional velocity perpendicular to the surface of BFS for different Ma	108
6.5	Slip velocity ratio along the upper and lower surfaces of BFS for different Ma	109
6.6	Variation of the non-dimensional pressure perpendicular to the surface of BFS for different Ma	111
6.7	Variation of the non-dimensional temperature perpendicular to the surface of BFS for different Ma	112
6.8	Variation of the non-dimensional rotational, overall, and translational temperature perpendicular to the surface of BFS at $X = 46\text{ mm}$ for different Ma	114
6.9	Temperature jump ratio along the upper and lower surfaces of BFS for different Ma	115
6.10	Variation of the non-dimensional density perpendicular to the surface of BFS for different Ma	117
6.11	Variation of pressure coefficient C_p along the upper and lower surfaces of BFS for different Ma	119
6.12	Variation of skin friction coefficient C_f along the upper and lower surfaces of BFS for different Ma	121
6.13	Variation of heat transfer coefficient C_h along the upper and lower surfaces of BFS for different Ma	122
6.14	Variation of the non-dimensional velocity perpendicular to the surface of BFS for different T_w	124
6.15	Slip velocity ratio along the upper and lower surfaces of BFS for different T_w	125

6.16	Variation of the non-dimensional pressure perpendicular to the surface of BFS for different T_w	127
6.17	Variation of the non-dimensional temperature perpendicular to the surface of BFS for different T_w	128
6.18	Variation of the non-dimensional rotational, overall, and translational temperature perpendicular to the surface of BFS at $X = 46$ mm for different T_w	129
6.19	Temperature jump ratio along the upper and lower surfaces of BFS for different T_w	130
6.20	Variation of the non-dimensional density perpendicular to the surface of BFS for different T_w	132
6.21	Variation of pressure coefficient C_p along the upper and lower surfaces of BFS for different T_w	133
6.22	Variation of skin friction coefficient C_f along the upper and lower surfaces of BFS for different T_w	134
6.23	Variation of heat transfer coefficient C_h along the upper and lower surfaces of BFS for different T_w	135
6.24	Contours of non-dimensional flow-field properties for $H = 60$ mm, $Ma = 25$ and $Kn = 1.06$	138
6.25	Compressibility (Z) contour for $H = 60$ mm, $Ma = 25$ and $Kn = 1.06$	139
6.26	Variation of the non-dimensional velocity perpendicular to the surface of BFS for different Kn	141
6.27	Streamlines near the step of BFS for (a) $Kn = 0.05$, (b) $Kn = 0.1$, (c) $Kn = 1.06$, (d) $Kn = 10.33$, (e) $Kn = 21.10$	142
6.28	Slip velocity ratio along the upper and lower surfaces of BFS for different Kn	143
6.29	Variation of the non-dimensional pressure perpendicular to the surface of BFS for different Kn	145
6.30	Variation of the non-dimensional temperature perpendicular to the surface of BFS for different Kn	147
6.31	Variation of the non-dimensional rotational, overall, and translational temperature perpendicular to the surface of BFS for $Kn = 0.05, 21.10$	148
6.32	Temperature jump ratio along the upper and lower surfaces of BFS for different Kn	149
6.33	Variation of the non-dimensional density perpendicular to the surface of BFS for different Kn	151
6.34	Variation of pressure coefficient C_p along the upper and lower surfaces of BFS for different Kn	152
6.35	Variation of skin friction coefficient C_f along the upper and lower surfaces of BFS for different Kn	153
6.36	Variation of heat transfer coefficient C_h along the upper and lower surfaces of BFS for different Kn	155
6.37	Schematic of the 2D FFS.	156
6.38	Meshed domain of the FFS.	157

6.39	Variation of the non-dimensional velocity perpendicular to the surface of FFS for different Ma .	159
6.40	Variation of the non-dimensional pressure perpendicular to the surface of FFS for different Ma .	160
6.41	Variation of the non-dimensional temperature perpendicular to the surface of FFS for different Ma .	161
6.42	Variation of pressure coefficient C_p along the lower and upper surfaces of FFS for different Ma .	162
6.43	Variation of skin friction coefficient C_f along the lower and upper surfaces of FFS for different Ma .	163
6.44	Variation of heat transfer coefficient C_h along the lower and upper surfaces of FFS for different Ma .	164
6.45	Variation of the non-dimensional velocity perpendicular to the surface of FFS for different T_w .	166
6.46	Variation of the non-dimensional pressure perpendicular to the surface of FFS for different T_w .	167
6.47	Variation of the non-dimensional temperature perpendicular to the surface of FFS for different T_w .	168
6.48	Variation of pressure coefficient C_p along the lower and upper surface of FFS for different T_w .	169
6.49	Variation of skin friction coefficient C_f along the lower and upper surfaces of FFS for different T_w .	170
6.50	Variation of heat transfer coefficient C_h along the lower and upper surfaces of FFS for different T_w .	171
6.51	Contours of non-dimensional flow-field properties for $H = 60mm$, $Kn = 25$ and $Kn = 1.06$.	173
6.52	Variation of the non-dimensional velocity perpendicular to the surface of FFS for different Kn .	174
6.53	Variation of the non-dimensional velocity along the length of FFS for different Kn .	176
6.54	Streamlines near the step of FFS for (a) $Kn = 0.05$, (b) $Kn = 0.1$, (c) $Kn = 1.06$, (d) $Kn = 10.33$, (e) $Kn = 21.10$.	177
6.55	Variation of the non-dimensional pressure perpendicular to the surface of FFS for different Kn .	179
6.56	Variation of the non-dimensional pressure along the length of FFS for different Kn .	180
6.57	Variation of the non-dimensional temperature perpendicular to the surface of FFS for different Kn .	182
6.58	Variation of the non-dimensional temperature along the length of FFS for different Kn .	183
6.59	Variation of pressure coefficient C_p along the lower and upper surfaces of FFS for different Kn .	184
6.60	Variation of skin friction coefficient C_f along the lower and upper surfaces of FFS for different Kn .	185

6.61	Variation of heat transfer coefficient C_h along the lower and upper surfaces of FFS for different Kn	186
6.62	Schematic of the 2D open cavity.	188
6.63	Meshed domain of the 2D open cavity.	189
6.64	Variation of the non-dimensional velocity perpendicular to the surface of open cavity for different Ma	191
6.65	Variation of the non-dimensional velocity along the length of open cavity for different Ma	192
6.66	Variation of the non-dimensional pressure perpendicular to the surface of open cavity for different Ma	193
6.67	Variation of the non-dimensional pressure along the length of open cavity for different Ma	194
6.68	Variation of the non-dimensional temperature perpendicular to the surface of open cavity for different Ma	196
6.69	Variation of the non-dimensional temperature along the length of open cavity for different Ma	197
6.70	Variation of pressure coefficient C_p for open cavity for different Ma . . .	199
6.71	Variation of skin friction coefficient C_f for open cavity for different Ma . .	200
6.72	Variation of heat transfer coefficient C_h for open cavity for different Ma . .	202
6.73	Variation of the non-dimensional velocity perpendicular to the surface of open cavity for different T_w	204
6.74	Variation of the non-dimensional velocity along the length of open cavity for different T_w	205
6.75	Variation of the non-dimensional pressure perpendicular to the surface of open cavity for different T_w	206
6.76	Variation of the non-dimensional pressure along the length of open cavity for different T_w	207
6.77	Variation of the non-dimensional temperature perpendicular to the surface of open cavity for different T_w	209
6.78	Variation of the non-dimensional temperature along the length of open cavity for different T_w	210
6.79	Variation of pressure coefficient C_p for open cavity for different T_w . . .	211
6.80	Variation of skin friction coefficient C_f for open cavity for different T_w . .	213
6.81	Variation of heat transfer coefficient C_h for open cavity for different T_w . .	214
6.82	Variation of the non-dimensional velocity perpendicular to the surface of open cavity for different Kn	216
6.83	Variation of the non-dimensional velocity along the length of open cavity for different Kn	218
6.84	Streamlines inside the cavity for (a) $Kn= 0.05$, (b) $Kn= 0.1$, (c) $Kn= 1.06$, (d) $Kn= 10.33$, (e) $Kn= 21.10$	219
6.85	Variation of the non-dimensional pressure perpendicular to the surface of open cavity for different Kn	221
6.86	Variation of the non-dimensional pressure along the length of open cavity for different Kn	222

6.87	Variation of the non-dimensional temperature perpendicular to the surface of open cavity for different Kn	223
6.88	Variation of the non-dimensional temperature along the length of open cavity for different Kn	225
6.89	Variation of pressure coefficient C_p for open cavity for different Kn	226
6.90	Variation of skin friction coefficient C_f for open cavity for different Kn	228
6.91	Variation of heat transfer coefficient C_h for open cavity for different Kn	229
6.92	Schematic of the 2D wall-mounted cube.	231
6.93	Meshed domain of the 2D wall-mounted cube.	232
6.94	Variation of the non-dimensional velocity along the length of wall-mounted cube for different Ma	233
6.95	Variation of the non-dimensional pressure along the length of wall-mounted cube for different Ma	234
6.96	Variation of the non-dimensional temperature along the length of wall-mounted cube for different Ma	235
6.97	Variation of pressure coefficient C_p for wall-mounted cube for different Ma	237
6.98	Variation of skin friction coefficient C_f for wall-mounted cube for different Ma	238
6.99	Variation of heat transfer coefficient C_h for wall-mounted cube for different Ma	239
6.100	Variation of the non-dimensional velocity along the length of wall-mounted cube for different T_w	241
6.101	Variation of the non-dimensional pressure along the length of wall-mounted cube for different T_w	242
6.102	Variation of the non-dimensional temperature along the length of wall-mounted cube for different T_w	243
6.103	Variation of pressure coefficient C_p for wall-mounted cube for different T_w	244
6.104	Variation of skin friction coefficient C_f for wall-mounted cube for different T_w	246
6.105	Variation of heat transfer coefficient C_h for wall-mounted cube for different T_w	247
6.106	Variation of the non-dimensional velocity along the length of wall-mounted cube for different Kn	249
6.107	Variation of the non-dimensional pressure along the length of wall-mounted cube for different Kn	250
6.108	Variation of the non-dimensional temperature along the length of wall-mounted cube for different Kn	251
6.109	Variation of pressure coefficient C_p for wall-mounted cube for different Kn	252
6.110	Variation of skin friction coefficient C_f for wall-mounted cube for different Kn	253
6.111	Variation of heat transfer coefficient C_h for wall-mounted cube for different Kn	255

6.112	Contours of different temperature components of open cavity for $H = 60\text{mm}$, $Kn = 25$ and $Kn = 1.06$	257
6.113	Comparison of for reacting and non-reacting cases of open cavity for different Kn	259
6.114	Comparison of the non-dimensional overall temperature along the length of the open cavity for different Kn	260

List of Abbreviations

BE	Boltzmann Equation
DSMC	Direct Simulation Monte Carlo
LDC	Lid Driven Cavity
MD	Molecular Dynamics
NSF	Navier-Stokes Fourier
PPC	Particles Per Cell
FFS	Forward-Facing Step
BFS	Backward-Facing Step
WMC	Wall-Mounted Cube

List of Symbols

Symbol	Definition	Units
A	Surface area	m^2
c	Molecular velocity	m/s
c'	Thermal velocity of the molecules	m/s
c_0	Macroscopic mean velocity	m/s
C_p	Pressure coefficient	-
C_f	Skin friction coefficient	-
C_h	Heat transfer coefficient	-
d	Particle diameter	m
f	Velocity distribution function	-
h, L	Characteristic length	m
k	Boltzmann constant	-
Kn	Knudsen Number	-
m	Molecular mass	kg
Ma	Mach Number	-
n	Number density	m^{-3}
N	Number of molecules	-
N_c	Maximum number of particle pairs for binary collisions	-
p	Pressure	Pa
q	Heat Flux	W/m^2
R	Gas constant	$J/mol.K$
Re	Reynolds Number	-
t	Time	s

T	Temperature	K
x	Axial coordinate in x direction	m
y	Axial coordinate in y direction	m
X	Mole fraction	-
Z	Compressibility factor	-
Greek symbol	Definition	Units
ρ	Density	kg/m^3
μ	Viscosity	Ns/m^2
σ	Collision cross section	m^2
α	Power law exponent	-
Ω	Solid angle	sr
ω	Viscosity index	-
λ	Mean free path	m
τ	Shear stress	N/m^2
ζ	Degree of freedom	-
δ	Boundary layer thickness	-
Subscripts	Definition	Units
w	Wall	-
*	Post-collision value	-
∞	Free stream	-
0	Overall value	-
i	Incident molecule	-
r	Reflected molecule	-
ref	Reference value	-

Chapter 1

Introduction

In this chapter, a brief background of the motivation in carrying out the research is stated. The Knudsen number is defined, followed by the classification of different regimes based on the Knudsen number. A brief comparison of the various approaches to model a fluid flow problem is provided. A bird's eye view of the Direct Simulation Monte Carlo (DSMC) method, the computational methodology adopted in this study, is given. The scope of the present work is explained, and finally, the outline of the thesis is presented.

1.1 Background of rarefied gas flows

Transport phenomena are one of the essential areas of engineering, whose thorough understanding is essential for the design of better technologies. There have been numerous advances in this domain in the recent years, owing to the developments in experimental and more particularly, numerical methods. Typically, the fluid flow and heat transfer aspects are modeled mathematically with the help of several critical assumptions, one of

them being the continuum assumption of a fluid. This is however not a valid assumption for specific kinds of flows called rarefied gas flows, for which the mean free path (λ) of the molecules is comparable to the characteristic length scale (L) of the problem. This typically happens at low densities or small length scales and is described by a dimensionless quantity called Knudsen number.

The rarefied gas dynamics finds applications for low Knudsen number flows. They often occur in the flows in the outer atmosphere and MEMS/NEMS devices. Airbag accelerometers, Knudsen pumps, disposable medical devices, electrostatic actuators, micro-turbines, and micro-pumps are some of the MEMS/NEMS applications [1]. Other applications of this study are in high-altitude rocket plumes, spacecraft propulsion, vacuum technology to name a few. Some of the applications are shown in Figure 1.1.

The study of high-speed re-entry vehicles entering the earth's atmosphere is one of the widely studied problems in the space community. This interest is mainly due to the design of new generation space vehicles that can improve the existing space shuttle designs. The re-entry vehicles coming into the earth's atmosphere have velocities of several orders of km/s. Furthermore, they usually experience different rarefaction regimes, ambient temperatures, and intricate flow patterns, including shocks [2]. Also, the flow field properties are greatly influenced at higher altitudes [3] due to the rarefied environment. When these vehicles enter into the atmosphere, they encounter friction due to the earth's atmosphere resulting in the slowing down of the vehicles. However, these friction effects result in the increased surface temperature, which increases the thermal and aerodynamic loads on the surfaces of the vehicle [4]. Thus, the design of the vehicle should be made in accordance with the surface temperatures such that the material used in the construction

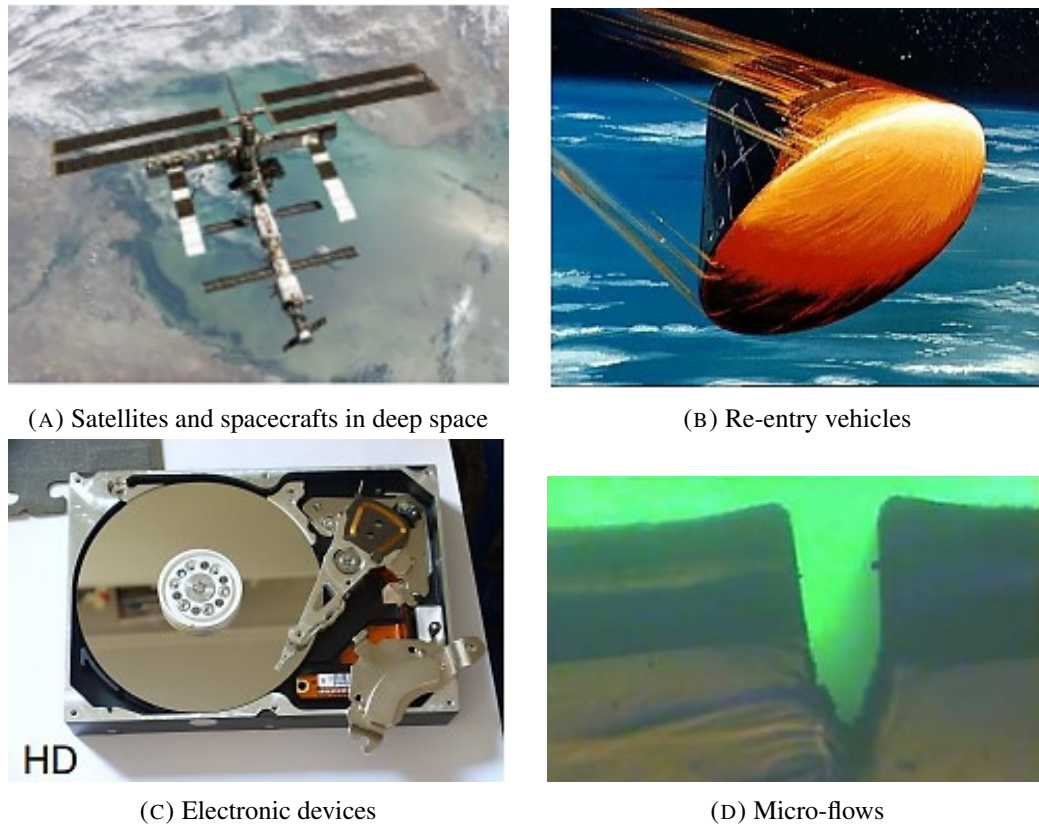


FIGURE 1.1: Applications of rarefied gas flows (retrieved from <https://en.wikipedia.org/wiki/>)

can withstand those temperatures and protect the crew onboard. During the design stage of the vehicles or during the flight, there sometimes exists certain surface disturbances which are in the form of steps, gaps, cavities, perturbances. These surface discontinuities are occasionally inevitable due to placement of certain sensors, parachute placement, or the landing gears that are all essential for the vehicle's safe functioning. Also, the debris from the space may collide with the vehicle and cause these imperfections. When these vehicles enter back, the hot gases prevalent in the atmosphere flow across these surface imperfections, thereby increasing the vehicle's safe design limits, leading to a catastrophe (Figure 1.2). Furthermore, these hot gases may alter the mechanical properties of the material used in the construction and cause complex flow behavior. These thermal and aerodynamic loads can also change the shape of the existing cavities, steps, gaps and

cause the formation of stagnation points, flow separation, circulation, shocks, and other complex flow phenomena such as transition towards turbulence.

For instance, the space shuttle Columbia experienced a catastrophic failure during its re-entry on February 1, 2003. The fatality occurred at an altitude of about 61.3km from the earth's surface, and the vehicle was traveling at a speed of Mach 18. The post fatality investigations [5–7] carried out by various teams at NASA showed that there was high temperature recorded on the side fuselage. However, it was not accurately ascertained that this high temperature was the culprit for the vehicle's catastrophe. Also, many experimental and numerical studies were conducted to verify the cause of the failure. After extensive studies, it was determined that the fragment of the insulation foam from the fuel tank had broken off during the take-off and had hit the left-wing, which was one of the probable causes of the failure. This incident reiterates the complexity involved in the design of hypersonic vehicles and how minor surface discontinuities can ultimately cause the vehicle's failure. Furthermore, it also shows the importance of modeling and predicting the flow field and aerodynamic surface properties for the safe design of atmospheric re-entry vehicles. The estimation of these thermal and aerodynamic loads can be carried out either by experimentation, which is a very costly affair. Numerical modeling and computations can be performed, which is relatively feasible and is steadily gaining significance [8,9].

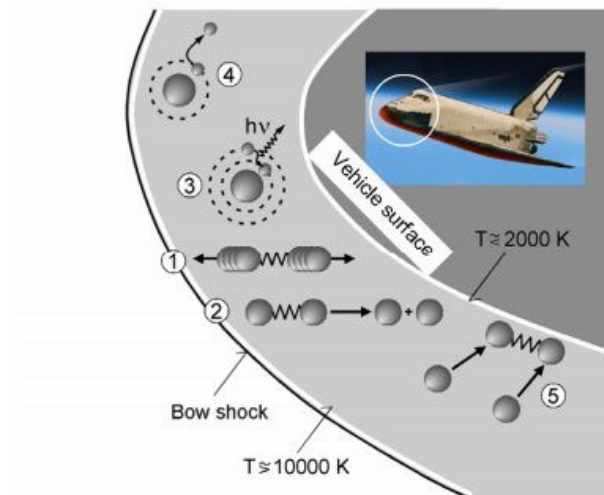


FIGURE 1.2: Effects of temperature during re-entry. (adapted from <https://core.ac.uk/download/pdf/11133242.pdf>)

1.2 The Knudsen number

In fluid dynamics, the continuum fluid approximation breaks down when the average distance traveled by the molecules between collisions becomes comparable with the system's characteristic dimension. In order to classify such flows, a non-dimensional number known as the Knudsen number (Kn) is defined, which is defined as “the ratio of the mean free path traveled by molecules between collisions to the characteristic length of the body.”

$$Kn = \frac{\lambda}{L} \quad (1.1)$$

The local Knudsen number in a similar way is defined as the ratio of the local mean free path (λ) to a characteristic length (l) determined using the gradient of any macroscopic property.

$$l = \frac{\varphi}{\nabla\varphi} \quad (1.2)$$

The mean free path is defined as the average distance traveled by the molecules between successive collisions and is given by,

$$l = \frac{1}{\sqrt{2}\pi n d^2} \quad (1.3)$$

Where, n denotes the number density of the gas molecules, and d indicates the diameter of the gas molecules.

The Knudsen number is also defined in terms of the Reynolds number (Re) and Mach number (Ma) and is given by,

$$Kn = \sqrt{\frac{\gamma\pi}{2}} \frac{Ma}{Re} \quad (1.4)$$

In the above equation Ma and Re are defined as,

$$Ma = \frac{U_\infty}{\sqrt{\gamma RT}} \quad (1.5)$$

$$Re = \frac{\rho_\infty U_\infty L}{\mu} \quad (1.6)$$

Where, ρ_∞ , U_∞ , L , μ , γ represent the gas density, free-stream velocity, characteristic length, gas dynamic viscosity, and ratio of specific heats respectively.

1.3 Classification of flow regimes

The re-entry vehicles, while entering back into the earth's atmosphere, experience various Mach regimes such as subsonic, supersonic, and hypersonic. Also, they encounter

different flow regimes such as slip, transition, and free molecular. Figure 1.3 shows the flow regime classification. Based on Kn , the flows are classified into the following regimes [10–12]: (1) continuum flow regime, where $Kn < 0.001$. The collision frequency between gas molecules is greater here than that among gas molecules and walls and can be approximated by the traditional Navier-Stokes-Fourier (NSF) equations; (2) slip flow regime, where $0.001 < Kn < 0.1$. The velocity drop arises at the gas-solid boundary interface here, and the rarefaction effects affect the fluid behavior and can be approximated using NSF equations with slip boundary conditions; (3) transitional flow regime, where $1 < Kn < 10$. The interaction between gas molecules, walls and gas molecules cannot be overlooked in this regime, also due to the molecular nature of the fluid, the continuum model is ineffective; and (4) free-molecular regime, where $Kn > 10$. Here, the collision frequency among gas molecules and walls is greater than among gas molecules and must therefore be based on accurate molecular motion. In the transitional and free-molecular regime, the NSF equations cannot model gas behavior. The above-mentioned slip regime range is controversial for complex 2D/3D geometries and should be dealt with accordingly [10]. Also, the Boltzmann equation can model the flows in all the regimes, having the Knudsen numbers ranging from zero to infinity. As Kn increases beyond 0.1, the rarefaction effects are more predominant, leading to the failure of the continuum hypothesis. In such circumstances, alternate numerical methods such as molecular dynamics (MD) [13], direct simulation Monte Carlo (DSMC) [14], and solution of full Boltzmann equations (BE) [15] are standard techniques for studying rarefied gas flows [16].

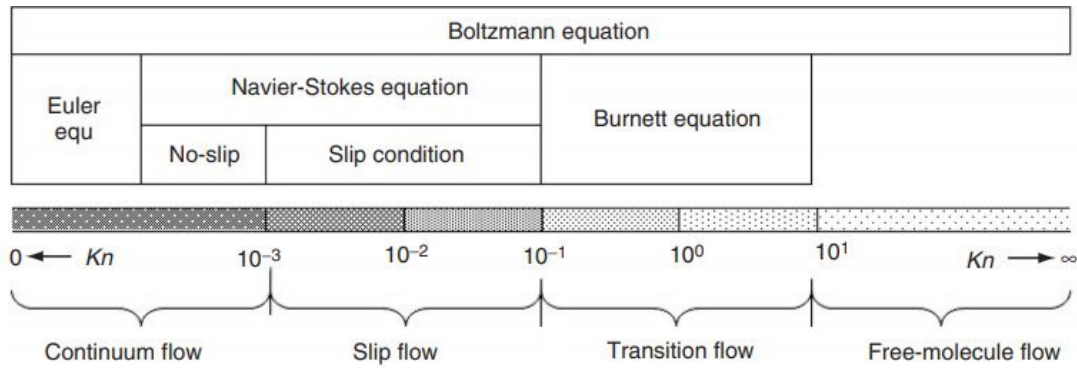


FIGURE 1.3: Flow regimes in terms of Knudsen number.(adapted from <http://repository.ias.ac.in/115048/1/1759-3093.2.1.1.pdf>)

1.4 Macroscopic and Microscopic approaches

For almost several decades, the fluid flow and heat transfer phenomena are modeled using either the macroscopic or microscopic approaches. Even though they adopt different strategies, they ultimately end up with a similar set of macroscopic equations for the same model under consideration. In the macroscopic view, the molecular nature of each individual molecule is neglected. The primary focus is on estimating the parameters such as velocity, pressure, temperature, and density by solving the Navier-Stokes equation, a non-linear form of partial differential equations (PDE). These equations are then solved either by finite difference, finite element, or finite volume methods. The majority of the CFD methods are based on the formulation mentioned above.

Contrary to the macroscopic approach, the microscopic approach considers the molecular behavior and does not directly solve the PDE. This approach involves either solving the microscopic equations or the mesoscopic equation, such as the Boltzmann equations, by considering a certain number of simulated molecules representing a fraction of the actual molecules. Then the position, velocity, and state of the simulated molecules

are determined accurately. The required macroscopic PDE's can then be obtained by multi-scale analysis [17]. The microscopic method can either be deterministic, such as the molecular dynamics method, or probabilistic, such as the DSMC method. In this study, the DSMC method is adapted, and a brief overview is provided in the next section.

1.5 Overview of the DSMC method

The DSMC process, pioneered by G.A. Bird [18], uses a particle-based technique for simulating rarefied gas flows. In DSMC, the simulated molecules represent large amounts of real molecules. The motion of particles and their collision interactions describe the physics of gas. The transportation of mass, momentum, and energy at the microscopic level is assessed. Movements are modeled in a deterministic way, whereas the collisions in a stochastic manner. Separation of the deterministic molecular movements and the stochastic inter-molecular collisions form the central hypothesis of the DSMC technique. DSMC is mainly used in simulating high-speed rarefied gas flows having higher levels of rarefaction. This phenomenon is present in different fields of research, which include high-speed, high-altitude vehicles, such as space shuttles, re-entry vehicles, to name a few. DSMC is also used to investigate flows at a micro-scale, such as flow-through micro/nano channels that have various applications. The technique can also be implemented in the continuum regime, but it requires enormous computer resources or is computationally expensive. The DSMC method has evolved to be one of the reliable computational methods for modeling the physics of the rarefied gas flows, and many researchers have approved its accuracy.

1.6 Scope of the present work

In this study, initially, the rarefied flow physics for internal flows is investigated. The problem has several applications in the fields of melt spinning, coating and drying technologies, and the aircraft industry. The conventional lid-driven case is used as a test case for validation, and the rarefied flow behavior in the double-sided and four-sided lid-driven cavity is investigated. Then the rarefied flow physics for the external flows are analyzed at length. For this purpose, the flow past a backward-facing step, forward-facing step, flow past an open cavity and flow over wall mounted cube are the various configurations that are examined. These are some of the common surface discontinuities observed on the re-entry vehicles' surface, whose study plays a critical role in designing such vehicles, as mentioned in section 1.1. The flow-field and aerodynamic properties are investigated and presented in detail in the subsequent chapters. The scope of this work is mainly numerical; however, the validations are performed using the experimental results in the published literature. The various flow configurations are modeled numerically and analyzed using the DSMC approach. Furthermore, various parametric studies are carried out which involve different expansion ratios, Mach numbers, Wall temperatures, Knudsen numbers to bring out a comprehensive picture of the various configurations.

1.7 Outline of the thesis

The research work presented in this thesis is split into seven chapters. A brief description of each chapter is presented below:

Chapter 1 describes the introduction of the work. The purpose and motivation for carrying out the study are presented. The non-dimensional number known as the Knudsen number, which classifies the flow regimes, is discussed. The various modeling approaches adopted while analyzing a fluid flow problem are also introduced. A brief overview of the computational methodology adopted in this study, i.e., the Direct Simulation Monte Carlo technique, is discussed. The different flow configurations which were analyzed are also discussed. Finally, the outline of the thesis is presented in this chapter.

Chapter 2 gives the various works in the literature pertaining to the physics of the rarefied gas flows. The different research works for internal flow configuration, such as the lid-driven cavity, are initially discussed. Then the review of various external flows such as flow over a backward-facing step, forward-facing step, open cavity, and the wall-mounted cube is discussed. Based on the past literature, various gaps have been identified, and the objectives of the present work have been formulated and presented in this chapter.

Chapter 3 presents a detailed overview of the computational methodology adopted in this study. The Direct Simulation Monte Carlo method is discussed at length, along with the algorithm involved and the solver used for the analysis. Also, various collision models and sampling schemes used in the DSMC and the evaluation of different macroscopic parameters are discussed briefly. The chapter concludes with certain limitations of the DSMC methodology.

Chapter 4 deals with various validation studies that were performed. Initially the different independence studies are shown in detail to confirm the accuracy of the results. Then

the validation studies conducted for both the internal and external flows are presented. Also, the validations for the chemically reacting flows are discussed.

Chapter 5 gives a detailed analysis of the physics of the rarefied flow in internally bounded flows. The lid-driven cavity for both double-sided and four-sided wall movements is analyzed at length, and various flow parameters are investigated in this chapter.

Chapter 6 deals with the external flow configurations. The different flow configurations as mentioned in section 1.6 are thoroughly examined. The various flow and aerodynamic properties investigated and parametric studies carried out are presented in this chapter.

Chapter 7 gives the significant conclusions from this study, the specific contributions made, usefulness of the work, some limitations and future scope of work.

Chapter 2

Review of the past work

In this chapter, a broad literature review about the various flow configurations is given. The literature of the rarefied gas flows in internal flow configurations such as the lid-driven cavity and the various methods adopted are presented in detail. Next, the previous work regarding the flow past a backward-facing step is presented. Similarly, a review of the work carried out for the forward-facing step, open cavity, and wall-mounted cube is shown. The various gaps identified after the literature was examined are stated, and subsequently, the various objectives outlined in this study are summarized.

2.1 Lid-driven cavity

Several studies have been performed for the driven cavity flows using various computational and experimental methods, mainly for the single-sided and double-sided lid-driven cavity [19–21]. Extensive studies have been conducted on single lid-driven cavity by many researchers [22–24] with the help of conventional numerical methods like finite

difference, finite element, stream function vorticity approach for incompressible flows and methods like DSMC, Unified gas kinetic scheme, Bhatnagar-Gross-Krook (BGK) model and Lattice Boltzmann method for rarefied gas flows. Furthermore, most of the studies conducted on a single lid-driven cavity have been in the continuum regime as a benchmark for validation purposes. In contrast, in the rarefied regime, limited studies have been performed.

Several authors have studied the hydrodynamic and thermal aspects of rarefied gas flow for the single-lid driven cavity case at different degrees of rarefaction and different length scales using various techniques [25–28]. Auld and Lan [25] studied the microcavity flow utilizing parallelized DSMC method. Their results matched well with those obtained using the Lattice-Boltzmann method and Navier-Stokes-Fourier equations. Mohammadzadeh *et al.* [10] investigated the thermal characteristics of micro-nanocavity flow in the slip regime using the DSMC method and introduced entropy density as an innovative tool to study the non-equilibrium effects. Mohammadzadeh *et al.* [26] also studied entropy behavior and heat flux in Micro/Nano cavities in the slip and transition regimes with the help of the DSMC method. Liu *et al.* [27] investigated heat transfer in a vacuum package in continuum and early transition regimes in Micro-Electro-Mechanical-Systems (MEMS) devices, whereas Cai *et al.* [28] performed a similar study in the continuum and free molecular regimes.

Rana *et al.* [29] used the Finite-Difference scheme in the transition regime to study the lid-driven cavity flow and compared the solutions obtained using the DSMC method, Integro Moment Method (IMM), and regularised 13 moments (R13) equations which were all in good agreement. Moghadam *et al.* [30] investigated the hydrothermal

behavior of fluid in the slip and transition regime using the DSMC method. Eskandari *et al.* [31], conducted a similar study but with a Time Relaxed Monte Carlo (TRMC) scheme. John *et al.* [32] investigated the heat transfer phenomena in the transition regime using the DSMC method. Counter-Intuitively, heat transfer from cold to hot regions was observed; due to the influence of expansion cooling and viscous dissipation. John *et al.* [33] in another study investigated the incomplete surface accommodation and its effects on the heat transfer mechanisms for the driven cavity flows. Naris and Valougeorgis [34] studied the flow aspects in a single lid-driven cavity using DSMC across all rarefaction regimes. Aoki *et al.* [35] performed a similar study using the Bhatnagar-Gross-Krook (BGK) model to numerically investigate the rarefied flow behavior of the molecular velocity distribution.

Huang *et al.* [36] formulated a unified gas-kinetic scheme based on the kinetic model for flow in a lid-driven cavity. They concluded that their kinetic model had superior capability compared to conventional Navier-Stokes solver in capturing rarefied flow behavior. Venugopal and Girimaji [37] also used the unified gas kinetic scheme to study lid-driven cavity flow in the near-continuum/slip regime. Wu *et al.* [38] investigated the effect of the oscillating frequency and aspect ratio on the rarefied lid-driven cavity flow using the Boltzmann equation in its linearized form. Wang *et al.* [39] in a recent study investigated the thermal and flow characteristics in the rarefaction regime on oscillatory flow in a single lid-driven square cavity using the kinetic theory of gases in all flow regimes. Bhopalam *et al.* [40] in another recent study has studied the two-sided cavity problem using the Lattice Boltzmann method having parallel and anti-parallel wall motions.

Another configuration that has great importance from both benchmarking and application viewpoint is the four-sided cavity. The flow here results from the tangential movement of all the cavity boundaries facing each other with uniform velocities. Despite the plethora of literature available on lid-driven cavities, most of them were performed for single lid-driven-cavity. Very few studies have looked at flows in the four-sided cavity [41].

2.2 Backward-facing step

Many researchers have reported several studies that involve the experimental, analytical, and numerical studies of flow over simple geometries involving protuberances [42–45], notches [46, 47], cavities [48–51], and gaps [52–54]. Also, the investigations performed involve the subsonic [55, 56], supersonic [57, 58], and hypersonic flows [59, 60] past the Backward facing step (BFS), but the majority of them are in the continuum regime. Furthermore, many researchers have investigated the flow past BFS at different rarefaction regimes, mainly for the low-speed microscale flows. There have also been studies on macroscale flows that differ from the microflows in a few aspects, even though the flow is analyzed in the same regime. The pressure drop in microflows is considerable when compared to macroscale flows even though they are at the same Kn . Also, the large surface to area ratio in microscale flows makes the surface properties significant. Furthermore, in microscale flows, the existence of rough surfaces and high gradients in the fluid flow properties affect the nature of flow transport. However, the shockwave effects are more substantial in macroscale flows compared to the microscale counterparts.

In the slip flow regime, Choi *et al.* [61] proposed the Langmuir slip boundary condition combined with the continuum-based compressible Navier-Stokes equation and implemented the same for the flow over BFS. Hsieh [62] investigated the fluid flow properties in the slip regime for the flow over 3D microscale BFS using the DSMC method. Beskok [63] developed a velocity-slip boundary condition, based on obtaining the information of slip at a distance of one mean free path away from the surface and compared the same with the DSMC results, which were found to agree with each other. Celik and Edis [64] formulated a characteristic based Navier-Stokes FEM solver and studied the rarefied gas flow through a BFS duct. Rached and Daher [65] numerically studied the rarefied gas flow through a BFS in the slip regime using a control volume-based numerical method. Similarly, Baysal *et al.* [66] also used the Navier-Stokes equation with slip/jump boundary conditions and investigated the control of separated flow past a BFS. Xue and Chen [67] studied the micro BFS flows using the DSMC method, both in the slip and transitional regimes for different Kn. Xue *et al.* [68] also performed a similar study.

In the transitional flow regime, Kursun and Kapat [69] numerically studied the rarefied gas flow through BFS using the DSMC-IP (Information preservation) method. Bao and Lin [70] used the continuum-based Burnett equations to study the microscale BFS flows in the transitional regime. Darbandi and Roohi [71] used the DSMC method to study subsonic flow through micro/nano BFS over a considerable range of rarefaction regimes. Mahdavi *et al.* [72] studied the nano/micro BFS flow using the slip/jump boundary conditions with N_2 as working fluid and compared the CFD and DSMC solutions. The CFD studies used the Maxwell Slip (MS) and hybrid slip/jump Langmuir-Maxwell Smoluchowski (LMS) boundary conditions. The tangential momentum accommodation

and thermal accommodation coefficient were fixed to 1 for both CFD and DSMC. They compared their CFD results with the DSMC data. It was observed that the hybrid slip/jump boundary conditions had a better prediction of flow and thermal properties compared to the results using Maxwell/Smoluchowski boundary conditions. Gavasane *et al.* [73] studied argon flow through a micro-BFS for different Kn and pressure ratios. From the above discussion, it can be observed that most of the studies either considered monoatomic argon or diatomic nitrogen as the fluid in their investigations. Recently Leite *et al.* [74] also studied the hypersonic air flow past BFS using the DSMC method and analyzed the effects of step heights on the surface properties.

2.3 Forward-facing step

Existing literature provides plenty of references to the physics of flow past Forward facing step (FFS). However, the majority are in the continuum regime, so we outline only a few of them in this overview. Bogdonoff & Kepler [75] experimentally examined the flow separation and shockwave boundary-layer interaction for the FFS flow and reported flow separation at Mach 3 and pressure ratio of 2, respectively. Rogers & Berry [76] experimentally tested FFS in the supersonic flow of roughly Mach 2, with a thick laminar boundary layer. The study showed that the highest-pressure surge existed on the step face; moreover, this pressure surge was influenced by the ratio of $(\frac{h}{L})$, i.e., step height (h) to the distance from the leading edge of flat-plate to the step position (L). Similarly, Driftmyer [77] performed an experimental study on FFS for the specific case where step height (h) was below the boundary layer thickness (δ) for a free-stream Mach number of 4.9 and Reynolds number between $(0.8 - 4) \times 10^6$. Results showed that the pressure

distribution measured in the region of separation before the step was influenced by Re and (h/δ) .

Pullin & Harvey [78] computationally evaluated a 2D, rarefied hypersonic FFS flow with N_2 as the fluid and free-stream Mach number of 22. Their results indicated rapidly decelerating flow, accompanied by compression near the vicinity of the step. Furthermore, their numerical findings matched well with the experimental results. Grotowsky & Ballmann [79] also numerically investigated laminar hypersonic flow over both FFS and BFS using the Navier-Stokes equations for a free-stream Mach number of 8, Reynolds number of the order of 10^8 , at an altitude of 30 km. Although their numerical results matched well with experimental data from the literature, they indicated significant differences in the wall heat flux analysis, perhaps because of its imprecise measurement. Leite *et al.*[80] performed a numerical study using DSMC for rarefied flow over FFS for different step heights. Their research showed that a formidable compression region in front of the frontal face influenced the flow characteristics upstream of the step. Furthermore, high-pressure regions and high heating loads occurred on the upstream and frontal face.

2.4 Open cavity

Several studies featuring experimental, numerical, and analytical were carried out previously for analyzing the thermal and aerodynamic loads [81–84] on the surfaces of aerospace re-entry vehicles. However, we shall describe studies that have been carried out in the past to study the flow field structure around open cavities. Nestler *et al.* [84]

experimentally investigated the hypersonic turbulent flow past cavity and steps and analyzed the pressure distributions. Everhart *et al.* [85] also experimentally investigated the hypersonic flow past rectangular cavity and investigated pressure gradient influence on the surface properties. Creighton and Hillier [86] carried out several studies on the hypersonic flow over annular cavities. They studied the effect of cavity length to depth ratios on the flow field. Morgenstern Jr. and Chokani [49] used the CFD approach to study the unsteady hypersonic cavity flow and investigated the influence of Reynolds number and cavity length to height ratios ($\frac{L}{H}$) on the heat transfer rates. Palharini *et al.* [87] used the DSMC approach to investigate the cavity flow and studied three-dimensionality's effect on the aerodynamic properties. Santos *et al.* [88] studied the impact of change in cavity height for a range of ($\frac{L}{H}$) ratio on the aerodynamic properties in a hypersonic cavity flow using DSMC. Guo *et al.* [2] applied the DSMC approach to numerically investigate the rarefied hypersonic flow over various cavity shapes. They studied the effect of length-to-depth ratio, rear wall-to-front wall height ratio, and the inclination of the front wall and rear wall on the flow field properties. Guo *et al.* [89] also studied the 2-D hypersonic cavity flow for various Knudsen numbers ranging from continuum to transition regime and investigated the associated flow-field. Palharini *et al.* [90] employed Quantum Kinetic (QE) modeling using the DSMC method to simulate chemical reactions for investigating the flow-field structure characteristics in a 3-D hypersonic flow over a cavity in the transitional regime for several length-to-depth ($\frac{L}{D}$) ratios. In another study, Palharnini *et al.* [91] applied the DSMC method and carried out a detailed investigation on the effect of change in cavity length for different ($\frac{L}{D}$) ratios in the cavity, involving non-reacting hypersonic flow in the transitional regime and evaluated the surface properties. The impact of the Maxwellian accommodation coefficient on the

rarefied hypersonic flows over 3-D cavity flows in the transitional regime was studied by Jin *et al.* [92] using the DSMC approach.

2.5 Wall-mounted cube

The wall-mounted cube is one of the simplest geometries with corners. Compared to flow around a cylinder, the flow around a cube separates at fixed points. The analysis of the physics of the flow over a wall-mounted cube is one of the primary concerns to researchers owing to its large number of practical applications. In the continuum regime, it has applications in understanding the flow around buildings. In the rarefied regime, it finds application in the flow around atmospheric re-entry vehicles and in designing better microfluidic systems sensors at the microscale. In the continuum regime, experimental studies by Castro and Robins [93] for the uniform flow over a surface-mounted cube were analyzed for the mean surface pressure and mean fluctuating velocity. Similar studies on cubes with different angles of attack were carried out by Hoxey *et al.*[94], whereas Sousa [95] measured the velocity field around a wall-mounted cube using Particle Image Velocimetry (PIV). Nakamura *et al.*[96] investigated the fluid flow and heat transfer properties around a cube mounted on a surface. Various numerical studies on flow past wall-mounted cube are reported in the literature in the continuum regime. Yakhot *et al.*[97] performed Direct Numerical Simulations (DNS) of flow over the 3D cube. Lim *et al.*[98] and Murakami and Mochida [99] used the Large Eddy Simulations (LES) to evaluate the flow properties over a 3D cube. Although much work has been carried out in analyzing the external flow over various bluff bodies in the continuum regime, very

few researchers have studied the flows in the other regimes, viz., (slip, transitional, and free molecular).

2.6 Gaps identified in the literature

It can be understood from the above literature review that several experimental and numerical studies have been carried out in the rarefied flow domain. Also, the majority of the numerical studies employ the DSMC method due to its capability of modeling flows involving different rarefaction regimes. Nonetheless, the aerothermodynamic conditions encountered by hypersonic re-entry vehicles are challenging to analyze due to the various complexities that are not adequately recorded in the open literature. Most of the past research primarily investigated the rarefaction effects at lower Knudsen numbers. Moreover, only a handful of studies have analyzed the range of rarefaction regimes that the hypersonic re-entry vehicles encounter, but they are limited to the transitional flow regime. However, the re-entry vehicles typically experience higher levels of rarefaction at higher altitudes, and the rarefaction levels reduce as they descend back to the earth. However, to the best of the authors' knowledge, a handful of studies provide a comprehensive analysis of the effects of rarefaction on the flow and surface properties that a re-entry vehicle typically encounters during its flight, particularly in the free molecular regime. Furthermore, a comprehensive analysis of the effects of Mach number and wall temperature is also scarce and explored in the present study. Hence the identified research gaps are as mentioned below.

- i. The literature review shows very few works on rarefied flow in double-sided and four-sided lid-driven cavities. The various flow features have not been reported for various wall movements, such as the anti-parallel and parallel motion of the walls and the effects of Mach numbers, Knudsen numbers on flow physics are also scarce.
- ii. The literature available on the rarefied gas flow behavior in a cavity (i.e., combined backward facing step and forward-facing step (BFS-FFS) using the DSMC method is scarce. There is ample scope for investigating this problem.
- iii. The fluid flow problem past a wall-mounted cube is one of the fundamental fluid dynamics problems and has been studied extensively for the continuum flows. However, this problem has not been investigated for the rarefied flows to the required extent.
- iv. Till date, a handful of researchers have addressed the effects of the free-stream Mach number, free-stream Knudsen number, and different wall temperatures on the flow field and aerodynamic characteristics for only a limited number of flow configurations. This study aims to bridge the gap and explore the flow-field and aerodynamic properties for various flow configurations. Also, the influence of different surface irregularities (such as BFS, FFS, Open cavity, Wall-mounted cube) on re-entry vehicles that arise due to sensor installations, manufacturing tolerances, and the placement of thermal protection system tiles are not thoroughly documented.

2.7 Objectives of the present work

Based on the comprehensive literature review conducted, the main objectives formulated for the present study is given below:

- I. Analysis of rarefied flow behavior inside a lid-driven cavity for different wall movements.
- II. Study of rarefied gas flows over an open cavity (combined BFS-FFS).
- III. Study of rarefied gas flows over a wall mounted cube.
- IV. Explore the physical flow features for various Mach numbers, Knudsen numbers, and different wall temperatures. Furthermore, carry out an in-depth study of the flow-field and aerodynamic properties for various flow configurations mentioned above.

The schematic of the different flow configurations investigated are as follows (see figure 2.1):

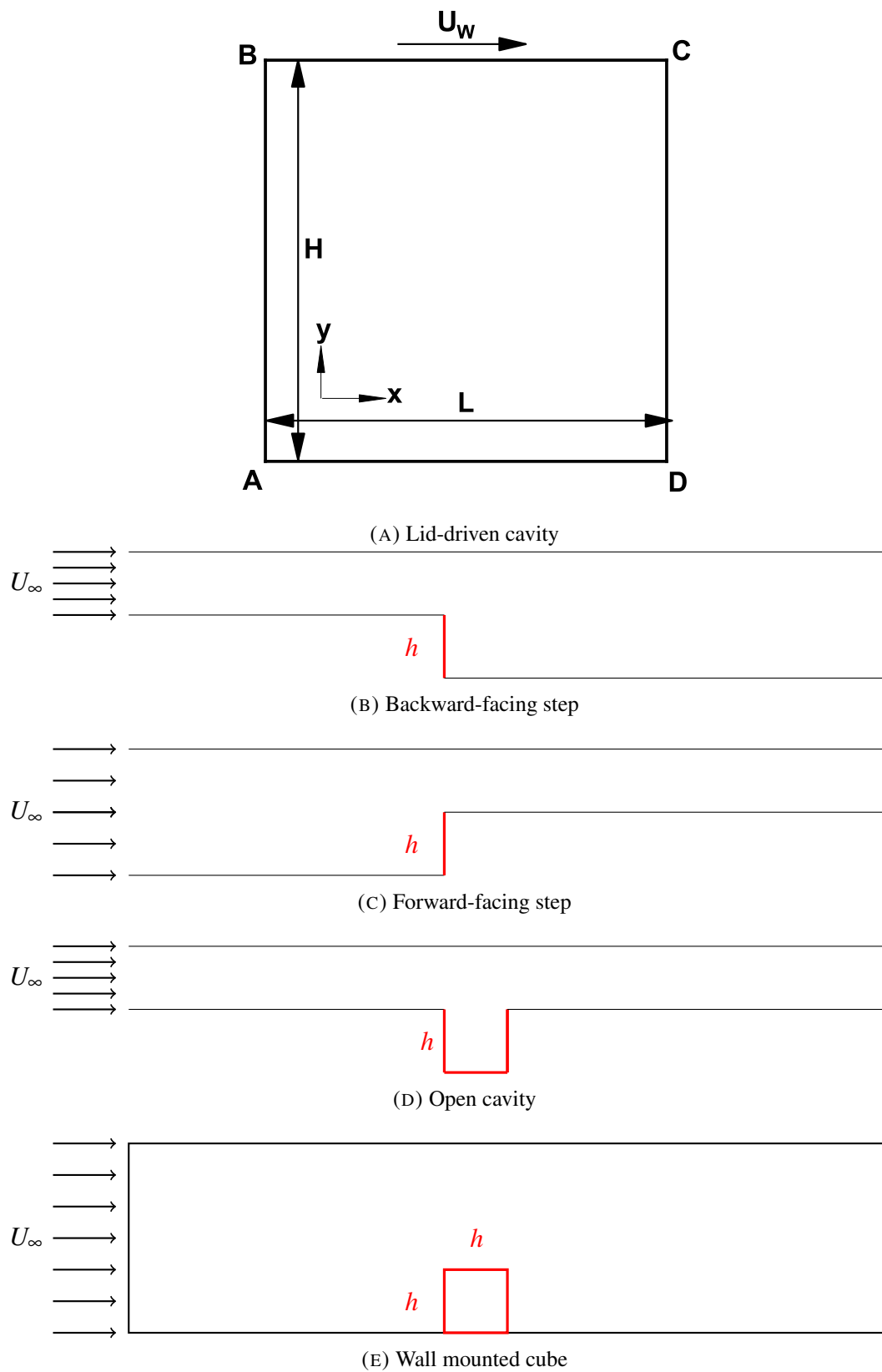


FIGURE 2.1: Schematics of the studied configurations.

Chapter 3

Computational methodology adopted in the present work

In this chapter, the computational approach followed for analyzing the framed objectives is given in detail. A detailed overview of the Direct Simulation Monte Carlo (DSMC) method, along with the DSMC algorithm is shown. This chapter concludes with a few limitations of the DSMC approach.

3.1 Direct Simulation Monte Carlo (DSMC)

3.1.1 Background of DSMC

Pioneered by Bird [14] in the early 1960s, the DSMC method is one of the most popular and successful techniques to model rarefied gas flows. The DSMC method is a probabilistic method for modeling gas flows in a rarefied regime. DSMC method

utilizes probabilistic (Monte Carlo) simulation to solve the Boltzmann Equation for a finite Knudsen number, and it has been developed subsequently. The DSMC is based on individual particle mechanics that, in the limit of infinite simulated particles, infinitely small cell size and infinitely small timestep converges to the solution of Boltzmann equation[100–102], which is given below

$$\frac{\partial(nf)}{\partial t} + c \frac{\partial(nf)}{\partial r} + F \frac{\partial(nf)}{\partial c} = J(f, f^*) \quad (3.1)$$

In equation 3.1, n is the number density, f is the velocity distribution function, r the position vector of the molecule, c velocity vector of the molecule, $J(f, f^*)$ non-linear integral and F represents the external force. The superscript $*$ represents the post collision properties. The collision integral is given by,

$$J(f, f^*) = \int_{-\infty}^{\infty} \int_0^{4\pi} n^2 (f^* f_1^* - f f_1) c_r \sigma_T d\Omega dc_1 \quad (3.2)$$

In equation 3.2, f and f_1 are the velocity distribution function at c and c_1, c_r is the relative speed, σ_T is the cross-section of the molecule and Ω is the solid collision angle.

The DSMC method is a stochastic technique and a successful method for simulations of rarefied gas flows [103]. DSMC is used in aerospace technology, vacuum science and engineering, materials processing and manufacturing, material handling, and nanotechnology sectors [104]. Even though the DSMC method is a time-consuming process [105], but due to its innate accuracy, it is widely used in the simulation of rarefied gas flows [106]. The main benefit of the DSMC is its numerical stability, and it does not depend on similarity parameters like the Mach number, Reynolds number, [107], furthermore,

with the development of supercomputers [108], the DSMC technique in the latest years, has become a diverse and successful one [109]. The DSMC method models the flow as a collection of particles or molecules having a position, velocity, and internal energy. The concept of this process is to independently calculate at every time step the movement and inter-molecular collision of a finite number of fictitious particles separately, considering that each particle constitutes a considerable number of actual particles.

3.1.2 Choice of simulation parameters

DSMC technique relies on the correct selection of four parameters, namely cell width, time step, particles per cell, and the number of samples for obtaining accurate results. Typically, cell width is selected to be less than one-third of the mean free path [110, 111]. The time step should be less than the mean time of the collision [112, 113], and the simulated particle should not cross the whole width of the cell in a single time-step. The cell width is selected in the current simulations to be less than one-third of the freestream mean free path (λ_∞). Similarly, the time-step is also chosen such that it is less than one-third of the mean collision time. Also, 25 particles per cell are chosen [114].

3.1.3 DSMC Algorithm

The DSMC algorithm involves the following steps:

1. Read the grid data and define the initial and boundary conditions.
2. Calculate the number of DSMC molecules and initialize them in the domain.

3. Model the interaction of DSMC molecules with the boundaries.
4. Index the simulated DSMC molecules.
5. Use probabilistic sampling to model the collision of the simulated DSMC molecules.
6. Sample the flow field and repeat steps 3-6.
7. Output the sampled flow field variables. The DSMC Algorithm is summarized below in Figure 3.1.

The initialization of the computational domain is based on the freestream conditions of the flow. During each time step, various physical properties like density, velocity, internal energy, and temperature are specified according to the given boundary conditions for the particles entering the computational domain.

A linear combination of the thermal velocity and the freestream velocity is used to calculate the velocity of the simulated particle. Initially, at time zero, the boundary conditions corresponding to the flow are imposed. After a sufficiently large time, a steady-state flow is established. Thus, a time average is calculated after reaching the steady-state to obtain the desired steady result.

3.1.4 Particle motion and wall collision

The next step involves the DSMC particles' movement in the computational domain appropriate to their velocity components and time step size. Their new locations are thus determined. Particles that leave the computational domain are removed from the flow, and therefore new particles are introduced into the computational domain in their place.

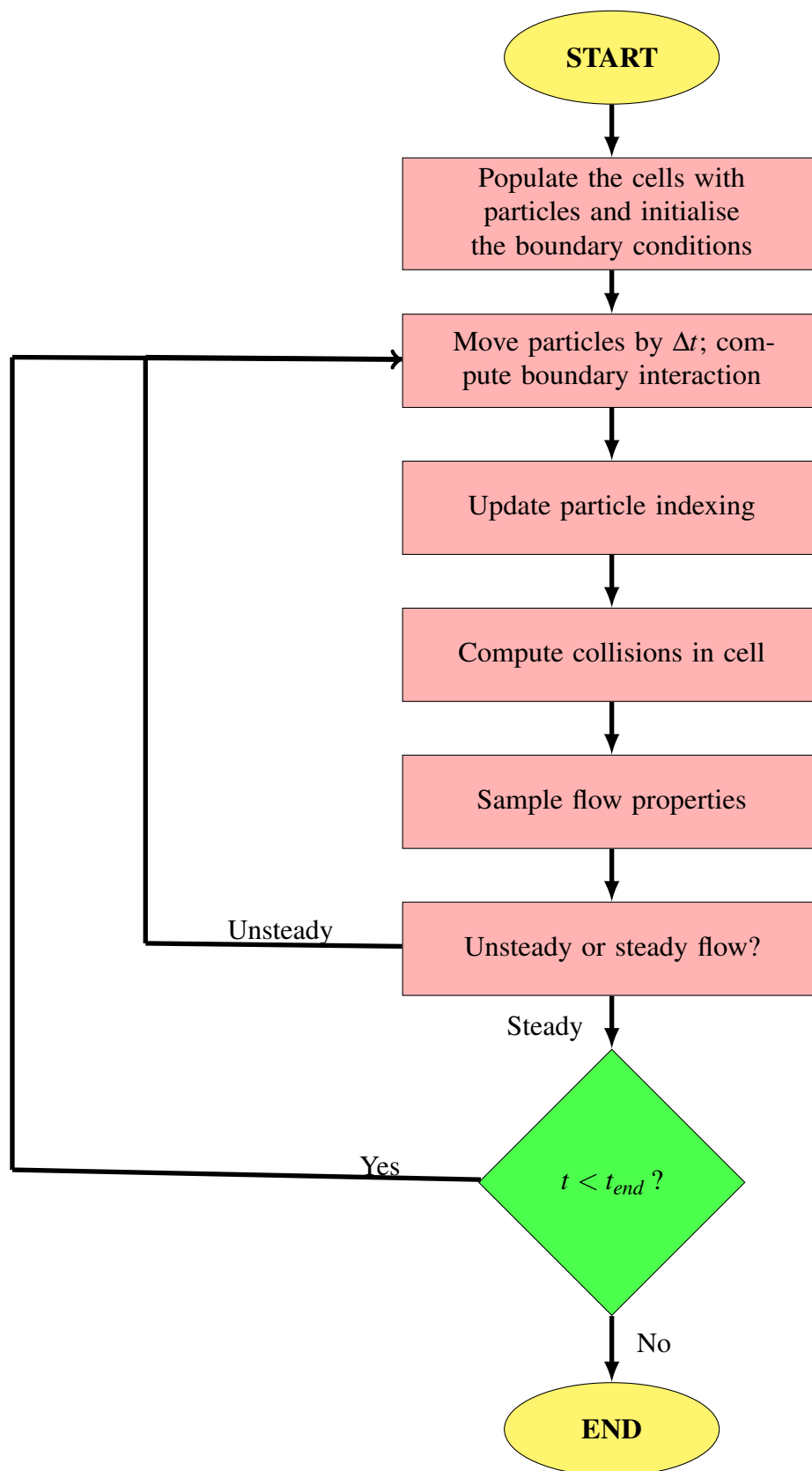


FIGURE 3.1: Flowchart of a standard DSMC simulation

For surface collisions, the treatment requires the application of the conservation laws and the application of the Maxwellian velocity distribution function. These collisions can be treated as specular, diffuse, or a combination of these two types. Following this, the particles are indexed by cell location so that calculation of inter-molecular collisions and sampling of the flow field can be done.

3.1.5 Modeling inter-molecular collisions

There are various collision pair selection schemes in DSMC, such as Time Counter (TC), Nearest Neighbor (NN), Null collision, Modified Nanbu, Ballot Box, No Time Counter (NTC) [115], Bernoulli's Trials, Simplified and Generalized Bernoulli Trials [116–121], a review of which is indicated in [122]. In the present analysis, the No Time Counter scheme (NTC) is used to select collision pairs, where the number of simulated particles dictates the computational cost. In the No Time Counter scheme, the maximum number of particle pairs N_c considered for binary collisions i is given by,

$$N_c = \frac{1}{2} \frac{N(N-1)F_N(\sigma_{TCr})_{max} \Delta t}{V_c} \quad (3.3)$$

where, N is the number of particles in the cell, F_N is the number of real molecules that are represented by each particle $(\sigma_{TCr})_{max}$ represents the maximum value of the product of collision cross-section and relative particle velocity, Δt is the time step and V_c is the volume of the cell.

Similarly, there are various collision models in DSMC, such as Hard-Sphere (HS) model, Generalized Hard-Sphere (GHS) model, Generalized Soft-Sphere (GSS) model, Variable

Hard-Sphere (VHS) model, Variable Soft-Sphere (VSS) model, and Variable Sphere (VS) molecular model. A description of these models can be found in ref [123]. These models are selected based on the degree of realism required in predicting the gas flow behavior. The present analysis uses a Variable Hard Sphere collision model [14] to model the collision kinetics, and internal energy exchange is handled using the Larsen-Borgnakke scheme [124].

The VHS theory implies that a molecule's cross-section varies with collision energy as per specific power-law. The total collision cross-section is given by,

$$\sigma_T = \sigma_{ref} \left(\frac{T_{ref}}{T} \right)^\alpha \quad (3.4)$$

where, σ_{ref} is the reference value of the cross-section at the reference temperature T_{ref} and α is the inverse power law exponent related to ω , the viscosity-temperature index as $\alpha = \omega - 0.5$ and $\sigma_T = \pi d^2$, where d is the collision diameter.

Based on VHS, the local mean-free path (λ) of the gas is given by,

$$\lambda = \frac{2}{15} (5 - 2\omega)(7 - 2\omega) \frac{\mu}{\rho} \sqrt{\frac{m}{2\pi kT}} \quad (3.5)$$

where, ω , m , k , T , μ , ρ are viscosity-temperature index, the mass of the gas, Boltzmann constant, temperature of the gas, viscosity of the gas, and density of the gas, respectively.

The molecules collide with each other and with solid surfaces. For the wall, the boundary is regarded as diffuse reflectors with full momentum and thermal accommodation. Full momentum accommodation specifies that the wall tangential momentum and that of

reflected molecules are equivalent. Similarly, full thermal accommodation specifies that the energy flux corresponding to the wall temperature and that of reflected molecules is equivalent. The final velocity of the reflected molecules is allocated as per half-range Maxwellian distribution, which depends on the imposed wall temperature (T_w).

3.1.6 Sampling flow properties

The macroscopic properties of velocity, pressure, temperature and density are obtained from the DSMC method by sampling the microscopic properties and are given by [80],

$$c_0 = \frac{\sum_{i=1}^N (mc)_i}{\sum_{i=1}^N (m)_i} \quad (3.6)$$

In equation 3.6, the number of molecules, the molecular mass and the velocity vector of the molecules is given by N, m and c respectively. $c_0 = u\hat{\mathbf{i}} + v\hat{\mathbf{j}} + w\hat{\mathbf{k}}$ gives the macroscopic mean velocity.

$$p = \frac{1}{3V_c} \sum_{i=1}^N \frac{(mc'^2)_i}{N} \quad (3.7)$$

In equation 3.7, N, m and V_c represent the number of molecules, the molecular mass and the volume of the cell and $c' = c - c_0$ represents the thermal or peculiar velocity.

$$T_0 = \frac{\zeta_T T_T + \zeta_R T_R + \zeta_V T_V}{\zeta_T + \zeta_R + \zeta_V} \quad (3.8)$$

In equation 3.8, ζ represents the degree of freedom and subscripts T, R, V represent translation, rotation and vibration respectively.

The following equations give the translational, rotational, and vibrational temperatures,

$$T_T = \frac{1}{3k_b} \frac{\sum_{j=1}^N m_j c'^2}{N} \quad (3.9)$$

$$T_R = \frac{2}{k_b \xi_R} \frac{\sum_{j=1}^N (\varepsilon_R)_j}{N} \quad (3.10)$$

$$T_V = \frac{\Theta_V}{\ln \left(1 + \frac{k_b \Theta_V}{\sum_{j=1}^N (\varepsilon_V)_j} \right)} \quad (3.11)$$

where ε_R and ε_V represent the average rotational and vibrational energies, respectively, k_b is the Boltzmann constant, and Θ_V denotes the characteristic vibrational temperature, having a value equal to 3371K and 2256K for N_2 and O_2 respectively. The rotational and vibrational collision relaxation number considered in the study was 5 and 50, respectively.

$$\rho = \frac{1}{V_c} \sum_{i=1}^N m_i \quad (3.12)$$

In equation 3.12, N , m and V_c represent the number of molecules, the molecular mass and the volume of the cell.

$$Z = \frac{p}{\rho RT} \quad (3.13)$$

In equation 3.13, Z represents the compressibility factor, ρ the macroscopic density, R the gas constant and T the overall temperature respectively.

The DSMC method is computationally intensive but can be significantly accelerated by using efficient parallelization techniques using OpenMPI [125]. The open-source CFD software, OpenFOAM [126, 127], is used in the present work. The *dsmcFoam* solver, written under the framework of OpenFOAM, is used for computational modeling.

3.1.7 Chemical reaction modeling

Over the years, several chemical reaction models for DSMC have been developed. Introduced by Bird, the Total Collision Energy (TCE) model is one such popular chemical reaction model that uses the equilibrium kinetic theory to translate the Arrhenius rate coefficients into collision probabilities. Alternatively, Bird [128] proposed the Quantum-Kinetic (Q-K) chemistry model. This molecular-level chemistry model employs the fundamental molecular properties instead of the classical TCE model, which relies on experimental data availability. The Q-K model has limited dependence on macroscopic properties. The present study uses the Q-K chemistry model to simulate a 5-species air model's chemical reactions with a total of 19 chemical reactions in *dsmcFoam+* [129], as shown in Table 3.1. Relevant to the present discussion are two chemical reaction types - Dissociation (No. 1-15) and Exchange reactions (No. 16-19) in Table 3.1.

3.2 Limitations of DSMC

1. Solving three-dimensional problems using DSMC is computationally expensive.
2. The DSMC technique is susceptible to significant statistical errors as it is probabilistic centered and relies on multiple thousands or millions of simulated molecules.

TABLE 3.1: List of chemical reactions employed.

No.	Reaction	The heat of formation (10^{19}) J
1.	$O_2 + N \rightarrow O + O + N$	8.197
2.	$O_2 + NO \rightarrow O + O + NO$	8.197
3.	$O_2 + N_2 \rightarrow O + O + N_2$	8.197
4.	$O_2 + O_2 \rightarrow O + O + O_2$	8.197
5.	$O_2 + O \rightarrow O + O + O$	8.197
6.	$N_2 + O \rightarrow N + N + O$	15.67
7.	$N_2 + O_2 \rightarrow N + N + O_2$	15.67
8.	$N_2 + NO \rightarrow N + N + NO$	15.67
9.	$N_2 + N_2 \rightarrow N + N + N_2$	15.67
10.	$N_2 + N \rightarrow N + N + N$	15.67
11.	$NO + N_2 \rightarrow N + O + N_2$	10.43
12.	$NO + O_2 \rightarrow N + O + O_2$	10.43
13.	$NO + NO \rightarrow N + O + NO$	10.43
14.	$NO + O \rightarrow N + O + O$	10.43
15.	$NO + N \rightarrow N + O + N$	10.43
16.	$NO + O \rightarrow O_2 + N$	2.719
17.	$N_2 + O \rightarrow NO + N$	5.175
18.	$O_2 + N \rightarrow NO + O$	-2.719
19.	$NO + N \rightarrow N_2 + O$	-5.175

Quantitative research showed that such a mistake was inversely proportional to the sample size square root. Therefore, an exact DSMC simulation should involve an appropriate number of particles in a cell, generally 15–20, for this potentially significant error to be decreased.

3. The DSMC method is relatively less efficient for modeling microscale flows compared to macroscale high-speed flows. In DSMC, the computational cost increases with the number of simulated molecules. It has drawbacks such as slow convergence (i.e., the solution is considered steady-state when the average linear kinetic energy of the system shows no significant variation). Also, it has a requirement of a large number of simulated molecules; a thorough description is given in [130] and [131].

Chapter 4

Validation studies

In this chapter, the different validation studies conducted to confirm the accuracy of the results are presented. Firstly, the grid, timestep and particles per cell independence studies are performed to confirm the accuracy. Next, for internal flows, the validation study of the standard benchmark problem of the lid-driven cavity is shown. For the external flow configurations, validations are performed for flow over a flat plate, BFS, and an open cavity. Then the chemically reacting flow over a cylinder is validated.

4.1 Grid, timestep and particles per cell independence

The DSMC method primarily has computational errors such as discretization errors and statistical errors [132], which are evaluated in the present section. The verification was carried out for all the configurations. However, for illustration, the open cavity case results are presented here.

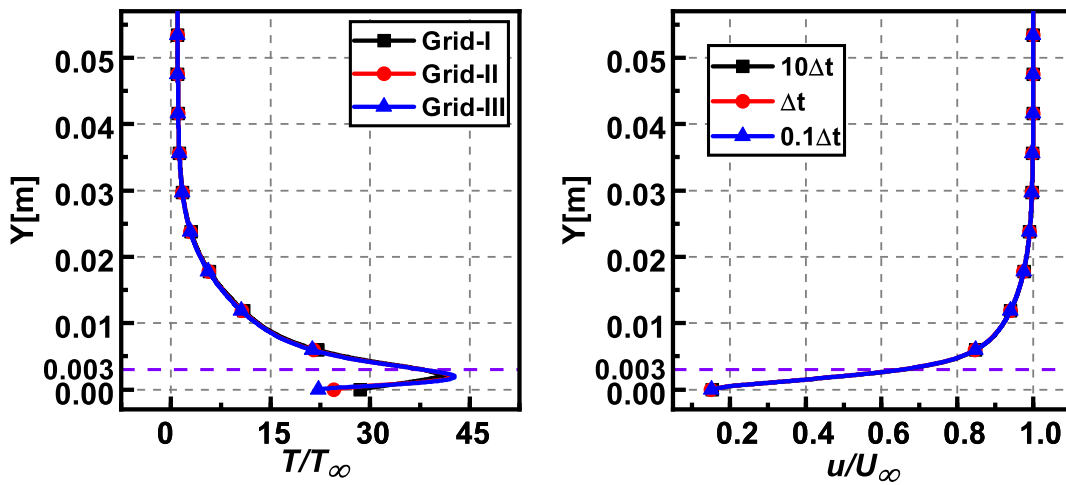
To study the independence of the results with the grid size, the flow past cavity for $Ma = 25$, $Kn = 21.10$, $\lambda_\infty = 6.33 \times 10^{-2}m$ and $H = 60mm$ were investigated for different grids, namely, grid-I, grid-II, and grid-III. The grid-I consisted of 50% fewer cells than the grid-II, whereas 50% additional cells were present in the grid-III. Furthermore, the cell ratio (Δx) to mean free path (λ) considered was 0.32. Figure 4.1a shows the non-dimensional temperature at $X = 59mm$ for the grids considered. The profile shows a close match for the grid-II and grid-III. Thus, grid-II was used in all the simulations to reduce the computational time.

Likewise, for three different timestep, i.e., $10\Delta t$, Δt , and $0.1\Delta t$, a time-independence evaluation was carried out. The ratio of $\Delta t/\Delta t_{mc}$ was 1.174×10^{-4} , where Δt_{mc} denotes the free-stream mean collision time. Thus, Δt considered was much smaller than mean-collision time, fulfilling the necessity of DSMC timestep. Figure 4.1b represents the non-dimensional velocity for the timestep, which show a close match for Δt , and $0.1\Delta t$. Thus, a $\Delta t = 2 \times 10^{-8}s$ was adopted.

Also, to select an optimum particle per cell (PPC), simulations were performed for three distinct PPC, namely 10, 25, and 40. Figure 4.1c shows the non-dimensional pressure at $X = 120mm$ for the PPC considered, showing an overlapping trend for PPC of 25,40. Hence a PPC of 25 was adopted.

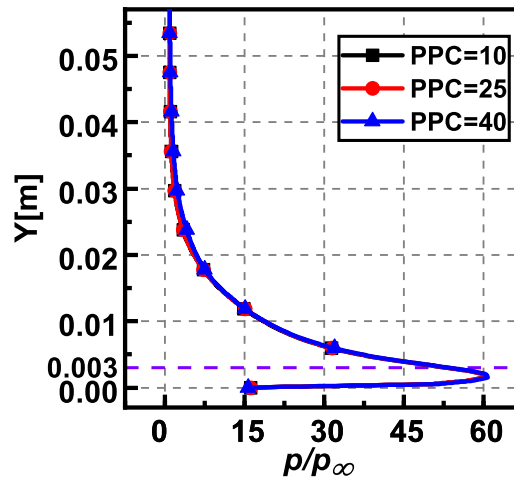
4.2 Validation of flow inside a lid-driven cavity

In the present study, numerical simulations are carried out using the *dsmcFoam* solver. Various validations were performed to validate the solver, considering different flow



(A) Non-dimensional temperature.

(B) Non-dimensional velocity.



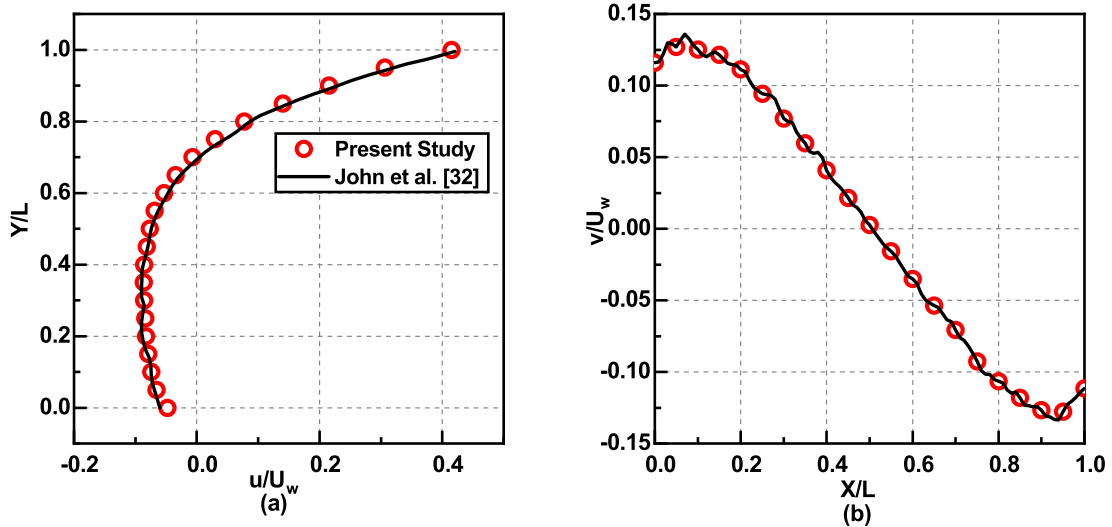
(C) Non-dimensional pressure.

FIGURE 4.1: Verification studies for open cavity in the transverse direction at $X = 59\text{mm}$ and $Kn = 21.10$.

configurations, and were compared with the literature's experimental and numerical results. For the case of rarefied flow inside a lid-driven cavity, a similar problem of the lid-driven cavity is compared with the numerical findings of John *et al.*[32]. According to John *et al.*, a rarefied flow of argon in a single-sided lid-driven cavity was used for the computational investigation.

Figure 4.2 shows the u and v velocity components in the x and y directions along a

vertical and horizontal line crossing the cavity center for $U_w = 50m/s$ at $Kn = 1$. From the profiles, it can be observed that a close agreement is obtained among the results, thus validating the solver. The figures reveal that the velocity profiles match, and it is apparent that there is a near consensus between the current DSMC computations and the other literature findings.



(A) Non-dimensional u -velocity profile plotted along a vertical line crossing the cavity center.

(B) Non-dimensional v -velocity profile plotted along a horizontal line crossing the cavity center.

FIGURE 4.2: Validation study of lid-driven cavity.

4.3 Validation of flow over a flat plate

A test case of flow over a flat plate was considered to compare the experimental results from the literature. It has experimental research by Becker *et al.* [133] and a computational study by Hermina *et al.* [134] that makes it a viable choice. The test case parameters are mentioned in Table 4.1. The study involved a Helium flow across a flat plate with a length of 50.8mm and a width of 25.4mm, respectively. The plate was maintained at 290K. In the numerical study of Hermina *et al.*, a general surface

accommodation model was used that permitted the independent specification of the accommodation coefficients. Figure 4.3a-4.3c depicts the non-dimensional velocity, density, and temperature, in the perpendicular direction $x = 2.5mm$ from the inlet. The ordinate represents the distance in the perpendicular direction standardized by the mean free path (λ_∞). As seen in Figure 4.3, reasonable consensus exists between the outcomes, validating the computational method adopted.

TABLE 4.1: Details of the chosen test case for flat plate validation with Becker *et al.*

T_∞	ρ_∞	U_∞	p_∞	n_∞	μ_∞	λ_∞
K	kg/m^3	m/s	N/m^2	m^{-3}	Ns/m^2	m
10.7	1.52×10^{-5}	1723	0.3379	2.285×10^{21}	1.865×10^{-5}	1.286×10^{-3}

4.4 Validation of flow over a backward-facing step

For the comparable case of flow over BFS, the results predicted by the current model using the DSMC method are compared with the numerical results of Guo *et al.* [135]. Guo *et al.* investigated the flow characteristics of a hypersonic BFS in the slip and transitional regime using the DSMC method. The simulation parameters adopted for the case of $H = 30km$ are shown in Table 4.2. The wall temperature was fixed to 226.5K. This study employed a diffusion reflection with a full thermal and momentum accommodation coefficient. Firstly, for visual validation, the velocity contours reported by Guo *et al.* were compared and are presented in Figure 4.4, which shows a good agreement.

Additionally, the streamwise velocity and the pressure normal to the BFS surface at $X/h = 5$ is shown in Figure 4.5. Where X represents the axial distance normalized by the

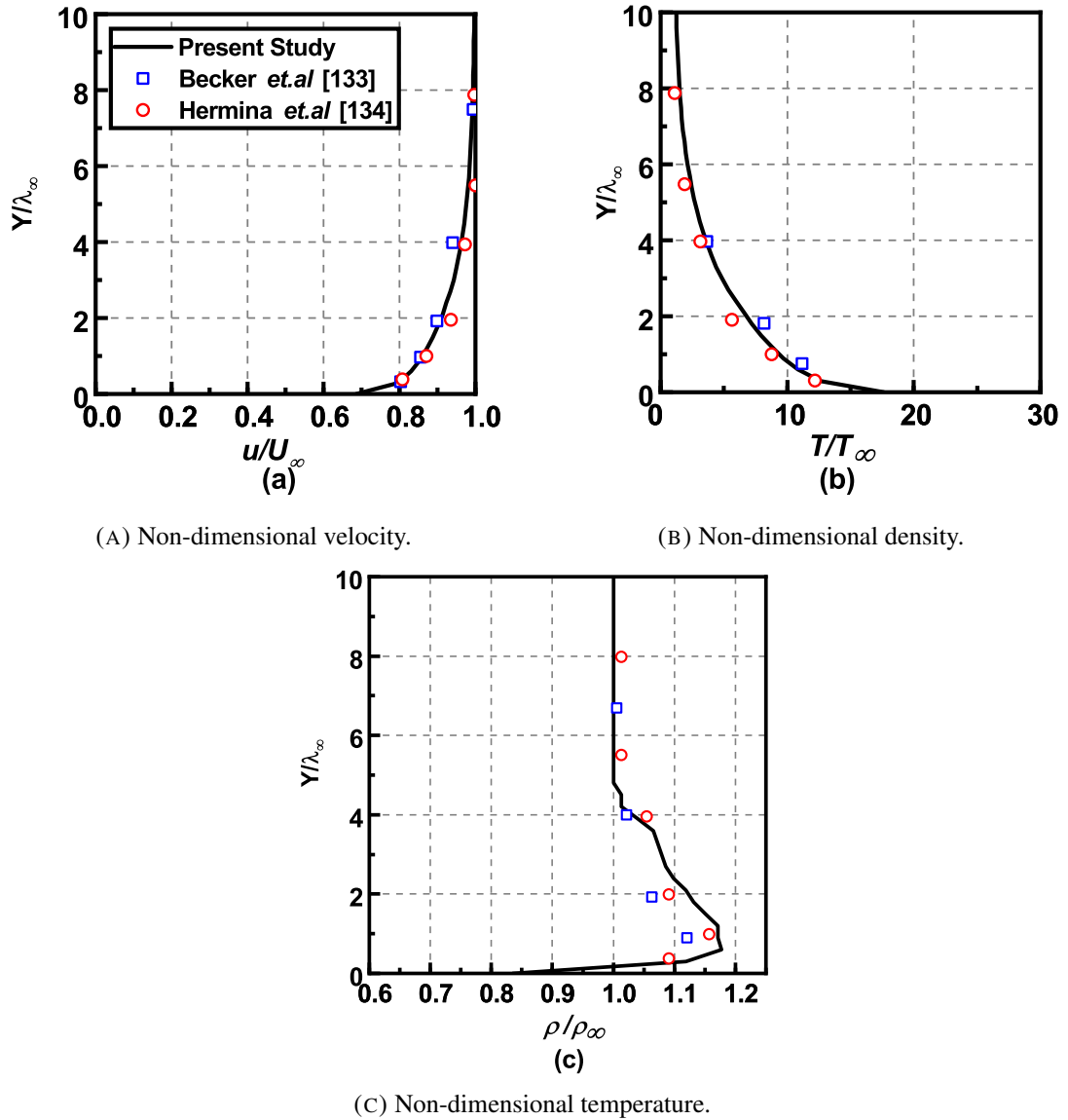


FIGURE 4.3: Validation study of flow over a flat plate.

TABLE 4.2: Details of the chosen test case for BFS validation with Guo *et al.*[135]

H	P_0	T_0	Ma_∞	h	λ	f	ρ_∞
km	Pa	K	—	mm	m	$1/s$	kg/m^3
30	1197	226.5	6	10	4.41×10^{-6}	9.22×10^7	1.5×10^{-2}

free-stream step height (h). From the streamwise velocity profile, it is observed that both the results show reasonable agreement, with a slight discrepancy near the wall. Also, the comparison of the pressure shows a fair match between our results with the published results. Thus, our findings match well with Guo *et al.*, thus validating the current study.

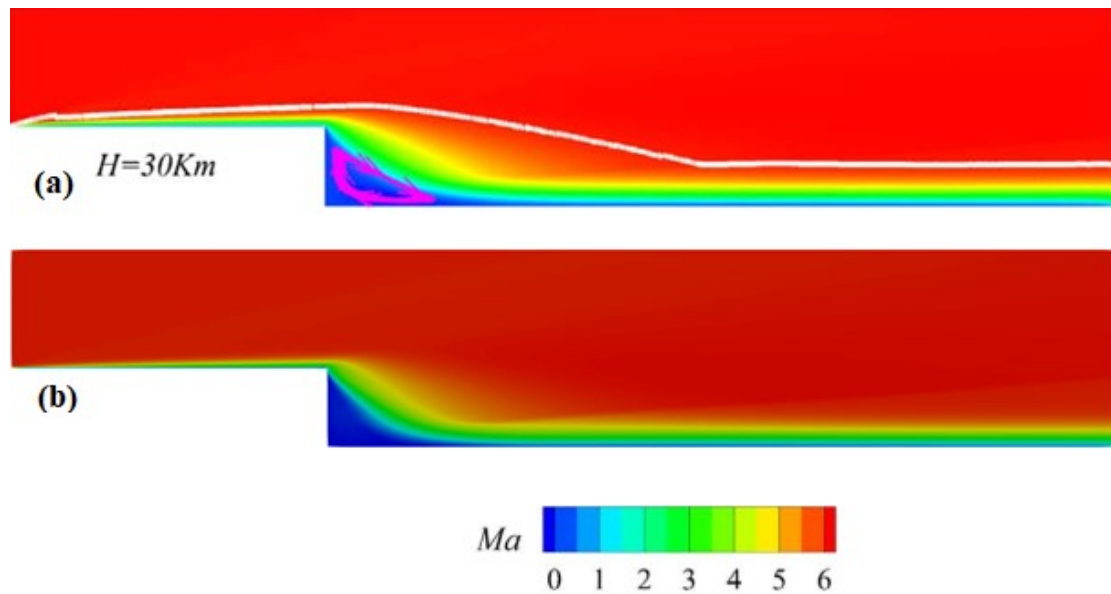
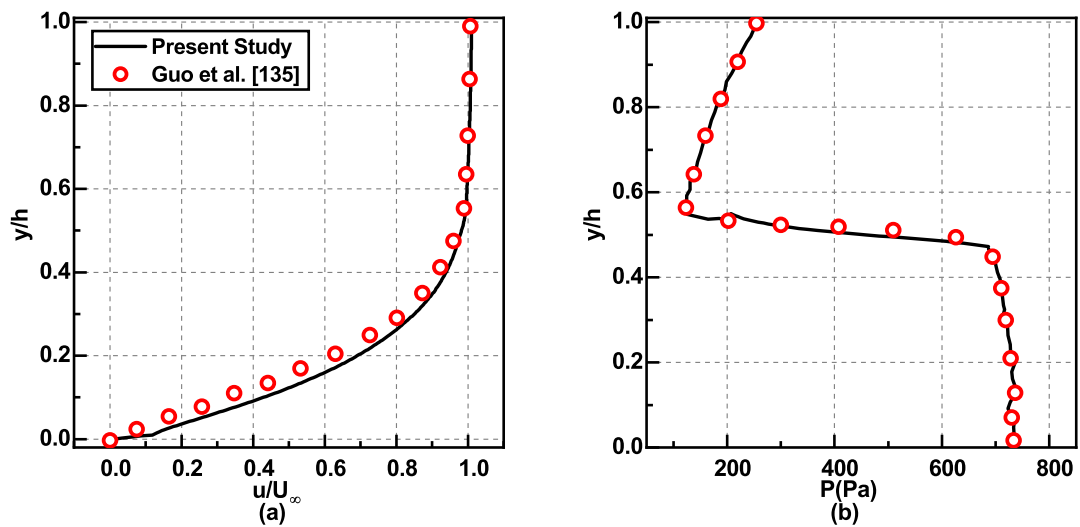


FIGURE 4.4: Comparison of velocity contour for the case of $H = 30\text{km}$ (a) published results [135] (b) simulation results.



(A) Comparison of streamwise velocity along the vertical line of $X/h = 5$ for the case of $H = 30\text{km}$.

(B) Comparison of pressure along the vertical line of $X/h = 5$ for the case of $H = 30\text{km}$.

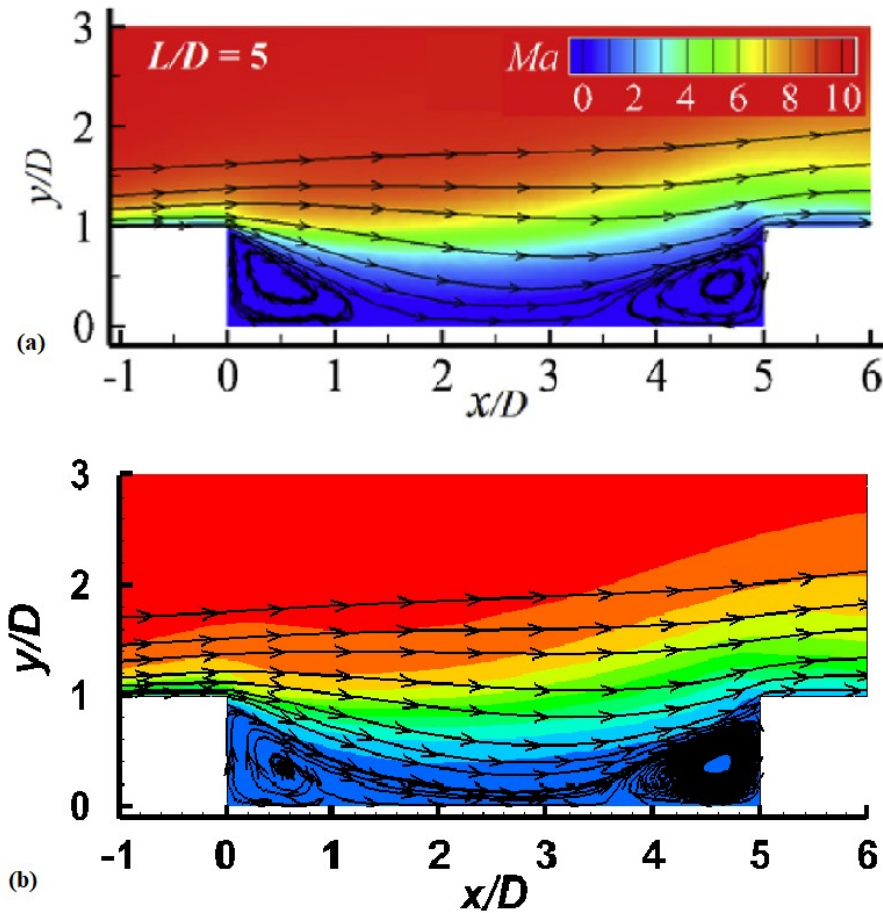
FIGURE 4.5: Validation study of flow over a BFS.

4.5 Validation of flow over an open cavity

For a comparable case of flow over the cavity, the validation studies were carried out, and the results were compared against that of Guo. *et al.* [2]. Guo. *et al.* studied the

TABLE 4.3: Details of the chosen test case for open cavity validation with Guo. *et al.*[2]

T_∞	p_∞	Ma_∞	ρ_∞	λ_∞	Kn
K	N/m^2	–	kg/m^3	m	–
219.59	5.221	10	8.28×10^{-5}	9.81×10^{-4}	0.327

FIGURE 4.6: Distribution of Mach number contours and streamlines for cavities with $L/D = 5$ (a) Published results [2], (b) Present study.

flow over a cavity in different regimes for different L/D ratios of the cavity. L denotes the cavity length, and D represents the cavity depth, respectively. The specifics of the case compared with are shown in Table 4.3.

For visual validation, the Mach number contours and the streamlines are compared. The simulated results are reasonably similar to the published results of Guo. *et al.*, as

observed in Figure 4.6. Furthermore, the Mach number and temperature profile along the surface at a depth $D = 0.5$ for an $L/D = 5$ is shown in Figures 4.7a-4.7b. Comparing the simulated results with Guo. *et al.* reveal no significant deviation in the profiles depicting close alignment between present DSMC computations and the other literature findings.

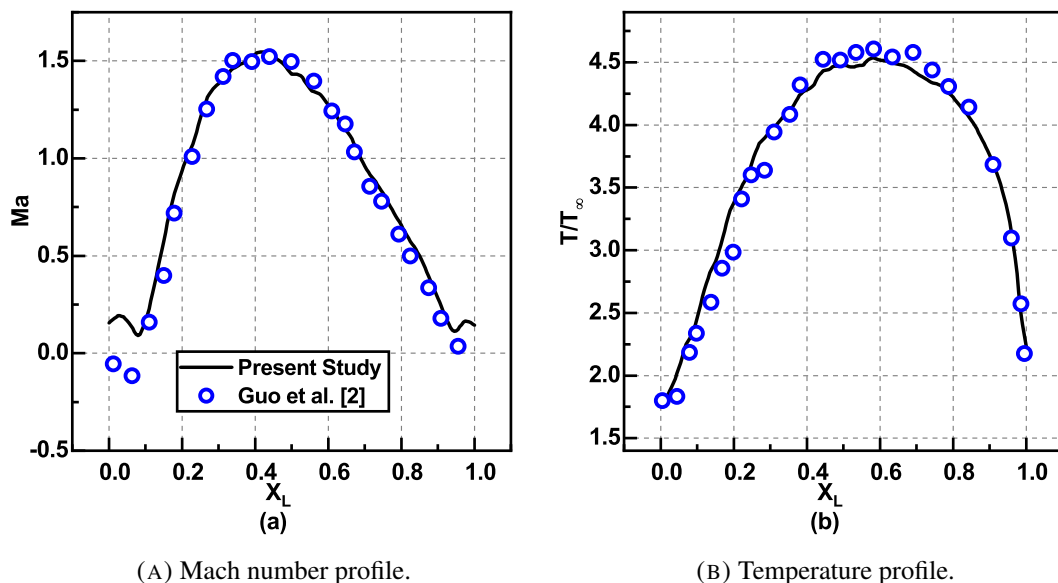


FIGURE 4.7: Validation study of flow over an open cavity.

4.6 Validation of chemically reacting flow over a cylinder

Finally, the cylinder's test case was simulated to validate the solver by incorporating the chemical reactions. A two-dimensional hypersonic rarefied airflow over a circular cylinder with a diameter of 2 m, investigated by Scanlon *et al.* [126], was used as a benchmark case. The Quantum-Kinetics (Q-K) chemical reaction model was considered. The free-stream and flow conditions for atmospheric altitude, $H = 86\text{km}$, are shown in Table 4.4. The cylinder was maintained at a temperature of 1000K and the cylinder walls are fully diffuse with full thermal and momentum accommodation coefficients.

TABLE 4.4: Details of the chosen test case for cylinder validation with Scanlon *et al.*

H	T_∞	Ma_∞	d	λ	f	ρ_∞
km	K	–	m	m	$1/s$	kg/m^3
86	187	25	2	1.23×10^{-2}	2.96×10^4	1.43×10^{-5}

Figure 4.8a compares Mach number contours reported by Scanlon *et al.* and the present simulation. Figure 4.8b depicts the species' number density along the stagnation line in front of the cylinder. The results obtained match well with the Q-K results of obtained Scanlon *et al.*, thus, supporting the validity of our results for chemically reacting rarefied flow in the present work.

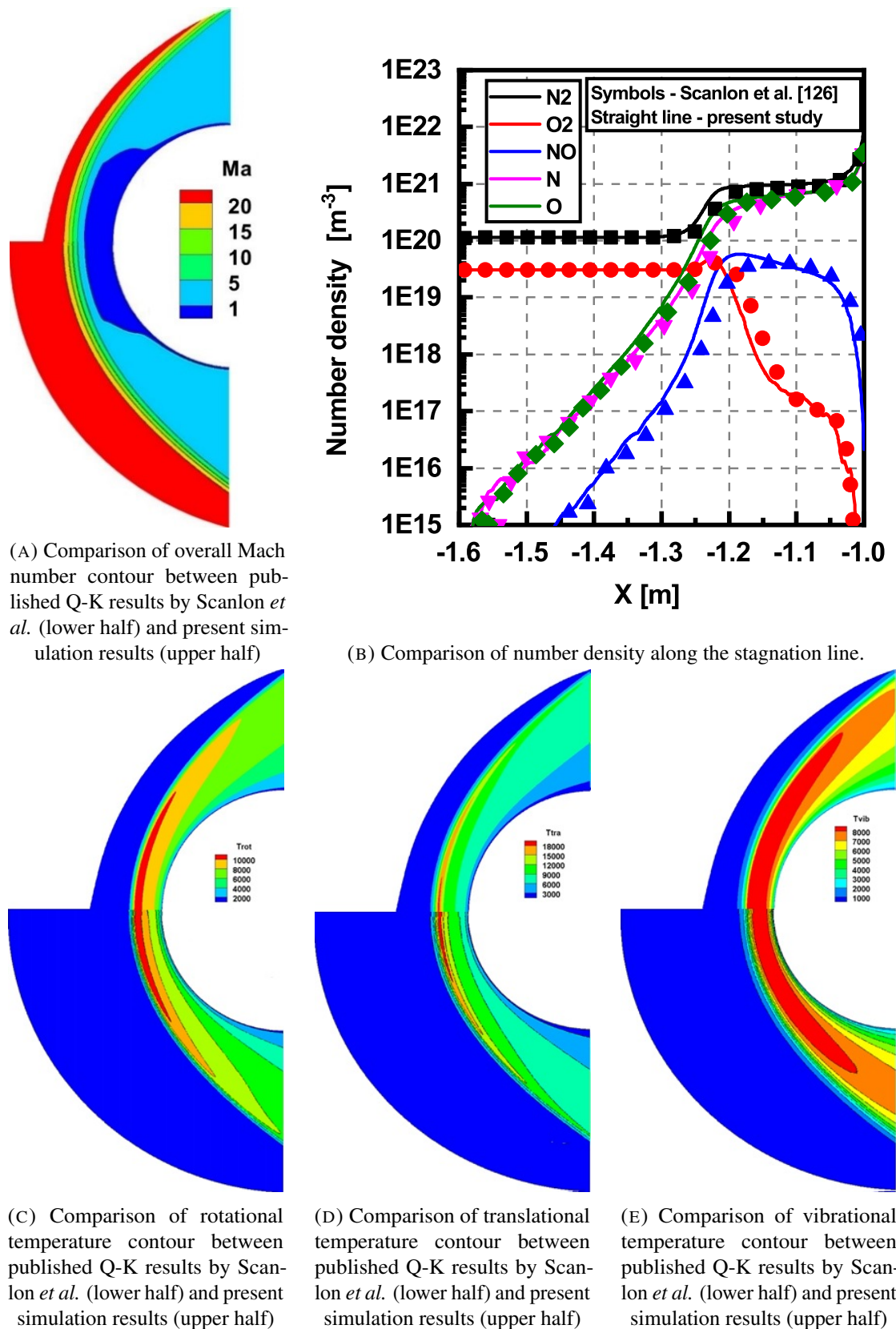


FIGURE 4.8: Validation study of chemically reacting flow over an cylinder.

Chapter 5

Modeling and investigation of the rarefied flow physics of internal flows

In this chapter, the rarefied flow physics of the internally bounded flows is thoroughly investigated. This chapter begins with a brief introduction to lid-driven cavity flows. The double-sided lid-driven cavity results are presented first, followed by the four-sided lid-driven cavity. After that, the DSMC results are compared with NSF results.

5.1 Introduction

Lid-driven cavity flow has been widely benchmarked using different computational methods for several decades and continues to be a widely investigated problem [136]. It has also been extended to study the flows in different length scales and varying degrees of rarefaction. It is an academically interesting problem [137, 138] as it incorporates various fluid phenomena like vortex dynamics, flow bifurcations, hydrodynamic stability from

an elementary geometry setting [41]. The problem described in this paper is a part of the category of internally bounded flows in the cavity induced by the movement of one or more boundaries and in turn, imparting motion to the fluid [139]. Industrial application of lid-driven flow is found in, but not limited to, the fields of melt spinning, coating and drying technologies, and the aircraft industry. Lid-driven cavities are classified based on their geometric shapes, such as square, rectangular, triangular, and cross-shaped. Furthermore, for the specific case of square and rectangular types, based on the number of sides which impart motion to the fluid, they are categorized into single-sided, double-sided, and four-sided cavities.

Geometry:

The geometry of the lid-driven cavity is shown in Figure 5.1. The flow is assumed to be two-dimensional. The length and height of the cavity are L and H , which are $1m$, respectively. A , B , C , D denote the four corners of the cavity. For the parallel motion(5.1b), the top and bottom sides (BC & AD) move in the same direction (i.e., positive x -direction); also, the left and right sides (AB & CD) move in the same direction (i.e., positive y -direction). For the anti-parallel motion (5.1a), the top & bottom sides (BC & AD) and the left & right sides (AB & CD) move in the opposite direction. The flow for different Mach numbers (Ma) and Knudsen numbers (Kn) are studied. All the cavity walls are maintained at the same temperature as the initial temperature, i.e., $T_w=T_0= 273K$. The lid-velocities used in the study are 10, 50, 100, and 200m/s, which correspond to a Mach number of 0.03, 0.17, 0.35, and 0.70, respectively. The Knudsen numbers considered are 0.01, 0.1, 1, 10, and 20, which covers all the rarefaction regimes.

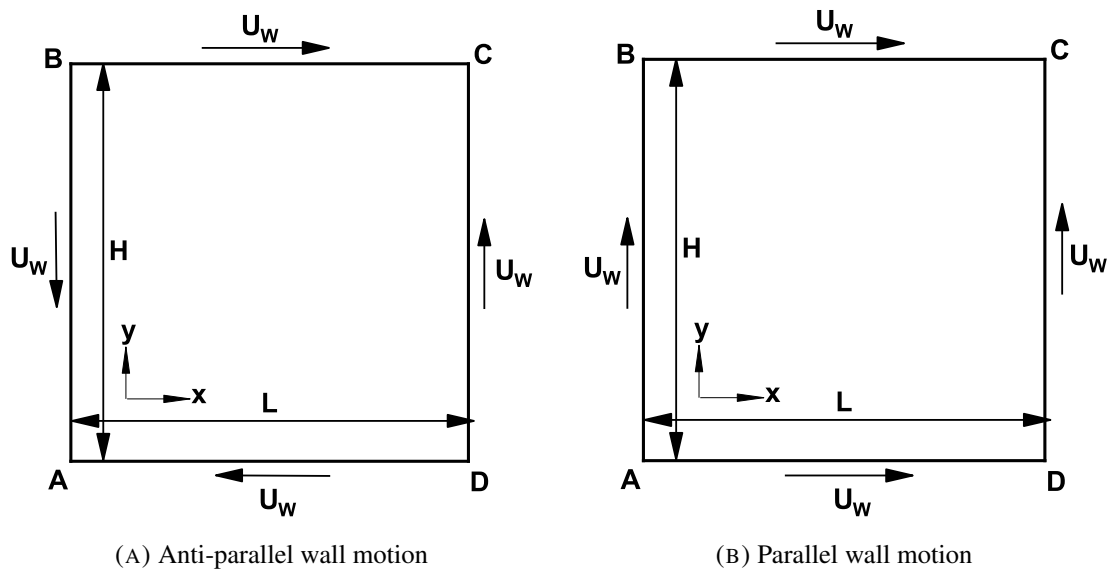


FIGURE 5.1: Configuration of the lid-driven cavity flow problem

Initial and flow conditions:

The geometry parameters, initial conditions, gas properties, and simulation parameters used in the present study are tabulated in Table 5.1. The fluid considered is Argon. All the cases studied are simulated up to 1s of physical flow time. The simulations were carried out on a 16-core Intel Xeon E5-2630 processor. On average, each of the simulations took about 18-20 CPU hours and varied based on the flow regime considered.

Computational flow domain and grid:

Molecular collisions are modeled by dividing the computing domain into various cells, quadrilateral in shape, thus creating a structured grid. The cells provide a useful reference for gas properties sampling. The cells also help to assess the collision frequency when choosing collision partners. Furthermore, they also provide a useful guide for determining the macroscopic gas characteristics after sampling. Figure 5.2 shows the schematic of

TABLE 5.1: Simulation parameters for studying the cavity problem.

Geometry	
Domain size (x,y)	$(1, 1)[m]$
Aspect Ratio	1
Discretization	
Time step (Δt)	$5 \times 10^{-6} [s]$
Cell width ($\Delta x, \Delta y$)	$0.01[m]$
Simulation	
Total number of time steps	200,000
Number of sampling time steps	50,000
The average number of particles per cell	25
Gas model (Argon)	
Gas-Gas interaction	Variable hard-sphere (VHS)
Gas-Wall interaction	Diffuse Reflection
Molecular mass (m)	$6.63 \times 10^{-26}[kg]$
Reference diameter (d)	$4.17 \times 10^{-10}[m]$
Reference temperature (T_{ref})	$273[K]$
Viscosity (μ)	$2.117 \times 10^{-5}[Ns/m^2]$
Viscosity exponent (ω)	0.81
Degree of freedom (ξ)	3
Number density m^{-3}	
$Kn = 0.01$ (Slip Regime)	1.6658×10^{20}
$Kn = 0.1$ (Slip Regime)	1.6658×10^{19}
$Kn = 1$ (Transition Regime)	1.6658×10^{18}
$Kn = 10$ (Transition Regime)	1.6658×10^{17}
$Kn = 20$ (Free molecular Regime)	8.32×10^{16}
Initial conditions	
Initial temperature (T_0)	$273[K]$
Lid velocity (U_w)	$10, 50, 100, 200[m/s]$
Mach number (Ma)	$0.03, 0.17, 0.35, 0.70$

the computing domain. In this figure, all the surfaces are assigned a wall velocity U_w . Diffuse reflection with full thermal accommodation is assigned to all the surfaces. The particles are equally reflected in all directions in a diffuse reflection model. The cell width in the x and y directions are chosen to be less than $1/3^{rd}$ of the mean free path. The number of cells in x and y direction for a standard grid consisted of 100 cells (i.e., $N_x=N_y= 100$), each having a cell size of 0.01m.

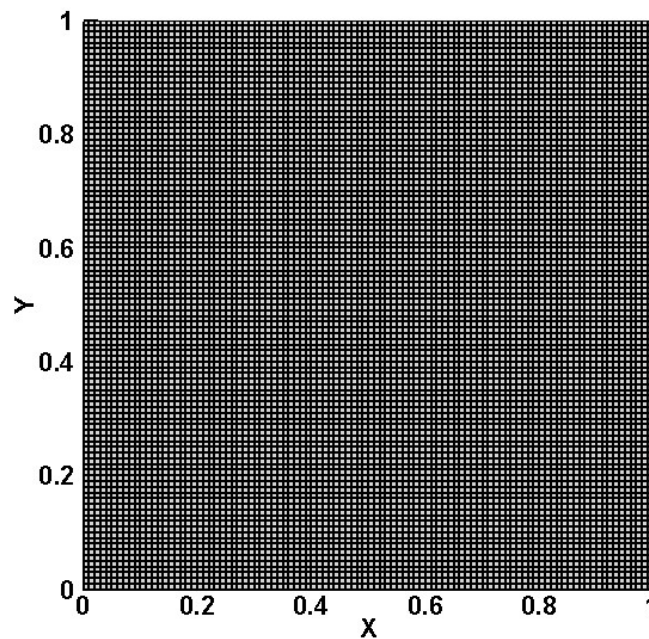


FIGURE 5.2: Meshed Domain of lid-driven cavity

5.2 Double-sided lid-driven cavity

This section presents the results for the double-sided lid-driven cavity. Here only the top and bottom walls (BC & AD) are in motion and the other walls are stationary. Initially, the effects of Mach number are discussed and are followed by effects of Knudsen number for both anti-parallel and parallel wall motions.

5.2.1 Anti-parallel wall motion

5.2.1.1 Influence of Mach number

Contour plots of flow field:

The contours of different flow field properties for $Ma = 0.70$ at $Kn = 1$ for anti-parallel wall motion are shown in Figure 5.3. The maximum flow velocity in the domain, which occurs adjacent to the driving walls, is almost half that of the driving wall velocity. This shows a definite slip between the driving wall and the fluid layer adjacent to it. This is the slip velocity phenomenon typically encountered in the rarefied gas flows.

The pressure contours exhibit a low-pressure region at the top left and bottom right corners and a high-pressure region at the other corners. The pressure remains constant in the center of the domain.

The regions of high temperature occur at the corners where the high-pressure regions exist. With increasing wall velocities, they gradually move closer to the moving walls. It can be attributed to competing factors like compressibility effects and viscous heat generation. The maximum temperature in the domain is observed near the driving walls and is above the fluid's reference temperature. This is attributed to the viscous dissipation effects.

The density contours follow the same trend as the pressure contour, with regions of high and low densities occurring at the same corners as that of the pressure contours. For the case of $Ma = 0.70$, the majority of the domain is engulfed by the zone of initial density.

Figure 5.4 shows the velocity streamlines for $Ma = 0.70$ case. The streamlines for all the other Mach numbers are similar in appearance; hence, only one plot is shown here. The streamlines are found to be symmetrical about both x and y axes and consists of a single vortex at the center of the domain. Also, the lid velocity increase has little effect on the center of the primary vortex, and it remains at the center of the cavity.

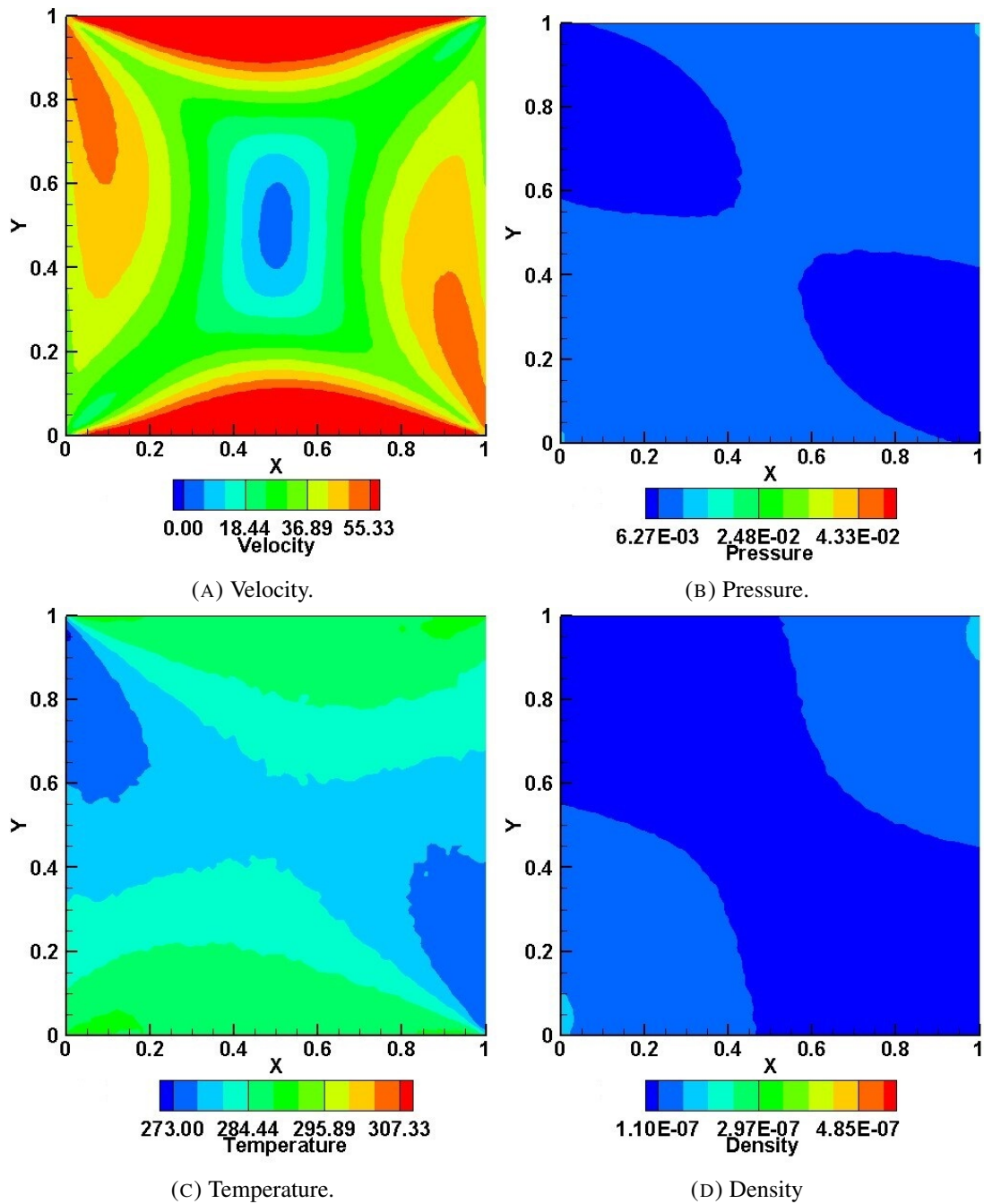


FIGURE 5.3: Contours of flow field for $Ma = 0.70$ at $Kn = 1$ for anti-parallel wall motion.

5.2.1.2 Influence of Knudsen number

Velocity profiles:

Figure 5.5 shows the v and u velocity components in the x and y directions along

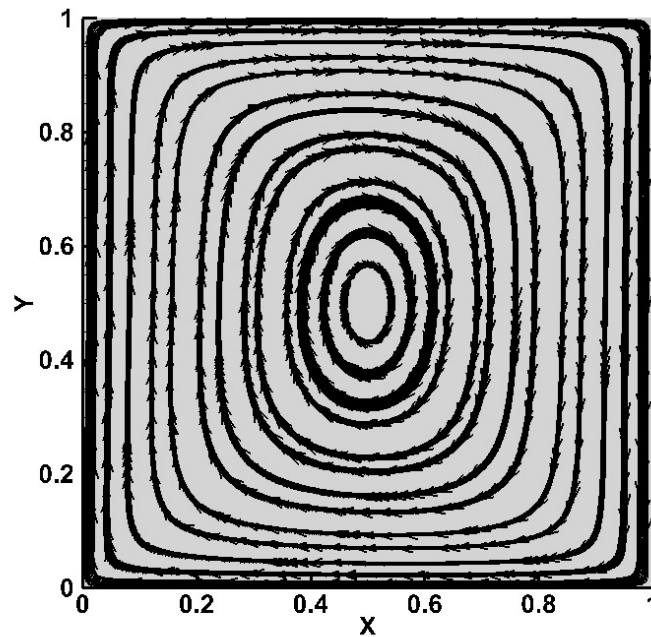


FIGURE 5.4: Velocity streamlines for $Ma = 0.70$ at $Kn = 1$ for anti-parallel wall motion.

horizontal and vertical lines crossing the cavity center at $Ma = 0.17$ for different Kn . The velocity profiles follow a wavy pattern along the length of the cavity. The v -velocity is close to zero for lower Kn at the two extremities of the cavity. As the Kn increases v -velocity slip increases and reaches a finite value; also, the flow is symmetric about the horizontal centerline. From Figure 5.5b, the u -velocity component fluctuates from a minimum to maximum changing direction at the center (i.e., $y/L = 0.5$).

Pressure profiles:

Figure 5.6 shows the non-dimensional pressure ratio in the x and y directions along horizontal and vertical lines crossing the cavity center at $Ma = 0.17$ for different Kn . The changes in pressure are more pronounced for higher Kn compared to lower Kn . The

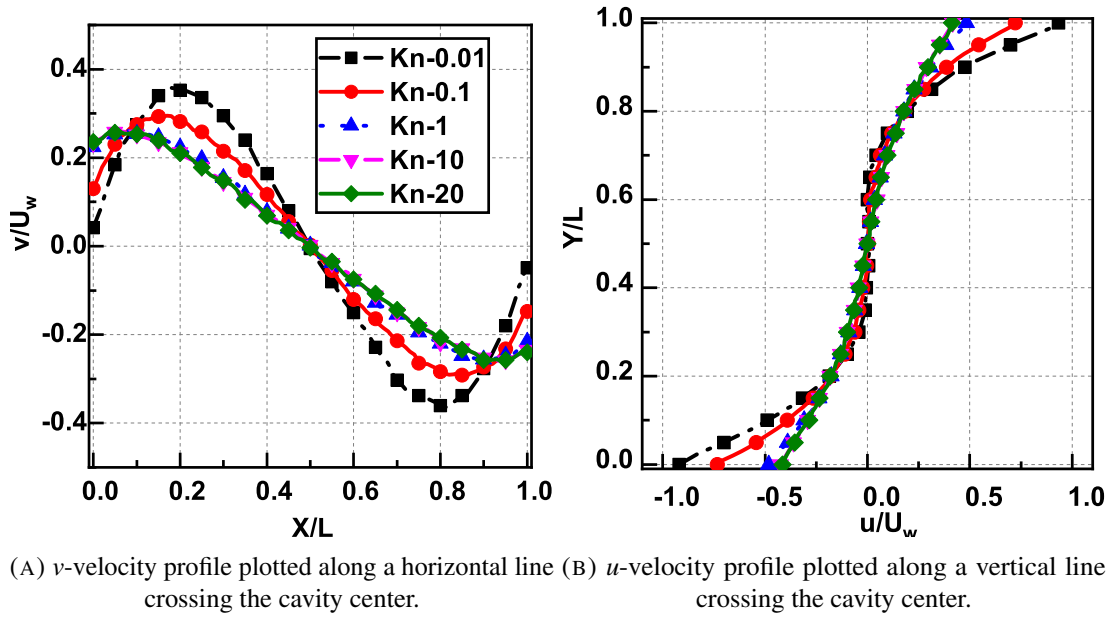


FIGURE 5.5: Comparison of non-dimensional velocity at $Ma = 0.17$ for different Kn for anti-parallel wall motion.

pressure is high at the cavity edges, with a pressure drop towards the cavity's midpoint. The pressure remains almost constant in the slip regime along the cavity's centerlines with minor fluctuations about the mean.

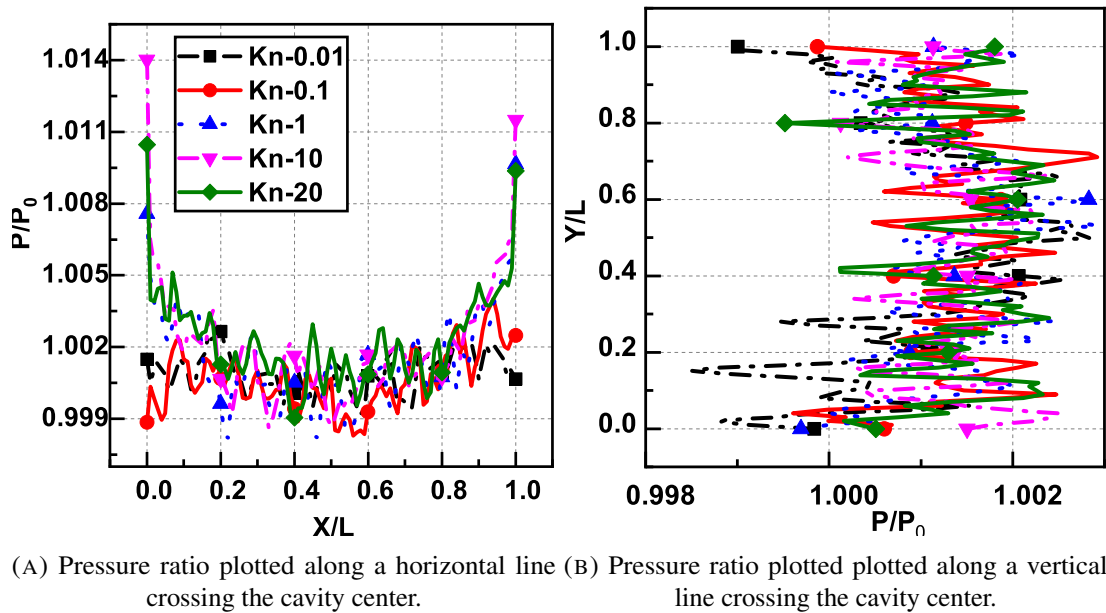


FIGURE 5.6: Comparison of non-dimensional pressure at $Ma = 0.17$ for different Kn for anti-parallel wall motion.

Temperature profiles:

The temperature ratio along the cavity walls at $Ma = 0.17$ for different Kn is shown in Figure 5.7. We see that the non-dimensional temperatures vary over a broader range when compared with those near the domain centerlines. The peaks in the temperatures occur at the corners of the domain due to both compression and viscous dissipation effects.

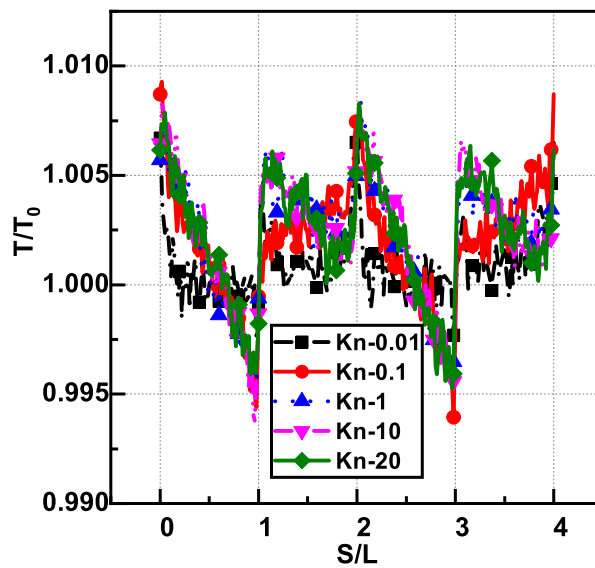


FIGURE 5.7: Variation of temperature ratio plotted along the four walls of the driven cavity at $Ma = 0.17$ for different Kn for anti-parallel wall motion.

Heat flux profiles:

The variations in heat flux along the four walls of the cavity, as a function of Kn , are shown in Figure 5.8. The wall heat flux (q_w) is given by equation 5.1,

$$q_w = q_i - q_r = \frac{F_N}{A \Delta t} \left\{ \sum_{j=1}^N \left[\frac{1}{2} m_j c_j^2 + e_{R_j} + e_{V_j} \right]_i - \sum_{j=1}^N \left[\frac{1}{2} m_j c_j^2 + e_{R_j} + e_{V_j} \right]_r \right\} \quad (5.1)$$

where, F_N denotes the number of real molecules represented by each simulated molecule, A is the surface area, Δt is the time step, N is the number of particles colliding with surface per unit time per unit area. Subscripts i and r denotes the incident and reflected particles.

In this figure, $q_0 = \frac{\mu RT_0}{L}$ is used to non-dimensionalize the heat-flux profiles. The heat flux is symmetric about the vertical centerline. The heat flux almost remains constant in the transition and free molecular regimes, whereas higher fluctuations are observed in the slip regime. The maximum heat flux peaks occur at the intersection of the driving lid with vertical walls, i.e., corners 0 and 2, due to heat accumulation as the flow occurs.

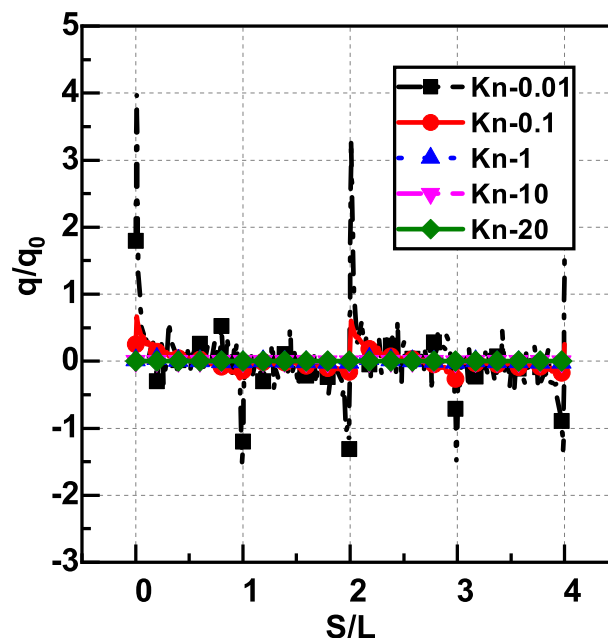


FIGURE 5.8: Variation of heat flux ratio plotted along the four walls of the driven cavity at $Ma = 0.17$ for different Kn for anti-parallel wall motion.

5.2.2 Parallel wall motion

5.2.2.1 Influence of Mach number

Contour plots of flow field:

The contours of different flow field properties for $Ma = 0.70$ at $Kn = 1$ for parallel wall motion are shown in Figure 5.9a-5.9d. Along the driving walls, the velocity magnitude is higher compared to the central domain. Also, for the lowest Ma case the fluctuations are higher than the other cases due to statistical scatter. Also, the peak magnitudes in the domain increase with Ma .

From the pressure contours, it is observed that the top left, bottom left corners of the cavity have a significant drop in pressure, whereas, at the other corners, there is a considerable pressure rise. This can be attributed to the expansion of the fluid at the top left corner and compression in the other corner due to the lid motion.

The maximum temperature in the flow can be seen to increase with increasing lid velocities. It is also observed that the cold region exists on the left side wall, whereas the hot region is observed on the right side edge. The for low lid velocities. The hot region shifts from the right side edge and moves towards the driving walls for increasing lid velocities. This can be attributed to the compression effects for low velocities and viscous dissipation at higher velocities, primarily observed near the driving walls.

The density contours follow the pressure profiles. At lower velocities, the density fluctuations are prominent inside the domain. These fluctuations are reduced as the

lid-velocity increases. For the highest case, most of the domain is covered by the initial density, with increased magnitudes at the corners.

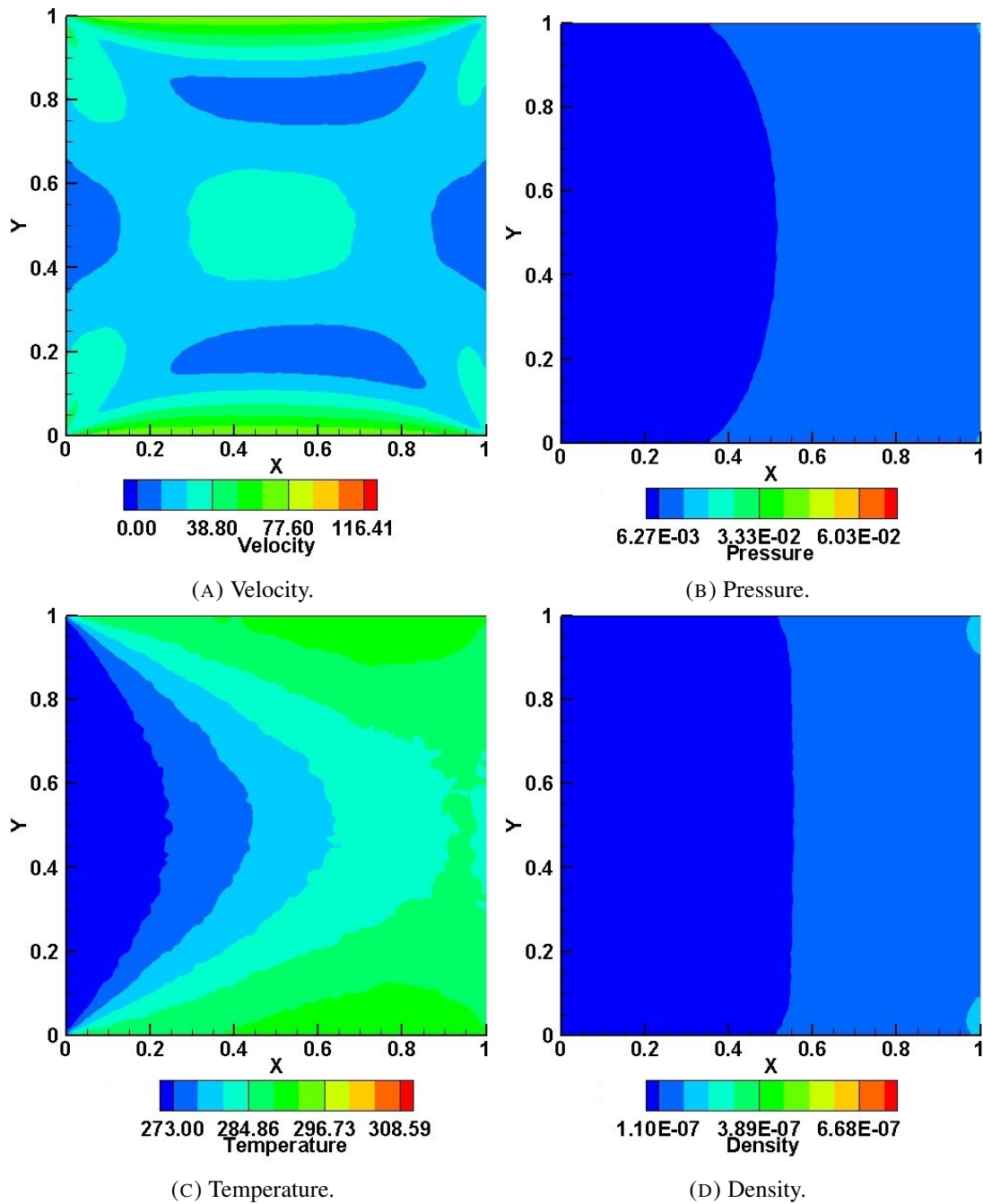


FIGURE 5.9: Contours of flow field for $Ma = 0.70$ at $Kn = 1$ for parallel wall motion.

Figure 5.10 shows the velocity streamlines for $Ma = 0.70$ case. The streamlines for all the other Mach numbers are similar in appearance; hence, only one plot is shown

here. The streamlines show two symmetric and counter-rotating primary vortices. These vortex centers shift towards the right side of the flow domain for higher lid velocities.

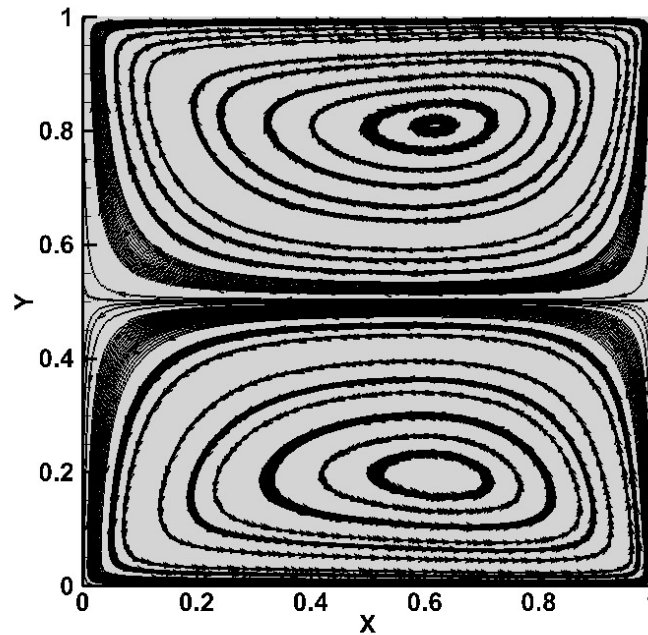


FIGURE 5.10: Velocity streamlines for $Ma = 0.70$ at $Kn = 1$ for parallel wall motion.

5.2.2.2 Influence of Knudsen number

Velocity profiles:

Figure 5.11 shows the v and u velocity components in the x and y directions along horizontal and vertical lines crossing the cavity center at $Ma = 0.17$ for different Kn . The v -velocity component follows a sinusoidal profile with a change in magnitude occurring at the cavity center. From the u -velocity profile, it can be observed that the profiles are symmetric about the horizontal centerline, and the velocity decreases first and then increases. It is interesting to note that the drop in velocity is more for $Kn = 0.01$. For higher Kn , there exists a large slip between the driving walls and the adjacent fluid

layers as expected. Thus, lesser kinetic energy is imparted to the flow resulting in smaller velocities of the fluid layers along the driving walls. This also manifests as smaller flow velocities along the horizontal centerline.

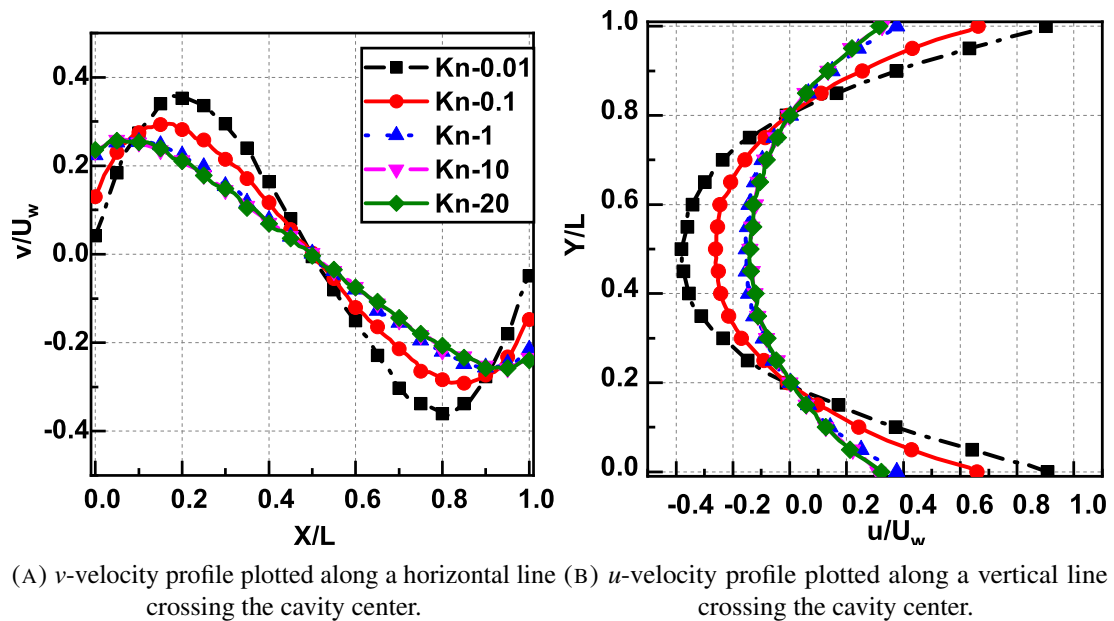


FIGURE 5.11: Comparison of non-dimensional velocity at $Ma = 0.17$ for different Kn for parallel wall motion.

Pressure profiles:

Figure 5.12 shows the non-dimensional pressure ratio in the x and y directions along horizontal and vertical lines crossing the cavity center at $Ma = 0.17$ for different Kn . The pressure variation along the horizontal centerline remains relatively uniform in the slip regime, whereas there is a significant pressure change in other regimes. The curves overlap for higher n cases indicating that the number density has minimal effect on the pressure fluctuations in the transition and free molecular regimes. Along the vertical centerline, the pressure change is, however, negligible.

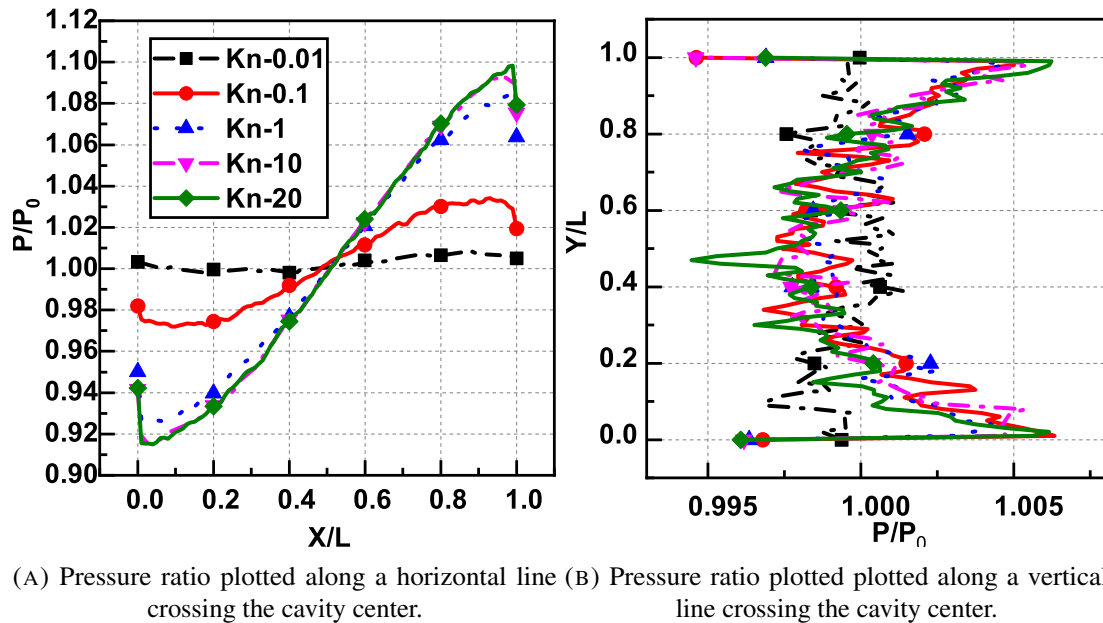


FIGURE 5.12: Comparison of non-dimensional pressure at $Ma = 0.17$ for different Kn for parallel wall motion.

Temperature profiles:

The temperature ratio along the cavity walls at $Ma = 0.17$ for different Kn is shown in Figure 5.13. It is observed that the deviation in non-dimensional temperature is high in magnitude near the driving walls due to high viscous dissipation. The plots show a significant variation of temperature as the flow progresses from the slip to the transition regime. In the slip regime, the temperature deviation from the initial value is negligible. The increase in Kn leads to further deviation in the gas temperature away from the initial temperature of the flow field.

A common feature among the velocity, temperature, and pressure plots is that the change in profiles is more pronounced at the onset of the transition regime (particularly about $Kn = 0.1$) than the slip or free molecular regimes.

Heat flux profiles:

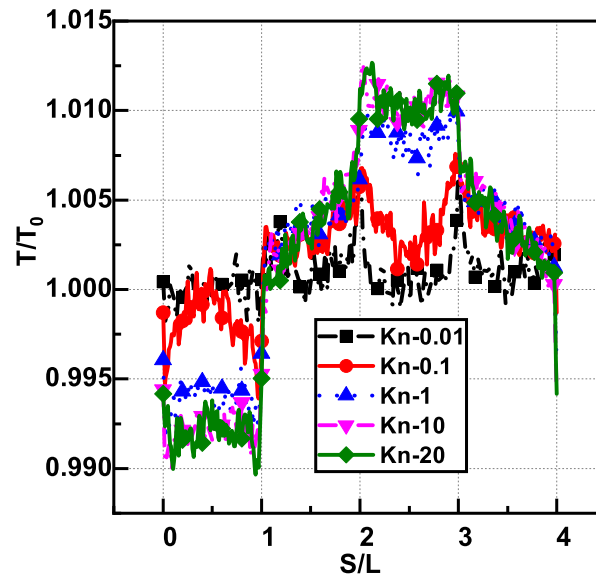


FIGURE 5.13: Variation of temperature ratio plotted along the four walls of the driven cavity at $Ma = 0.17$ for different Kn for parallel wall motion.

The variations in heat flux along the four walls of the cavity, as a function of Kn , are shown in Figure 5.14. In this figure, $q_0 = \frac{\mu RT_0}{L}$ is used to non-dimensionalise the heat-flux profiles. The variation in heat flux along the walls is more prominent in the slip regime. With an increase in Kn , the variations in heat flux along the walls reduce and tend to zero. Energy gain or loss of the molecules occurs when they interact with the cavity walls. Heat is absorbed from the surroundings by the cavity in the top left corner due to expansion. At higher Kn , compression and viscous dissipation effects due to the driving walls lead to a higher gas temperature near the right-side wall. This results in the heat flux peaks as observed at corners 2 and 3.

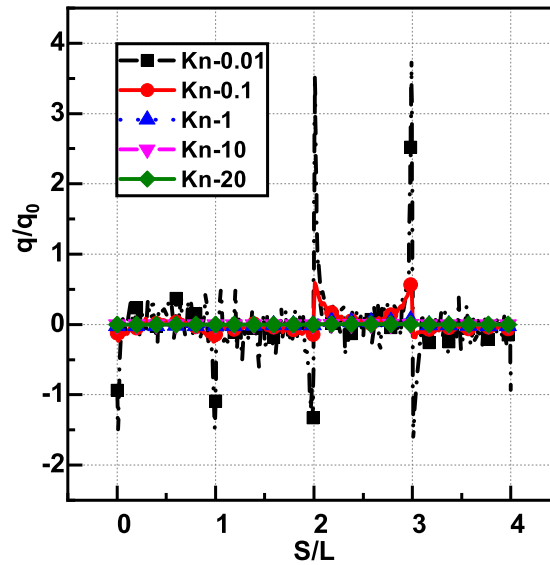


FIGURE 5.14: Variation of heat flux ratio plotted along the four walls of the driven cavity at $Ma = 0.17$ for different Kn for parallel wall motion.

5.3 Four-sided lid-driven cavity

This section presents the results for the four-sided lid-driven cavity. Initially, the effects of Mach number are discussed and are followed by effects of Knudsen number for both anti-parallel and parallel wall motions.

5.3.1 Anti-parallel wall motion

5.3.1.1 Influence of Mach number

Velocity profiles:

The velocity contours for different Mach numbers at $Kn = 1$ for anti-parallel wall motion are shown in Figure 5.15. It is observed that the fluid velocities near all four walls are

higher in the mid-portion and reduce towards the center of the domain. The profiles are found to be similar for all the cases. In all instances, the wall velocity is found to be approximately one-fourth of the imposed velocity U_w due to slip phenomenon observed for rarefied gas flows. There are stagnant zones near the corners and center of the cavity where the velocity is nearly zero. The contours are not symmetrical and show deviation with an increase in Mach number.

Figure 5.16 shows the velocity streamlines for $Ma = 0.70$ case. The streamlines for all the other Mach numbers are similar in appearance; hence, only one plot is shown here. The streamlines are found to be symmetrical about both x and y axes and consists of four vortices which are counter-rotating. The vortices appear in pairs that are symmetrical about the horizontal and vertical centerline. Interestingly though the velocity contours show asymmetry for higher Mach numbers, the streamline plots are symmetrical. This can be explained by the pressure contours (Figure 5.18). For low Mach number, the pressure changes are minimal in the domain. For higher Mach numbers, pressure changes are significant. However, this high-pressure region is limited to a tiny area near the corners. Therefore, the influence of change in pressure is not experienced by the bulk of the fluid, as seen in the streamline plots. Each of the vortices is located at a distance of $X = 0.5$, $Y = 0.18$ from the nearest driving wall.

Figure 5.17a-5.17b show the non-dimensional v and u velocity components in the x and y directions respectively for different Mach numbers at $Kn = 1$. From the profiles, it can be observed that in both cases, the variation is identical. Velocity increases first, decreases, and then finally increases. The profile follows a sinusoidal like shape for both

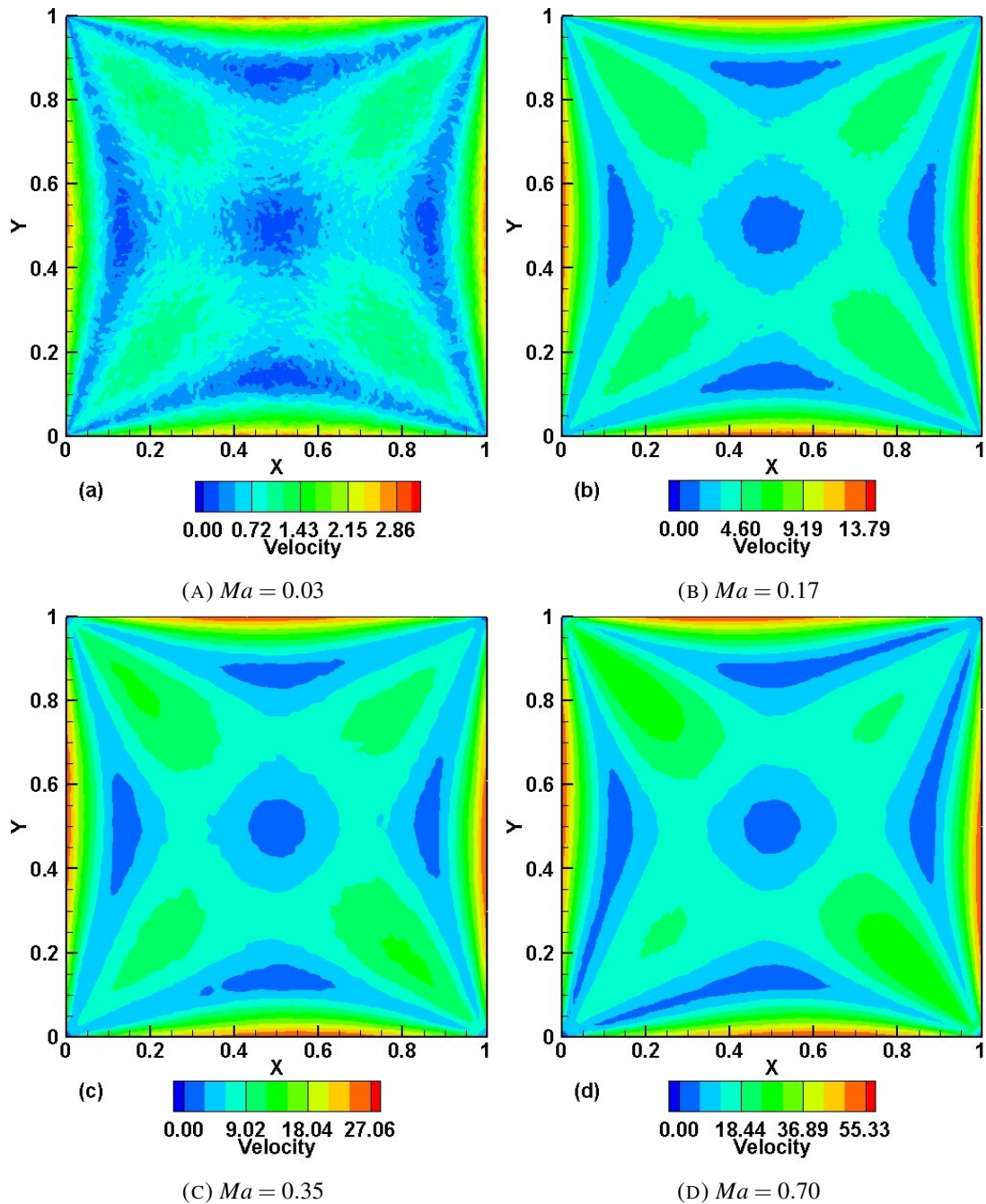


FIGURE 5.15: Velocity (m/s) contours at $Kn = 1$ for different Ma for anti-parallel wall motion.

cases. The velocity fluctuations are higher for the $Ma = 0.03$, whereas the profiles are smoother for other cases.

The slip velocity u_s , is defined as the magnitude of the difference between near-wall gas velocity and the lid velocity. The slip velocity can be obtained by direct sampling of the

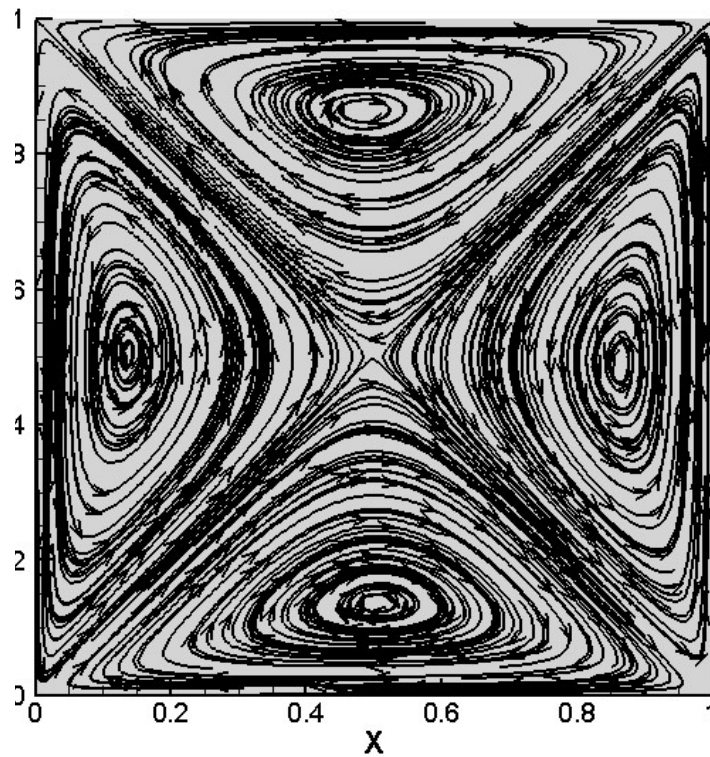
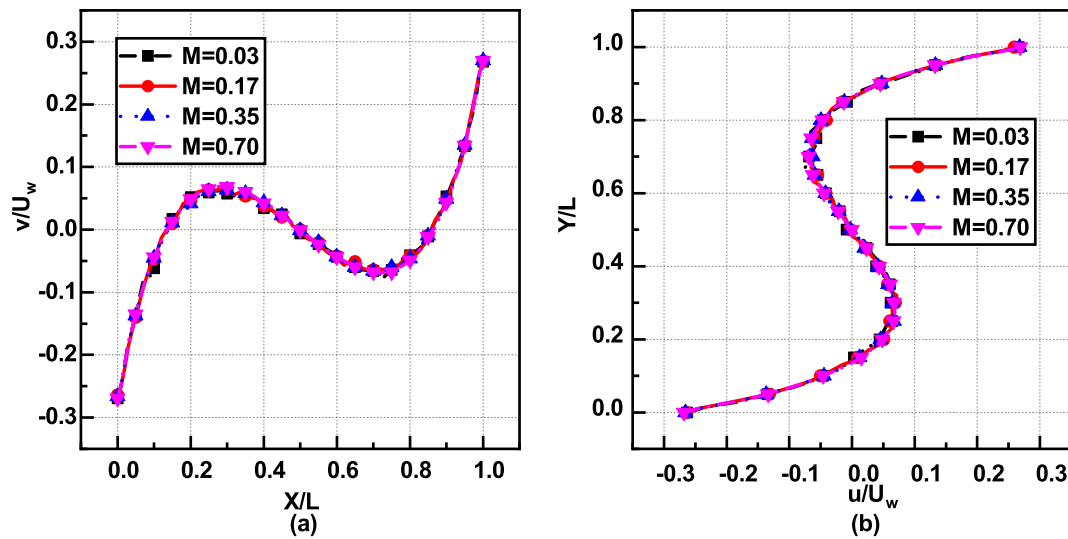


FIGURE 5.16: Velocity streamlines for $Ma = 0.70$ at $Kn = 1$ for anti-parallel wall motion.

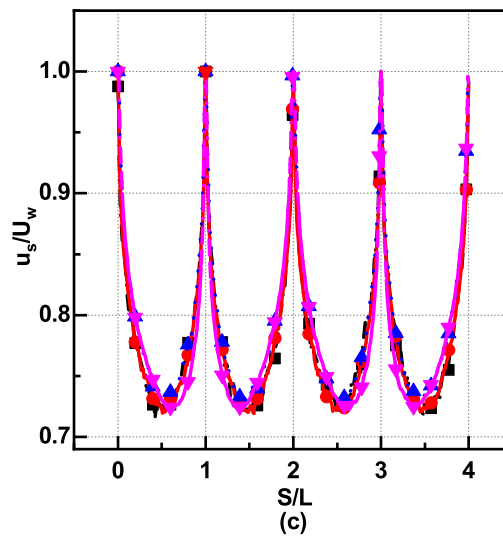
microscopic particles that impact the wall surface. Alternatively, it can be extracted from the macroscopic flow velocity in the cell adjacent to the wall [140], which is used in the present study. The slip velocity is normalized by the magnitude of lid velocity U_w to obtain the slip velocity ratio u_s/U_w .

Figure 5.17c shows the profiles of slip velocity ratio u_s/U_w along the walls of the cavity for different Mach numbers at $Kn = 1$. As expected, it is close to unity at the corners, where the flow is stagnant and attains a minimum near the center of each wall. For the present case of anti-parallel wall motion, variation along all the four walls is equivalent to each other due to the flow configuration's symmetry. This is also reflected in the streamlines plots shown in Figure 5.16, where the four vortices look alike. When Ma is varied, the slip velocity ratio is relatively the same, and the variation among the different

profiles is minimal. The variation is also symmetric along a given wall for lower Ma . However, the asymmetry becomes noticeable for higher Ma due to increased inertial effects.



(A) v -velocity profile plotted along a horizontal line (B) u -velocity profile plotted along a vertical line, crossing the cavity center.



(C) Slip velocity ratio plotted along the four walls of the driven cavity.

FIGURE 5.17: Comparison of non-dimensional velocity and slip velocity at $Kn = 1$ for different Ma for anti-parallel wall motion.

Pressure profiles:

The pressure contours for different Mach numbers at $Kn = 1$ for anti-parallel wall motion are shown in Figure 5.18. From the contours, it can be observed that the regions of high pressure occur at the top right and bottom left corners of the cavity which can be attributed to compression. In contrast, there are low-pressure regions at the top left and bottom right corners due to flow expansion. The pressure changes along the walls are found to increase with increasing Ma . Near the center of the cavity, the region of initial pressure transpires. For $Ma = 0.03$ the pressure is relatively uniform in the domain, whereas the pressure variation happens near the corners. For the other cases, the pressure variation observed is more significant throughout the domain. For $Ma = 0.70$ a diagonal band of initial pressure develops, with increased pressure distribution on either side of the band.

The pressure ratio profile along a horizontal line crossing the center of the cavity and along the walls of the cavity for different Mach numbers at $Kn = 1$ is shown in Figure 5.19a-5.19b. Figure 5.19a shows that the pressure ratio is high near the driving walls and reaches a minimum towards the center, where the flow stagnates. The pressure variation along the vertical centerline is identical to this and hence not depicted.

From Figure 5.19b, it can be observed that the pressure ratio increases with the Ma as more kinetic energy is imparted to the fluid, which in turn increases the pressure ratio. The peak pressures occur at points with $S/L=0, 2,$ and 4 because of the motion imparted by the driving wall. Compared to the pressure rise, the pressure drop at points $S/L=1$ and 3 is nominal. The peak pressure ratios are 1.04, 1.32, 2.00, and 7.64 for $Ma = 0.03, 0.17, 0.35,$ and 0.70 respectively.

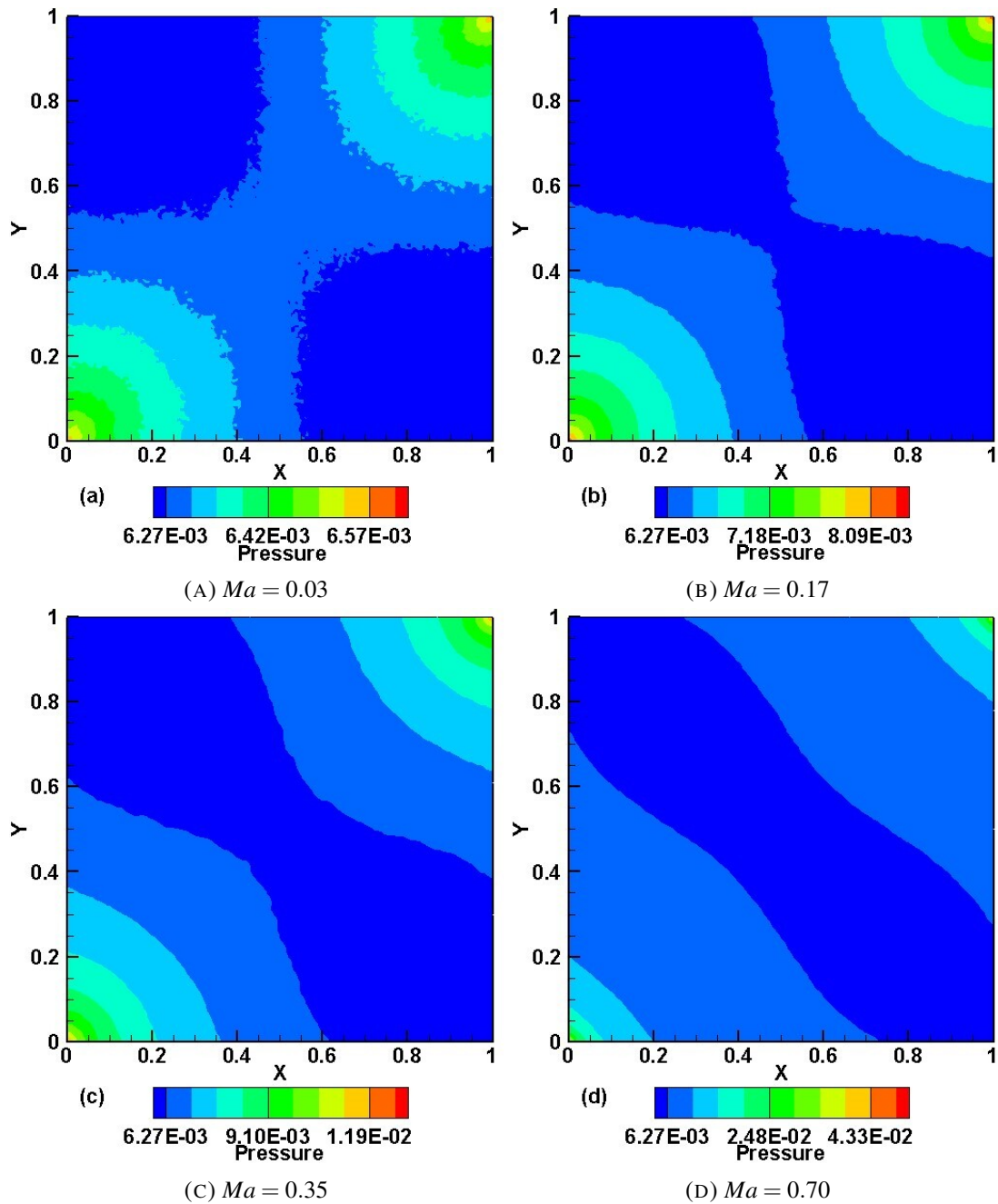
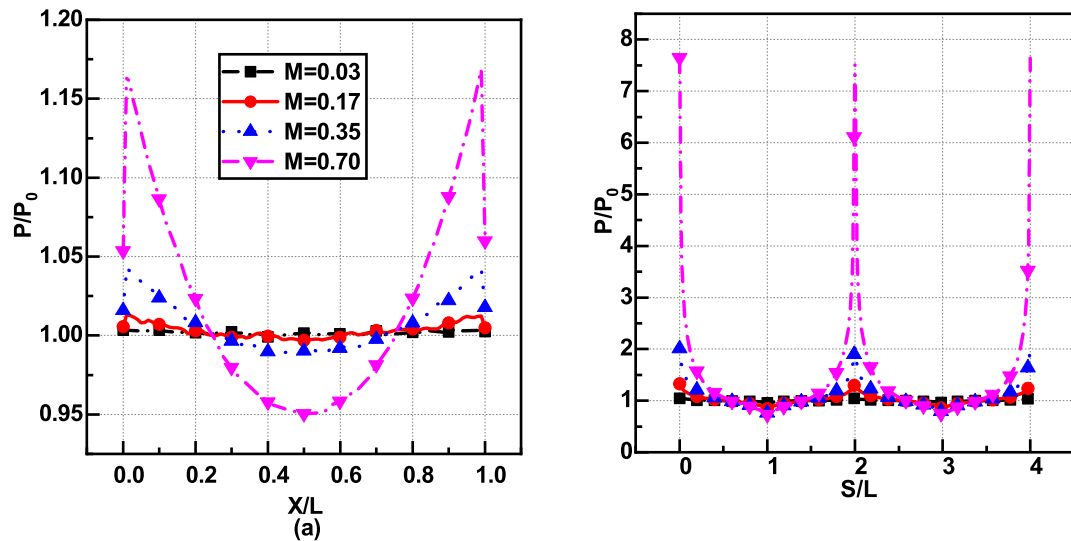


FIGURE 5.18: Pressure (Pa) contours at $Kn = 1$ for different Ma for anti-parallel wall motion.

Temperature profiles:

The temperature contours for different Mach numbers at $Kn = 1$ for anti-parallel wall motion are shown in Figure 5.20. The temperature contours follow a similar trend as the pressure profile, where the cold regions occur at the top left and bottom right corners.



(A) Pressure ratio along a horizontal line crossing the cavity center. (B) Pressure ratio along the four walls of the driven cavity.

FIGURE 5.19: Comparison of non-dimensional pressure at $Kn = 1$ for different Ma for anti-parallel wall motion.

In contrast, the hot regions appear at the other two opposite corners that are well above the fluid's initial temperature. The magnitude of the temperature distribution increases with an increase in the Mach numbers due to the viscous dissipation effects. For the case of $Ma = 0.03$ most of the flow domain has the temperature close to the initial temperature due to low viscous dissipation and compressibility effects. For the other cases, the regions of high temperature grow in size and occupy most of the flow domain.

The temperature ratio profile along a horizontal line crossing the center of the cavity and along the walls of the cavity for different Mach numbers at $Kn = 1$ is shown in Figure 5.21a. Like pressure ratios, the temperature ratios are high near the driving walls and reach a minimum towards the center, where the flow stagnates. The temperature variation along the vertical centerline is identical to this and hence not shown.

Figure 5.21b shows the temperature jump ratio (T_j/T_0) along the walls of the cavity for different Mach numbers at $Kn = 1$. In the plot, the temperature jump T_j is normalized

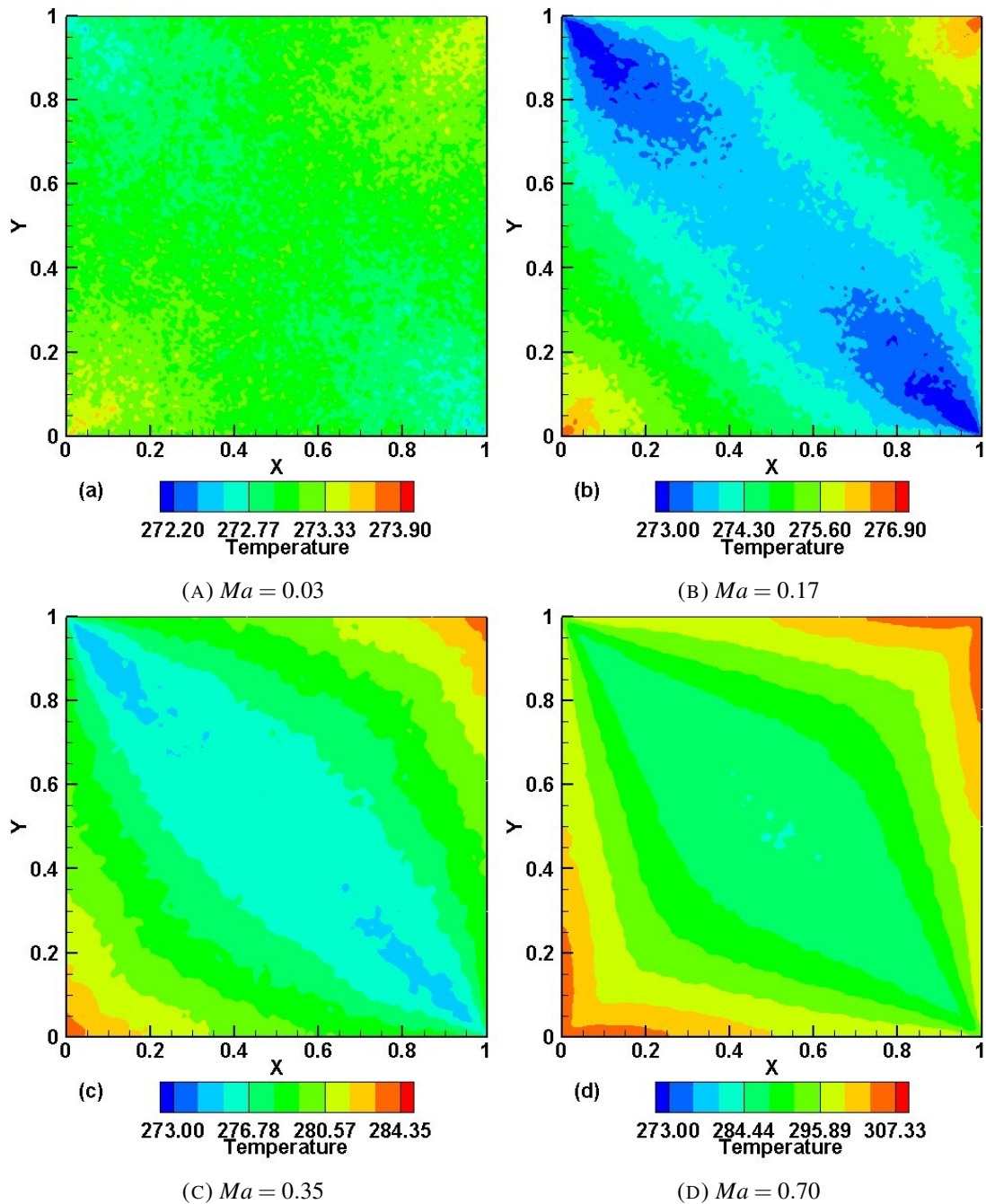


FIGURE 5.20: Temperature (K) contours at $Kn = 1$ for different Ma for anti-parallel wall motion.

by the initial wall temperature T_0 . Similar to the velocity slip, the temperature jump is also obtained by extracting the macroscopic flow properties from the cell adjacent to the wall. It can be observed that for lower Ma , the temperature jump is very minimal. As Ma increases, the fluid kinetic energy increases, leading to higher temperatures and

higher viscous dissipation near the walls, contributing to a higher temperature jump ratio. This phenomenon is mainly observed near the corners where the flow gradients are very high, owing to the change in the flow direction.

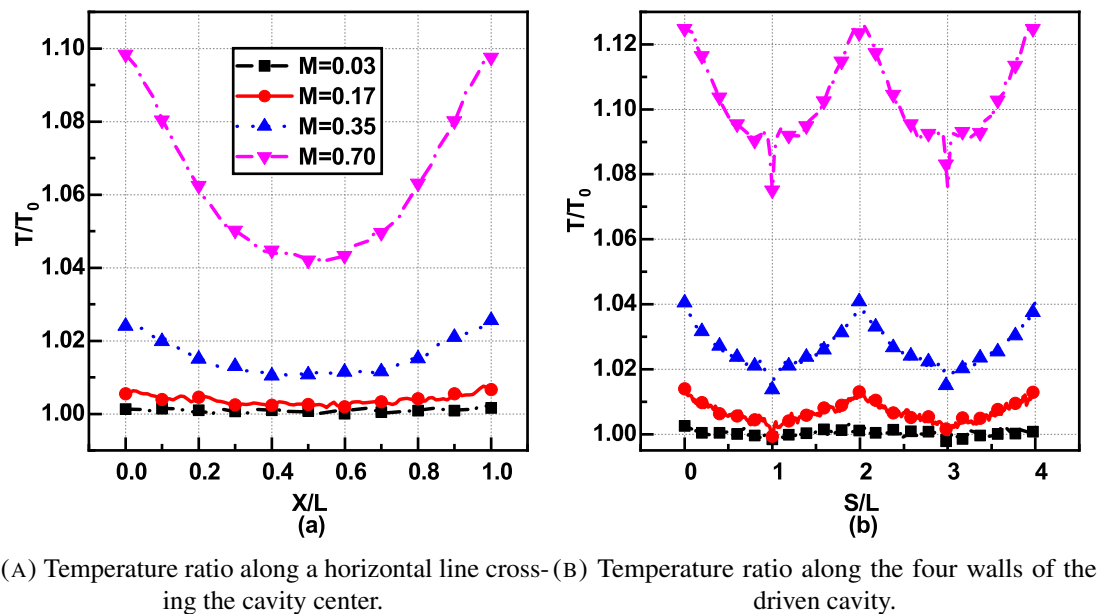


FIGURE 5.21: Comparison of non-dimensional temperature at $Kn = 1$ for different Ma for anti-parallel wall motion.

Cold to hot heat transfer:

In the rarefied flow conditions, the conventional Fourier's continuum-based method cannot accurately predict the heat transfer trends; consequently, more sophisticated constitutive models are required to assess heat transfer characteristics. In the present study, the constitutive model derived by Sone [141], which is a nonlinear form of the Boltzmann equation, is used to predict the heat flow patterns. This model takes into consideration the dependence of temperature on the thermal conductivity of the gas. In the present study, the temperature variations are relatively less, and hence the Sone's constitutive model is applied. The following relation gives the heat flow vector.

$$Q = KQ_1 + K^2Q_2 + K^3Q_3 \quad (5.2)$$

$$Q_1 = 0 \quad (5.3)$$

$$Q_2 = -\frac{5}{4}\gamma_2 \frac{\partial \tau^{**}}{\partial x_i} \quad (5.4)$$

$$Q_3 = -\frac{5}{4}\gamma_2 \frac{\partial \tau^{**}}{\partial x_i} - \frac{5}{4}\gamma_5 \frac{\partial \tau^{**}}{\partial x_i} + \frac{1}{2}\gamma_3 \frac{\partial^2 u_i^{**}}{\partial x_j^2} \quad (5.5)$$

$$K = Kn \frac{\sqrt{\pi}}{2} \quad (5.6)$$

$$\tau^{**} = \frac{T - T_0}{T_0} \quad u_i^{**} = \frac{u_i}{\sqrt{2RT_0}} \quad x_i = \frac{X_i}{L} \quad (5.7)$$

In equation 5.5, the second term is the Fourier term, and the third term consists of the second derivative of the velocity field. Thus as per ref.[141], the heat flux is a function of velocity field curvature at the given rarefied condition. Also, the other terms are defined as the functions given below,

where, τ^{**} is the non-dimensional temperature, T_0 is the initial temperature, R is the universal gas constant and x_i are the non-dimensional coordinates. The transport coefficients used in eq. 5.5 are set as $\gamma_2 = 1.9222$, $\gamma_3 = 1.9479$, and $\gamma_5 = 0.9611$ [141, 142]. Figure 5.22

shows the heat lines overlaid on temperature contours, predicted by individual terms of eq. 5.5 and the summation of the individual terms, respectively, for $Ma=0.70$ at $Kn=1$.

Figure 5.22a shows the contribution of the Fourier term to the heat flux, given by eq. 5.4. The direction of the heat lines indicates that the heat transfer occurs from the hot region of the flow field (near the walls) to the cold region (at the center) of the cavity. The heat lines exhibit the same behavior due to the second term in eq. 5.5 as seen from Figure 5.22b. In contrast, the direction of the heat lines given by the third term in eq. 5.5 is from the cold to hot region of the cavity, as shown in Figure 5.22c. The heat lines resulting from all the three terms' contribution are shown in Figure 5.22d, where we see that their direction is from the cold to hot region of the cavity. This indicates that the velocity curvature term of the eq. 5.5 is the most dominant one. This behavior is the dominant characteristic of flows at higher Knudsen numbers, as illustrated in ref. [141, 142].

Heat flux profiles:

The heat flux profile along the cavity walls for different Mach numbers at $Kn = 1$ is shown in Figure 5.23. The wall heat flux (q_w) is given by eq.5.1. In this plot, the heat flux is normalized by $q_0 = \frac{\mu RT_0}{L}$. The heat flux profile has a similar trend as the pressure and temperature variation. It is very minimal for lower Mach numbers due to smaller temperature changes. High viscous dissipation for higher Mach numbers increases the temperature change, increasing the heat flux.

5.3.1.2 Influence of Knudsen number

Velocity profiles:

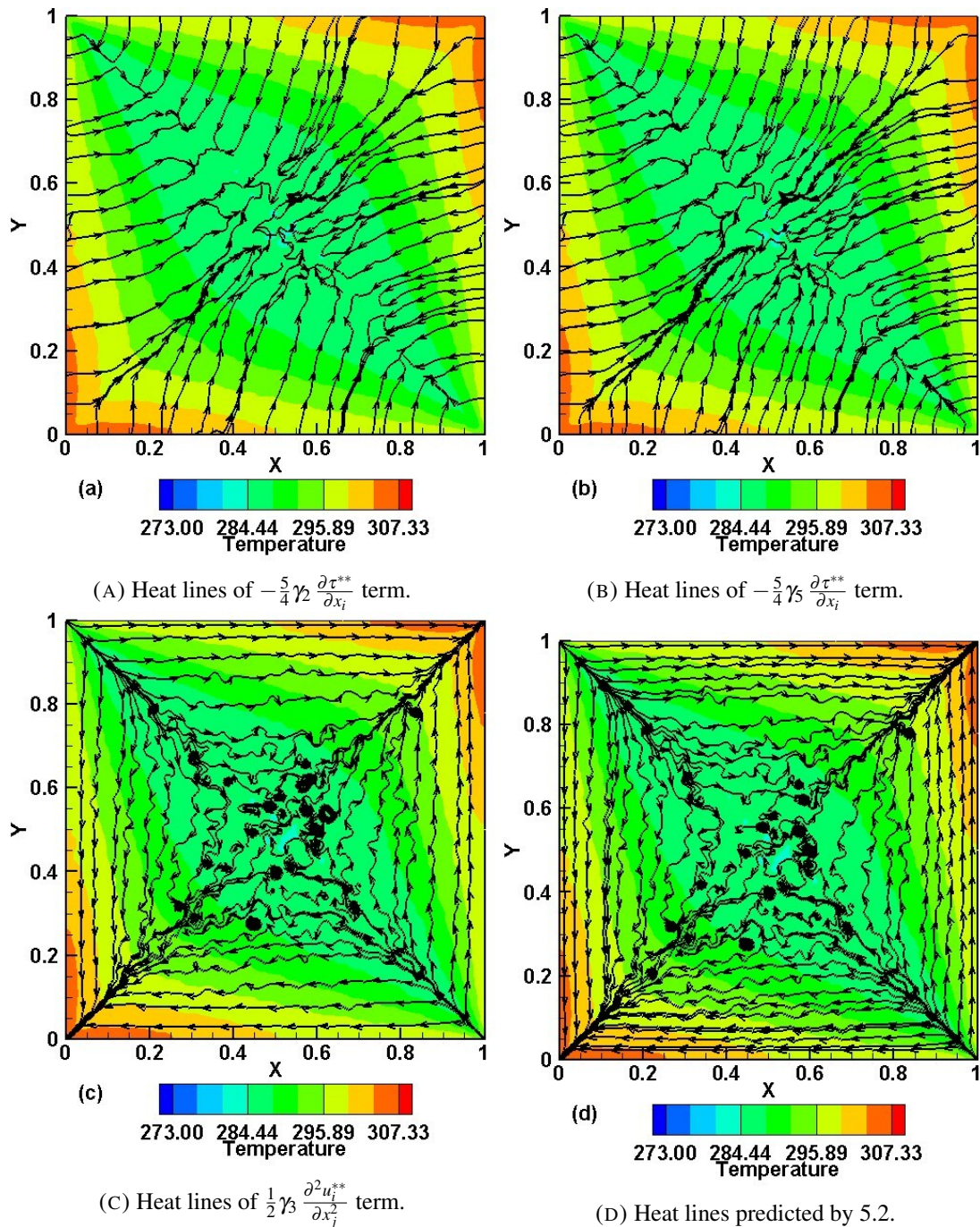


FIGURE 5.22: Contours of Heatlines at $Kn = 1$ for different $Ma = 0.70$ for anti-parallel wall motion.

Figure 5.24a-5.24b shows the v and u velocity components in the x and y directions along horizontal and vertical lines crossing the cavity center at $Ma = 0.17$ for different Kn . It can be observed that with an increase in Kn , the velocity slip near the walls is increasing. It is also observed that the velocity variations are decreasing with increasing

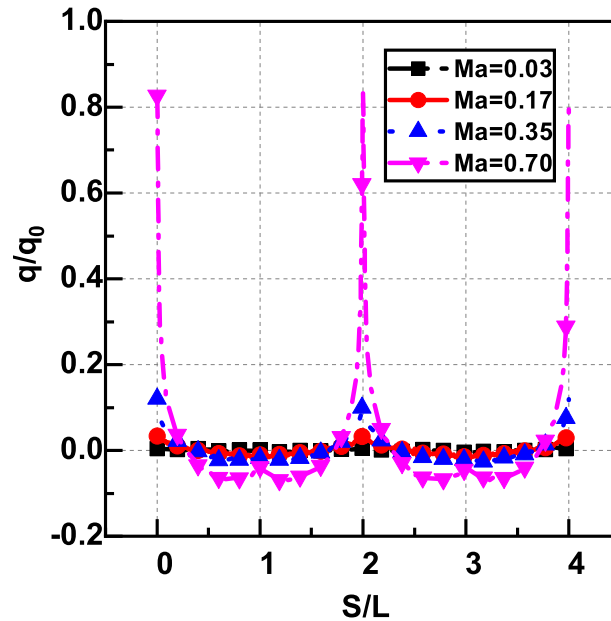
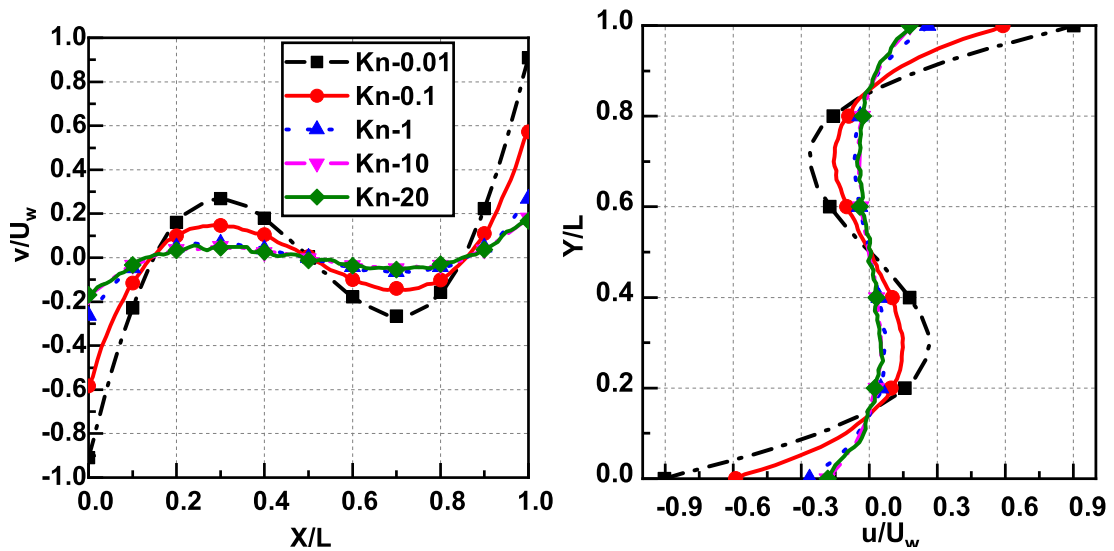


FIGURE 5.23: Variation of heat flux ratio plotted along the four walls of the driven cavity at $Kn = 1$ for different Ma .

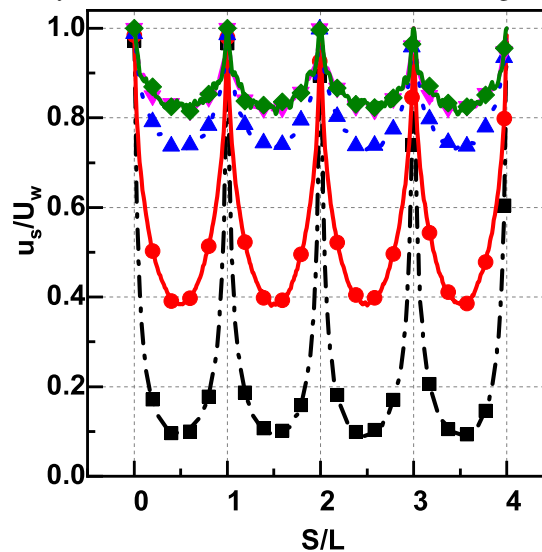
Kn . The profile forms a wavy pattern for both the velocity components. Profiles of the two velocity components are identical owing to the symmetry of the problem.

Figure 5.24c shows the slip velocity ratio (u_s/U_w) along the walls of the cavity at $Ma = 0.17$ for different Kn . The slip velocity ratio is unity at the corners and reaches a minimum away from them. The plots also look similar along the four walls as each wall is equivalent to the other owing to symmetry in the flow configuration. The variation along a given wall is almost symmetric as the Mach number has a relatively smaller magnitude of 0.17. Also, we see that the slip velocity ratio increases with Kn , as expected, due to increased rarefaction effects. This manifests as a relatively smaller drop in the slip velocity ratio for higher Kn .

Pressure profiles:



(A) v -velocity profile plotted along a horizontal line (B) u -velocity profile plotted along a vertical line crossing the cavity center.



(C) Slip velocity ratio plotted along the four walls of the driven cavity.

FIGURE 5.24: Comparison of non-dimensional velocity and velocity slip velocity at $Ma = 0.17$ for different Kn for anti-parallel wall motion.

Normalized pressure ratio along the cavity walls at $Ma = 0.17$ for different Kn is shown in Figure 5.25. In this plot, the pressure P is normalized by the initial pressure P_0 . For higher Kn , the pressure ratio is less, whereas the pressure ratio is highest for $Kn = 0.1$, which lies near the transition regime. Variation in pressure ratio is mainly due to the change in density in different regimes as the temperature remains relatively constant.

Since the Mach numbers are not significantly high in the present problem, the flow departs very little from thermodynamic equilibrium. The peak pressures occur at points $S/L = 0, 2,$ and $4,$ with considerable pressure drop occurring at $S/L = 1$ and $3.$ The peak pressure rise and peak pressure drop are highest for $Kn = 0.1.$ For $Kn > 1$ the profiles tend to be overlapping. Pressure variations along horizontal and vertical centerlines of the cavity are minimal ($< 2\%$) and hence not shown.

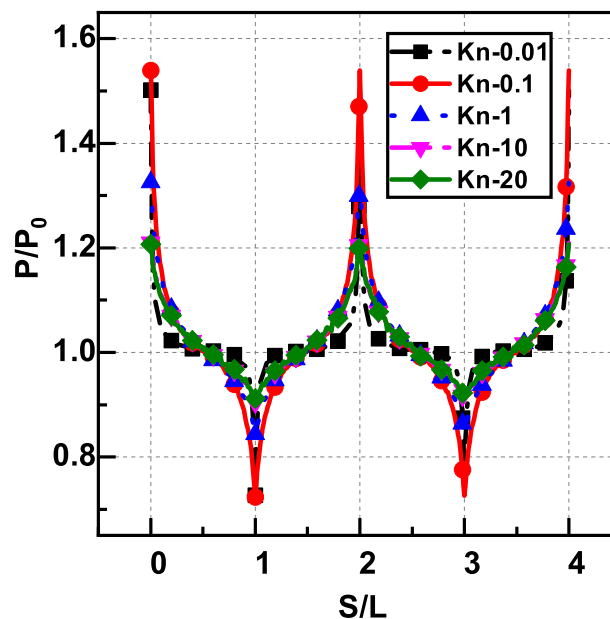


FIGURE 5.25: Variation of pressure ratio plotted along the four walls of the driven cavity at $Ma = 0.17$ for different Kn for anti-parallel wall motion.

Temperature profiles:

The temperature jump ratio (T_j/T_0) along the walls of the cavity at $Ma = 0.17$ for different Kn is shown in Figure 5.26. In this plot, the temperature jump T_j is normalized by the initial temperature $T_0.$ The temperature jump plot follows a similar trend as the pressure profile. For $Kn = 0.01,$ the temperature variation is minimal, and the temperature is very close to the initial temperature. For the case of $Kn = 0.1,$ the

peaks are higher due to the temperature jump at the onset of the transition regime and the effects of the Knudsen layer [143]. For $Kn > 10$ the profiles are found to be overlapping. The departure of near-wall temperature from the initial value increases with Kn . However, for all Kn , similar values of peak temperatures occur at $S/L = 0, 2,$ and 4 due to compressibility. It can be observed that the temperature jump ratio increases with Kn . However, it is not significant owing to the relatively lower magnitude of $Ma = 0.17$. Appreciable change in the magnitudes of temperature jump ratios are expected for higher Mach numbers. Temperature variations along horizontal and vertical centerlines of the cavity are minimal ($< 1\%$) and hence not shown.

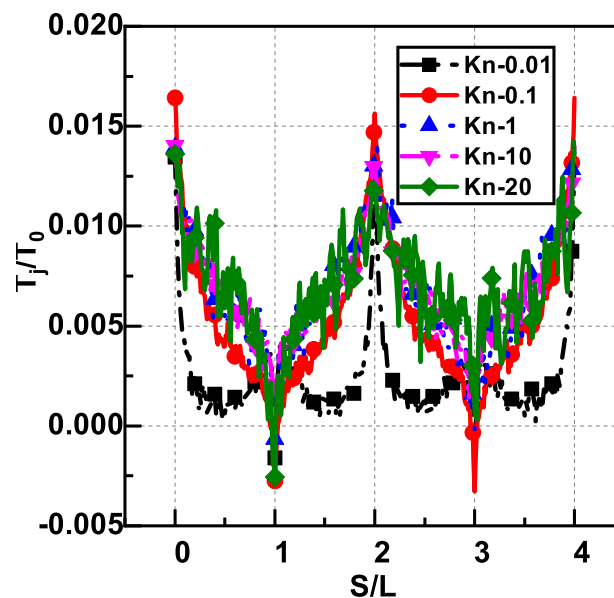


FIGURE 5.26: Variation of temperature jump ratio plotted along the four walls of the driven cavity at $Ma = 0.17$ for different Kn for anti-parallel wall motion.

Heat flux profiles:

The heat flux profile along the cavity walls at $Ma = 0.17$ for different Kn is shown in Figure 5.27. The heat flux is normalized by q_0 as explained previously. From the figure, it can be observed that the heat flux variation is more significant for $Kn = 0.01$ with a

positive peak in heat flux at $S/L = 0, 2, 4$ and a negative peak in heat fluxes at $S/L = 1, 3$. The profiles overlap, and the heat flux magnitude decreases with Kn . This trend is in contrast to the temperature changes (Figure 5.26), which increase with Kn .

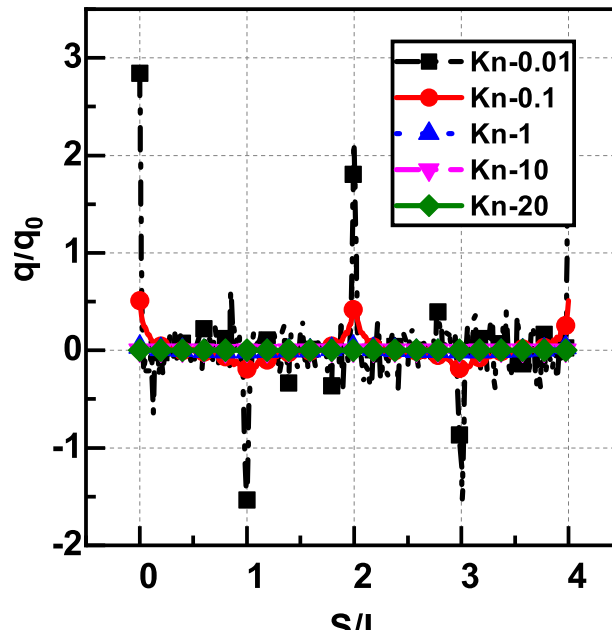


FIGURE 5.27: Variation of heat flux ratio plotted along the four walls of the driven cavity at $Ma = 0.17$ for different Kn for anti-parallel wall motion.

5.3.2 Parallel wall motion

5.3.2.1 Influence of Mach number

Velocity profiles:

The velocity contours for different Mach numbers at $Kn = 1$ for parallel wall motion are shown in Figure 5.28. Similar to the anti-parallel wall motion, the wall velocities at all four sides are higher and reduce towards the center. The contours are found to be identical for all the cases. In all the cases, the maximum near-wall velocity is found to be approximately one-half of the imposed velocity U_w . The low-velocity zone increases

in size, with an increase in Mach number. The contours are not symmetrical and show deviation with an increase in Mach numbers.

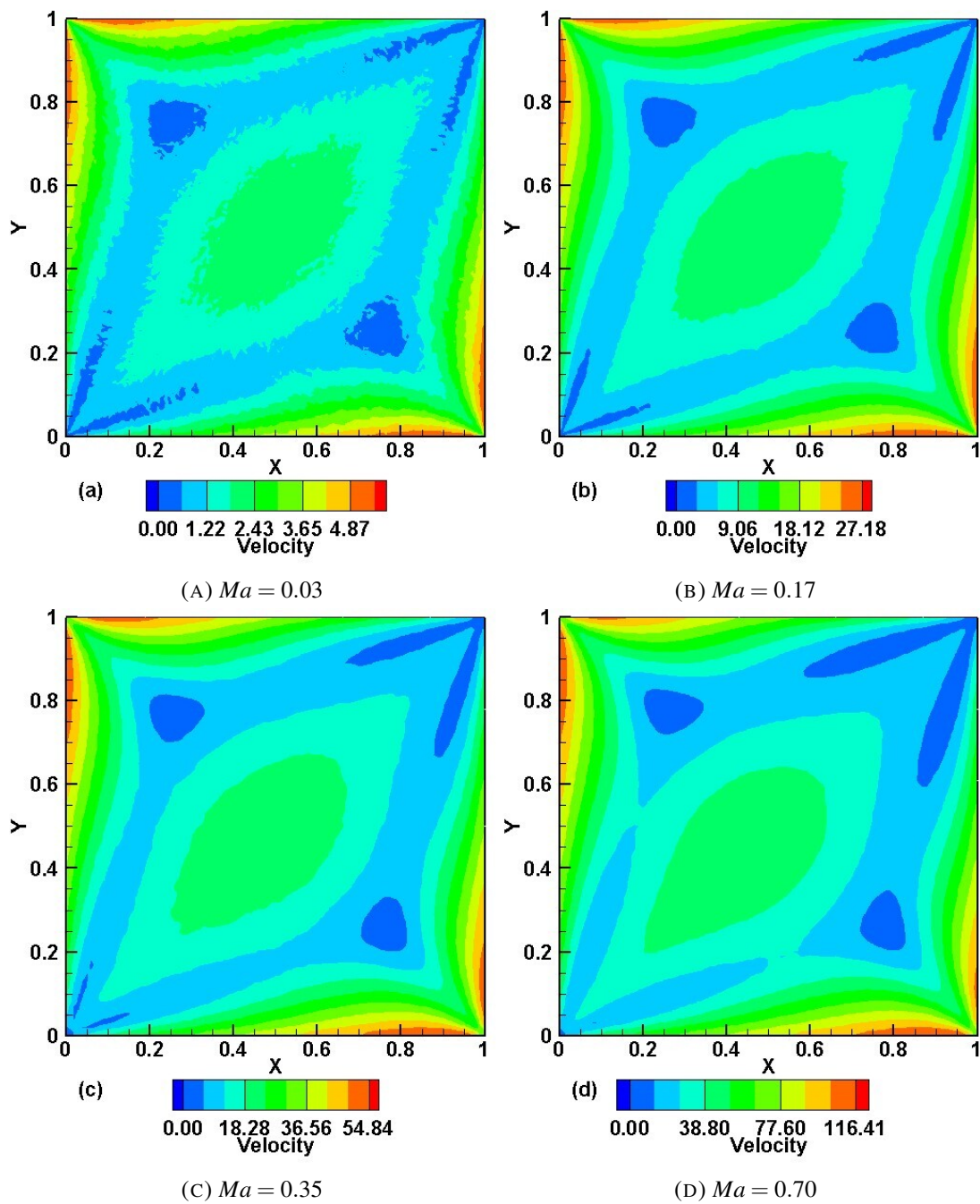


FIGURE 5.28: Velocity (m/s) contours at $Kn = 1$ for different Ma for parallel wall motion.

Figure 5.29 shows the velocity streamlines for $Ma = 0.70$ case. The streamlines for all the other Mach numbers are similar in appearance; hence, only one plot is shown

here. The streamlines are symmetrical about the diagonal and consist of two primary vortices that are counter-rotating. Each of the vortices is located at a distance of $X = 0.76$, $Y = 0.24$ from the nearest driving wall.

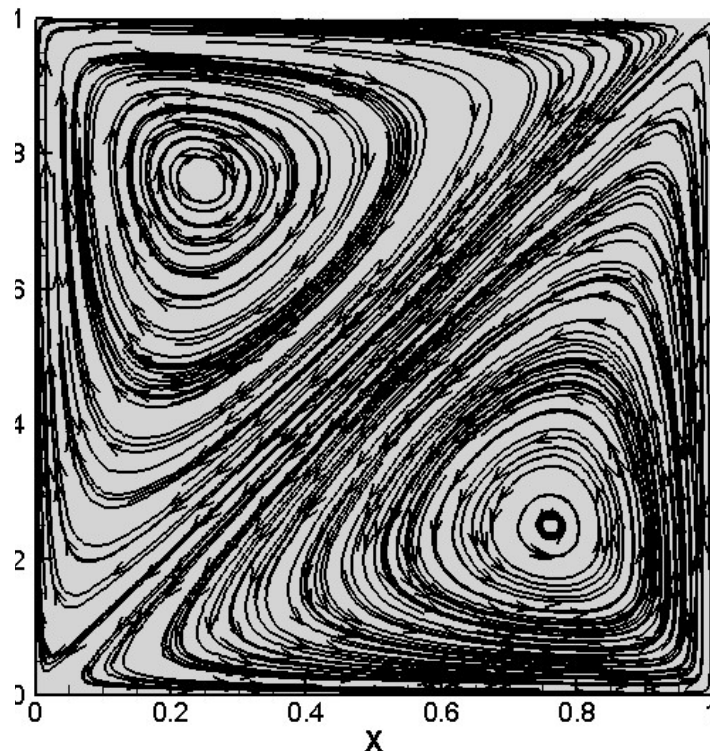


FIGURE 5.29: Velocity streamlines for $Ma = 0.70$ at $Kn = 1$ for parallel wall motion.

Figure 5.30a-5.30b shows the v and u velocity components in the x and y directions along a horizontal and vertical line crossing the cavity center for different Mach numbers at $Kn = 1$. The non-dimensional u and v velocity profiles are symmetric, resemble a parabolic shape, and overlap very well for other Mach numbers. In both the plots, the velocity decreases first and then increases at the horizontal and vertical centerline of the cavity.

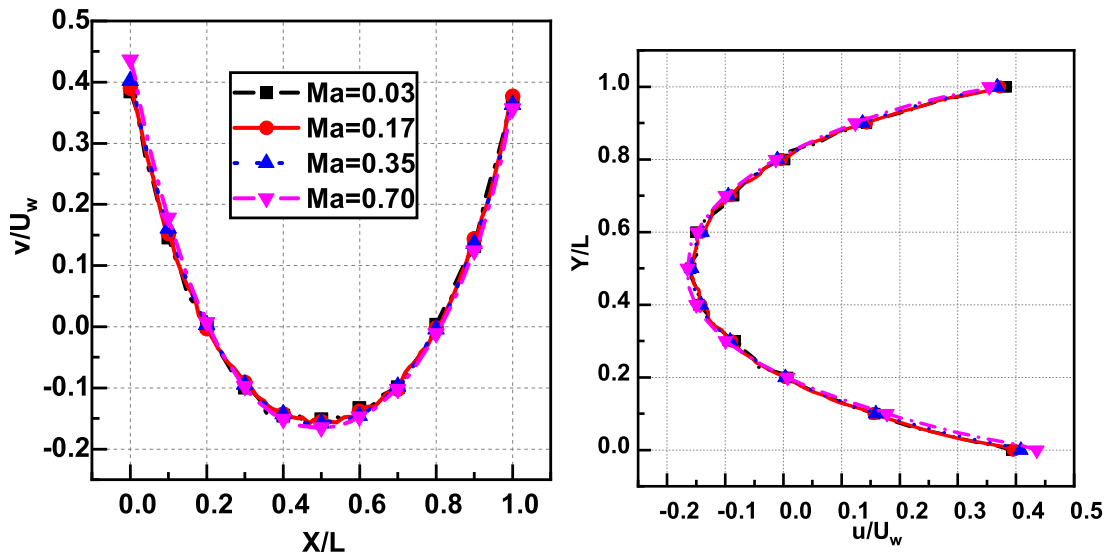
Figure 5.30c shows the profiles of the slip velocity ratio u_s/U_w along the walls of the cavity for different Mach numbers at $Kn = 1$. Due to flow stagnation at the corners,

the slip velocity ratio is high. The slip velocity ratio change is higher for parallel wall motion compared to the anti-parallel wall motion. For the parallel wall motion, only two walls are equivalent, as can be observed from the streamlines plot, where symmetry occurs along the diagonal of the cavity. In particular, the wall segments AB and BC are potentially non-equivalent because corner A is the region of low pressure, and corner C is the region of high pressure. In contrast, the wall segments AB and AD are equivalent as both are responsible for moving the fluid from the low-pressure corner, A. Like the anti-parallel case, the increase in slip velocity ratio with Ma is nominal, as essentially the flow is in the same rarefaction regime. For higher Mach numbers, due to higher inertial forces, a noticeable asymmetry is observed near the corners (i.e., $S/L = 1, 3$).

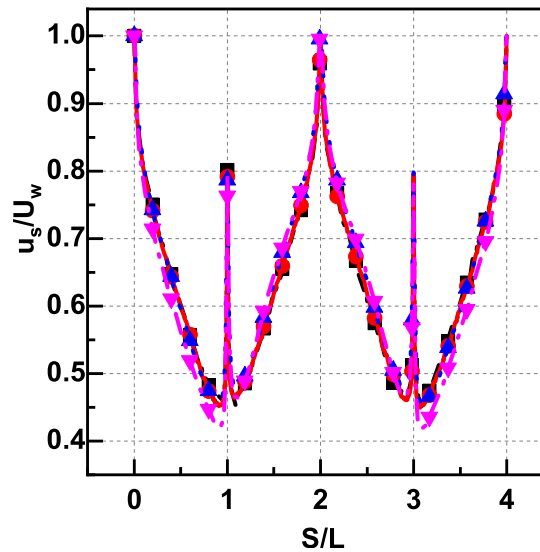
Pressure profiles:

The pressure contours for different Mach numbers at $Kn = 1$ are shown in Figure 5.31. From the contours, it can be observed that, unlike the anti-parallel wall motion, the high-pressure regions transpire only at the top right corner of the cavity, which can be attributed to compression. The low-pressure regions occur at the other corners due to flow expansion. Similar to the anti-parallel case, the peak pressure near the top right corner increases with increasing Mach numbers. Near the center of the cavity, the region of initial pressure arises. For all the cases, one half of the domain, symmetrical about the diagonal, has initial pressure, whereas considerable pressure changes are observed on the other half of the domain.

Comparison of pressure ratio along a horizontal line crossing the center of the cavity and along the walls of the cavity for different Mach numbers at $Kn = 1$ is shown in



(A) v -velocity profile plotted along a horizontal line (B) u -velocity profile plotted along a vertical line, crossing the cavity center.



(C) Slip velocity ratio plotted along the four walls of the driven cavity.

FIGURE 5.30: Comparison of non-dimensional velocity and slip at $Kn = 1$ for different Ma for parallel wall motion.

Figure 5.32. It can be observed that the pressure change increases with increasing Mach numbers. The pressure ratio along the cavity walls is shown in Figure 5.32b, where the peak pressure manifests at the top-right corner (i.e., $S/L = 2$).

Temperature profiles:

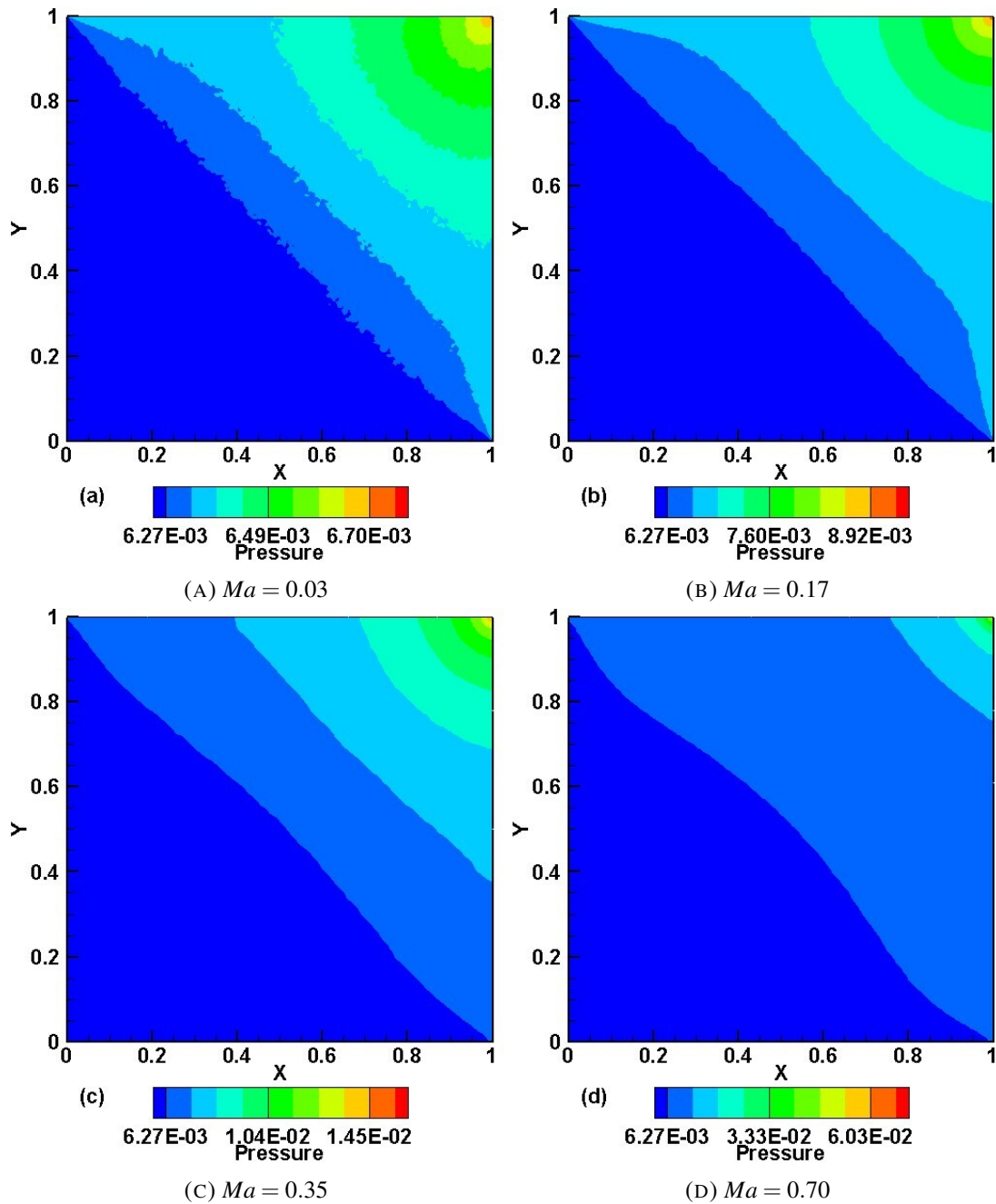


FIGURE 5.31: Pressure (Pa) contours at $Kn = 1$ for different Ma for parallel wall motion.

The temperature contours for different Mach numbers at $Kn = 1$ for parallel wall motion are shown in Figure 5.33. Similar to the pressure contours, the temperature contours follow a similar trend where the regions of high temperature, which are greater than the initial temperature, occur near the top right corners. The viscous dissipation effects

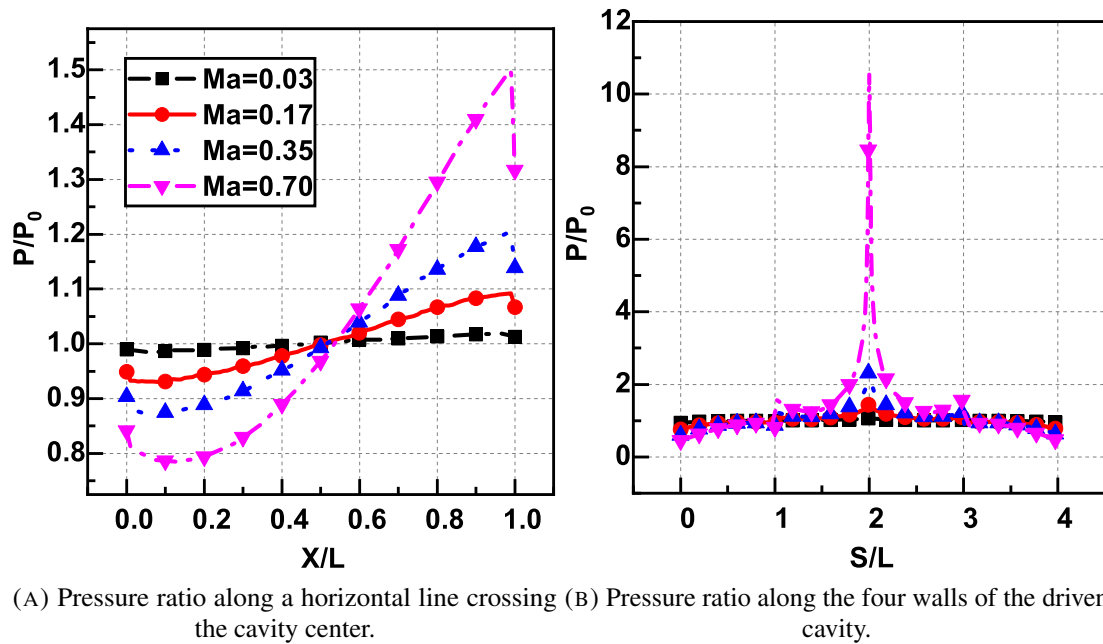


FIGURE 5.32: Comparison of non-dimensional pressure at $Kn = 1$ for different Ma for parallel wall motion.

(which increase the magnitude of the flow temperature) are proportional to the Mach number. For the case of $Ma = 0.03$ majority of the domain has a temperature equal to the initial temperature, and the temperature rise in the domain is minimal. For the other cases, the regions of high temperature grow in magnitude and size and occupy most of the domain.

Comparison of temperature ratio along a horizontal line crossing the center of the cavity for different Mach numbers at $Kn = 1$ is shown in Figure 5.34a. It can be observed that the magnitude of the temperature ratio increases with increasing Mach numbers like pressure profiles.

Figure 5.34b shows the temperature jump ratio (T_j/T_0) along the walls of the cavity for different Mach numbers at $Kn = 1$. It can be observed that similar to the anti-parallel case, for lower Ma the temperature jump is very minimal. Again as Ma increases, the

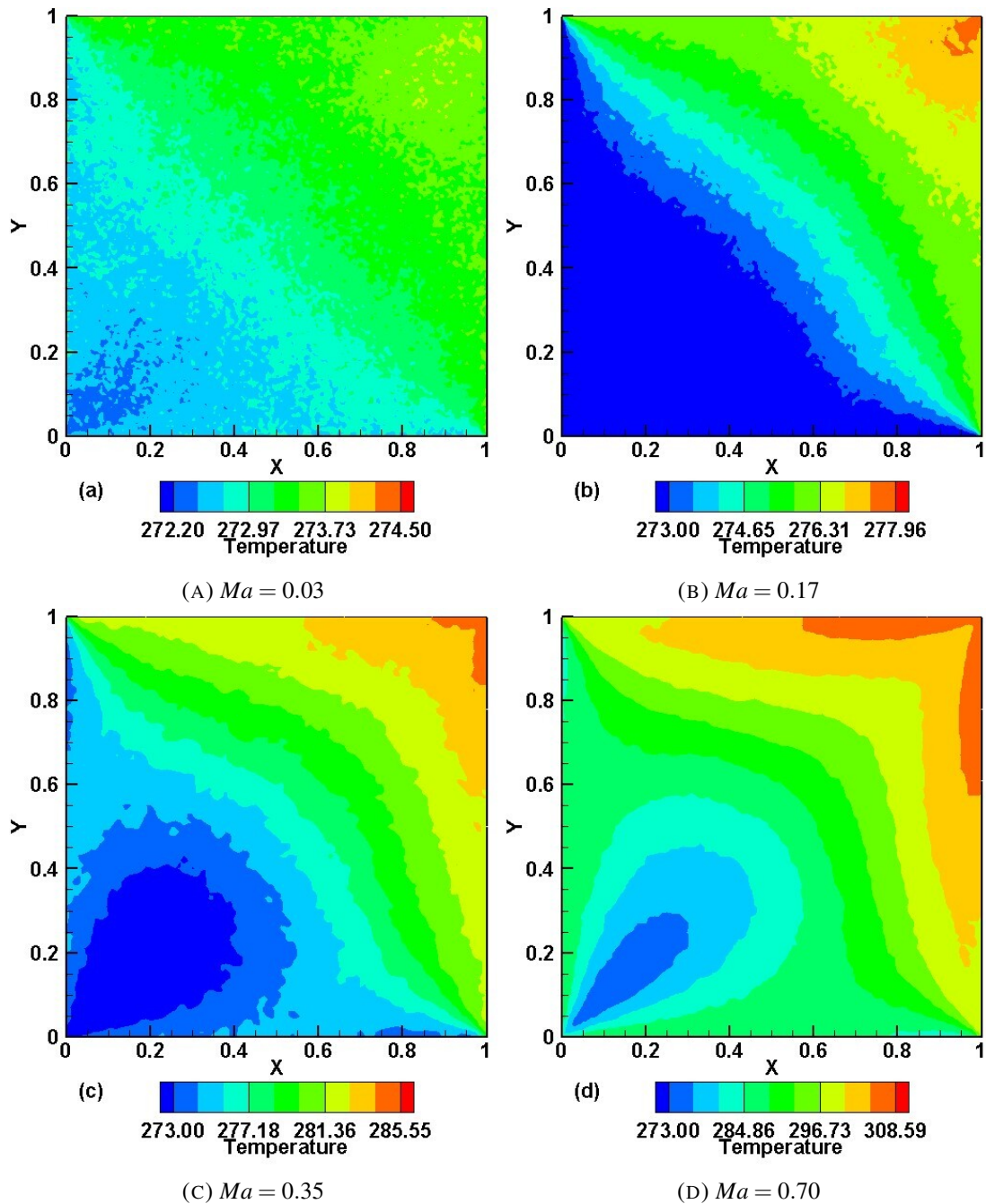
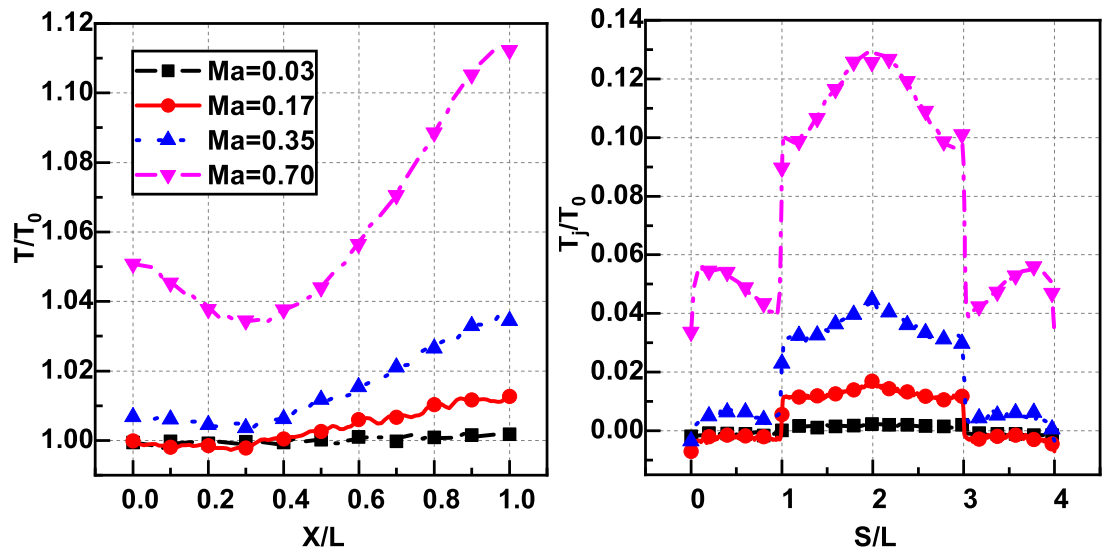


FIGURE 5.33: Temperature (K) contours at $Kn = 1$ for different Ma for parallel wall motion.

magnitude of the temperature jump increases owing to the increased contribution from the combined effects of fluid kinetic energy and higher viscous dissipation rates. The peak value of temperature jump ratio is observed at $S/L = 2$, as the flow from the walls BC and DC impinge, leading to a higher temperature and increased non-equilibrium

effects.



(A) Temperature ratio along a horizontal line cross- (B) Temperature ratio along the four walls of the
 ing the cavity center. driven cavity.

FIGURE 5.34: Comparison of non-dimensional temperature at $Kn = 1$ for different Ma for -parallel wall motion.

Cold to hot heat transfer:

Figure 5.35 shows the heat lines overlaid on temperature contours predicted by individual terms of eq. (5.5) and the summation of the individual terms, respectively, for $Ma=0.70$ at $Kn=1$. Figure 5.35a, 5.35b shows the contribution of the first and second terms of eq. 5.2 to the heat flux, respectively. The direction of the heat lines indicates that the heat transfer occurs from the hot region of the flow field (near the walls) to the cold region (at the center) of the cavity. This is the direction of heat transfer expected from the classical theory of heat transfer. In contrast, the direction of the heat lines given by the third term in eq. 5.5 is from the cold to hot region of the cavity, as shown in Figure 5.35c. The heat lines resulting from the contribution of all the three terms are shown in Figure 5.35d, where we see that their direction is from the cold to hot region of the cavity. This

indicates that the velocity curvature term of the eq. 5.5 is the most dominant one, similar to the case with anti-parallel wall motion.

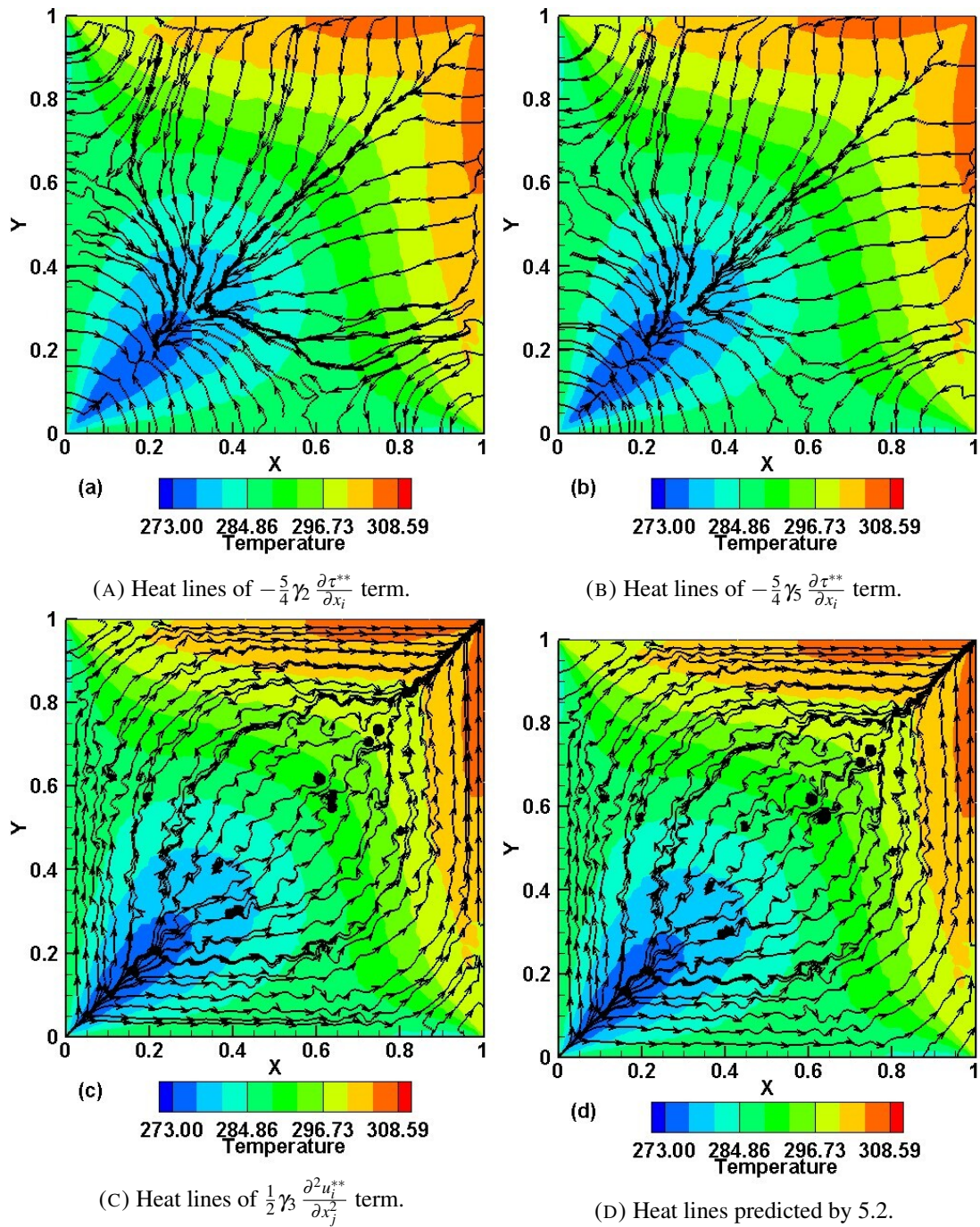


FIGURE 5.35: Contours of Heatlines at $Kn = 1$ for different $Ma = 0.70$ for parallel wall motion.

Heat flux profiles:

The heat flux profile along the cavity walls for different Mach numbers at $Kn=1$ is shown in Figure 5.36. In this plot, the heat flux is normalized by $q_0 = \frac{\mu RT_0}{L}$. The heat flux is found to increase with increasing Mach number, which is a manifestation of the increased temperature. The profiles follow a similar trend for all Ma with the peak occurring at $S/L=2$.

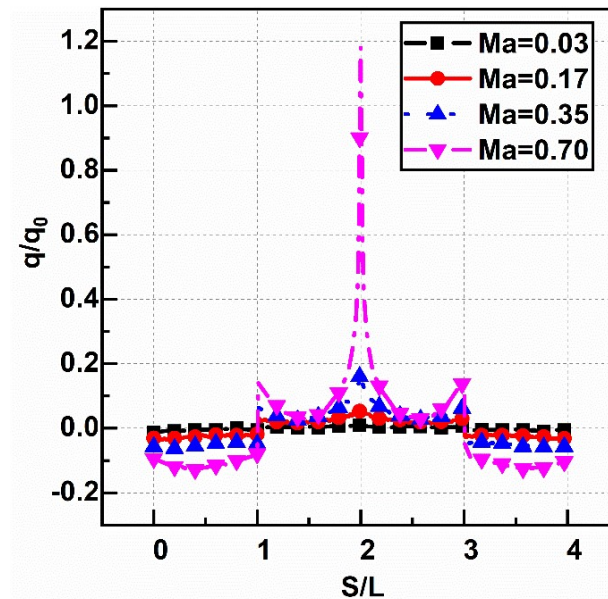


FIGURE 5.36: Variation of heat flux ratio plotted along the four walls of the driven cavity at $Kn = 1$ for different Ma for parallel wall motion.

5.3.2.2 Influence of Knudsen number

Velocity profiles:

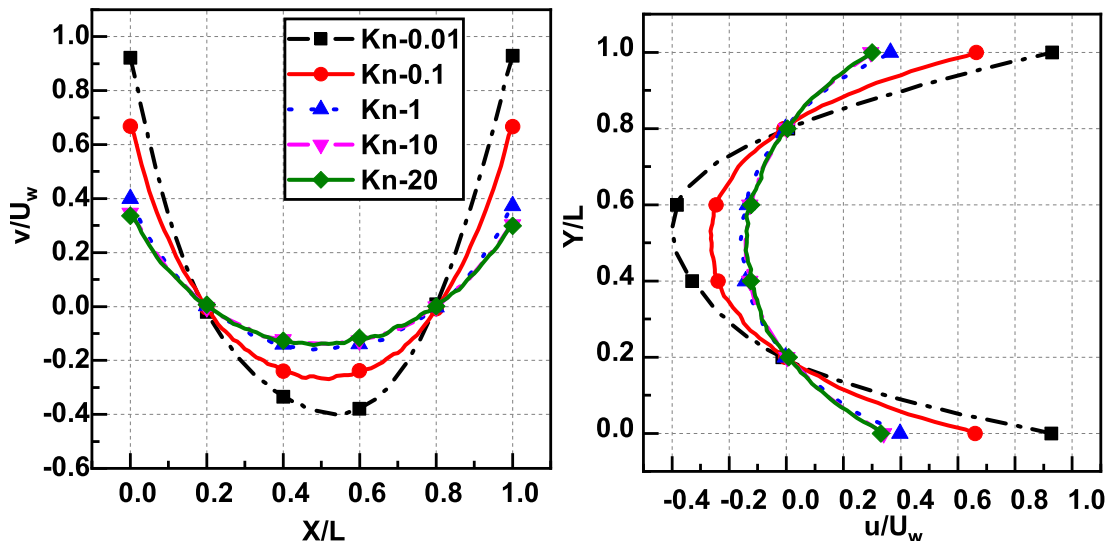
5.37a-5.37b shows the v and u velocity components in the x and y directions along a horizontal and vertical line crossing the cavity center at $Ma = 0.17$ for different Kn . From the profile, it can be observed that the profiles resemble a parabolic shape. The velocity variations decrease with increasing Kn . In both the profiles, the velocity decreases first

and then increases. The velocity profiles are found to be overlapping for $Kn = 10$ and $Kn = 20$.

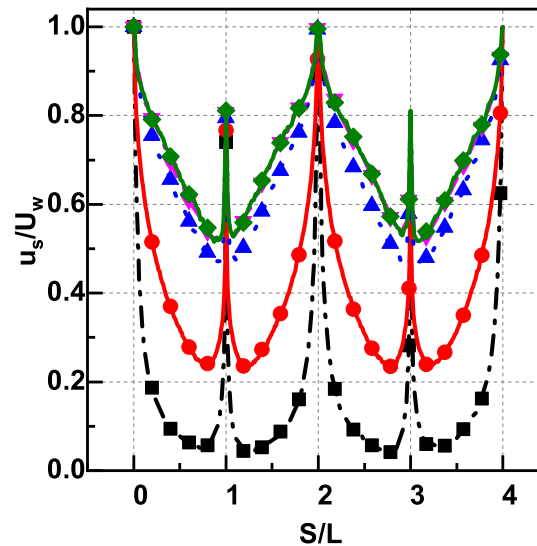
Figure 5.37c shows the slip velocity ratio (u_s/U_w) along the walls of the cavity at $Ma = 0.17$ for different Kn . It can be observed that at any given corner, the slip velocity ratio reduces first, reaches a minimum, and then increases. The minimum is reached near corners B and D of the cavity, where the flow originating from corner A first begins to change its direction. The minimum slip velocity ratio is also less than that of the anti-parallel wall motion case for a given Kn and Ma . This is possibly due to the fact that in the parallel wall motion case, the wall motion is such that they impart kinetic energy to the fluid resulting in only two vortices. This leads to lower energy loss and hence lower slip velocity ratio. Furthermore, as the rarefaction increases, the slip velocity ratio increases.

Pressure profiles:

The normalized pressure ratio plotted along a horizontal line crossing the center of the cavity and along the cavity walls at $Ma = 0.17$ for different Kn are shown in Figure 5.38a-5.38b. The pressure P in these plots is normalized by the initial pressure P_0 . The pressure ratio along the x and y directions is found to be symmetrical; hence, only one plot is shown. The pressure changes are relatively uniform in the slip regime compared to other regimes. From Figure 5.38 5.38b, the peak pressure ratio is highest for $Kn = 0.1$, which lies in the transition regime. The pressure variation is mainly dictated by the change in the number density in different regimes. The peak pressures occur at points $S/L = 2$, with considerable pressure drop occurring at points $S/L = 0, 1, 3,$ and 4 . The



(A) v -velocity profile plotted along a horizontal line (B) u -velocity profile plotted along a vertical line crossing the cavity center.



(C) Slip velocity ratio plotted along the four walls of the driven cavity.

FIGURE 5.37: Comparison of non-dimensional velocity and slip at $Ma = 0.17$ for different Kn for parallel wall motion.

peak pressure rise and peak pressure drop are highest for $Kn = 0.1$. For $Kn > 1$ the profiles tend to be overlapping.

Temperature profiles:

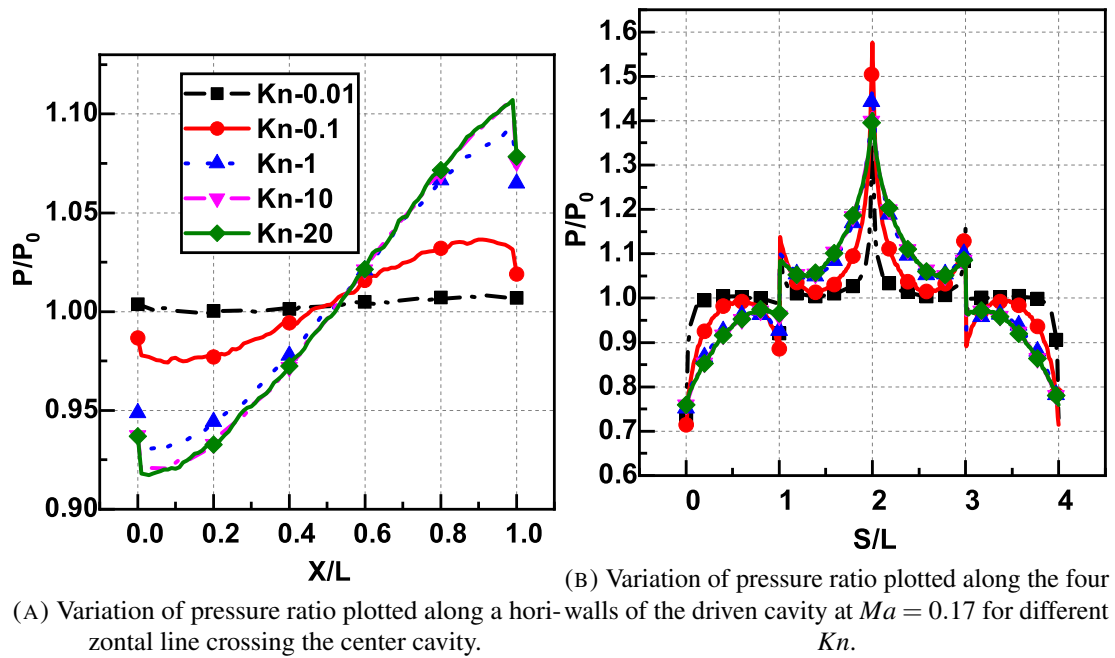


FIGURE 5.38: Comparison of non-dimensional pressure at $Ma = 0.17$ for different Kn for parallel wall motion.

The temperature jump ratio (T_j/T_0) along the walls of the cavity at $Ma = 0.17$ for different Kn is shown in Figure 5.39. In this plot, the temperature jump T_j is normalized by the initial temperature T_0 . The variation of temperature ratio along the horizontal and vertical lines passing through the cavity center is slightly less than that along the sidewalls and not shown here. It is observed that the magnitude of temperature jump ratio increases with Kn as expected. However, this increase is marginal as the Ma for these cases has a relatively small magnitude of 0.17. Also, as the flow progresses from the slip to the transition regime, the side-walls temperature changes are significant, leading to higher temperature jump. In the slip regime, the temperature variation from the initial temperature is less compared to other regimes, causing a lower temperature jump. Furthermore, the temperature jump ratio is highest for $Kn = 20$, which lies in the free molecular regime.

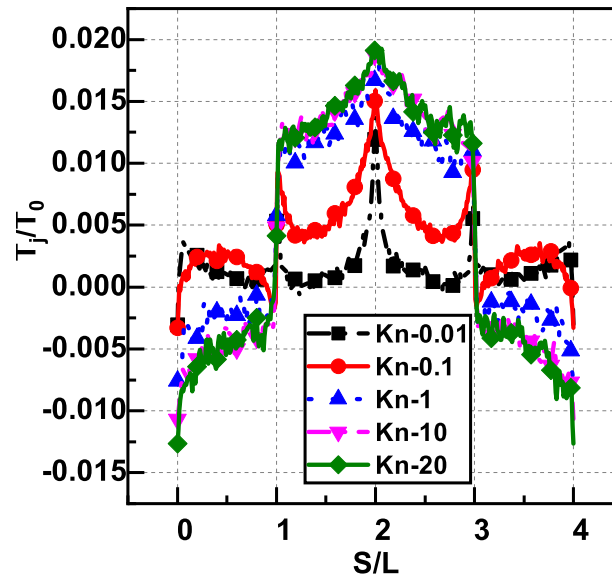


FIGURE 5.39: Variation of temperature ratio plotted along the four walls of the driven cavity at $Ma = 0.17$ for different Kn for parallel wall motion.

Heat flux profiles:

The heat flux profile along the cavity walls at $Ma = 0.17$ for different Kn is shown in Figure 5.40. The heat flux is normalized by q_0 as explained previously. Again, as found in the anti-parallel case, the heat flux variation is more significant for $Kn = 0.01$ with heat flux peaks and valleys occurring at $S/L = 1, 2,$ and 3 . The profiles overlap, and the heat flux decreases with Kn .

5.4 Comparison with NSF equations

In the slip regime, the NSF equations with velocity slip and temperature jump can predict the flow features equally well. Therefore, a comparative analysis is carried out for four-sided cavity for both the parallel and anti-parallel case of $U_w = 50\text{m/s}$ and $Kn = 0.01$ using both the NSF and DSMC methods. In the slip regime, the *rhoCentralFoam*

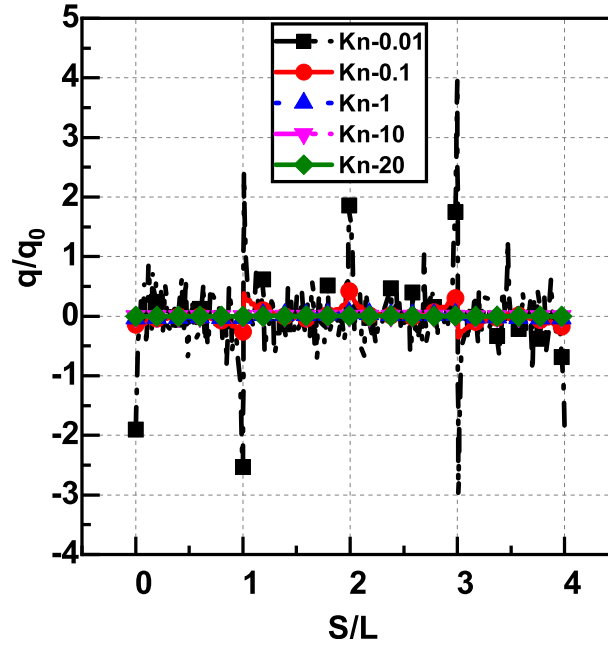


FIGURE 5.40: Variation of heat flux ratio plotted along the four walls of the driven cavity at $Ma = 0.17$ for different Kn for parallel wall motion.

solver with velocity slip and temperature jump boundary conditions is employed. The *rhoCentralFoam* solver is modeled on the central upwind schemes of Kurganov and Tadmor [144–146]. It solves the continuity, momentum, and energy equations given below.

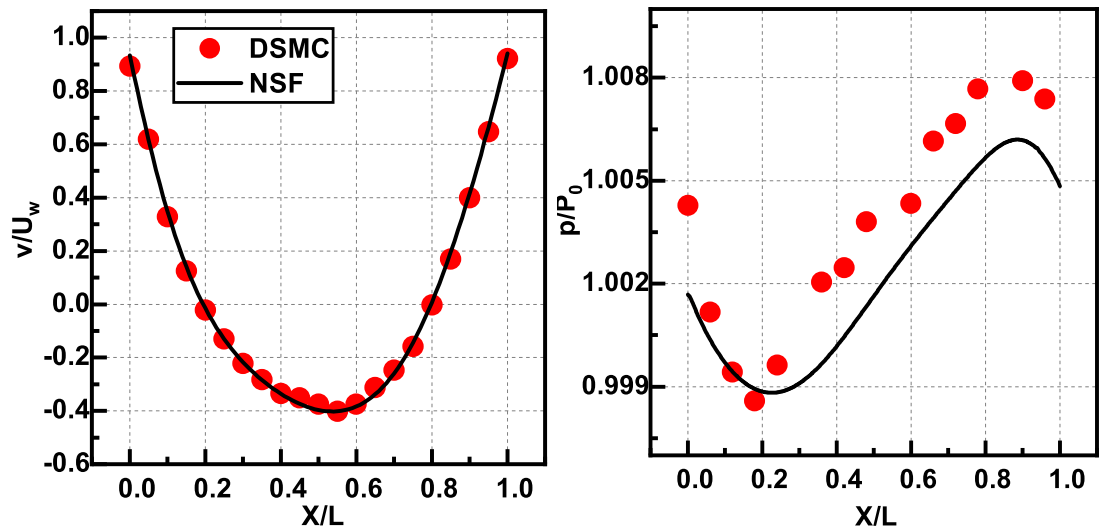
$$\frac{\partial \rho}{\partial t} + \nabla \cdot (\rho V) = 0 \quad (5.8)$$

$$\frac{\partial (\rho V)}{\partial t} + \nabla \cdot (V (\rho V)) + \nabla p + \nabla \cdot \tau = 0 \quad (5.9)$$

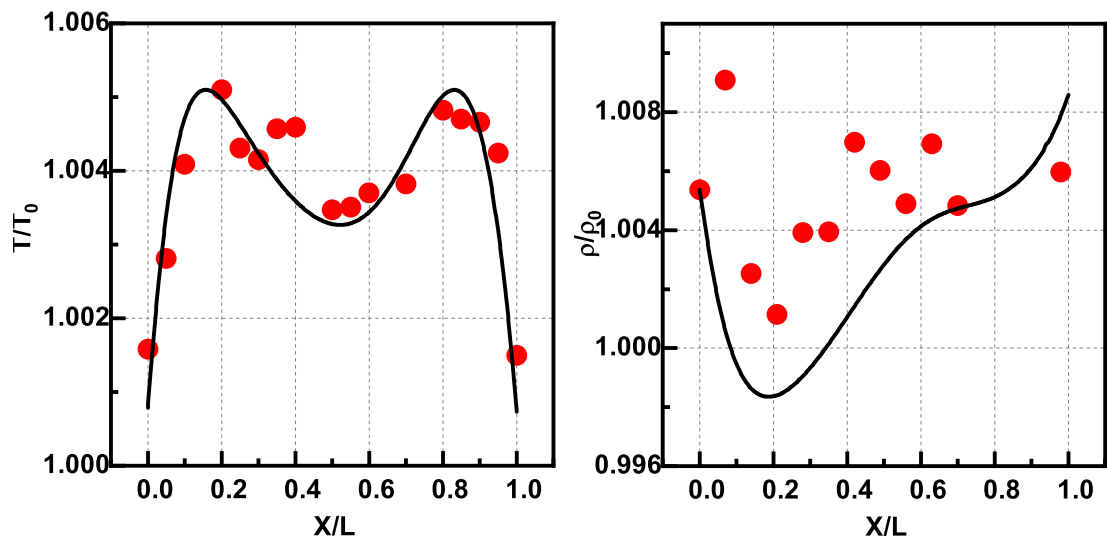
$$\frac{\partial (\rho E)}{\partial t} + \nabla \cdot (V (\rho E)) + \nabla \cdot (V p) + \nabla \cdot (V \cdot \tau) + \nabla \cdot q = 0 \quad (5.10)$$

where, ρ denotes the fluid density, p the pressure, q the conductive heat transfer, τ the shear stress tensor derived from the Stokes law and is related to the velocity field as $\tau = -2\mu \text{dev}(D)$, $D = 0.5[\nabla V + (\nabla V)^T]$ where μ is the dynamic viscosity, and 'dev' denotes the deviatoric of a tensor, $D - (1/3)\text{tr}(D)I$, where I is the unit tensor, and tr is the trace of a tensor. $E = e + \frac{|V|^2}{2}$ denotes the total energy, and e denotes the internal energy.

Figure 5.41 and Figure 5.42 show the non-dimensional values of v velocity component, pressure, temperature, and density along a horizontal centerline, respectively, for $U_w = 50\text{m/s}$ and $Kn = 0.01$ for both parallel and anti-parallel wall motion. From the profiles, it can be noticed that a good agreement is found among them for the velocity profiles, whereas for the other cases, a minimal discrepancy of ($< 0.5\%$) is observed. This discrepancy is possibly due to the microscopic nature, which affects the flow properties in DSMC. Thus, it can be concluded that NSF and DSMC method can both predict the flow features in the slip regime.

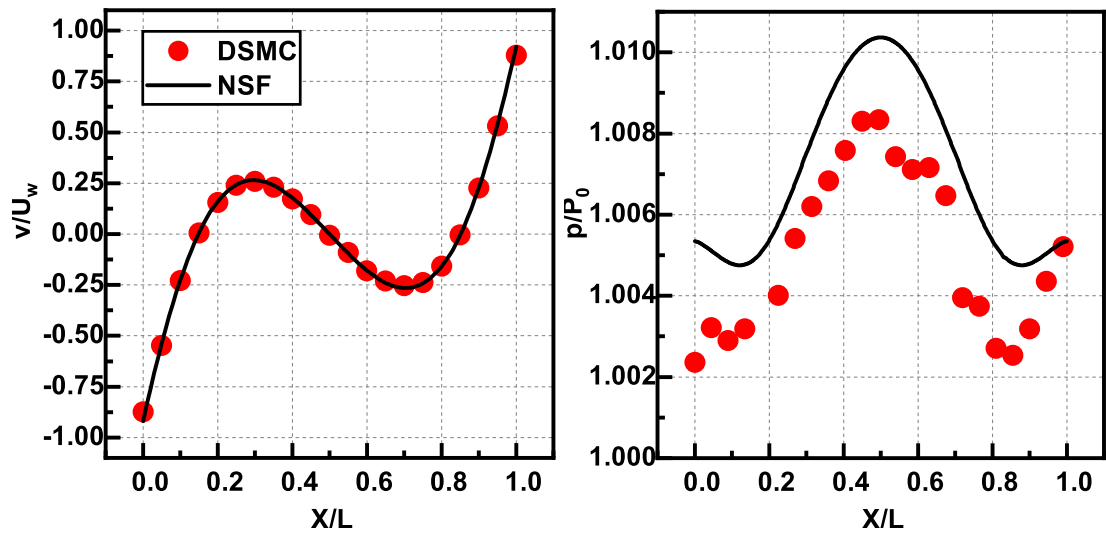


(A) Non dimensional v -velocity along horizontal centerline crossing the cavity center. (B) Non dimensional pressure along horizontal centerline crossing the cavity center.

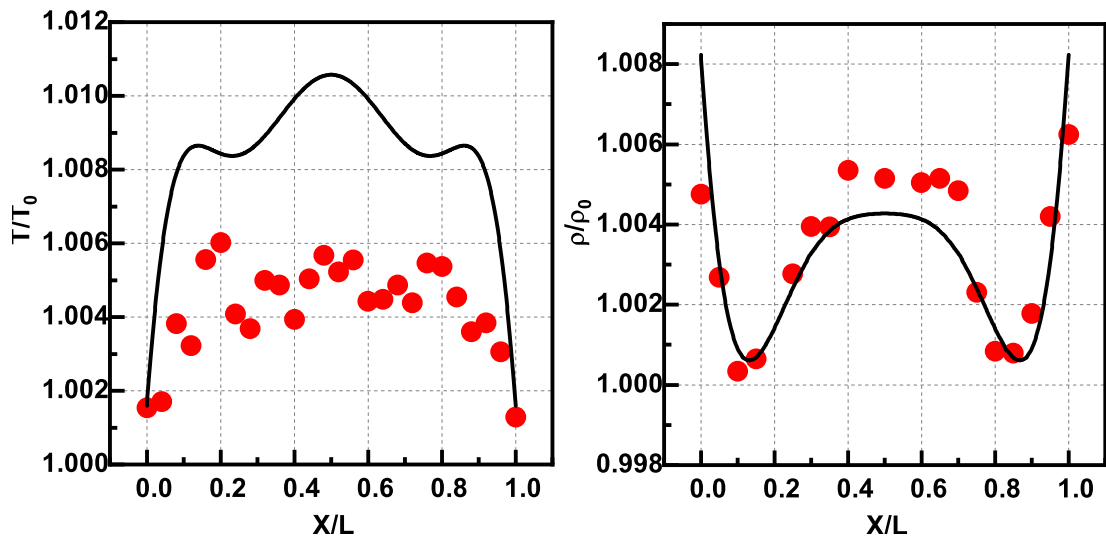


(C) Non dimensional temperature along horizontal centerline crossing the cavity center. (D) Non dimensional density along horizontal centerline crossing the cavity center.

FIGURE 5.41: Comparison of non-dimensional flow-field properties computed by the DSMC and NSF for parallel wall motion.



(A) Non dimensional v -velocity along horizontal centerline crossing the cavity center. (B) Non dimensional pressure along horizontal centerline crossing the cavity center.



(C) Non dimensional temperature along horizontal centerline crossing the cavity center. (D) Non dimensional density along horizontal centerline crossing the cavity center.

FIGURE 5.42: Comparison of non-dimensional flow-field properties computed by the DSMC and NSF for anti-parallel wall motion.

Chapter 6

Modeling and investigation of the rarefied flow physics of external flows

In this chapter, the rarefied flow physics of the external flows are thoroughly investigated. This chapter begins with an analysis of flow over BFS. Similarly, the rarefied flow behavior over FFS, cavity, and the wall-mounted cube is thoroughly investigated and presented. The effects of Mach number, wall temperature variation, and Knudsen number are explained in detail. Then a comparative analysis is carried out by incorporating specific chemical reactions, and these results are briefly presented.

6.1 Analysis of rarefied flow over backward facing step

This section describes the analysis of the rarefied flow past a BFS. The geometry, boundary conditions, and free-stream conditions are described initially, followed by the analysis of the results.

Geometry and computational domain:

The rarefied flow over a 2D BFS, as shown in Figure 6.1, is the geometry considered for analysis. The fluid moves from left to right. X and Y denote the Cartesian coordinates along the streamwise and transverse directions. The upstream length was kept at 0.045m initially, and later, a 0.015m of symmetry region was introduced. The downstream length considered was 0.105m, and the step was located at 0.06m from the inlet and is far enough from both the inlet and outlet. For all simulations, the step height (h) was set at 3 mm, whereas the channel height at the outlet was fixed at $H = 0.06\text{m}$ after conducting an influence study on the flow properties shown in the next section.

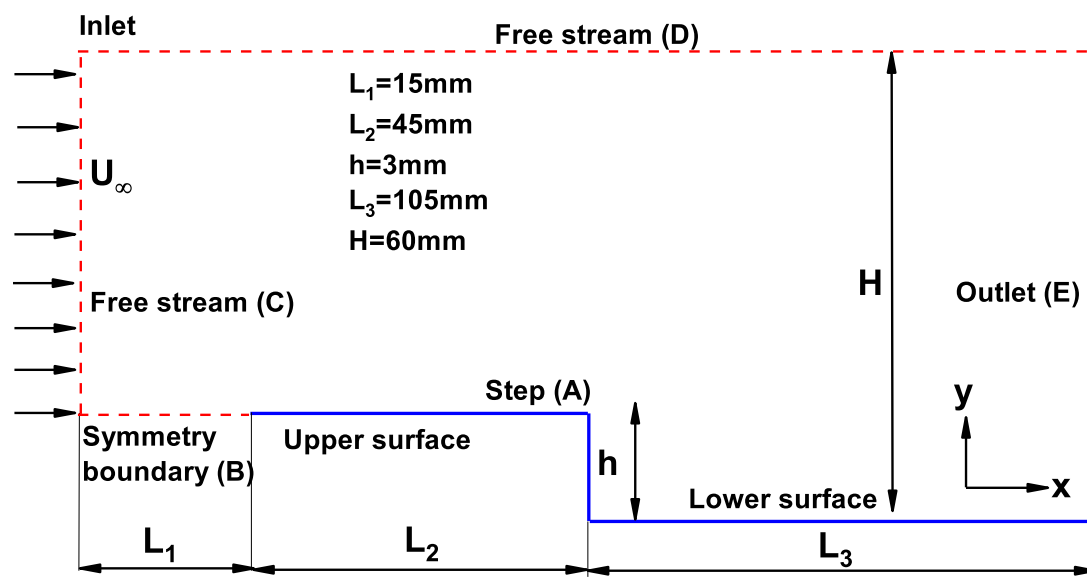


FIGURE 6.1: Schematic of the 2D BFS.

Boundary conditions and mesh:

The different surfaces are marked alphabetically, as shown in the computational domain in Figure 6.1. Surface-A represents the BFS, which is given a diffused reflection with

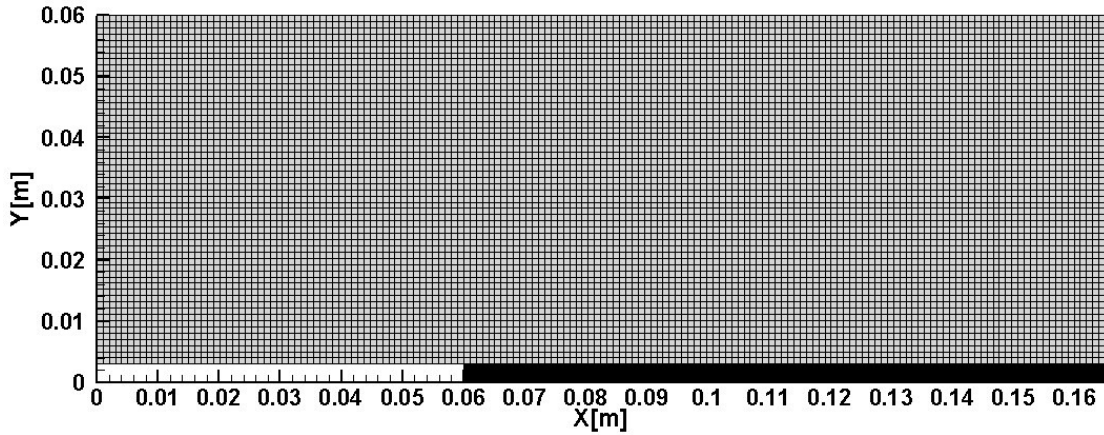


FIGURE 6.2: Meshed domain of the BFS.

full thermal accommodation condition. In a diffuse reflection model, the simulated molecules are equally reflected in all directions. The surface-B represents symmetry and is used to accomplish a precise velocity in the perpendicular directions [147]. This surface is analogous to a specular reflecting model. The surfaces-C, D, represent the free-stream inlet through which the simulated particles easily enter and leave the domain. The surface-E is given an outflow condition, which allows only the particles to leave the computational domain.

The computational domain is divided into several blocks and meshed in a structured manner, as shown in Figure 6.2. The cell widths in both X and Y directions were maintained below the mean free path, i.e., $\Delta x_{cell}, \Delta y_{cell} < 0.3\lambda_{\infty}$. The total number of cells for the case of $Kn = 1.06$ was about 11,250 cells. Also, the cell count varied for other cases depending on the corresponding mean free path.

Flow conditions:

Table 6.1 shows the gas properties employed in the present simulations. Such flow characteristics are experienced by a hypersonic vehicle during its re-entry and are taken

TABLE 6.1: Gas properties.

	χ	m, kg	d, m	ω	ζ
O_2	0.237	5.312×10^{-26}	4.07×10^{-10}	0.77	5
N_2	0.763	4.650×10^{-26}	4.17×10^{-10}	0.74	5

from the U.S. standard atmosphere charts [148]. In the initial studies, the fluid considered was non-reacting air, and the chemical reactions were relaxed. This assumption has been used in numerous published studies [80, 87, 91, 92]. Also, the fluid was assumed to have a molecular weight of about 28.96 g/mol with a major composition of 76% N_2 and 23% O_2 .

In Table 6.1, χ denotes the mole fraction, m denotes the molecular mass, d the molecular diameter ω represents the temperature dependent viscosity index and ζ represents the degrees of freedom.

Table 6.2 lists the flow and simulation parameters, which show the different atmospheric altitudes examined, ranging from 55km to 95km. All the simulations were performed for about 1.5 ms, which consisted of 75,000-time steps and employed about 2,76,500 simulated particles. The Knudsen number and Reynolds number were estimated by choosing the corresponding characteristic dimension based on the geometry (Step height h in this case).

TABLE 6.2: Flow and simulation parameters.

Altitude	55.02 km	60.5 km	77 km	91.5 km	95 km
Free stream velocity (U_∞) [m/s]	8050.75	7829.25	7134.5	6851.38	6887.03
Inlet gas temperature (T_∞) [K]	259.39	245.64	204.49	186.89	188.84
Wall temperature (T_w) [K]	1037.56	982.56	817.96	747.56	755.36
Free stream pressure (p_∞) [Pa]	39.86	20.51	1.72	0.14	0.069
Free stream density (ρ_∞) [kg/m^3]	5.35×10^{-4}	2.90×10^{-4}	2.94×10^{-5}	2.61×10^{-6}	1.27×10^{-6}
Mean free path (λ_∞) [m]	1.51×10^{-4}	3×10^{-4}	3.19×10^{-3}	3.1×10^{-2}	6.33×10^{-2}
Number density (n_∞) [m^{-3}]	1.11×10^{22}	5.62×10^{21}	5.29×10^{20}	5.45×10^{19}	2.66×10^{19}
Reynolds number (Re)	783.11	431.10	46.61	4.29	2.08
Knudsen number (Kn)	0.05	0.10	1.06	10.33	21.10

Influence of top free surface:

The surface (D) position and the type of boundary condition applied to it have a decisive role such that the surface has no potential influence on the flow physics. Therefore, to select a suitable height, simulations were carried out for $Ma = 25$, $Kn = 21.10$ considering five different channel heights ranging from $H = 12\text{mm}$ to $H = 60\text{mm}$. As the change in Knudsen number significantly influences the flow-field properties, the case of $Kn = 21.10$ was considered. Figure 6.3 illustrates the variation of non-dimensional flow-field properties for different channel heights at $X = 120\text{mm}$. The graphs demonstrate that for $H = 12\text{mm}$, the flow physics is significantly affected due to the reduced area available for the flow to transpire. However, for $H \geq 30\text{mm}$, the profile relatively overlaps for different flow-field properties, signifying that the flow physics is unaffected by the surface placement.

6.1.1 Influence of Mach number

To present the results, we begin with the Mach number's effect on the flow properties and surface properties. To evaluate the effects of Mach number (Ma) on the flow and surface properties over the BFS four different Mach numbers in various Mach regimes, i.e., $Ma = 5$ (Supersonic), 10 (Hypersonic), 25 (High-Hypersonic) and 30 (Reentry speeds) were considered. These amount to free stream velocities of 1430, 2860, 7149, and 8578 m/s, respectively, and Reynolds numbers of 8.61, 17.22, 43.05, and 51.65. For all instances in this section, $H = 30\text{mm}$, $Kn = 1.06$ and $T_w = 4T_\infty$ is used. Henceforth, the variation of sampled results with Y are presented at the locations $X = 44\text{ mm}$, 46 mm , and 100 mm respectively.

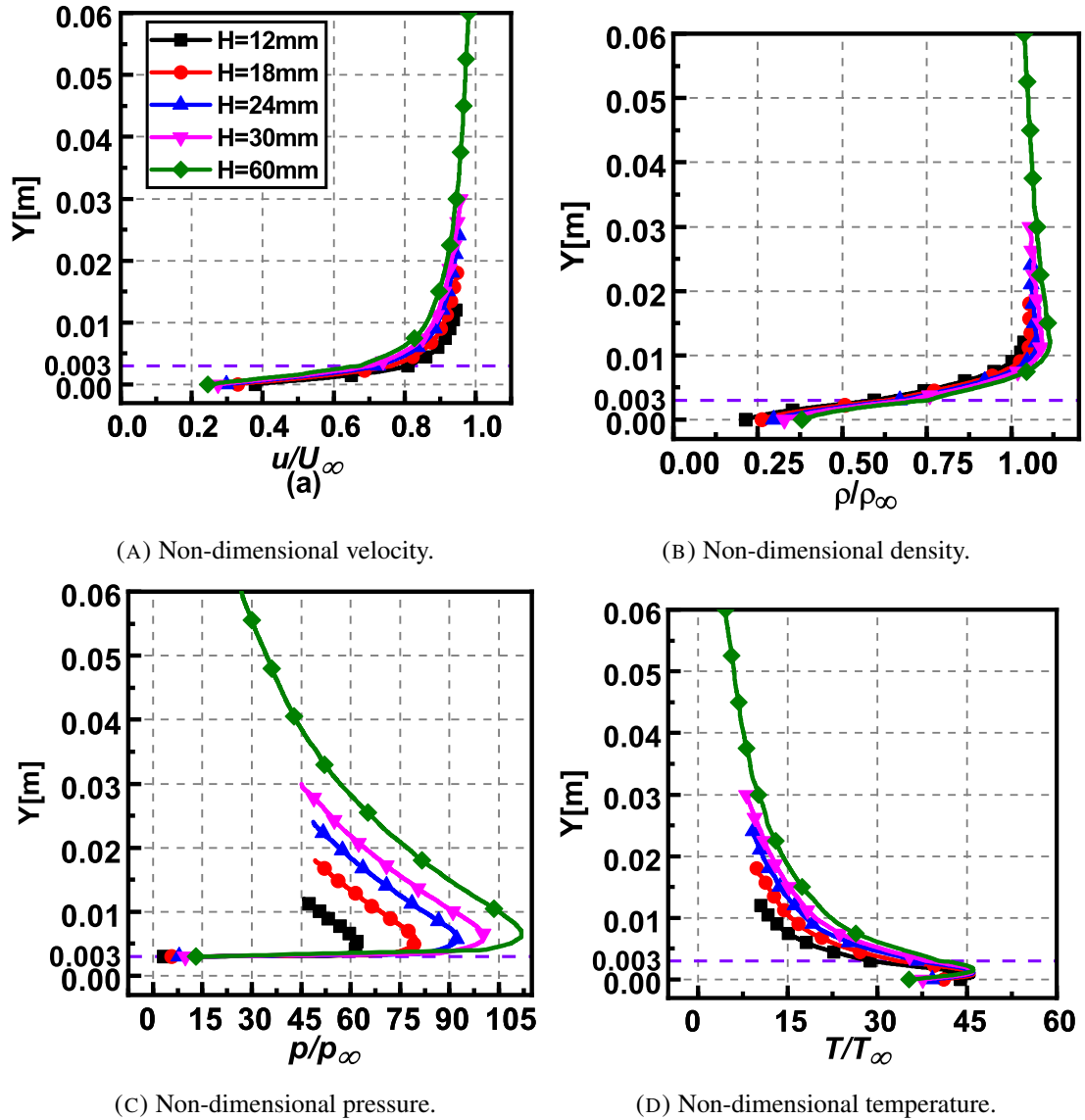


FIGURE 6.3: Influence of the top surface of BFS for various various flow-field properties at $X = 120\text{mm}$.

Velocity field:

Figure 6.4 shows the plots of velocity ratio (u/U_∞) for different Ma at sections $X = 44\text{ mm}$, $X = 46\text{ mm}$, and $X = 100\text{ mm}$ along the length of the BFS. In the plots, the streamwise velocity u is normalized by the free-stream velocity U_∞ . Y represents the axial distance in the y -direction above the surface of the BFS. In section $X = 44\text{ mm}$, that is just before the step; the flow is undisturbed by the presence of the step. Figure 6.4a also qualitatively

TABLE 6.3: Recirculation lengths of BFS for different Ma .

Ma	05	10	25	30
$X_L(\text{mm})$	1.60	1.61	1.47	1.60
$Y_L(\text{mm})$	1.83	1.90	1.88	1.88

shows that the boundary layer thickness (δ) decreases with increasing Mach number. The velocity profiles show adverse velocities just after the step, characterizing the area of recirculation; a similar behavior was observed in the continuum regime investigation by Grotowsky and Ballmann [79].

Interestingly, in section $X = 46$ mm (at the edge of the recirculation region), the profiles for different Ma overlap up to the step height and soon diverge after that. At $X = 100$ mm, similar to those at the inlet, the profiles remain relatively unaffected. Table 6.3 shows the recirculation lengths for different cases, in which X_L and Y_L denote the axial extent of the recirculation region in x and y -directions respectively measured from the step corner (i.e., from $X = 45$ mm). For estimating the recirculation lengths, skin friction coefficient ($C_f = 0$) is the condition used [149–152]. It can be observed that X_L and Y_L remain fairly constant.

Slip velocity:

Figure 6.5 shows the plot of the slip velocity ratio (u_s/U_∞) along the upper and the lower surfaces of the BFS for different Ma . In the plots, the slip velocity u_s is normalized by the free-stream velocity U_∞ . X represents the axial distance in x -direction along the surface of the BFS. The slip velocity is defined as the difference in velocity between the wall and the gas adjacent to the wall. The slip velocity can be extracted either by direct sampling of the microscopic particles that impact the wall surface or by extracting

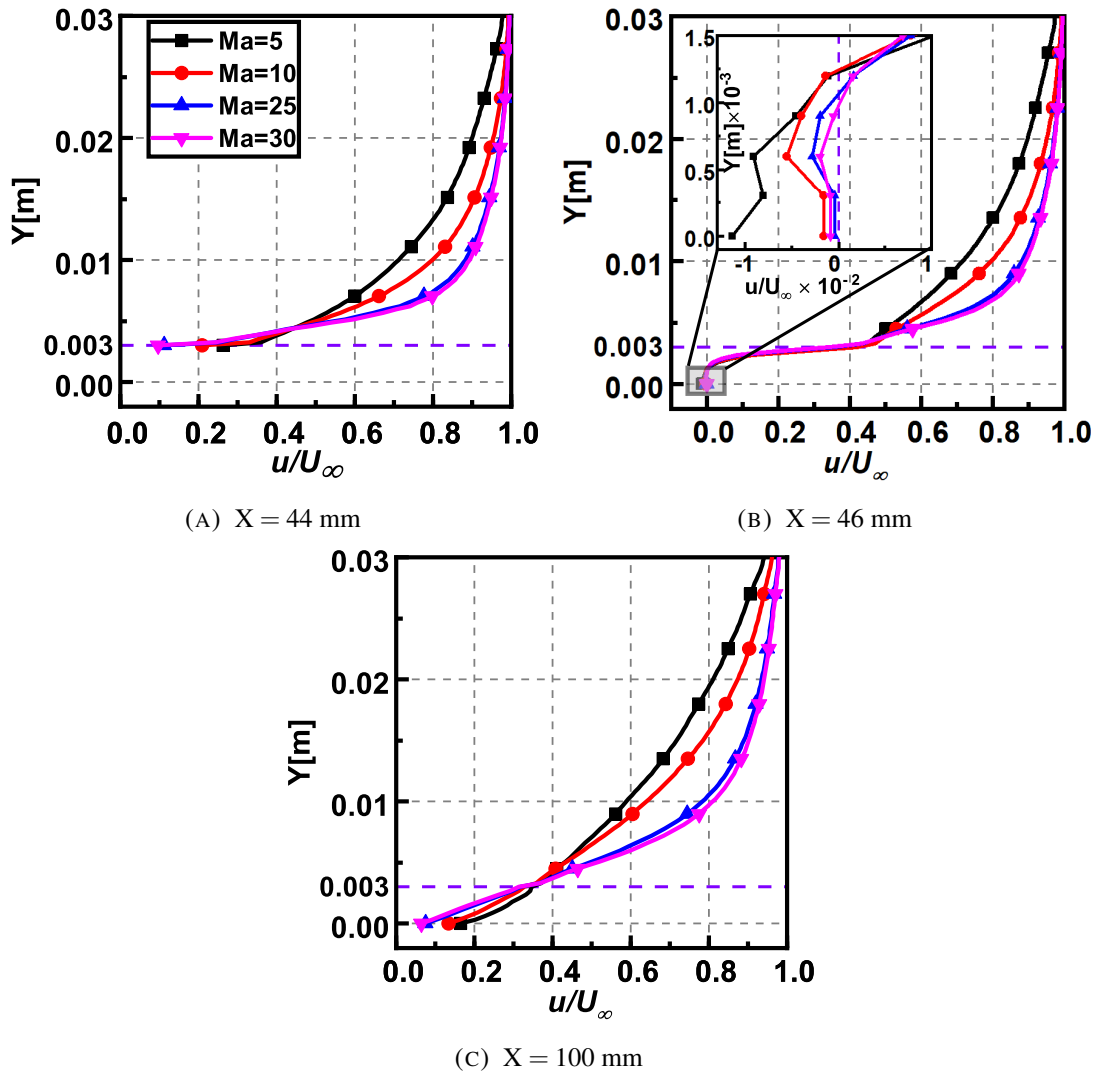


FIGURE 6.4: Variation of the non-dimensional velocity perpendicular to the surface of BFS for different Ma .

the macroscopic flow characteristics in the cell adjacent to the wall [140], which is the method used in the present study to extract the slip velocity. The slip velocity ratio decreases along the flow direction. This decrease can be attributed to the reduction of the velocity gradient transverse to the flow direction upstream of the step.

From the plot, for lower Ma , the slip velocity ratio at a given location is more compared to the other cases. The slip velocity magnitude increases with Ma . Furthermore, behind the step, the molecules are momentarily slowed down due to the presence of two wall

surfaces, which leads to an increase in the number of collisions, contributing to the slip.

The slip velocity ratio at the step for $Ma=5$ is about 2.57 times higher than $Ma=30$.

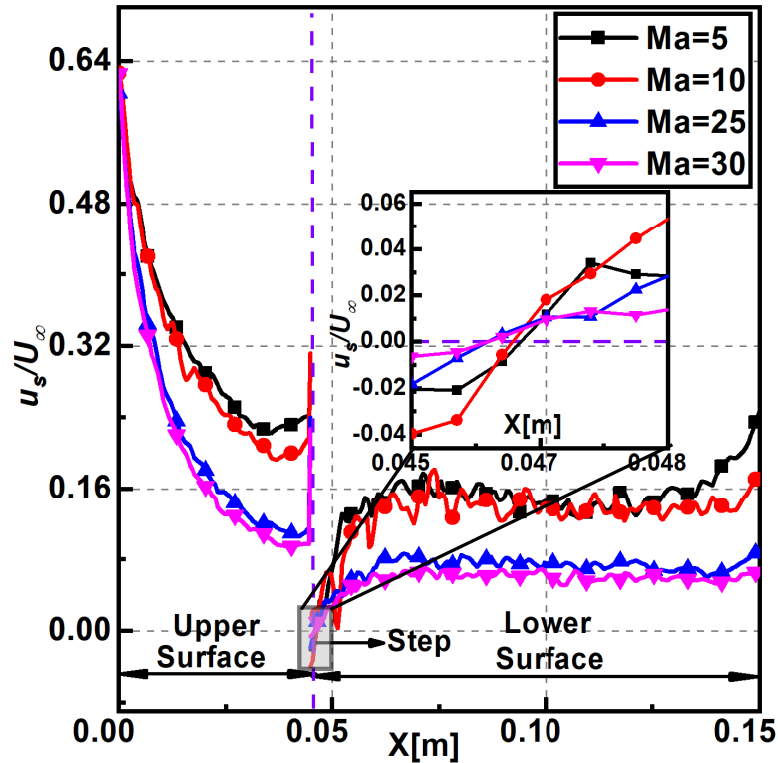


FIGURE 6.5: Slip velocity ratio along the upper and lower surfaces of BFS for different Ma .

Pressure field:

Figure 6.6 shows the pressure ratio (p/p_∞) profiles for different Ma at sections $X = 44$ mm, $X = 46$ mm, and $X = 100$ mm along the length of the BFS. In this group of plots, the pressure ratio refers to the pressure p normalized by the free stream pressure p_∞ . The pressure ratios near the step are of an order of magnitude higher than the free-stream values found far away from the step. Below the shear layer located at the step height, the flow expands, and hence the pressure ratios drop rapidly into the recirculation region. As the flow occurs over the step, the pressure ratios drop (from $X = 44$ mm to 46 mm)

due to an increase in cross-section area. Downstream of the step, the pressure ratios decrease only marginally along the flow direction. In the entire domain, the pressure is observed to be directly proportional to Ma . This is because the presence of the wall leads to stagnation of the flow, which increases with Ma . At the section $X = 46$ mm, in the wake region of the step, the near-wall pressure is relatively close to the free stream value for all Ma , depicting that the pressure is independent of the change in Ma . For comparison, in section $X = 46$ mm, the maximum pressure ratios are 3.29, 7.12, 41.49, and 59.90 for Mach numbers 5, 10, 25, and 30, respectively.

Temperature field:

Figure 6.7 shows the overall temperature ratio (T_{ov}/T_∞) profiles for different Ma at sections $X = 44$ mm, $X = 46$ mm, and $X = 100$ mm along the length of the BFS. In this group of plots, the temperature ratio refers to the overall temperature T_{ov} normalized by the free stream temperature T_∞ .

The variation of temperature ratio for transverse location is also similar to that of the pressure ratio. At the step height, in the shear layer, the temperature ratio attains exceptionally high values due to viscous dissipation, and it increases with Ma .

The variation of temperature ratio along the flow direction is similar to that of the pressure ratio with minor changes. As the flow occurs over the step, the temperature ratio is virtually unaffected despite the increase in cross-section area, unlike the pressure ratio. Also, as the flow continues beyond the step, the temperature ratio increases marginally, unlike the pressure ratio.

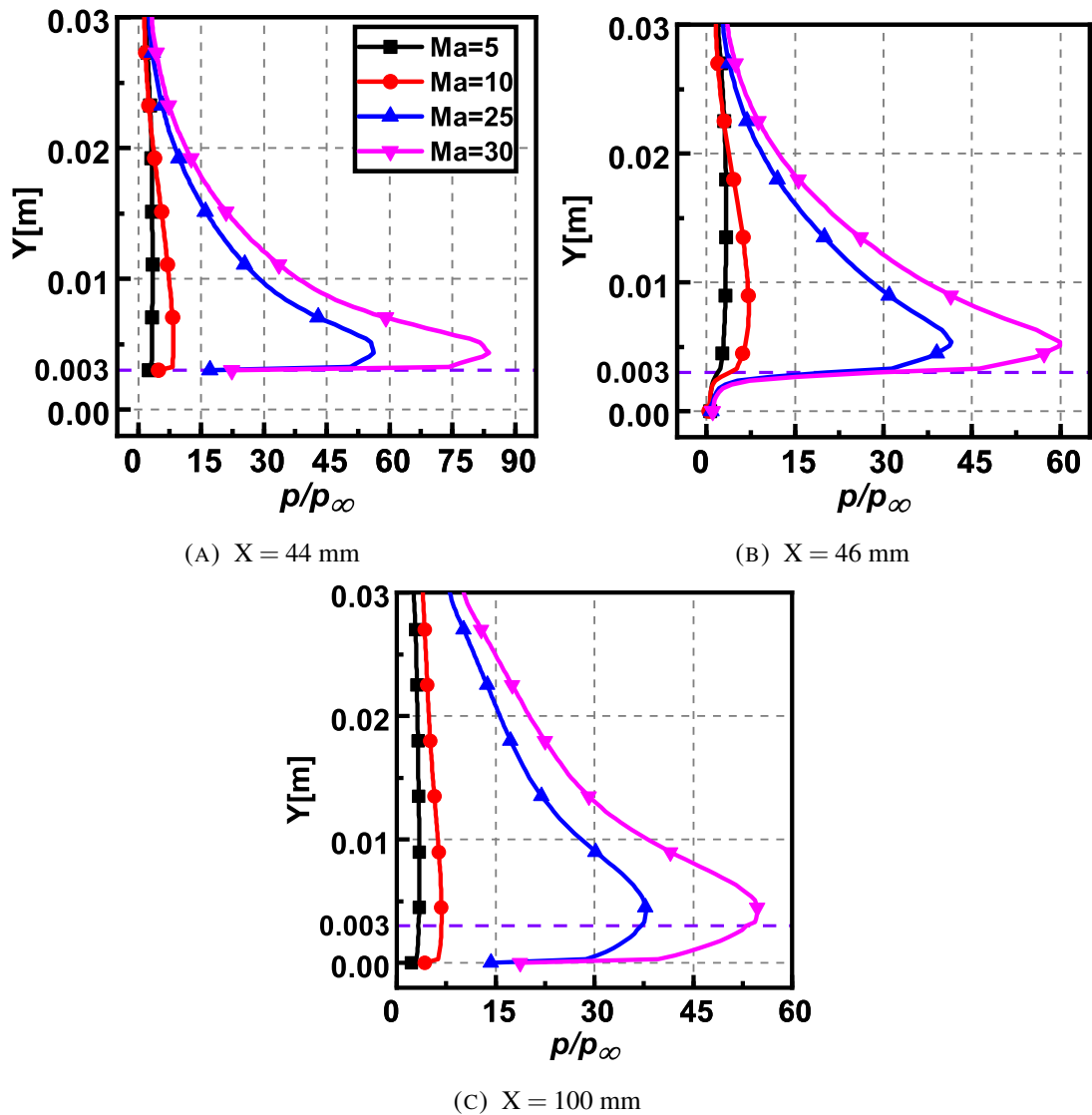


FIGURE 6.6: Variation of the non-dimensional pressure perpendicular to the surface of BFS for different Ma .

Temperature ratio increases with Ma , similar to pressure ratio in the entire domain. In section $X = 46$ mm, the maximum temperature ratios are 4.22, 8.03, 37.56, and 53.44 for Mach numbers 5, 10, 25, and 30, respectively. Overall, the temperature ratios have similar trends at all the sections except that near the wall, at $X = 46$ mm, they are close to the imposed wall temperature ratios. This similarity is because the flow is relatively stagnant in the wake region of the step, due to which it acquires temperatures close to that of the wall.

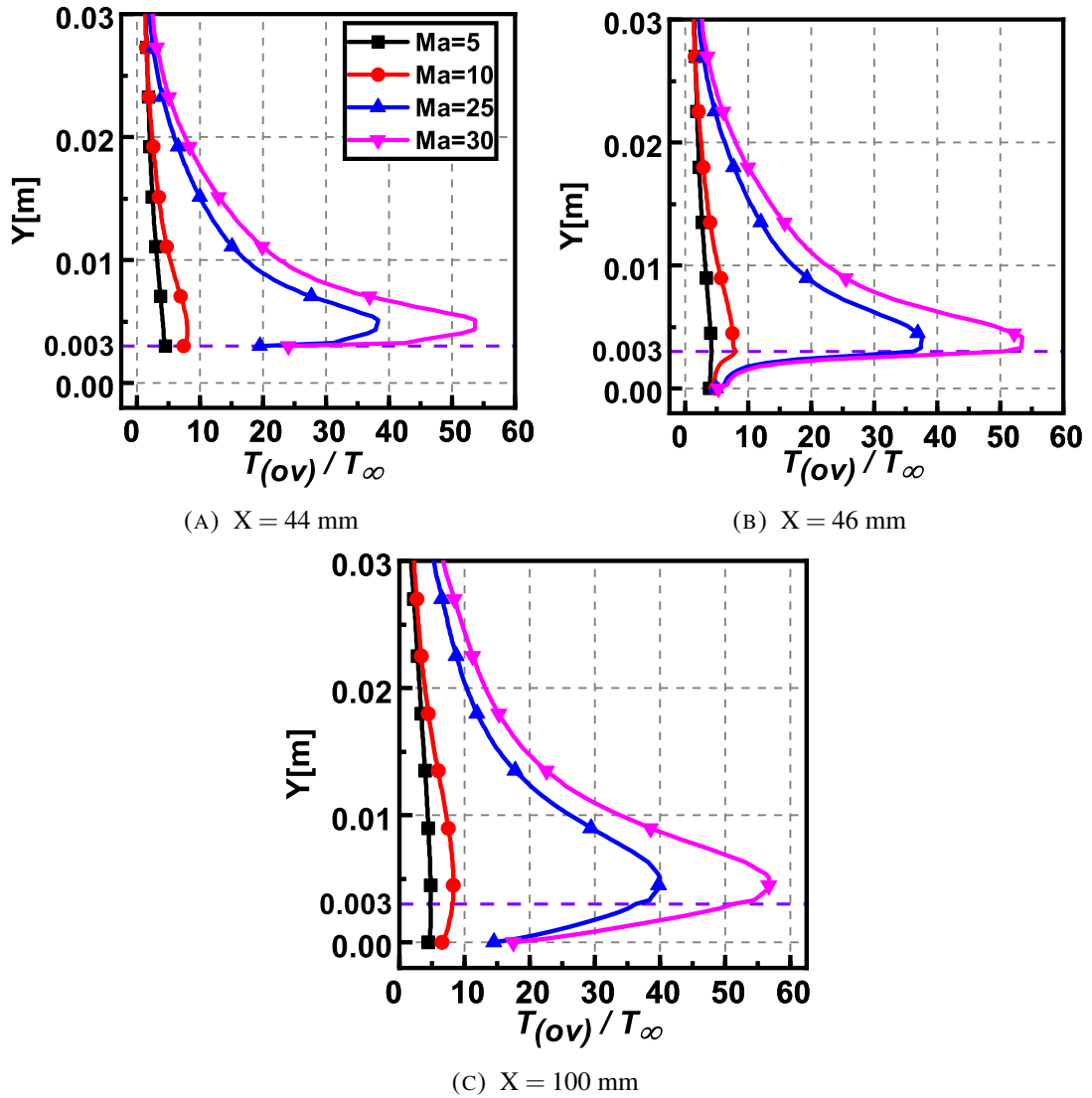


FIGURE 6.7: Variation of the non-dimensional temperature perpendicular to the surface of BFS for different Ma .

Figure 6.8 shows the rotational (T_R), overall (T_{OV}), and translational temperature (T_T) ratio profiles at $X = 46 \text{ mm}$ for $Ma=5, 10, 25$ and 30 perpendicular to the surface of the BFS. The present simulation does not include vibrational temperature, which is expected to be much smaller [80, 90, 153]. In the plots, each of the temperatures is normalized by the free stream temperature T_∞ . For a polyatomic gas, when the temperatures corresponding to the rotational, overall, and translational modes are dissimilar, it indicates thermal non-equilibrium, as observed in the present study. Moreover, the ideal gas

equation is not applicable in thermal non-equilibrium. For all Ma , at all X locations, the translational temperature dominates, and the rotational temperature is relatively much smaller. This trend is mainly seen in the shear layer, where the differences are more substantial, compared to the freestream, where the flow is least disturbed by surfaces and is closer to thermodynamic equilibrium. The peak temperature ratio for $Ma = 5$ approaches the value at the wall, unlike $Ma \geq 10$. This suggests that the near-wall shear rate developed for $Ma = 5$ due to viscous dissipation is not yet sufficient for the temperature rise to dominate.

At $X = 46$ mm (recirculation region), at the wall, all three temperatures are of the same magnitude demonstrating thermodynamic equilibrium. This similarity in temperatures can be attributed to lower wall shear rates. At locations $X = 44$ mm and 100 mm, a considerable difference in the temperature ratios at the wall is observed mainly for higher Ma . The other X locations' profiles are very similar to those shown in Figure 6.8, including the magnitude of the corresponding peak temperature ratios and hence not shown here.

Temperature jump:

Figure 6.9 shows the plot of the temperature jump ratio (T_j/T_∞) along the upper and the lower surfaces of the BFS for different Ma . In the plot, the temperature jump T_j is normalized by the free-stream temperature T_∞ . Temperature jump is obtained by extracting the macroscopic flow characteristics in the cell adjacent to the wall[154].

For $Ma= 5$, the temperature jump ratio is relatively constant along the wall surface. With an increase in Ma , the kinetic energy of the incoming fluid increases resulting in high

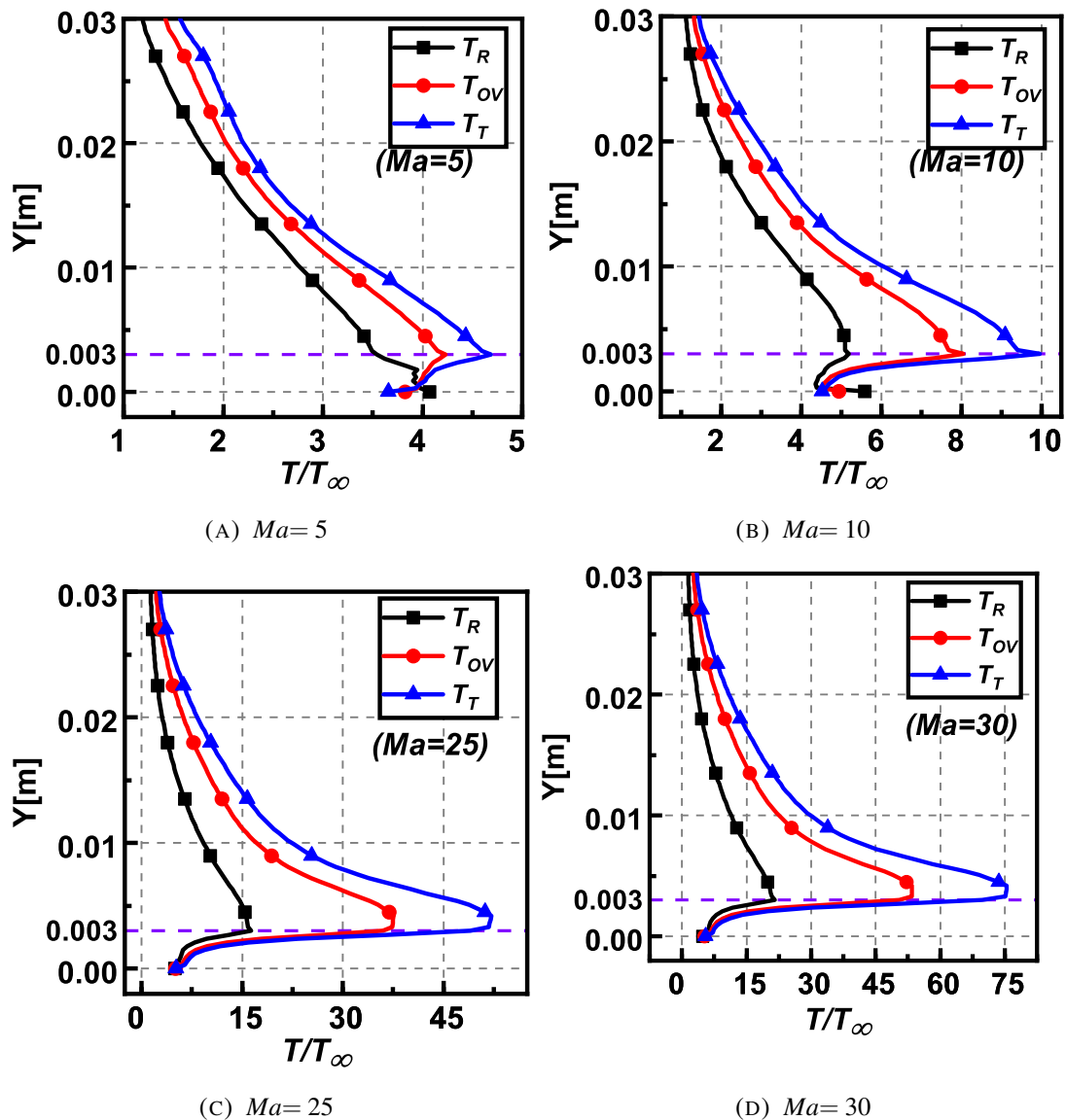


FIGURE 6.8: Variation of the non-dimensional rotational, overall, and translational temperature perpendicular to the surface of BFS at $X = 46$ mm for different Ma .

local temperatures due to increased viscous dissipation. This leads to a high-temperature gradient in the direction normal to the wall, increasing the temperature jump.

We see that normal to the wall, the velocity gradients and the temperature gradients are higher towards the inlet along the upper surface. This trend results in a higher temperature jump at the inlet, which decreases towards the step. In the wake region of the step, the magnitude of velocity is relatively small and constant until the outlet.

Therefore, normal to the wall, the velocity gradients and hence the temperature gradients are small, leading to smaller and more uniform temperature jump.

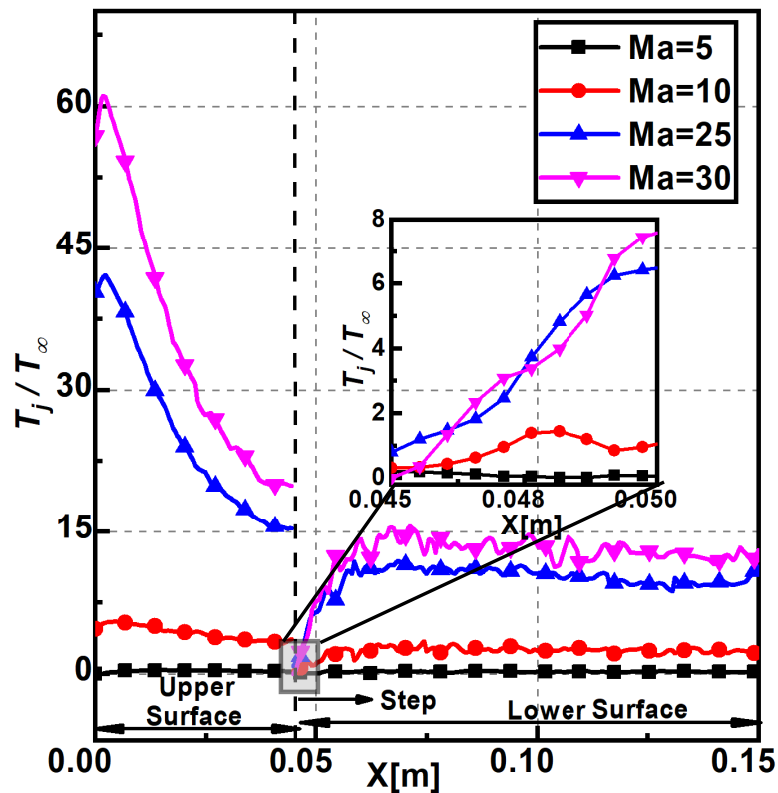


FIGURE 6.9: Temperature jump ratio along the upper and lower surfaces of BFS for different Ma .

Density field:

Figure 6.10 shows the density ratio (ρ/ρ_∞) profiles for different Ma at sections $X = 44$ mm, $X = 46$ mm, and $X = 100$ mm along the length of the BFS. In this group of plots, the density ratio refers to the density ρ normalized by the free stream density ρ_∞ .

In all the plots, there is considerable relative variation in density ratio along Y . These relative variations reach a maximum value of 1.5 in the entire domain and much smaller than those in velocity, pressure, and temperature. At sections $X = 44$ mm, 100 mm, the near-wall density ratios show significant variation from the freestream value and decrease

for a short distance away from the wall. Contrastingly at section $X = 46$ mm, the density ratio gradually increases up to the step height. In the vicinity of the wake region, the pressure, temperature, and density ratios increase from the lower surface towards the shear layer. This is unlike equilibrium flows and a result of the complex interplay of compressibility and non-equilibrium effects. Above the shear layer located at the step height, the density ratio increases first due to the shockwave's presence and then attains a value close to the freestream value near the top surface of the BFS.

The presence of the step causes density variation in the upstream. At section $X = 44$ mm, it is maximum for $Ma = 30$ near the wall and tends to 1 far away from the wall. At section $X = 46$ mm, which is just after the step, the near-wall densities for different Ma have similar magnitudes and are significantly low due to the recirculation region. Furthermore, these density ratios are fairly similar up to the step height and deviate after that, demonstrating that the density is relatively unaffected by the change in Ma . For comparison, at section $X = 46$ mm, the density ratios at the step height ($Y = 0.003$) are 0.41, 0.39, 0.40, and 0.40 for Mach number 5, 10, 25 and 30, respectively. At all three sections, the distance of peak density ratio from the wall increases as Ma decreases.

Pressure coefficient:

Figure 6.11 shows the distribution of the pressure coefficient C_p along the upper and the lower surfaces of the BFS for different Ma . The pressure coefficient C_p is defined as,

$$C_p = \frac{(p_w - p_\infty)}{\frac{1}{2} \rho_\infty U_\infty^2} \quad (6.1)$$

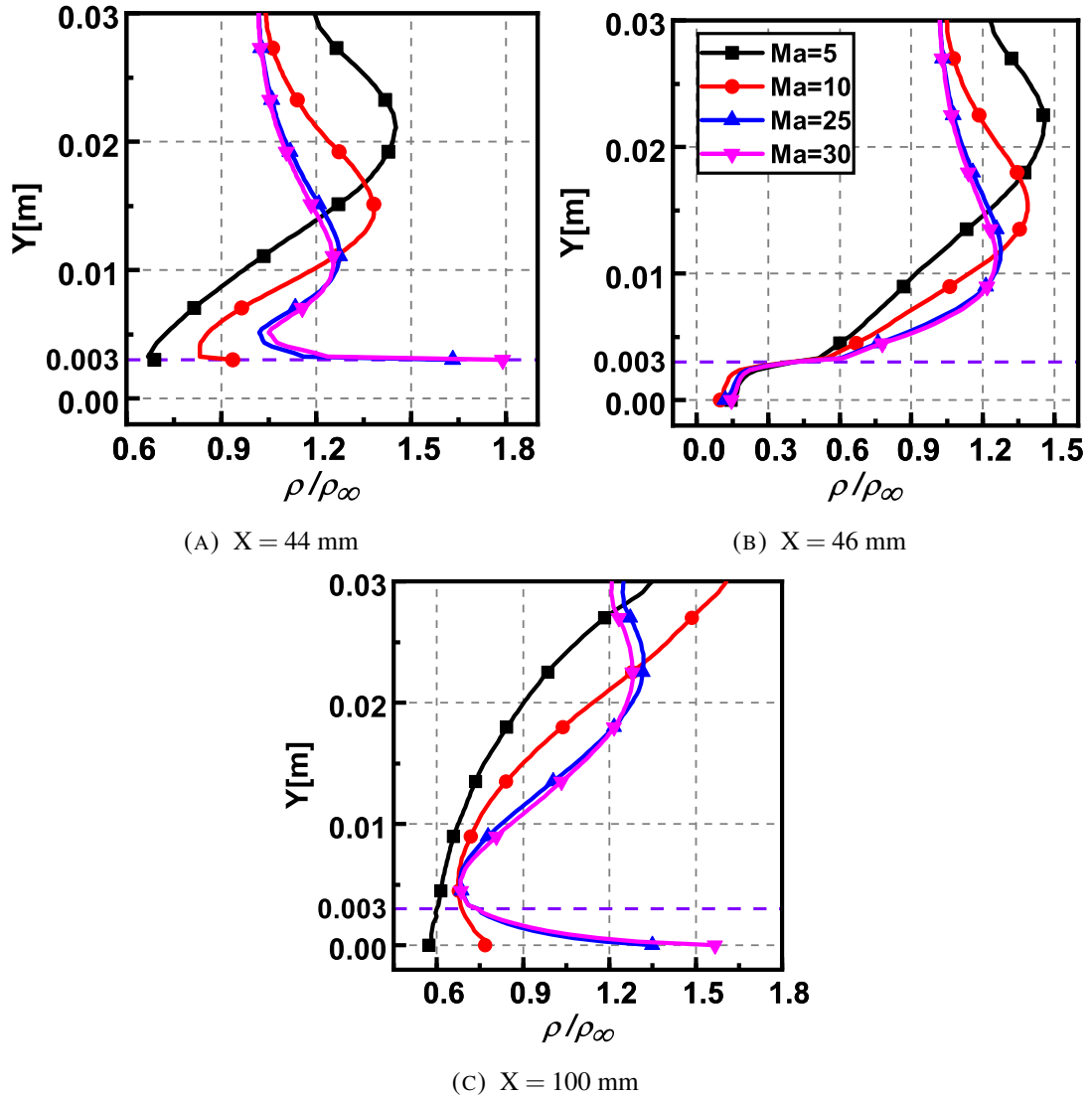


FIGURE 6.10: Variation of the non-dimensional density perpendicular to the surface of BFS for different Ma .

where, p_w is the wall pressure and p_∞ , ρ_∞ , and U_∞ are the free-stream pressure, density, and velocity, respectively. The wall pressure is obtained by calculating the sum of the normal momentum fluxes of the incident and reflected molecules at every time step and is given by,

$$p_w = p_i - p_r = \frac{F_N}{A \Delta t} \sum_{j=1}^N [(mv)_j]_i - [(mv)_j]_r \quad (6.2)$$

where, F_N denotes the number of real molecules represented by each simulated molecule, A is the surface area, Δt is the time step, N is the number of particles colliding with surface per unit time per unit area, m denotes the mass of the particles, v is the normal component of the velocity of particle j . Subscripts i and r represent the incident and reflected molecules, respectively.

The plot shows that the profiles follow a similar trend for all Ma . Along the upper surface, the pressure coefficient C_p increases from the leading edge and sharply decreases near the step due to the flow expansion. A small region close to the vicinity of the step affects the pressure coefficient C_p thereby causing its reduction. The pressure coefficient C_p reduces with an increase in Ma owing to the higher values of dynamic pressure caused by the incoming fluid stream. Near the base of the step the C_p values are negative, which indicates the wall pressure is lesser than the free-stream pressure. Downstream of the step on the lower surface, the pressure coefficient C_p shows a similar trend where it gradually increases as the flow progresses, reducing towards the outlet. It can be observed that at the outlet the C_p values are positive, indicating that the wall pressure is of higher magnitude than the free-stream pressure. It is observed that as Ma increases the pressure coefficient C_p reduces, owing to the increase in the inertial term $\frac{1}{2}\rho_\infty U_\infty^2$. As U_∞ increases, Ma increases which cause the reduction in pressure coefficient C_p .

Skin friction coefficient:

Figure 6.12 shows the distribution of the skin friction coefficient C_f along the upper and the lower surfaces of the BFS for different Ma . The skin friction coefficient C_f is defined as,

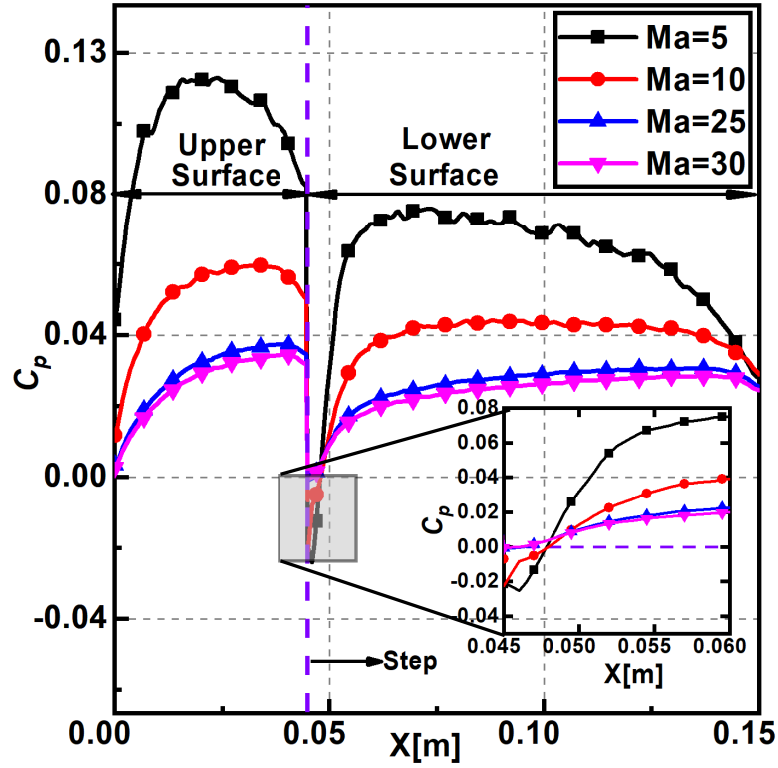


FIGURE 6.11: Variation of pressure coefficient C_p along the upper and lower surfaces of BFS for different Ma .

$$C_f = \frac{(\tau_w - \tau_\infty)}{\frac{1}{2} \rho_\infty U_\infty^2} \quad (6.3)$$

where, τ_w is the wall shear stress and ρ_∞ , U_∞ are the free-stream density and velocity, respectively. The wall shear stress τ_w is obtained by calculating the sum of the tangential momentum fluxes of the incident and reflected molecules at every time step and is given by,

$$\tau_w = \tau_i - \tau_r = \frac{F_N}{A \Delta t} \sum_{j=1}^N [(mu)_j]_i - [(mu)_j]_r \quad (6.4)$$

where u is the tangential component of the velocity of particle j .

For the diffuse reflection gas-surface interaction model used in the present study, the reflected molecules have zero tangential momentum as the particles, on average, lose their tangential velocity component. Hence the equation 6.4 is written as,

$$\tau_w = \tau_i = \frac{F_N}{A \Delta t} \sum_{j=1}^N [(mu)_j]_i \quad (6.5)$$

Similar to the pressure coefficient C_p , the profiles for the skin friction coefficient C_f follow a similar trend for all Ma . From the plot, at the inlet, due to high near-wall velocity gradients, the skin friction coefficient C_f values are higher in magnitude. From the leading edge, the skin friction coefficient C_f values gradually reduce towards the step. The skin friction coefficient C_f values are negative near the wake region of the step due to flow recirculation. On the lower surface C_f initially increases and remains reasonably constant towards the outlet. It is observed that as Ma increases the C_f reduces. According to the relation, $Kn = \sqrt{\frac{\pi\gamma}{2}} \frac{Ma}{Re}$, Ma is proportional to Re for a given Kn . As Re (and Ma) increases, it causes the dominance of inertial forces against viscous forces, hence a decrease in the skin friction coefficient. The variation of skin friction coefficient C_f with Ma along the flow direction is similar to that of the slip velocity ratio.

Heat transfer coefficient:

Figure 6.13 shows the distribution of the heat transfer coefficient C_h along the upper and the lower surfaces of the BFS for different Ma . The heat transfer coefficient C_h is defined as,

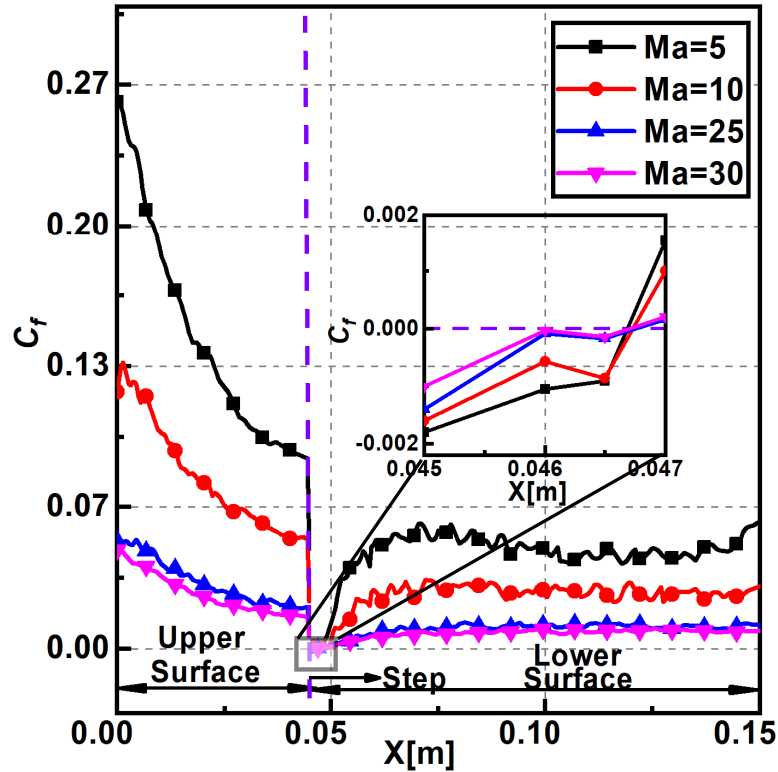


FIGURE 6.12: Variation of skin friction coefficient C_f along the upper and lower surfaces of BFS for different Ma .

$$C_h = \frac{q_w}{\frac{1}{2}\rho_\infty U_\infty^3} \quad (6.6)$$

where, q_w is the wall heat flux and ρ_∞ , U_∞ are the free-stream density and velocity, respectively. The wall heat flux q_w is obtained by calculating the net energy flux of impinging molecules on the surface, with the flux being positive toward the surface. The net flux is the sum of the translational, rotational, and vibrational energies of both incident and reflected molecules and is given by,

$$q_w = q_i - q_r = \frac{F_N}{A \Delta t} \left\{ \sum_{j=1}^N \left[\frac{1}{2} m_j c_j^2 + e_{R_j} + e_{V_j} \right]_i - \sum_{j=1}^N \left[\frac{1}{2} m_j c_j^2 + e_{R_j} + e_{V_j} \right]_r \right\} \quad (6.7)$$

where, c is the molecular velocity, e_R and e_V denote the rotational and vibrational energies, respectively, and other terms are defined earlier.

From the plot, along the upper surface, there is dissimilarity in profiles for different Ma . The heat transfer coefficient C_h values are higher for $Ma=10$, whereas they are lower for $Ma=5$. This discrepancy is probably due to the different boundary layer thickness at the separation [155]. The profiles for $Ma=25$ and $Ma=30$ are similar. Near the base of the step, heat transfer coefficient C_h reaches a minimum as the temperatures suddenly drop due to flow expansion. Along the lower surface the C_h values are again higher for $Ma=10$, and the profiles almost overlap for the other cases. The higher wall temperature downstream of the step due to viscous dissipation cause the heat transfer coefficient C_h values to be positive.

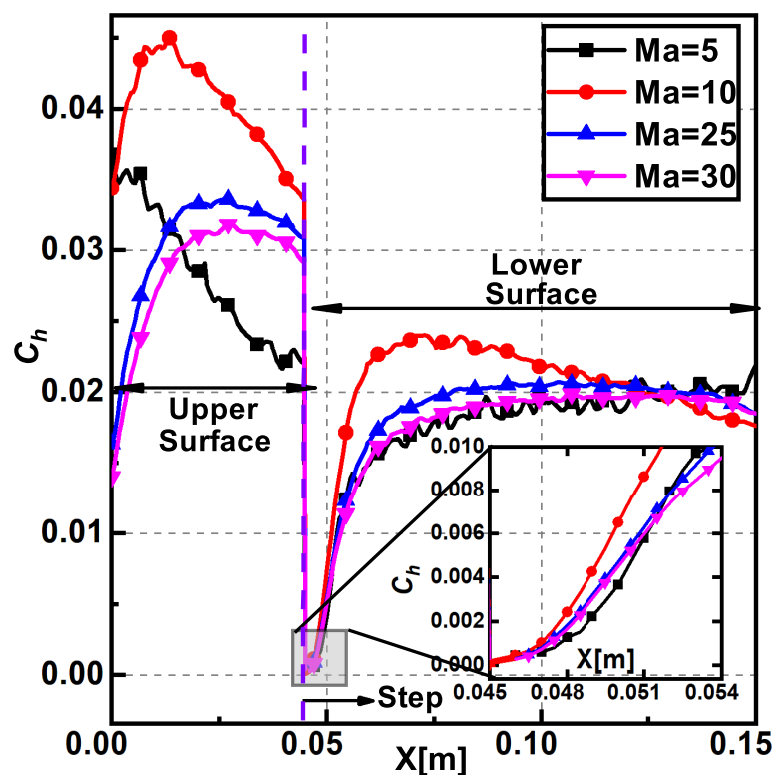


FIGURE 6.13: Variation of heat transfer coefficient C_h along the upper and lower surfaces of BFS for different Ma .

TABLE 6.4: Recirculation lengths for of BFS different T_w .

Wall temperature	$T_w=T_\infty$	$T_w=2T_\infty$	$T_w=4T_\infty$	$T_w=8T_\infty$
$X_L(\text{mm})$	1.40	1.50	1.47	1.50
$Y_L(\text{mm})$	1.78	1.74	1.88	1.96

6.1.2 Influence of Wall temperature

To evaluate the effects of wall temperature on the flow and surface properties over the BFS, the wall temperature (T_w) was set to four different values, i.e., T_∞ , $2T_\infty$, $4T_\infty$ and $8T_\infty$ where, $T_\infty = 204$ K. For all instances in this section, $H = 30\text{mm}$, $Kn = 1.06$, and $Ma = 25$ are used.

Velocity field:

Figure 6.14 shows the plots of velocity ratio (u/U_∞) for different T_w at sections $X = 44$ mm, $X = 46$ mm, and $X = 100$ mm along the length of the BFS. The increase in wall temperature increases the boundary layer thickness. At section $X = 44$ mm, the velocity ratio (u/U_∞) marginally increases with wall temperature. The particles are reflected in a greater distance due to a high wall temperature, which increases the extent to which the wall effect diffuses. Section $X = 46$ mm shows the same trend. At section $X = 100$ mm, which is downstream of the step, the profiles marginally differ for different wall temperatures. Table 6.4 denotes the recirculation lengths for different wall temperature, in which X_L and Y_L denote the axial extent of the recirculation region in x and y -directions, respectively measured from the step corner (i.e., from $X = 45$ mm). It can be observed that X_L remains fairly constant whereas Y_L shows an increasing trend.

Slip velocity:

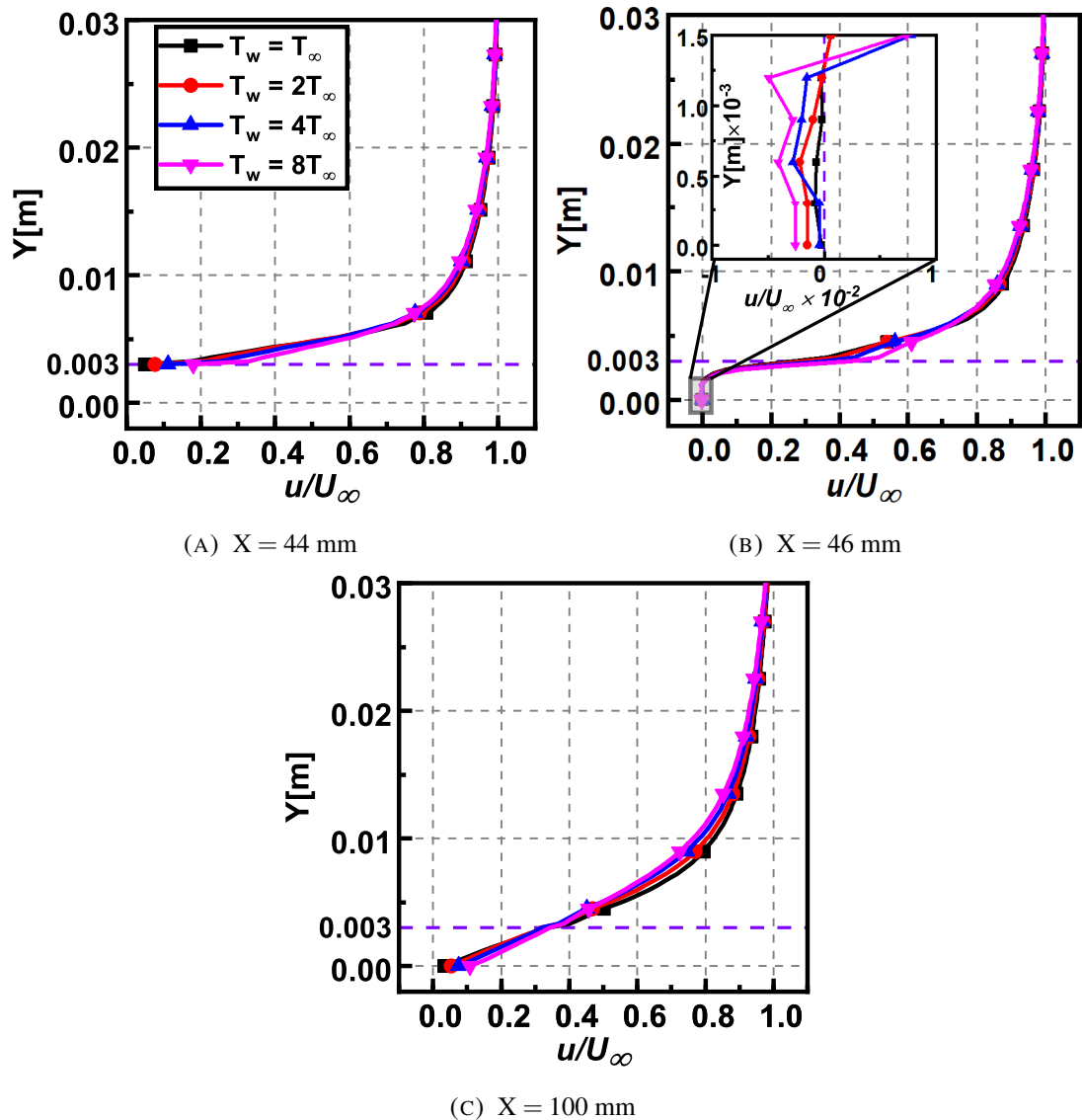


FIGURE 6.14: Variation of the non-dimensional velocity perpendicular to the surface of BFS for different T_w .

Figure 6.15 shows the plots of the slip velocity ratio (u_s/U_∞) along the upper and the lower surfaces of the BFS for different T_w . From the plot, it can be observed that for higher T_w the slip velocity ratio is more compared to the other cases. As the wall temperature increases, the thermal velocity of the gas molecules increases, and they gain more energy to traverse farther into the flow field. This increased molecular momentum increases the slip velocity magnitude, and it increases with T_w . The near

wall temperatures and hence the local mean free path of the molecules increases with T_w . This increases the rarefaction effects, which result in higher slip velocity for higher T_w . Starting from the wake region of the step until the outlet, as seen from Figure 6.24, the variation in the fluid temperature is negligible. This results in a reasonably constant local mean free path of the molecules and hence similar rarefaction effects and slip velocities. The slip velocity ratio at the step for $T_w = 8 T_\infty$ is about 3.65 times higher than $T_w = T_\infty$. Downstream of the step on the lower surface, the magnitude of variation in slip velocity ratio for different T_w is less compared to the upper surface, and they follow the same trend.

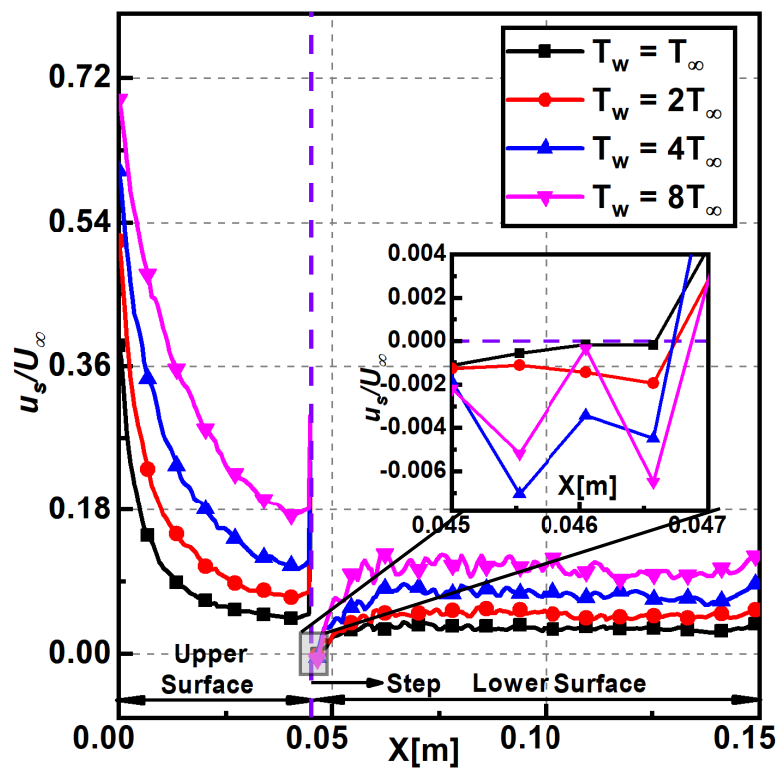


FIGURE 6.15: Slip velocity ratio along the upper and lower surfaces of BFS for different T_w .

Pressure field:

Figure 6.16 shows the pressure ratio (p/p_∞) profiles for different T_w at sections $X = 44$ mm, $X = 46$ mm, and $X = 100$ mm along the length of the BFS. In section $X = 44$ mm, the near-wall pressure increases with T_w . From the kinetic theory of gases, the product of density and square of thermal velocity gives pressure. Away from the wall, increase in T_w increases the thermal velocity (whereas the density does not change as seen from Figure 6.20), thus increasing the pressure. At section $X = 46$ mm, the profiles for different T_w overlap inside the recirculation region. Beyond $Y = 0.003$, i.e., the step height, the profiles deviate and follow a similar trend observed at section $X = 44$ mm. Downstream of the step at $X = 100$ mm, the profiles show significant variation. For comparison, in section $X = 100$, the maximum pressure ratios are 35.81, 36.15, 37.11, and 38.82 for T_w/T_∞ 1, 2, 4, and 8, respectively.

Temperature field:

Figure 6.17 show the overall temperature ratio (T_{ov}/T_∞) profiles for different T_w at sections $X = 44$ mm, $X = 46$ mm, and $X = 100$ mm along the length of the BFS, they follow similar trends as the pressure profiles. At section $X = 44$ mm, the near-wall temperature increases with T_w , but the difference in profiles is higher compared to the pressure ratio. In section $X = 46$ mm, unlike the pressure profiles, the temperature profiles do not overlap and show a deviation in the recirculation region. Farther downstream at $X = 100$ mm, the cumulative effects of viscous dissipation are more pronounced, which results in a considerable variation among the profiles. For comparison in section $X = 100$ mm, the maximum temperature ratios are 38.06, 38.43, 39.66, and 42.41 for T_w/T_∞ 1, 2, 4, and 8, respectively.

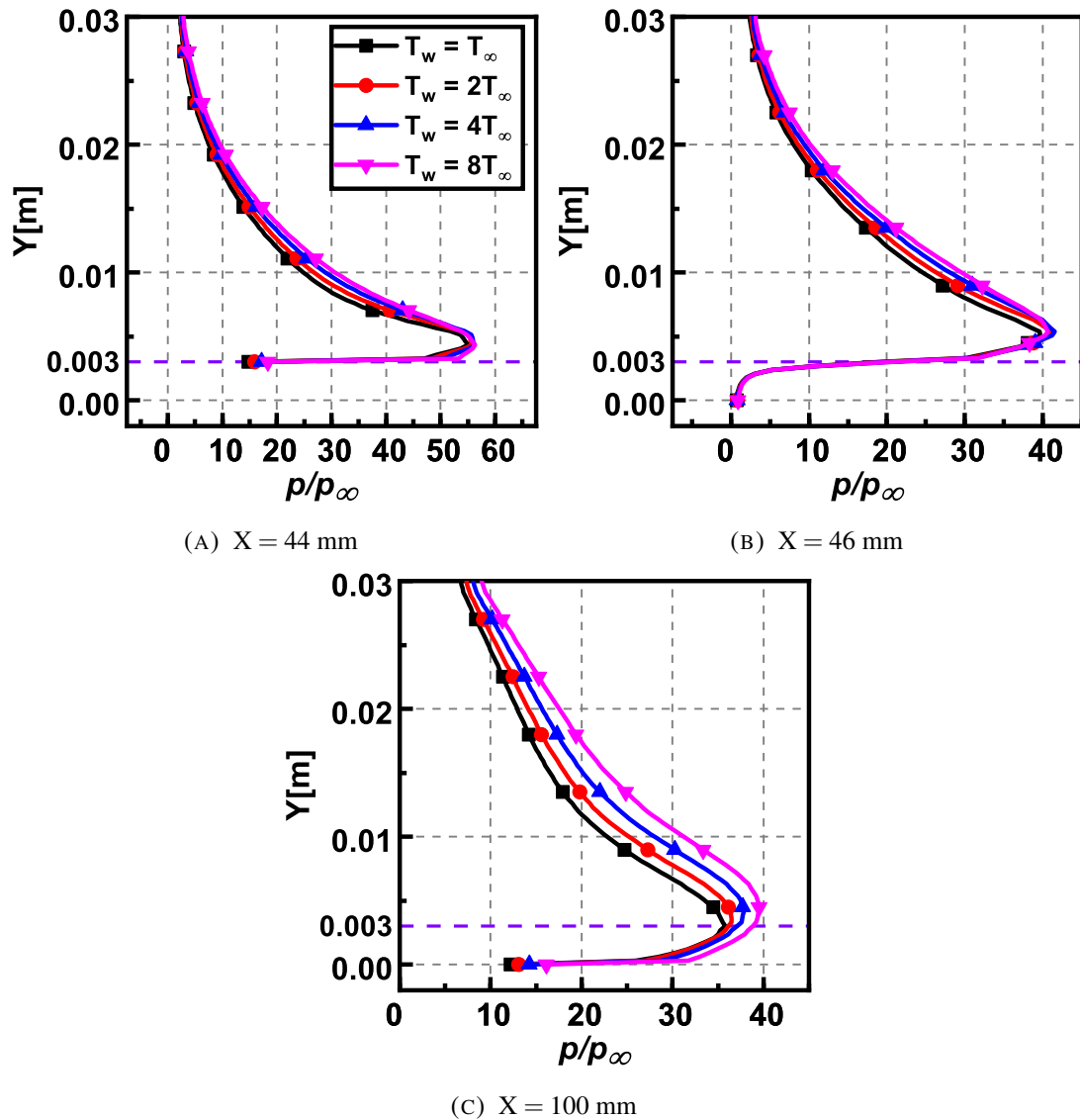


FIGURE 6.16: Variation of the non-dimensional pressure perpendicular to the surface of BFS for different T_w .

In all the profiles shown, the peak temperature ratio is about one order higher in magnitude than the free stream value. For a given T_w the peak temperature also shows negligible variation with X . With an increase in the wall temperature, the temperature ratios' profiles also increase due to higher conduction from the wall.

Figure 6.18 shows the rotational (T_R), overall (T_{OV}), and translational temperature (T_T) profiles for different T_w at sections $X = 46$ mm. The temperature ratio variation

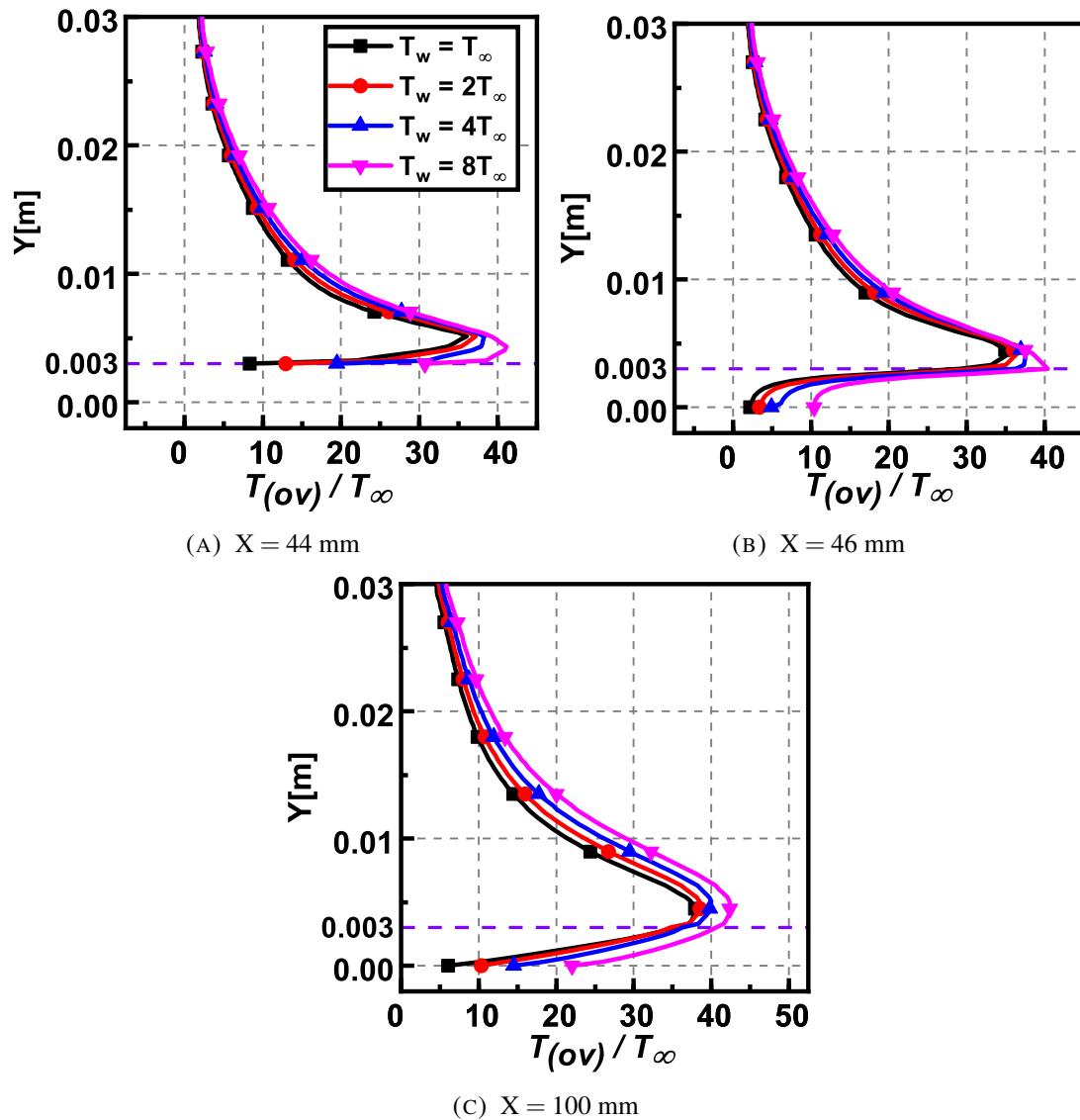


FIGURE 6.17: Variation of the non-dimensional temperature perpendicular to the surface of BFS for different T_w .

concerning the change in T_w is significantly less compared to the variation for the change in Ma . At the top surface, the temperatures are relatively the same indicating thermodynamic equilibrium. The temperatures show substantial deviation near the step ($Y = 0.003$), where the translational temperature is much larger than the rotational and overall temperature. At the lower surface ($Y \approx 0$) the temperatures are again of the relatively same order and attain a temperature above the imposed wall temperature,

signifying temperature jump as described in continuum formulation [156]. Near the wall, a considerable difference in the temperature ratios are observed, particularly for higher T_w at the other X locations like $X = 44$ mm and 100 mm. The profiles in other X locations are otherwise very similar to those shown below, including the magnitude of the corresponding peak temperature ratios and, therefore, not shown here.

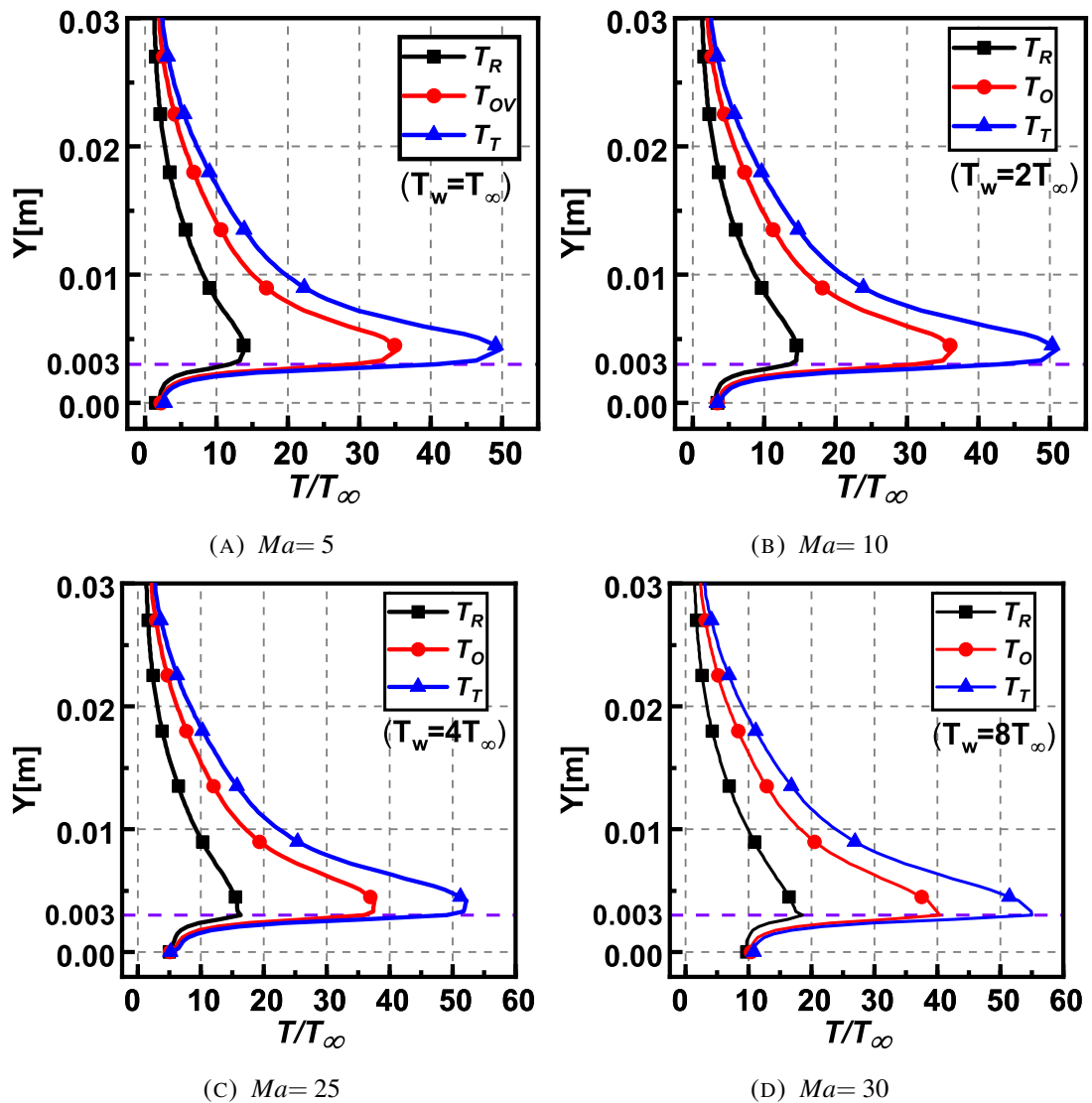


FIGURE 6.18: Variation of the non-dimensional rotational, overall, and translational temperature perpendicular to the surface of BFS at $X = 46$ mm for different T_w .

Temperature jump:

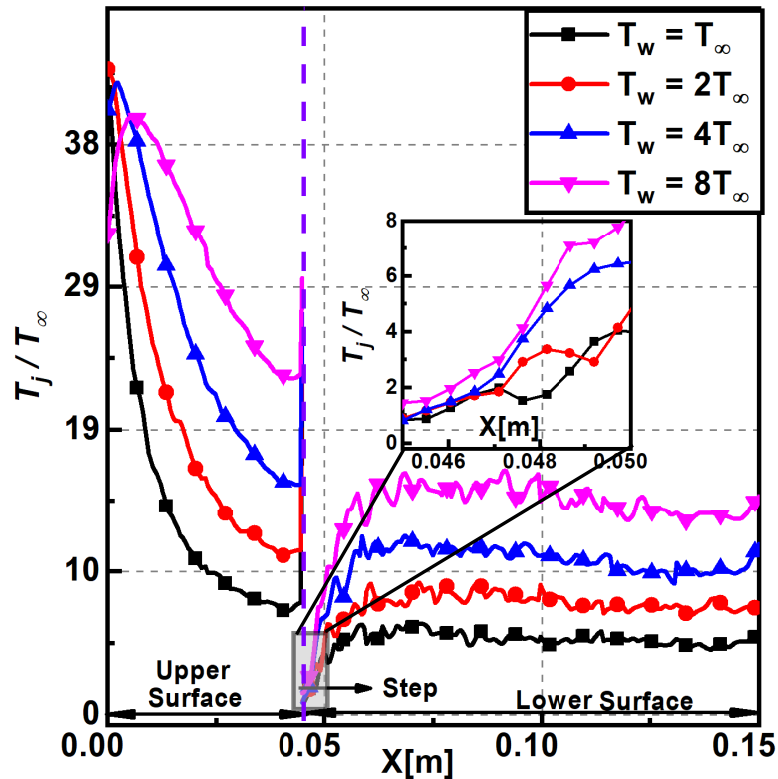


FIGURE 6.19: Temperature jump ratio along the upper and lower surfaces of BFS for different T_w .

Figure 6.19 shows the plots of temperature jump ratio (T_j/T_∞) along the upper and the lower surfaces of the BFS for different T_w . It can be observed that the temperature jump ratio at a given location increases with T_w .

The variation of temperature jump along the flow direction has already been explained in section 6.1.1. As the wall temperature increases, the near-wall fluid temperature also increases, resulting in a larger local mean free path. Therefore, the increased rarefaction effects near the wall lead to a more considerable temperature jump. This trend concerning varying T_w is seen all along the upper and lower surfaces. Furthermore, downstream of the step on the lower surface, significant variation in temperature jump ratio is observed for varying T_w when compared with that for varying Ma .

Density field:

Figure 6.20 shows the density ratio (ρ/ρ_∞) profiles for different T_w at sections $X = 44$ mm, $X = 46$ mm, and $X = 100$ mm along the length of the BFS. In section $X = 44$ mm, the near-wall density decreases with increasing T_w which is consistently observed in other sections also. In section $X = 46$ mm, the density ratio increases due to flow expansion and reaches a free-stream value far away from the lower surface. In section $X = 100$ mm, the density ratio decreases first and increases again due to shock and reaches a free-stream value far away from the wall. The density ratio profiles overlap for different T_w away from the wall at all sections in contrast to the pressure and temperature profiles.

Pressure coefficient:

Figure 6.21 shows the distribution of the pressure coefficient C_p along the upper and the lower surfaces of the BFS for different T_w . From the plot, the profiles follow a similar trend concerning the X coordinate for different T_w . Unlike the variation of pressure coefficient C_p where it reduced with increasing Ma , the C_p values increase with wall temperature. As the Ma is same for all the cases, the contribution of the dynamic pressure term is relatively less, and the pressure coefficient C_p mainly depends on the near-wall pressure p_w . Due to the increase in wall temperature, the thermal velocity of the molecules and hence the near-wall fluid pressure increase, which results in a higher value of pressure coefficient C_p . On the lower surface, a similar trend is observed but the magnitude of C_p is reduced due to the reduced pressure downstream of the step due to flow expansion. From the simulation results, we see that the local temperature and

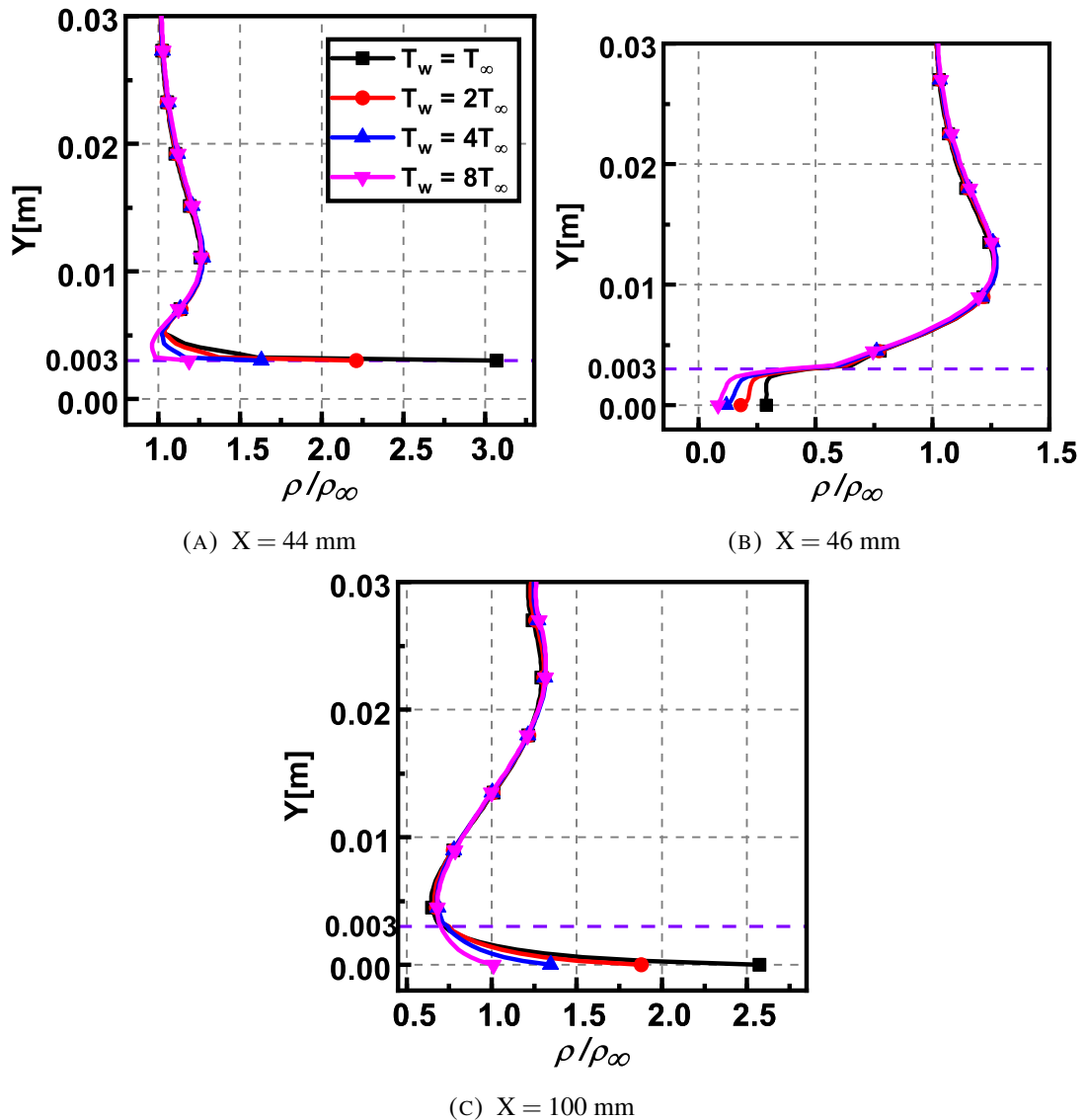


FIGURE 6.20: Variation of the non-dimensional density perpendicular to the surface of BFS for different T_w .

pressure increase along the lower surface, increasing the pressure coefficient C_p in the flow direction.

Skin friction coefficient:

Figure 6.22 shows the distribution of the skin friction coefficient C_f along the upper and the lower surfaces of the BFS for different T_w . As per the VHS model used in the current

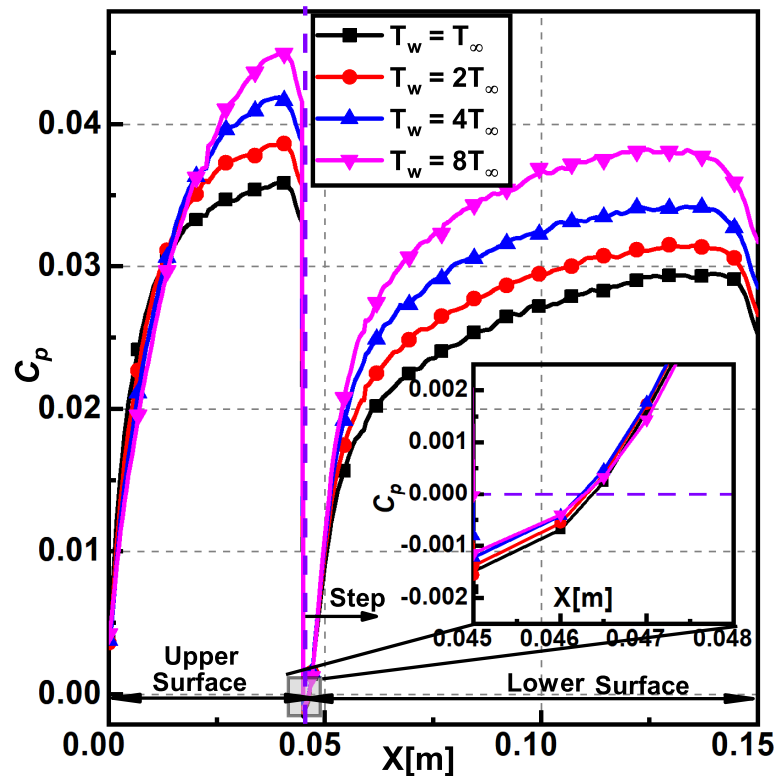


FIGURE 6.21: Variation of pressure coefficient C_p along the upper and lower surfaces of BFS for different T_w .

study, the fluid viscosity is directly proportional to the fluid temperature leading to an increase in the viscous forces. The higher magnitudes of viscous forces cause an increase in skin friction coefficient C_f . The C_f values are of the order of 10^{-2} (smaller than the values in continuum regime) as the flow is in the transitional regime, due to which fewer molecules strike the surface. This trend is in agreement with the subsonic flow results of Xue *et al.*[68].

The skin friction coefficient C_f reduces along the flow direction on the upper surface analogous to the continuum flows over a flat plate. The C_f values are negative behind the step due to recirculation. On the lower surface, C_f values are lesser than those on the upper surface as the flow expands past the step and decelerates, resulting in lesser velocity gradients. Considerable fluctuations are also observed throughout the length of

the BFS for different T_w . As per the eq. 6.5, skin friction coefficient C_f is proportional to the tangential mean flow velocity of the incident molecules. Along the flow direction on the lower surface, the flow velocity is roughly constant according to Figure 6.24a, which results in a negligible change in skin friction coefficient C_f .

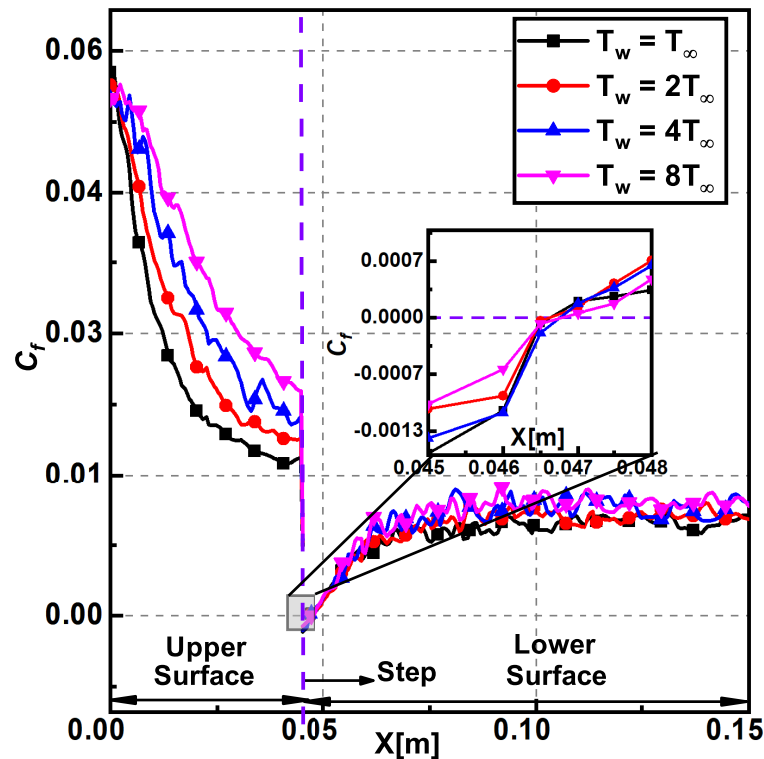


FIGURE 6.22: Variation of skin friction coefficient C_f along the upper and lower surfaces of BFS for different T_w .

Heat transfer coefficient:

Figure 6.23 shows the distribution of the heat transfer coefficient C_h along the upper and the lower surfaces of the BFS for different T_w . On both the surfaces the heat transfer coefficient C_h values increase with increasing T_w . With an increase in the wall temperature T_w , the near-wall fluid heats, and the local mean free path of the molecules increases. This increases the frequency of molecular collisions with the wall. Further, as

the local mean free path increases, inter-molecular collisions reduce, and the molecules further away from the wall also participate in the heat transfer process. Both these phenomena lead to a rise in the net wall heat flux q_w , leading to an increase in heat transfer coefficient C_h . Also, the increased viscous dissipation contributes to increasing the q_w . The viscous dissipation, which acts as a heat source increases with increasing T_w which then increases the magnitudes of the heat transfer coefficient C_h .

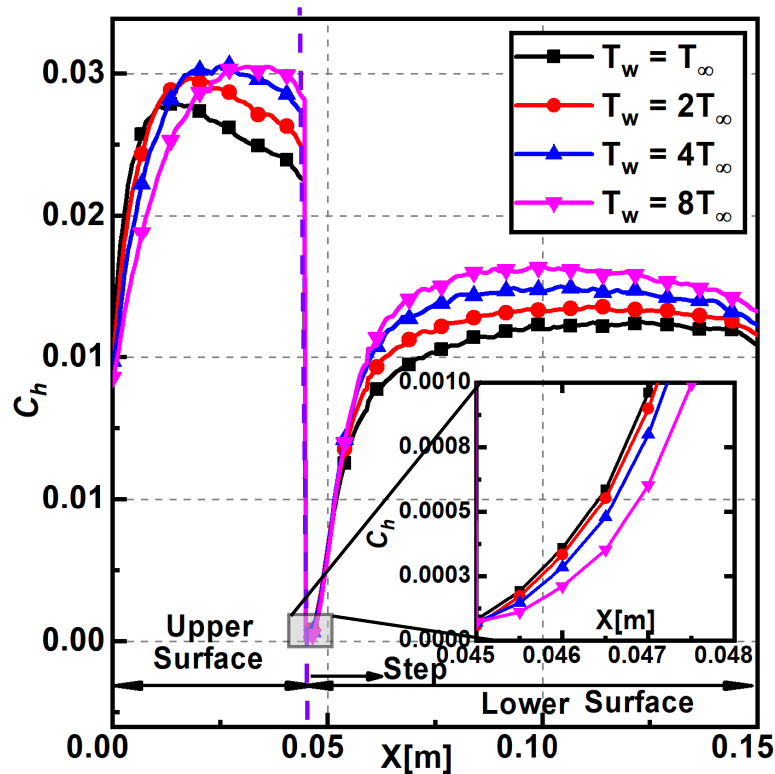


FIGURE 6.23: Variation of heat transfer coefficient C_h along the upper and lower surfaces of BFS for different T_w .

6.1.3 Influence of Knudsen number

This section presents the rarefaction effects on the flow past BFS. Five different Knudsen numbers (given in Table 6.2) in various rarefaction regimes are simulated, and the flow field and surface characteristics are analyzed. For all instances in this section, $H = 60\text{mm}$,

$h = 3\text{mm}$ and $T_w = 4T_\infty$ is used. Henceforth, the variation of sampled results with Y are presented at the locations $X = 30\text{mm}$, 59mm , 61mm and 120mm respectively.

Initially, the contours are presented. For the case of $Ma = 25$, $Kn = 1.06$, and $H = 60\text{mm}$, the various flow-field contours are shown in Figure 6.24. Figure 6.24a shows the non-dimensional velocity contour, depicting the hydrodynamic boundary layer's growth, with lower magnitudes at the wall and higher magnitudes away from it in the central domain. Downstream of the step owing to the formation of the recirculation region, the velocity magnitudes are very low. Also, the band of near-wall low velocity extends from the step to the outlet region.

The non-dimensional density contour is shown in Figure 6.24b, which offers a higher density near the upstream wall and a gradual reduction away from it. The density magnitude is close to one in the majority of the computational domain. The region close to the step has low-density magnitudes due to the recirculation and expansion effects. Furthermore, a high-density magnitude band arises from the upstream surface and traverses towards the top surface, causing a regionalized density rise.

The non-dimensional pressure contour is shown in Figure 6.24c, which attain greater values at the upstream wall and are one order greater than that of free-stream. Due to the minimal influence of the step in the central domain, pressure attains the free-stream value. In the downstream direction, the pressure magnitudes are very low due to the recirculation. Also, the wall pressures are lower than their upstream counterparts, primarily due to the flow expansion.

The non-dimensional temperature contour is shown in Figure 6.24d, which follows the

pressure contour and depicts higher magnitudes near the wall due to the viscous heating and compressibility phenomena. The band of high temperature at the step height level continues to dissipate the energy farther downstream of the step. Like the pressure contour, the non-dimensional temperature also shows lower magnitudes close to the step; however, these low temperatures are confined to a lower region than the pressure.

The Compressibility (Z) contour is shown in Figure 6.25. The compressibility factor shows the departure of the gas from the ideal behavior and is given by,

$$Z = \frac{p}{\rho RT} \quad (6.8)$$

where p denotes the pressure, ρ the density, R the gas constant, and T is the temperature. The regions of higher Z magnitudes are witnessed on the upstream surface due to the shear effects. A similar trend is noticed downstream of the step; however, the magnitudes of Z are lower compared to the upstream. In the region close to the step and also in the center of the domain, the magnitudes of Z are relatively low, depicting equilibrium.

Velocity field:

Figure 6.26 shows the non-dimensional velocity (u/U_∞) in the perpendicular direction at sections $X = 30\text{mm}$, $X = 59\text{mm}$, $X = 61\text{mm}$, and $X = 120\text{mm}$ for different Kn . Y represents the perpendicular distance in y -direction above the surface of the BFS.

The profiles at section $X = 30\text{mm}$ and $X = 59\text{mm}$ are similar, depicting the flow is undisturbed upstream of the step. At Section $X = 61\text{mm}$, the velocity profiles show adverse velocities, characterizing recirculation, a comparable phenomenon was found in

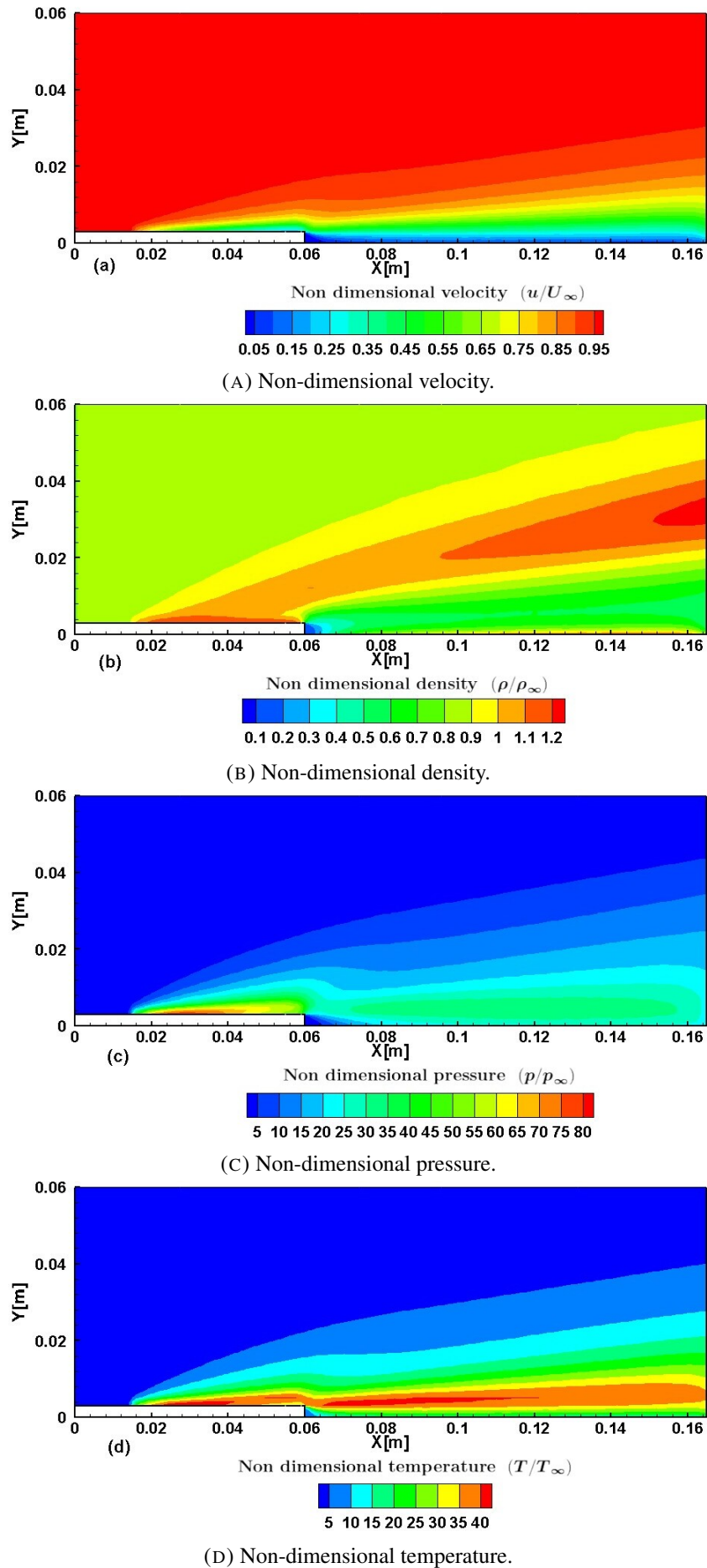


FIGURE 6.24: Contours of non-dimensional flow-field properties for $H = 60\text{mm}$, $Ma = 25$ and $Kn = 1.06$.

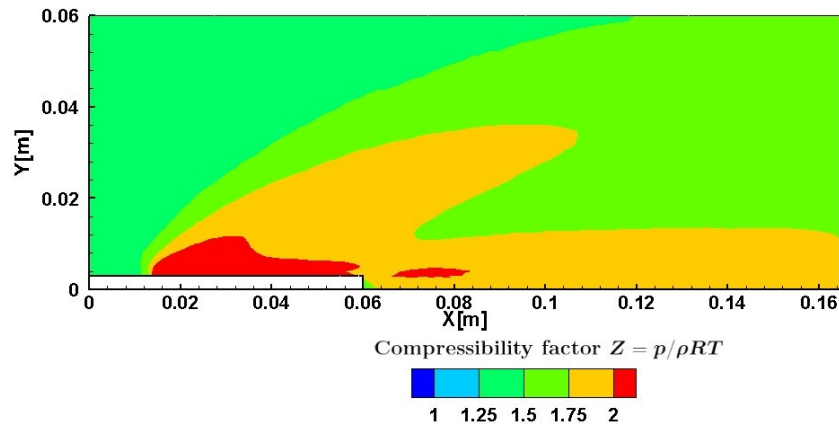


FIGURE 6.25: Compressibility (Z) contour for $H = 60\text{mm}$, $Ma = 25$ and $Kn = 1.06$.

Grotowsky and Ballmann's [79] continuum regime analysis. Interestingly, at the section $X = 61\text{mm}$ up to the step height, the (u/U_∞) profiles overlap for all regimes and show a diverging trend above the step. The profiles close to the outlet at $X = 120\text{mm}$ remain relatively unaffected, similar to those at the inlet. There is considerable velocity slip at the wall in all the sections except at $X = 61\text{mm}$ in the wake of the step, where the slip is relatively the same for all the regimes. This trend deviates from the traditional continuum results, which show zero velocity at the walls.

The rarefaction effects also reduce the non-dimensional velocity along Y . The increase in rarefaction reduces the inter-molecular collisions and increases the molecular mean free path. Consequently, the wall effects propagate more into the flow field, reducing the velocity. This is quantified by the boundary layer thickness, another important flow characteristic. Here, the boundary layer thickness (δ) is calculated by considering the point where $u/U_\infty = 0.99$. For the top surface location considered in the present study, the boundary layer is fully established for different Kn , except $Kn = 21.10$, which shows a developing trend. For a particular location of $X = 59\text{mm}$, (δ) and (δ/H) are given in Table 6.5.

TABLE 6.5: Boundary layer thickness (δ) for different Kn at $X = 59\text{mm}$.

Kn	0.05	0.10	1.06	10.33	21.10
$\delta(\text{mm})$	8.3	9.65	26.7	55.4	-
δ/H	0.13	0.16	0.44	0.92	-

TABLE 6.6: Recirculation lengths of BFS for different Kn .

Kn	0.05	0.1	1.06	10.33	21.10
$X_L(\text{mm})$	1.95	1.65	1.40	1.21	1.15
$Y_L(\text{mm})$	1.55	1.53	1.44	1.42	1.18

The near-wall velocity (slip) also increases with rarefaction. The profiles for different rarefaction regimes at a given Y location also differ only slightly from each other. At section $X = 61\text{mm}$, magnitudes of (u/U_∞) at $Y = 0.03$ are 1.00, 0.99, 0.99, 0.96 and 0.94 for Kn 0.05, 0.1, 1.06, 10.33 and 21.10 respectively.

The velocity streamlines for different Kn are depicted in Figure 6.27. It is observed that for all Kn , a recirculation region exists. Furthermore, streamlines of the free-molecular flow for the case of $Kn = 21.10$ suggests that there exists a secondary smaller recirculation region. The recirculation lengths for different Kn in x and y -direction calculated from the step corner (i.e., from $X = 60\text{mm}$) is denoted by X_L and Y_L , and is given in Table 6.6. For approximating these lengths, the skin friction coefficient ($C_f = 0$) is the condition used [150, 152]. Both X_L and Y_L show a diminishing value with Kn (as Re decreases as seen from eq.1.4). This behavior is analogous to the one found in continuum flows for decreasing Reynolds number.

The plots of non-dimensional velocity slip (u_s/U_∞) along the upper and the lower surfaces of the BFS for different Kn is shown in Figure 6.28. The difference in wall velocity and the fluid close to the wall gives the velocity slip. The velocity slip can be obtained by directly sampling the microscopic particles impacting the wall or extracting

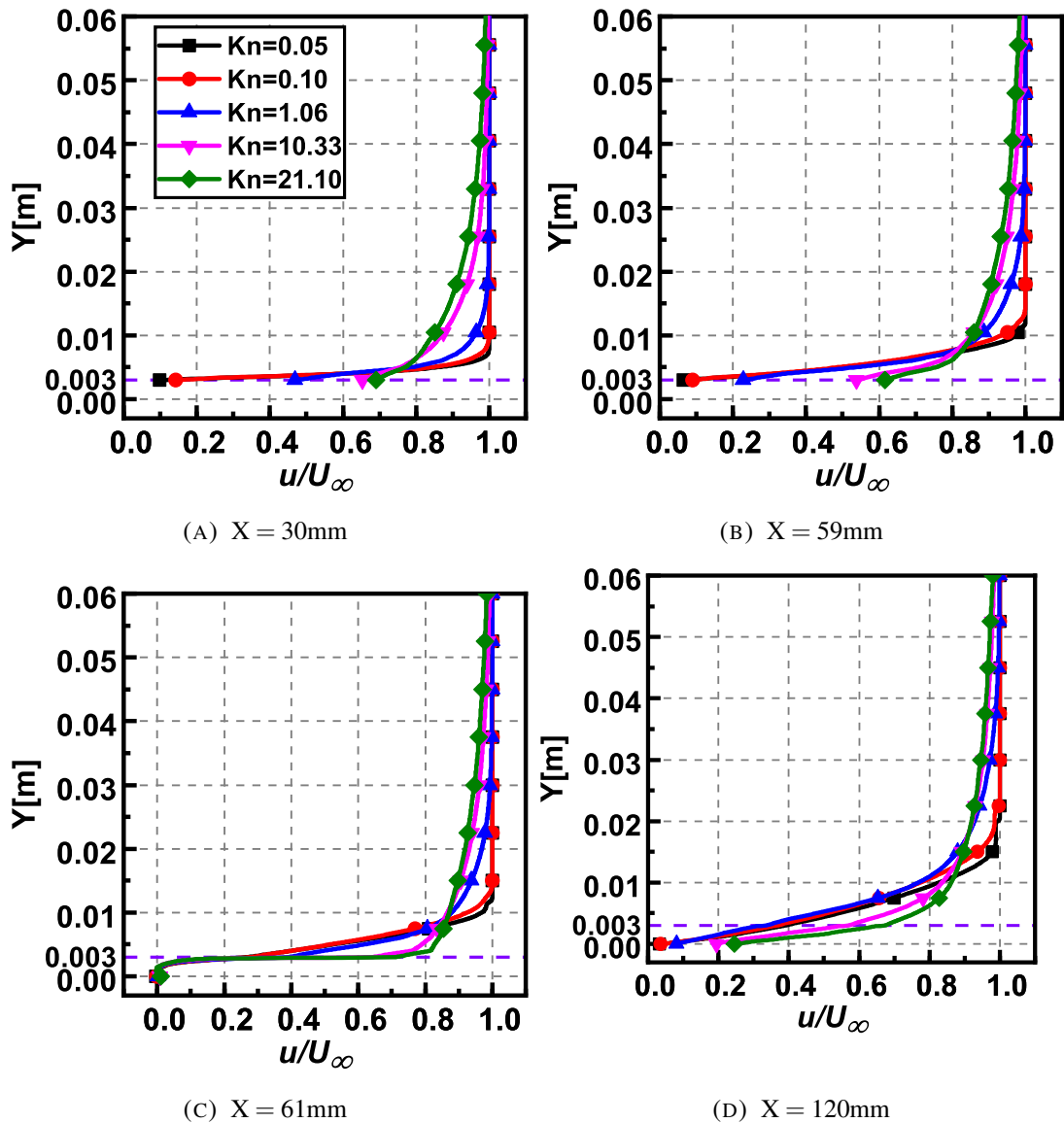


FIGURE 6.26: Variation of the non-dimensional velocity perpendicular to the surface of BFS for different Kn .

the macroscopic flow properties in the cell adjacent to the wall; the latter is used in this analysis.

The velocity slip reduces non-linearly towards the step. Towards the upper surface's leading edge, the velocity difference between the incoming flow and the wall is large, which leads to a peak in the velocity slip. This decreases downstream as the presence of

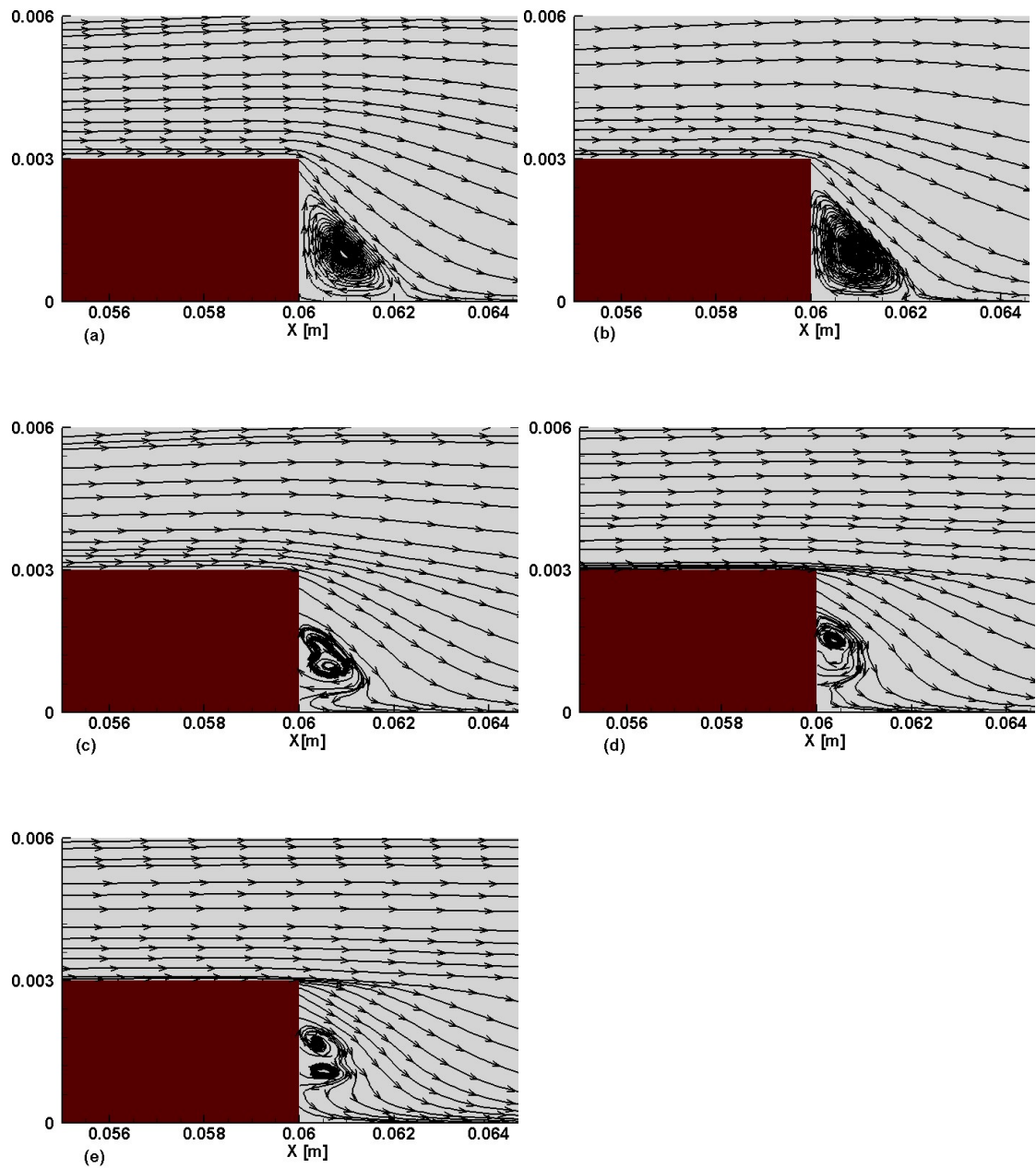


FIGURE 6.27: Streamlines near the step of BFS for (a) $Kn=0.05$, (b) $Kn=0.1$, (c) $Kn=1.06$, (d) $Kn=10.33$, (e) $Kn=21.10$.

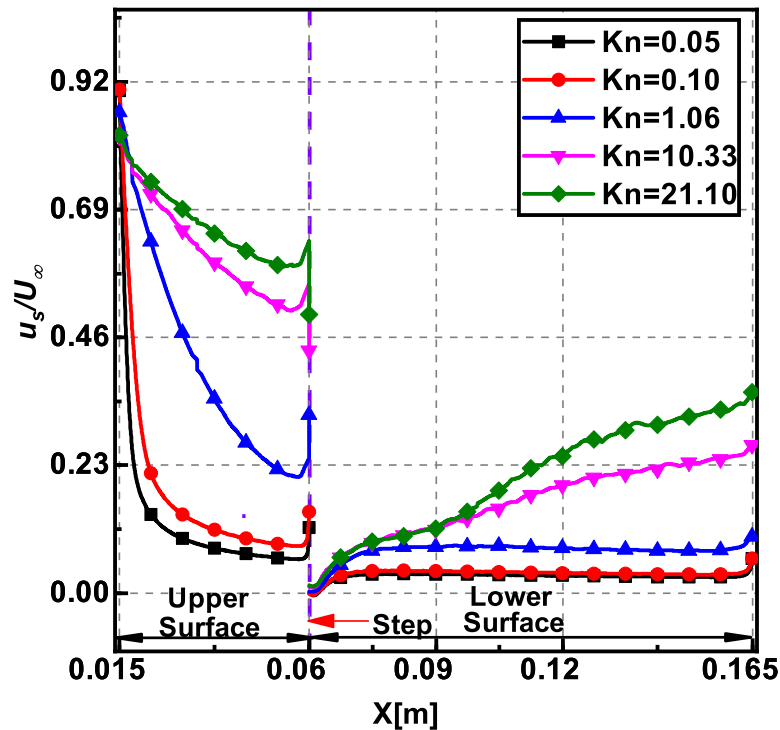


FIGURE 6.28: Slip velocity ratio along the upper and lower surfaces of BFS for different Kn .

the wall decelerates the flow. The velocity slip increases along the lower surface downstream of the step, possibly because a larger part of the flow domain gains temperature. This results in a larger local mean free path and hence increased rarefaction effects.

Upstream and downstream of the step, the velocity slip increases with Kn due to increased rarefaction effects. For lower Kn , the non-dimensional velocity slip at a given location is less and almost a constant compared to the other cases.

Pressure field:

Figure 6.29 shows the non-dimensional pressure (p/p_∞) in the perpendicular direction at sections $X = 30\text{mm}$, $X = 59\text{mm}$, $X = 61\text{mm}$, and $X = 120\text{mm}$ for different Kn . The non-dimensional pressure behaves similarly in all the sections and increases with increasing

Knudsen number. Also, close to the step, the pressure surpasses the free-stream values by order of magnitude. There is a considerable variation in the near-wall pressure for different Kn at all the sections, except at $X = 61\text{mm}$, where it is approximately the same. Moreover, the pressure at a given X attains the free-stream magnitude quicker in the slip regime than the other regimes. In section $X = 61\text{mm}$, the pressure is close to the free-stream value in the wake region of the step (for $Y < 0.003$). Further away from the wall (for $Y > 0.003$), the pressure reaches a peak (owing to the presence of shock layer upstream) and gradually decreases and attains a free-stream value. At section $X = 120\text{mm}$, the pressure profiles behave like those at section $X = 61\text{mm}$, but with a marginally lower magnitude. At sections $X = 61\text{mm}$, $X = 120\text{mm}$, downstream of the step, the sudden expansion causes the pressure to decrease. Also, owing to the compressibility effects of the free-stream flow, there is a pressure surge in all the plots near the step's face. For comparison at section $X = 61\text{mm}$, the peak pressure ratios are 15.10, 16.01, 36.35, 48.94 and 42.80 for Kn 0.05, 0.1, 1.06, 10.33 and 21.10 respectively.

Temperature field:

Figure 6.30 shows the non-dimensional temperature (T/T_∞) in the perpendicular direction at sections $X = 30\text{mm}$, $X = 59\text{mm}$, $X = 61\text{mm}$, and $X = 120\text{mm}$ for different Kn . The magnitudes of T/T_∞ increases with Kn at all the sections. Moreover, there is a considerable variation in the near-wall temperature at all the sections, except at $X = 61\text{mm}$. Because of the substantial flow speed, the viscous heating rates result in the high magnitude of near-wall temperatures. In contrast, at $X = 61\text{mm}$, in the wake of the step, the near-wall temperature is nearly the same for different Kn .

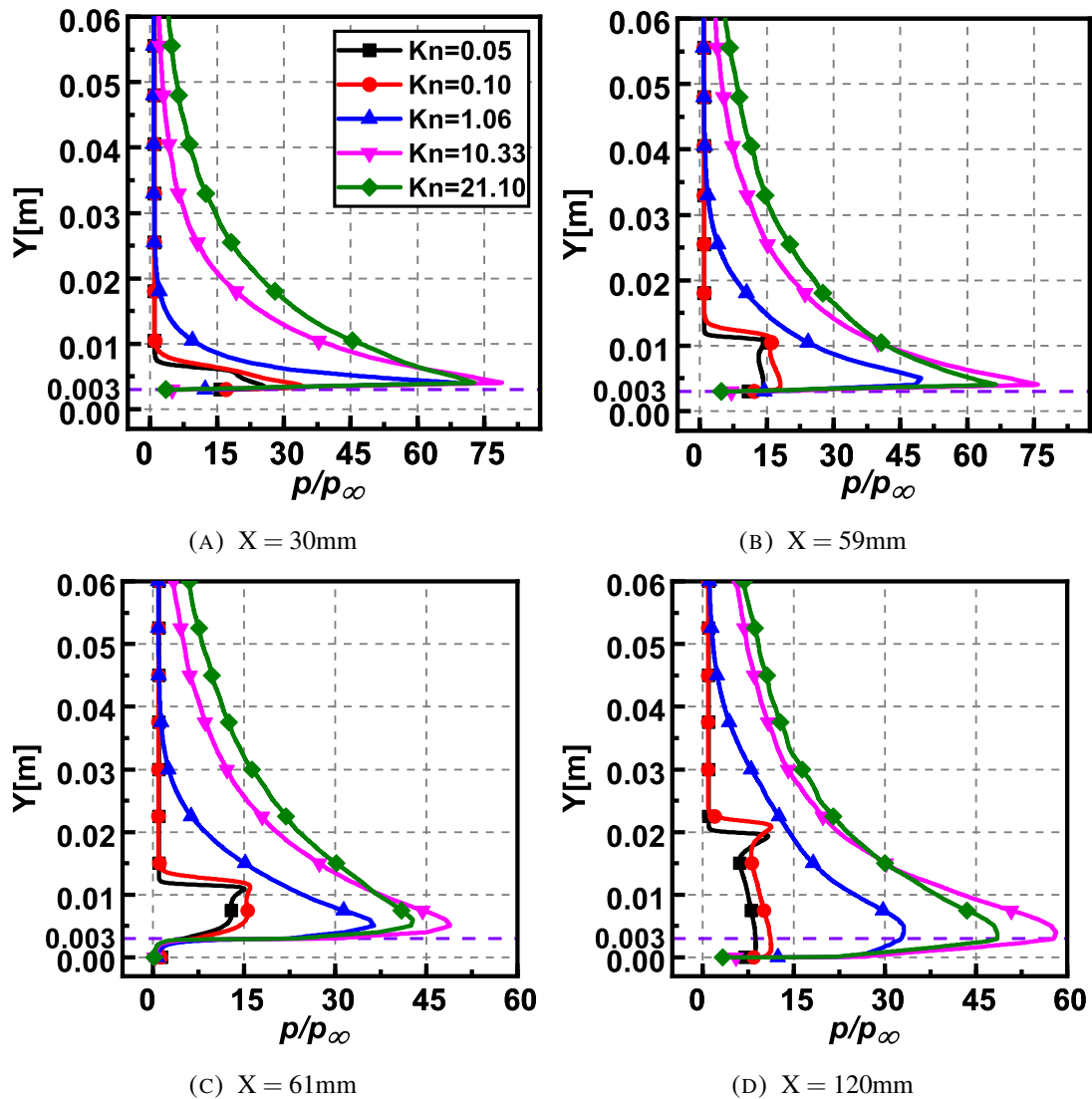


FIGURE 6.29: Variation of the non-dimensional pressure perpendicular to the surface of BFS for different Kn .

At the midpoint of the domain, at $Y = 0.03$, the non-dimensional temperature increases with Kn . As Kn increases, the number density of the molecules reduces; thus, the viscous heating occurring in the shear layer is dissipated among lesser molecules causing higher magnitudes of non-dimensional temperature. However, for smaller Kn in the slip and transitional regimes, the number density is of several orders higher than the free-molecular regime. Thus, the same viscous heating levels are dispersed among more molecules, causing the overall temperature reduction. For quantitative assessment, at the

section $X = 61\text{mm}$, the non-dimensional temperature at $Y = 0.03$ are 0.99, 0.99, 2.31, 7.73 and 9.92 for Kn 0.05, 0.1, 1.06, 10.33 and 21.10 respectively.

In the transverse direction from the BFS surface, the non-dimensional temperature surges quickly, then decreases and reaches values close to free-stream magnitudes. Again, for quantitative assessment at section $X = 61\text{mm}$, on the top face of the step, the peak temperature ratios are 29.38, 30.69, 37.65, 38.48, and 35.50 for Kn 0.05, 0.1, 1.06, 10.33 and 21.10, respectively. Thus, the non-dimensional temperature follows an identical pattern in all sections and reasonably shows an increasing trend with Kn .

Figure 6.31 shows the non-dimensional rotational (T_R), overall (T_{OV}), and translational temperature (T_T) in the perpendicular direction at sections $X = 30\text{mm}$, $X = 59\text{mm}$, $X = 61\text{mm}$, and $X = 120\text{mm}$ for $Kn = 0.05, 21.10$. The temperature profiles show a common trend in all sections. However, the magnitudes of the temperature in the free-molecular regime of $Kn = 21.10$ is greater than the slip regime of $Kn = 0.05$. This trend can again be attributed to the number density variation and the distribution of the viscous heating effects among a lesser number of particles at high Kn , as explained earlier. The thermal boundary layer thickness grows as the flow traverses downstream, which can be seen in the peaks near the step height ($Y = 0.003$) which grow in size. The rotational component of the temperature shows appreciable variation only in the slip regime, demonstrating that at higher degrees of rarefaction, the majority of the energy generated due to the wall and shear layer effects manifests itself in the translational and overall temperature components. Also, the change in the rotational component is noticed only at lower Kn , whereas at higher Kn the rotational component reasonably remains the

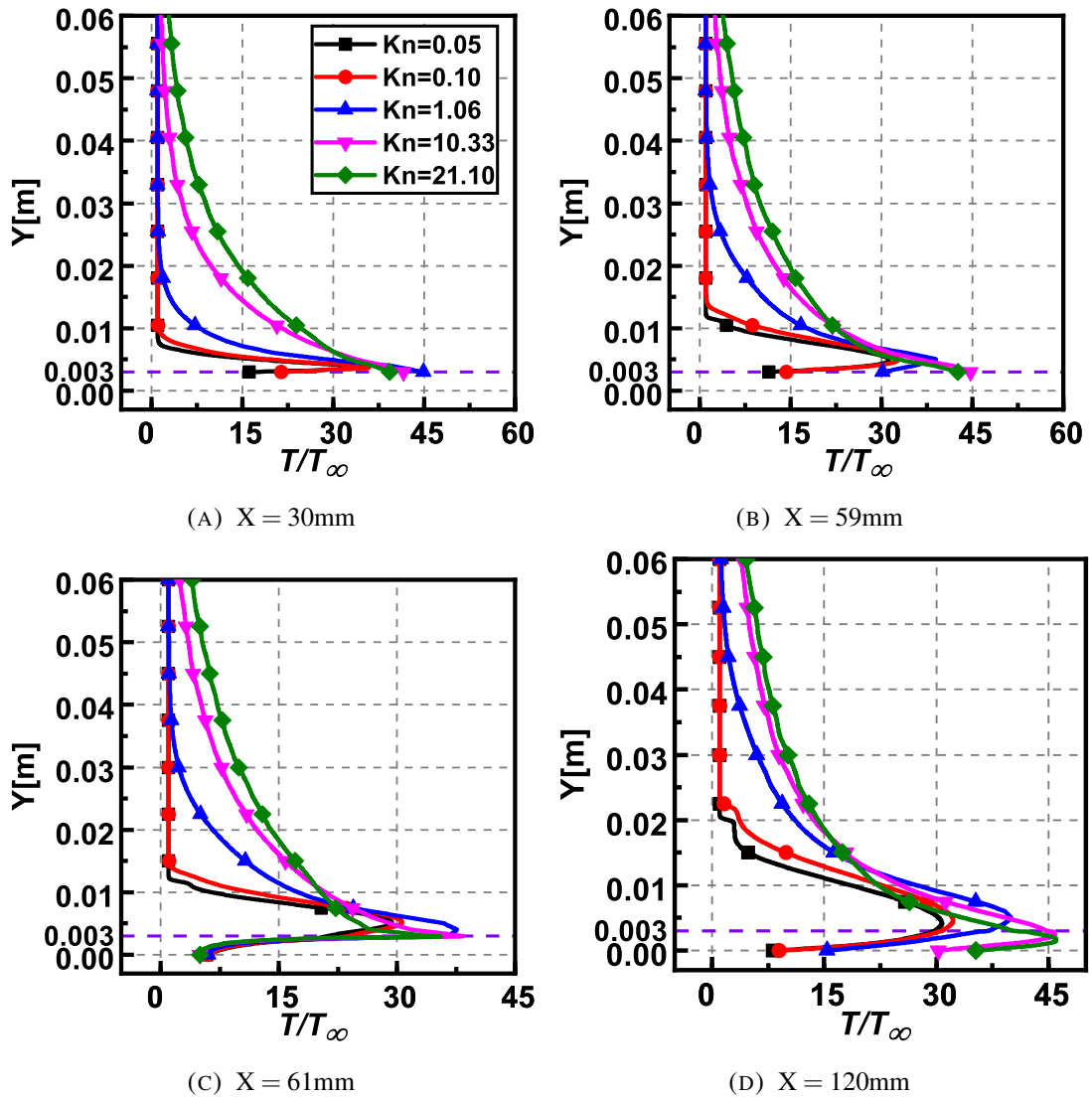


FIGURE 6.30: Variation of the non-dimensional temperature perpendicular to the surface of BFS for different Kn .

same at all sections. Furthermore, the rotational component at the wall increases close to the outlet section of $X = 120\text{mm}$ when compared to the wake of the step of $X = 61\text{mm}$.

The plots of the non-dimensional temperature jump (T_j/T_∞) along the upper and the lower surfaces of the BFS for different Kn is shown in Figure 6.32. The temperature jump is deduced similarly to the velocity slip by extracting the macroscopic flow characteristics in the cell adjacent to the wall. The temperature jump at a given location is found to

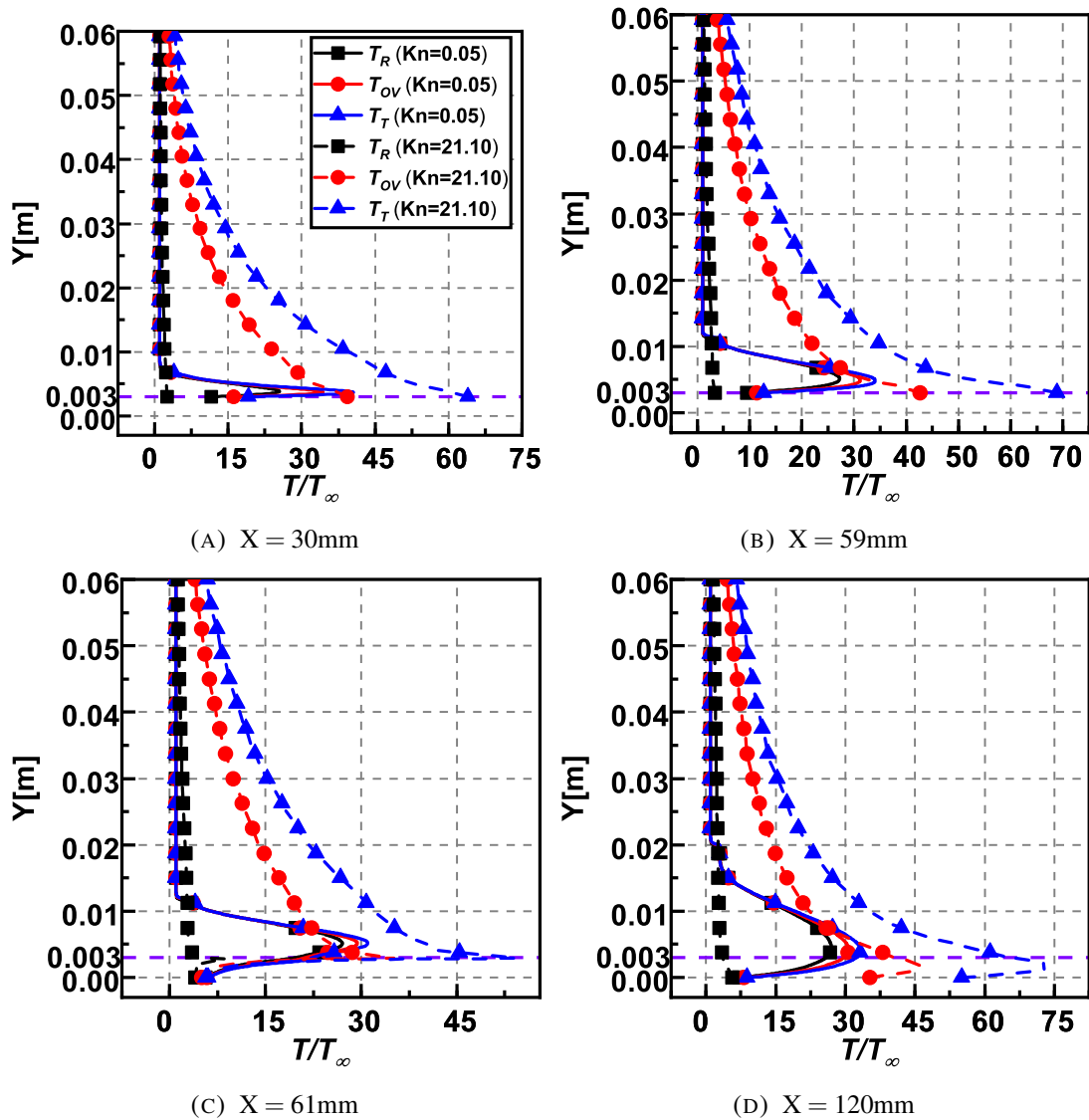


FIGURE 6.31: Variation of the non-dimensional rotational, overall, and translational temperature perpendicular to the surface of BFS for $Kn = 0.05, 21.10$.

increase with Kn . On the upstream surface in the slip and transitional regime, the temperature jump reaches a peak and decreases towards the step, whereas it continually increases in the free-molecular regime. The increase in the wall temperature causes the near-wall fluid temperature to increase, consequently increasing the local mean free path and the rarefaction. This increase in the rarefaction leads to an increase in the temperature jump. The wall shear rates soon decrease downstream of the leading edge and reduce the near-wall temperature and the resulting rarefaction effects. Moreover,

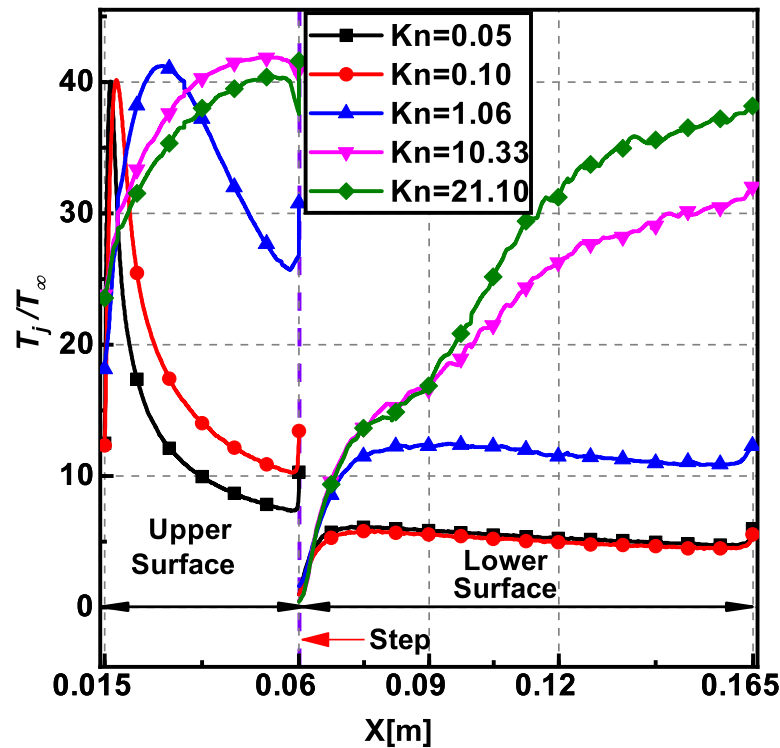


FIGURE 6.32: Temperature jump ratio along the upper and lower surfaces of BFS for different Kn .

the peak value of the temperature jump is about the same for different Kn . Additionally, downstream of the step, on the lower surface, the temperature jump increases with Kn similar to the non-dimensional temperature.

Density field:

Figure 6.33 shows the non-dimensional density (ρ/ρ_∞) in the perpendicular direction at sections $X = 30\text{mm}$, $X = 59\text{mm}$, $X = 61\text{mm}$, and $X = 120\text{mm}$ for different Kn . The non-dimensional density varies significantly in the transverse direction, and this is a common feature found in all sections. Another common feature is that the peak density in all sections is observed in the slip regime for $Kn = 0.05$ where it is about four times higher than the free-stream magnitude. At section $X = 30\text{mm}$, the non-dimensional

density variation for different Kn at a given Y is noticeable, whereas, in other sections, it is not. At section $X = 61\text{mm}$, which is in the wake region of the step, the near-wall densities are substantially smaller and almost overlap for different Kn . The densities for different Kn are relatively similar all along the face of the step. They show a deviating trend after that, signifying that density variation is uninfluenced by a change in Kn in the recirculation region. Far away from the step ($Y > 0.003$), the density decreases beyond the shock wave and eventually tends to the free-stream density. At section $X = 120\text{mm}$, near the outlet, the density reduces up to $Y = 0.003$, then experiences a rise, attributable to the shock region and, eventually, a reduction to attain the free-stream magnitude. For comparison at section $X = 61\text{mm}$, the peak density ratios are 3.751, 2.589, 1.100, 1.172 and 1.170 for Kn 0.05, 0.1, 1.06, 10.33 and 21.10 respectively.

Pressure coefficient:

The variation of pressure coefficient (C_p) for different Kn along the upper and the lower surfaces of the BFS is shown in Figure 6.34.

The profiles adopt similar patterns in the slip regime for $Kn = 0.05, 0.10$, and another common trend in the transitional and free-molecular regime for $Kn = 1.06, 10.33, \text{ and } 21.10$.

The pressure coefficient demonstrates different trends in different rarefaction regimes, the change being observed from $Kn = 1.06$ onwards. The pressure coefficient C_p on the upper surface increases along the BFS length; however, there is a sudden peak in the slip regime compared to the transitional and free-molecular regime where the C_p gradually increases. The early peaks in the slip regime can be attributed to the higher near-wall pressure arising from the stagnation pressure rise of the fluid stream (Figure

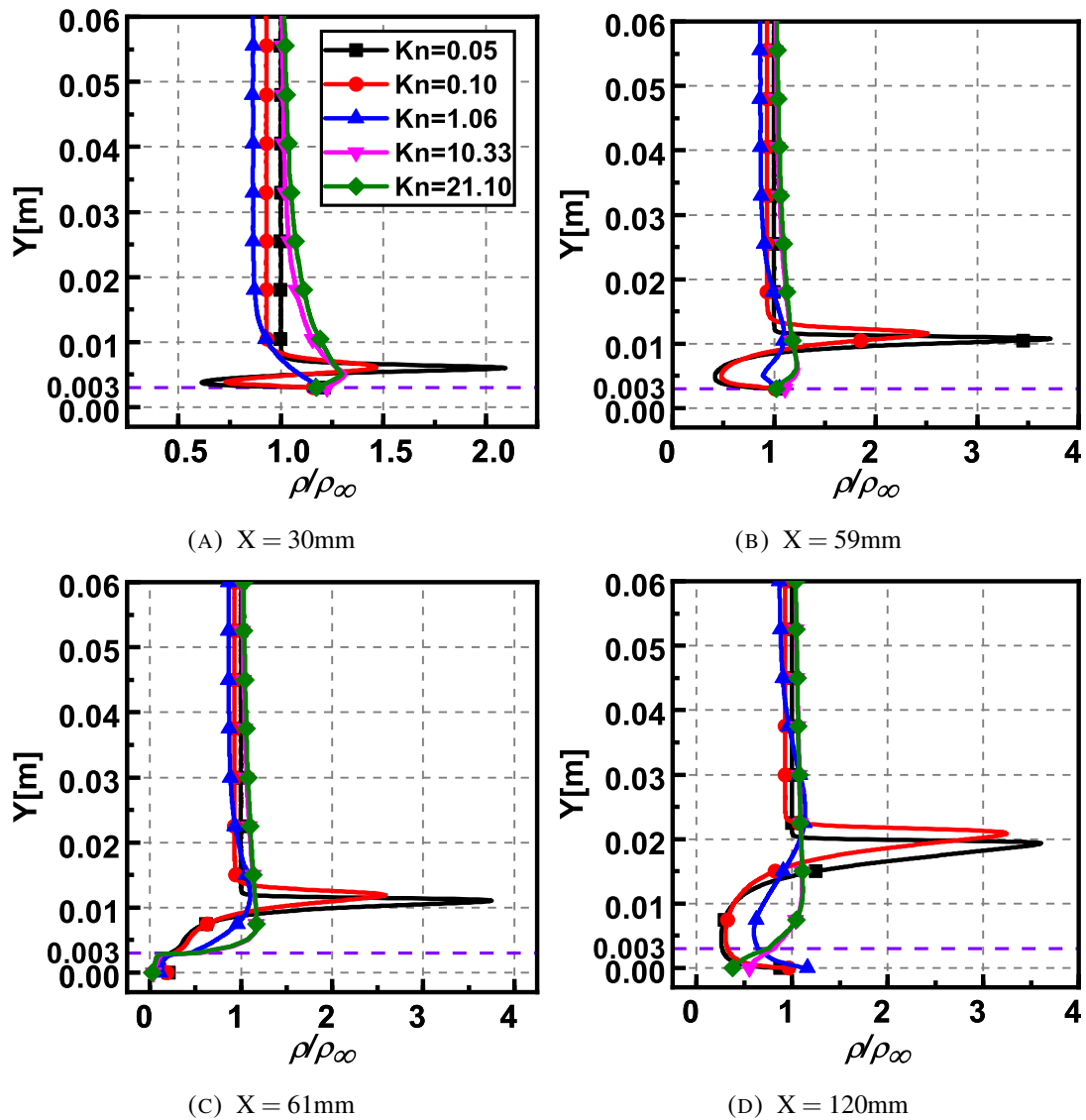


FIGURE 6.33: Variation of the non-dimensional density perpendicular to the surface of BFS for different Kn .

6.29). The peak C_p on the upper surface is observed at X locations of 0.01775, 0.0202, 0.05385, 0.05585 and 0.05595 for Kn 0.05, 0.1, 1.06, 10.33 and 21.10 respectively. Also, near the step, the magnitudes of C_p are below zero, owing to the formation of the recirculation region, which reduces the wall pressure below the free-stream value. The pressure coefficient C_p on the downstream surface behaves relatively similar for all cases, where the C_p increases and diminishes towards the outlet in the slip regime, whereas in the transitional and free-molecular regimes the C_p shows a gradually increasing trend.

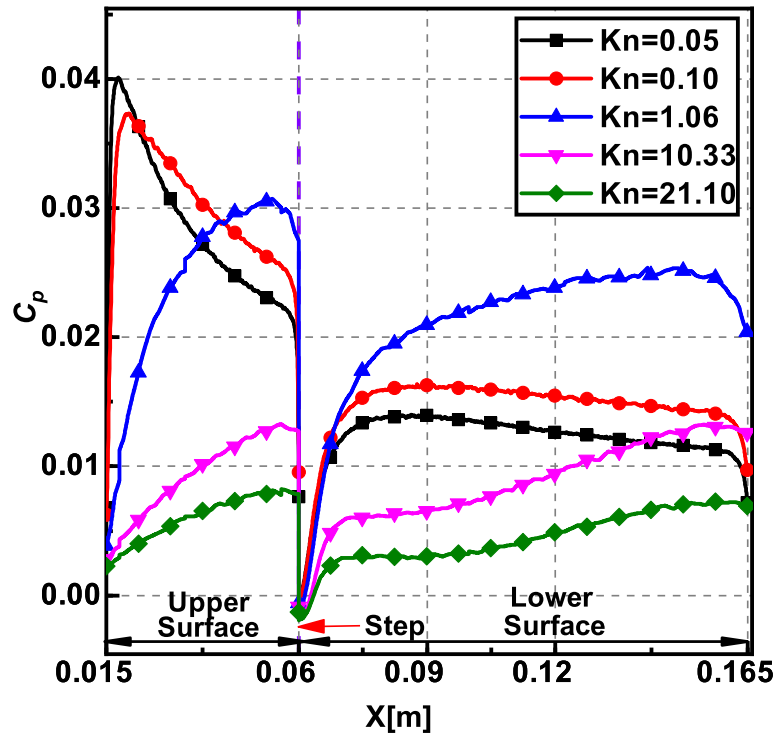


FIGURE 6.34: Variation of pressure coefficient C_p along the upper and lower surfaces of BFS for different Kn

Furthermore, for all the cases, the magnitudes C_p near the outlet are greater than zero signifying a net higher near-wall pressure than the free-stream pressure.

Skin friction coefficient:

The variation of skin friction coefficient (C_f) for different Kn along the upper and the lower surfaces of the BFS is shown in Figure 6.35, which offers larger values of the skin friction coefficient C_f on the upper surface at the inlet owing to the substantial velocity gradients near the wall. Also, the C_f increases with increase in the Knudsen number. Furthermore, there is a significant jump in the C_f values as the flow enters from transitional to the free-molecular regime. For instance, the C_f at inlet almost doubles as Kn increases from 10.33 to 21.10. From the leading edge the C_f gradually reduces

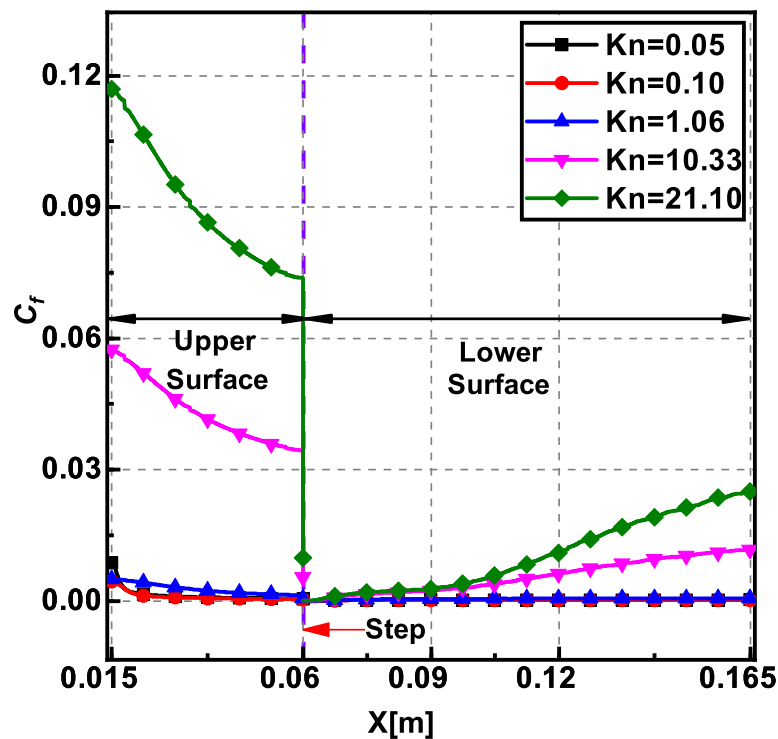


FIGURE 6.35: Variation of skin friction coefficient C_f along the upper and lower surfaces of BFS for different Kn

towards the step. The magnitude of C_f show negative values close to the step owing to flow recirculation. On the lower surface, C_f rises gradually increases towards the outlet for different Kn . The skin friction coefficient C_f is reasonably same in the slip and early transitional regimes, whereas in the free-molecular regime, the C_f gradually increases. As Kn increases, Re diminishes causing the viscous forces to dominate compared to the inertial forces, which leads to an increase in shear stress and C_f . At the step ($X = 0.06\text{m}$), the maximum values of C_f is found to be 4.38×10^{-4} , 3.30×10^{-4} , 5.60×10^{-4} , 5.29×10^{-3} and 9.56×10^{-3} for Kn 0.05, 0.1, 1.06, 10.33 and 21.10 respectively.

Heat transfer coefficient:

The variation of heat transfer coefficient (C_h) for different Kn along the upper and the lower surfaces of the BFS is shown in Figure 6.36. The plots of C_h and C_p are similar in appearance. Also, on the upper surface, the profiles are dissimilar for different Kn . Along the upper surface of the BFS, the heat transfer coefficient C_h show a sudden peak in the slip regime, whereas in the other regimes the C_h shows a gradually increasing trend. The peak C_h on the upper surface is observed at X locations 0.01615, 0.01745, 0.02085, 0.05575 and 0.05595 for Kn 0.05, 0.1, 1.06, 10.33 and 21.10 respectively. Near the base of the step, due to the effects of flow expansion, the temperature reduces, causing a drop in the heat transfer coefficient C_h . Along the lower surface the C_h values are relatively constant in the slip regime, whereas they show a gradual increase in the higher rarefaction regimes. As the rarefaction increases, molecules from the center of the computational domain participate in the collisions due to the increased mean free path, causing a rise in the heat transfer coefficient. Also, higher near-wall temperatures due to viscous heating cause the C_h values to be positive.

6.2 Analysis of rarefied flow over forward facing step

In this section, the analysis of the rarefied flow past an FFS is presented. The geometry, boundary conditions, and free-stream conditions are described initially and are followed by the analysis of the results.

Geometry and computational domain:

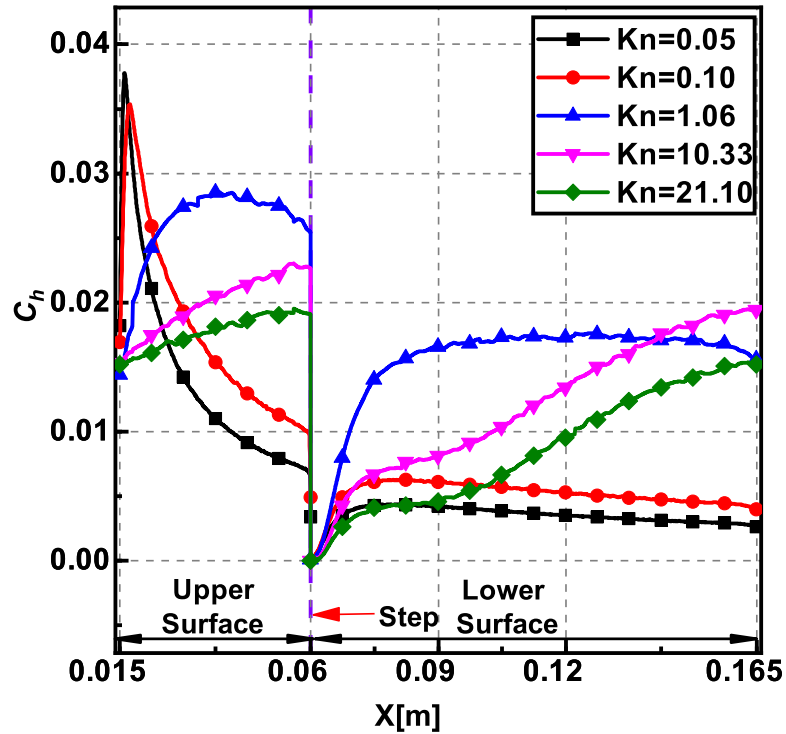


FIGURE 6.36: Variation of heat transfer coefficient C_h along the upper and lower surfaces of BFS for different Kn

TABLE 6.7: Geometric parameters of the 2D-FFS.

Parameter	Value
Upstream length	60mm
Downstream length	105mm
Channel Height (H)	60mm
Step Height (h)	3mm
Step position	$X = 60mm$
Leading-edge of the lower surface	$X = 15mm$

A schematic of the flow over a 2D forward-facing step is shown in Figure 6.37, where the flow traverses from left to right. The cartesian coordinates along X and Y represent the streamwise and transverse directions, respectively. The step height (h) was fixed to 3mm for all the cases. Various geometric parameters of the FFS considered in this study are shown in Table 6.7.

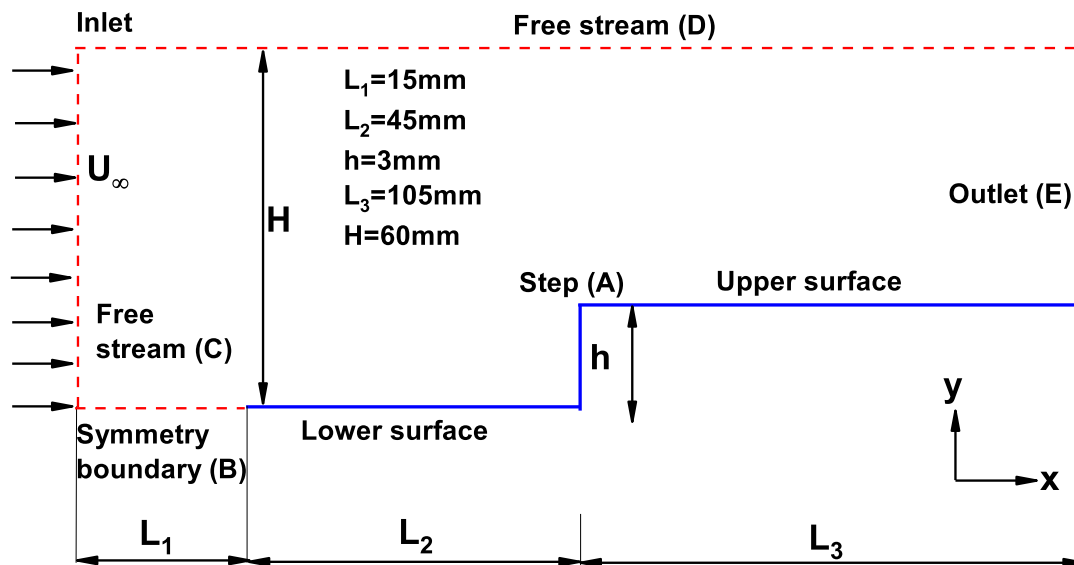


FIGURE 6.37: Schematic of the 2D FFS.

Boundary conditions and mesh:

The boundary conditions applied for different surfaces are given in Table 6.8. Surface-A includes the step, lower and upper surfaces and represents the FFS. It is given diffuse reflection conditions with full thermal accommodation, i.e., the impinging particles are reflected equally in all the directions according to half-range Maxwellian distribution. Surface-B extends for a distance of $5h$ from the inlet on the bottom surface and is given the symmetry condition to have an accurate transverse velocity distribution [157], and is comparable to the specular reflecting boundary. Surface-C is placed $20h$ upstream of the step and Surface-E at a distance of $35h$ downstream of the step. Surfaces-C and D represent the free-stream inlet boundaries where the molecules can freely enter and exit. Surface-E represents the outlet boundary where the flow is primarily supersonic [158, 159]; hence the molecules typically exit.

The flow domain is divided into blocks and meshed with a structured grid comprising of

TABLE 6.8: The implemented boundary conditions for the 2D-FFS.

Surface	A	B	C	D	E
Boundary condition	Wall	Symmetry	Free-stream inlet	Free-stream inlet	Outlet

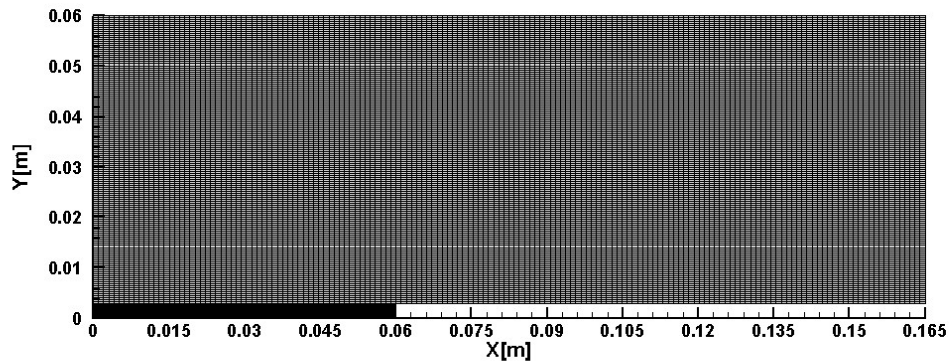


FIGURE 6.38: Meshed domain of the FFS.

quadrilateral cells and as shown in Figure 6.38. The flow conditions adopted are given in Table 6.2.

6.2.1 Influence of Mach number

This section describes the influence of Mach number (Ma) on the flow and surface properties over the FFS. The different Mach numbers studied are $Ma=5$ (Supersonic), 10 (Hypersonic), 25 (High-Hypersonic), and 30 (Reentry speeds). For all instances in this section, $H = 60\text{mm}$, $Kn = 1.06$ and $T_w = 4T_\infty$ is used.

Velocity field:

TABLE 6.9: Recirculation lengths of FFS for different Ma .

Ma	05	10	25	30
$X_L(\text{mm})$	-	-	2.25	2.70
$Y_L(\text{mm})$	-	-	0.83	0.86

Figure 6.39 shows the plots of velocity ratio for different Mach numbers at sections, $X = 30\text{mm}$, $X = 59\text{mm}$, $X = 61\text{mm}$, and $X = 120\text{mm}$. In these plots, the streamwise velocity u is normalized by the velocity of the free stream U_∞ and Y represents the distance above the surface of the FFS. At section $X = 59\text{mm}$ negative values of velocities occur for $Ma = 25, 30$ depicting a recirculation zone. At the section $X = 61\text{mm}$, and $X = 120\text{mm}$, it is observed that the profiles of $Ma = 5$ are different from the other profiles due to the low velocity of the incoming fluid. For $Ma = 25$ and $Ma = 30$ it is observed that there is a close match in the profiles. The lengths of the recirculation region for different Ma are shown in Table 6.9, in which X_L and Y_L respectively denote its axial distance in x and y direction from the corner (i.e., from $X = 60\text{mm}$). It can be observed that the recirculation lengths increase with Ma . The Recirculation lengths were calculated based on $C_f = 0$. Furthermore, the FFS plots are compared against the flat plate results of $Ma = 25$ which shows the variation among the two configurations.

Pressure field:

Figure 6.40 shows the pressure ratio profiles for different Mach numbers at sections, $X = 30\text{mm}$, $X = 59\text{mm}$, $X = 61\text{mm}$, and $X = 120\text{mm}$. In all the cases, it is observed that near the wall, the pressure ratio increases with Ma due to the high velocity of the incoming fluid stream. Away from the wall, the profiles overlap and attain the free-stream value. It is observed that at the top surface of the step ($Y \approx 3\text{mm}$), there is a sudden

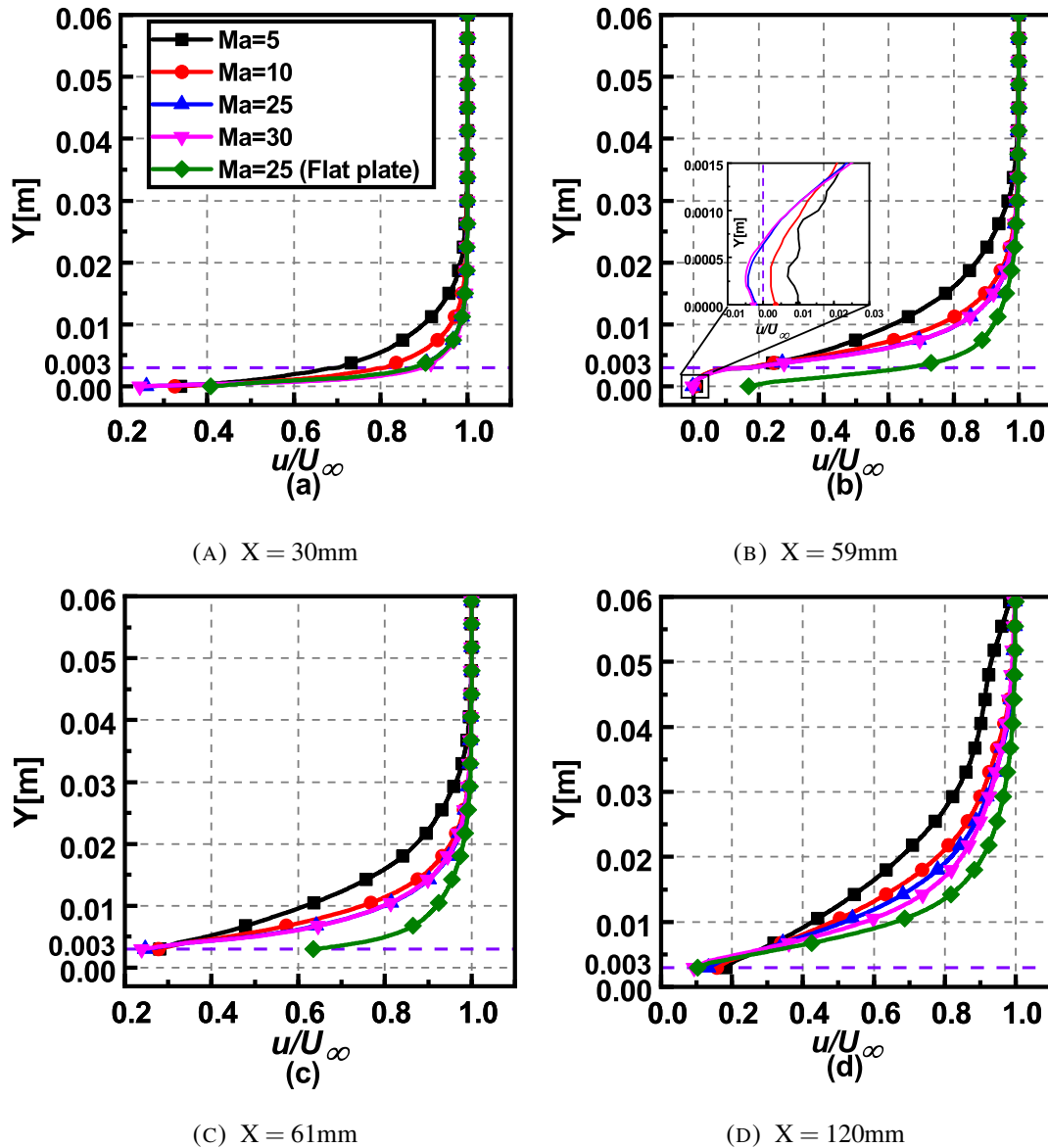


FIGURE 6.39: Variation of the non-dimensional velocity perpendicular to the surface of FFS for different Ma .

surge in the pressure ratio as the step acts as a stagnation zone. Beyond $X \geq 61\text{mm}$, away from the stagnation zone, the pressure ratio soon decreases considerably. However, the near-wall magnitude of pressure ratio is still of the order of 10^1 as a result of high gas temperature. The flat plate profiles in general show lesser magnitudes of pressure compared against the FFS profiles due to the presence of the step.

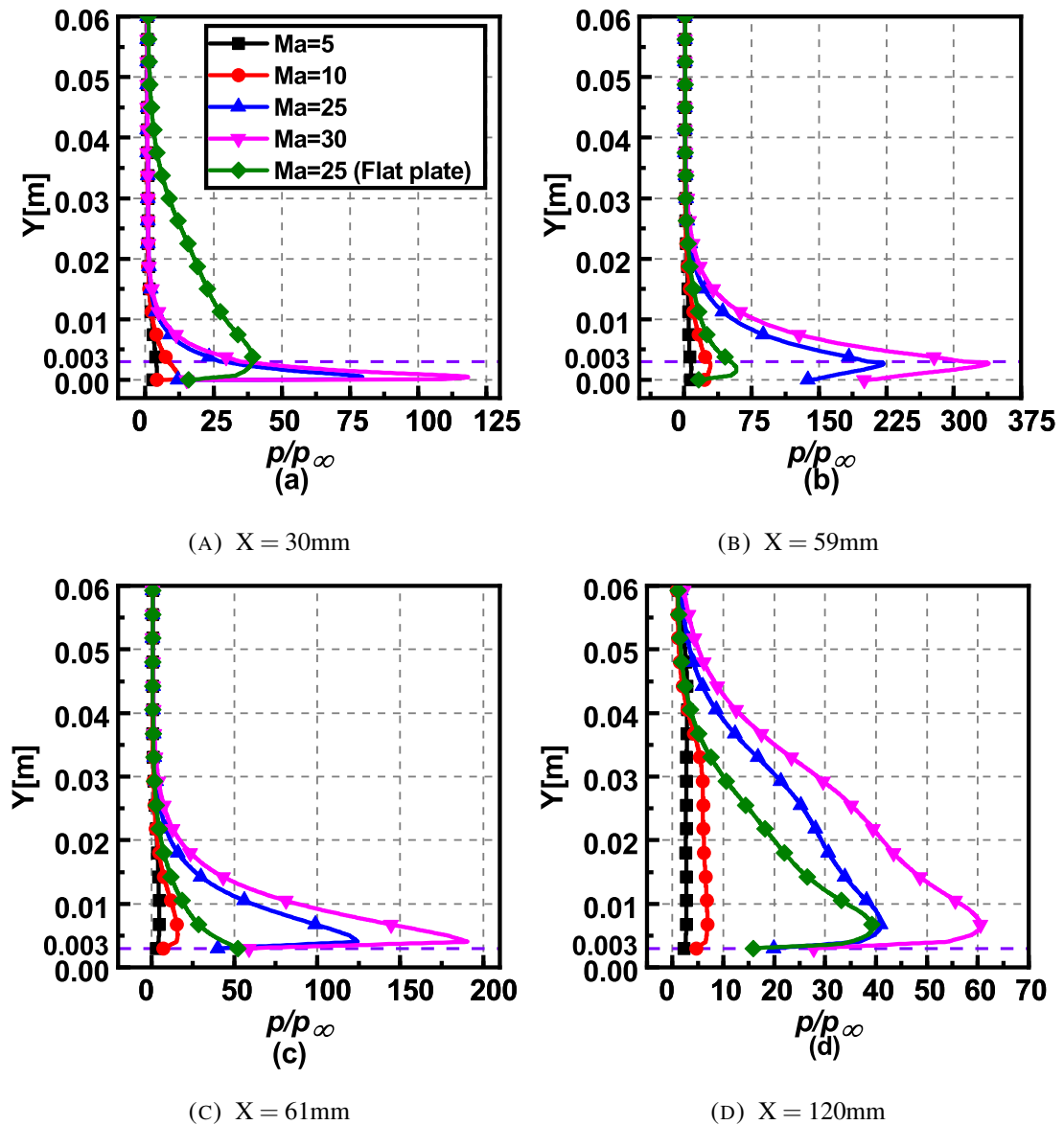


FIGURE 6.40: Variation of the non-dimensional pressure perpendicular to the surface of FFS for different Ma .

Temperature field:

Figure 6.41 shows the temperature ratio profiles for different Mach numbers at sections, $X = 30\text{mm}$, $X = 59\text{mm}$, $X = 61\text{mm}$, and $X = 120\text{mm}$. The temperature profiles follow a similar trend as those of pressure profiles, where the near-wall temperatures are higher than the free stream temperatures. The high incoming velocity of the fluid results in high-velocity gradients and hence high viscous dissipation. Therefore, the wall temperatures

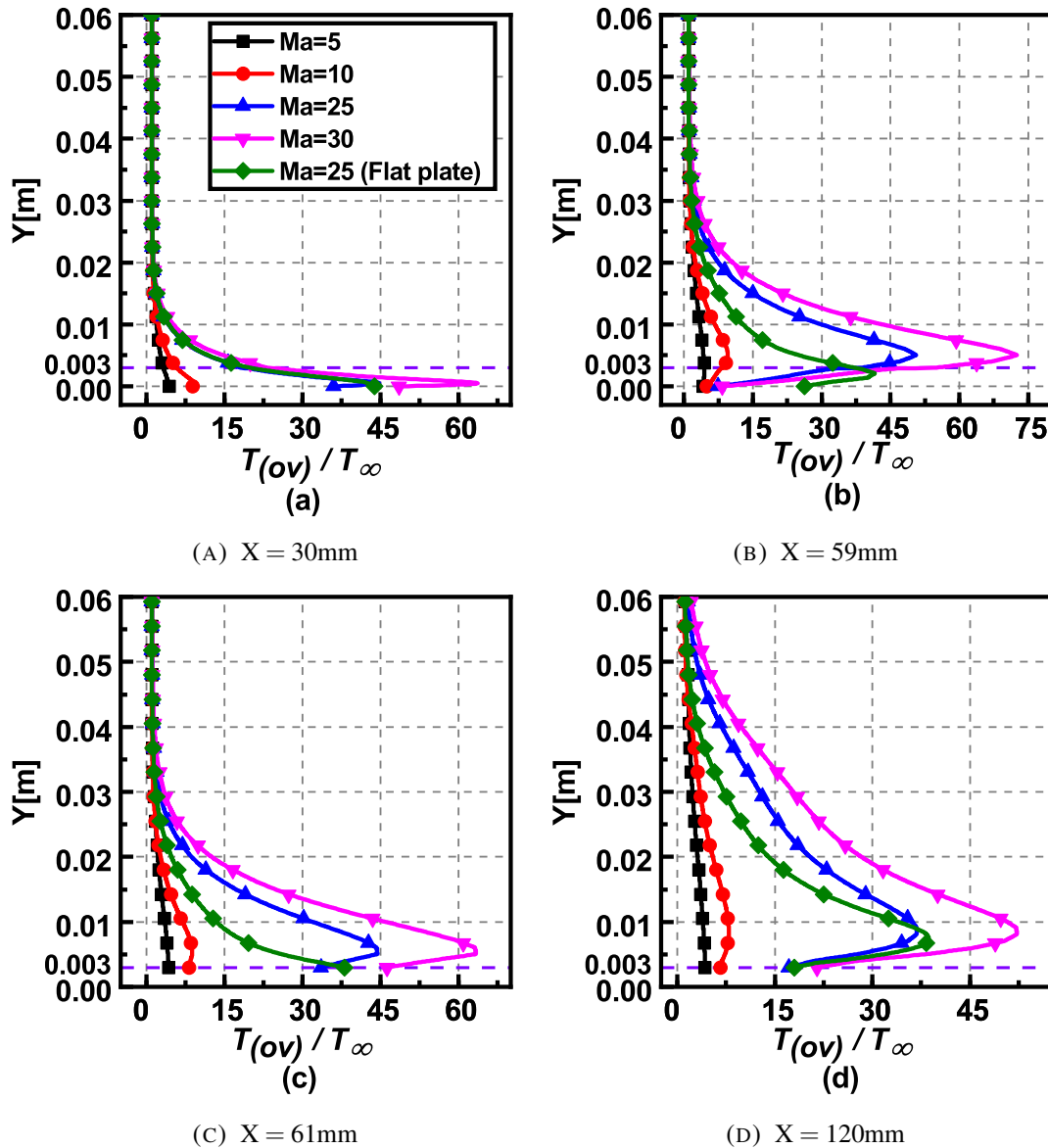


FIGURE 6.41: Variation of the non-dimensional temperature perpendicular to the surface of FFS for different Ma .

are of exceptionally high magnitude compared to the free-stream temperature. Along the flow direction, the near-wall peak temperatures reduce as the velocity gradients decrease due to increased boundary layer thickness. The temperature profiles for the flat plate again show reduced magnitudes compared to the FFS profiles.

Pressure coefficient:

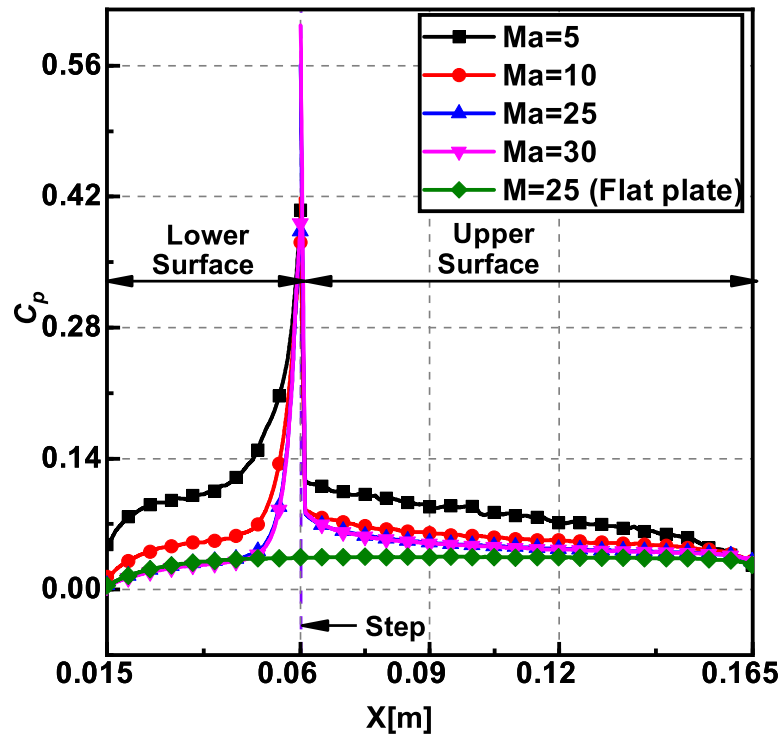


FIGURE 6.42: Variation of pressure coefficient C_p along the lower and upper surfaces of FFS for different Ma

The distribution of pressure coefficient (C_p) along the upper and lower surfaces of the FFS for different Ma is shown in Figure 6.42. The C_p increases along the lower surface and reaches a maximum at the stagnation point at the intersection of the lower surface and frontal face. Along the upper surface the C_p values gradually reduce towards the outlet after the step. The C_p values are lower for higher Ma due to the higher value of dynamic pressure of the incoming fluid stream. The comparison with flat-plate is also shown for $Ma = 25$.

Skin friction coefficient:

The distribution of skin friction coefficient (C_f) along the upper and lower surfaces of the FFS for different Ma is shown in Figure 6.43. For all Ma , the C_f values are

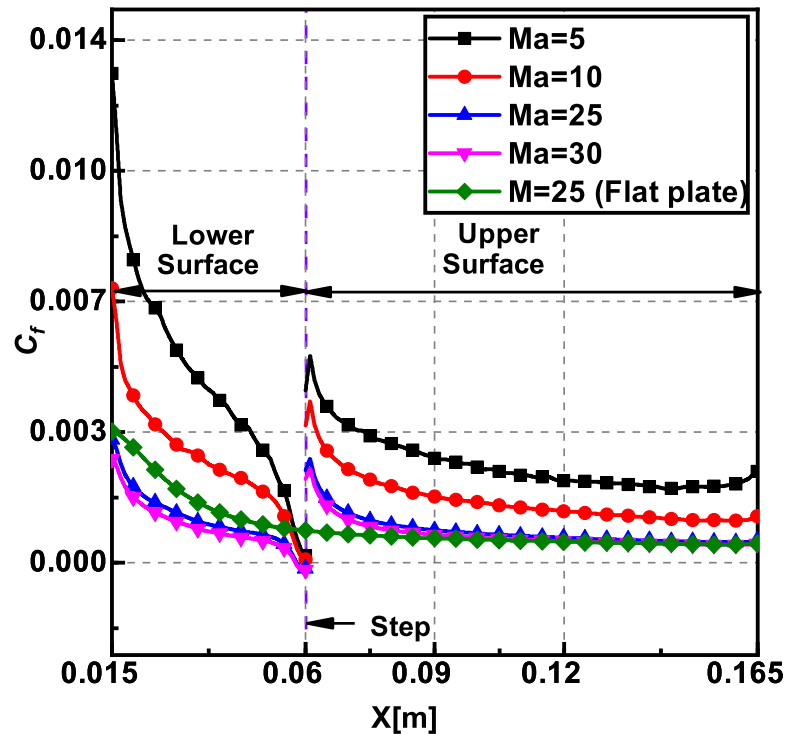


FIGURE 6.43: Variation of skin friction coefficient C_f along the lower and upper surfaces of FFS for different Ma

higher near the leading edge due to high-velocity gradients. Along the lower surface the C_f decreases from the leading edge up to the step. For $Ma=25,30$ the C_f values are negative, indicating flow separation. Along the upper surface the C_f is maximum at the step and gradually decreases towards the outlet. The C_f values are found to decrease with increasing Ma along lower and upper, analogous to the continuum flows. The flat-plate shows a continuous reducing trend.

Heat transfer coefficient:

The distribution of heat transfer coefficient (C_h) along the upper and lower surfaces of the FFS for different Ma is shown in Figure 6.44. Along the lower surface the C_h shows an increase, except for the lowest of $Ma=5$, where the C_h shows a gradual decline. At

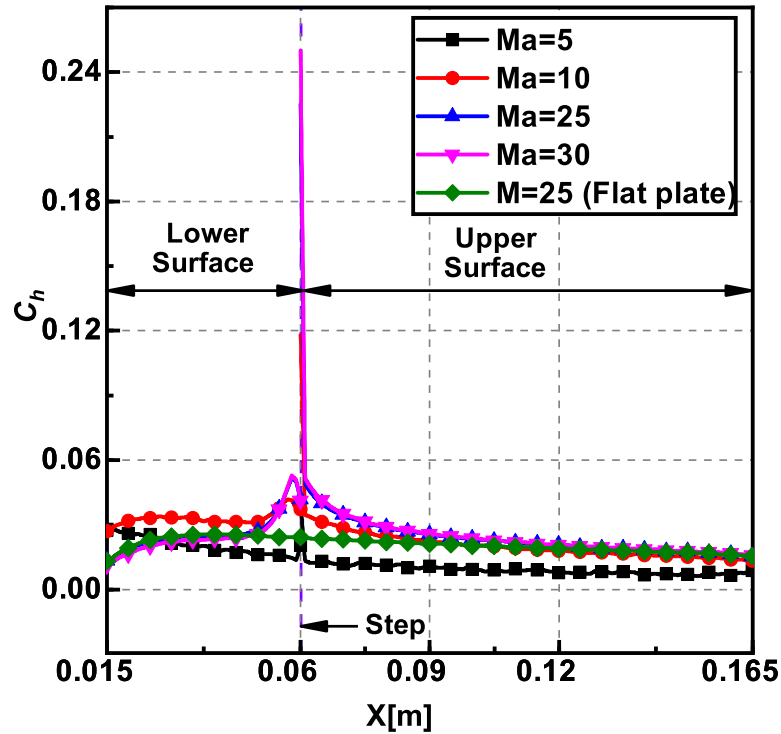


FIGURE 6.44: Variation of heat transfer coefficient C_h along the lower and upper surfaces of FFS for different Ma

the edge of the step, the peak C_h magnitudes are observed due to higher temperature magnitudes. Along the upper surface, the C_h is high in the beginning and then shows a gradual decline towards the outlet. Similar to C_f , the C_h for flat-plate shows a reducing trend.

6.2.2 Influence of Wall temperature

This section describes the influence of wall temperature (T_w) on the flow and surface properties over the FFS. The wall temperature (T_w) was set to four different values, i.e., T_∞ , $2T_\infty$, $4T_\infty$ and $8T_\infty$ where, $T_\infty = 204$ K. For all instances in this section, $H = 60$ mm, $Kn = 1.06$ and $Ma = 25$ are used.

TABLE 6.10: Recirculation lengths of FFS for different T_w .

Wall temperature	$T_w=T_\infty$	$T_w=2T_\infty$	$T_w=4T_\infty$	$T_w=8T_\infty$
$X_L(\text{mm})$	3.15	2.70	2.25	1.80
$Y_L(\text{mm})$	0.90	0.90	0.83	0.76

Velocity field:

Figure 6.45 shows the plots of velocity ratio for different wall temperatures at sections, $X = 30\text{mm}$, $X = 59\text{mm}$, $X = 61\text{mm}$, and $X = 120\text{mm}$. From the profiles, it can be observed that the boundary layer increases with an increase in wall temperature. The high wall temperature causes the particles to reflect with higher energies, increasing the distance for which the momentum of the flow diffuses. Thus, the decelerating effect of the wall (due to diffuse reflection) is experienced by the flow for a more considerable distance. The profiles show a smaller difference at sections $X = 59\text{mm}$ and $X = 61\text{mm}$, but further downstream of the step, at $X = 120\text{mm}$, substantial variation is observed among the different profiles. The recirculation lengths for different wall temperatures are shown in Table 6.10. The recirculation lengths decrease with increasing wall temperature.

Pressure field:

Figure 6.46 shows the plots of pressure ratio for different wall temperatures at sections, $X = 30\text{mm}$, $X = 59\text{mm}$, $X = 61\text{mm}$, and $X = 120\text{mm}$. The pressure at a point is proportional to the product of density and square of thermal velocity. The simulations show that the density of the flow is not a strong function of the wall temperature. Therefore, an increase in the wall temperature increases the thermal velocity of molecules leading to an overall increase in pressure. The difference in the profiles at $X = 120\text{mm}$ is significantly

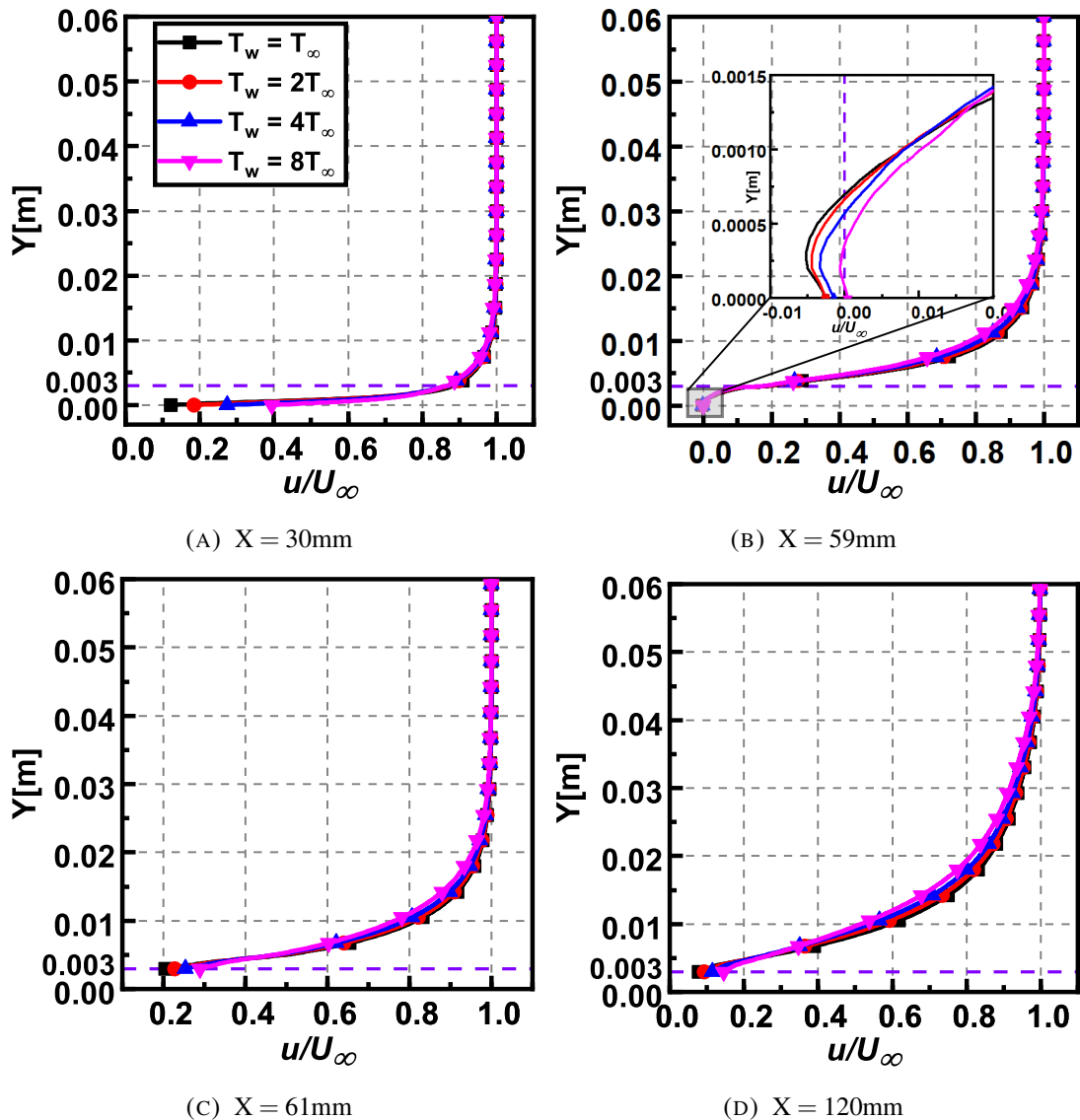


FIGURE 6.45: Variation of the non-dimensional velocity perpendicular to the surface of FFS for different T_w .

more than that at $X = 59\text{mm}$ and $X = 61\text{mm}$. This is due to a similar trend observed in the temperature variation in the flow domain, as seen in Figure 6.47c.

Temperature field:

Figure 6.47 shows the plots of temperature ratio for different wall temperatures at sections, $X = 30\text{mm}$, $X = 59\text{mm}$, $X = 61\text{mm}$, and $X = 120\text{mm}$. The temperature profiles follow

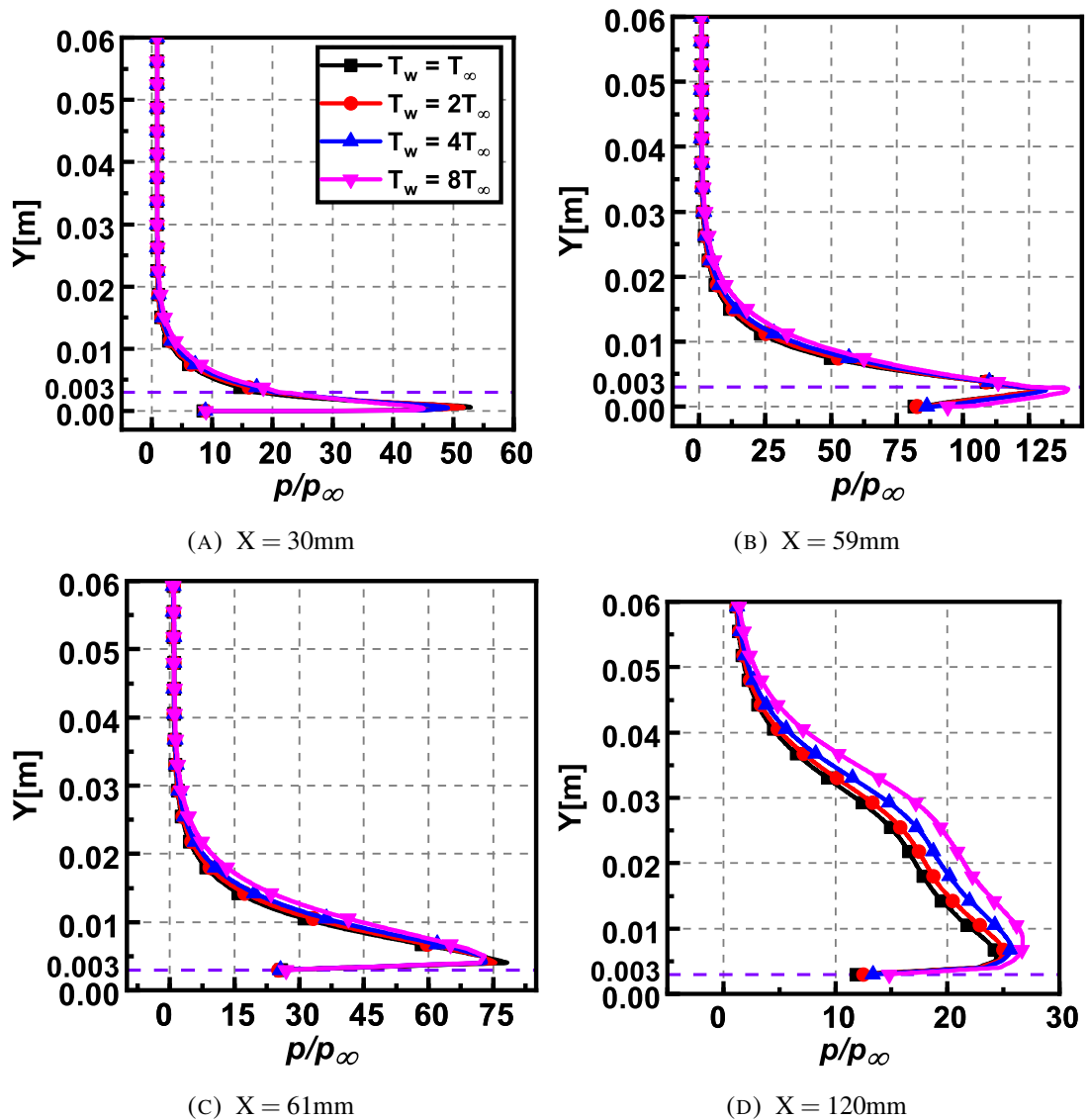


FIGURE 6.46: Variation of the non-dimensional pressure perpendicular to the surface of FFS for different T_w .

a similar trend as the pressure profiles. Increase in the wall temperature results in an increase in the temperature of the fluid. Also, as the flow progresses from inlet to outlet, higher wall temperature results in increased heat convection from the wall. As a result, an increase in the wall temperatures results in a more substantial difference in the profiles downstream.

Pressure coefficient:

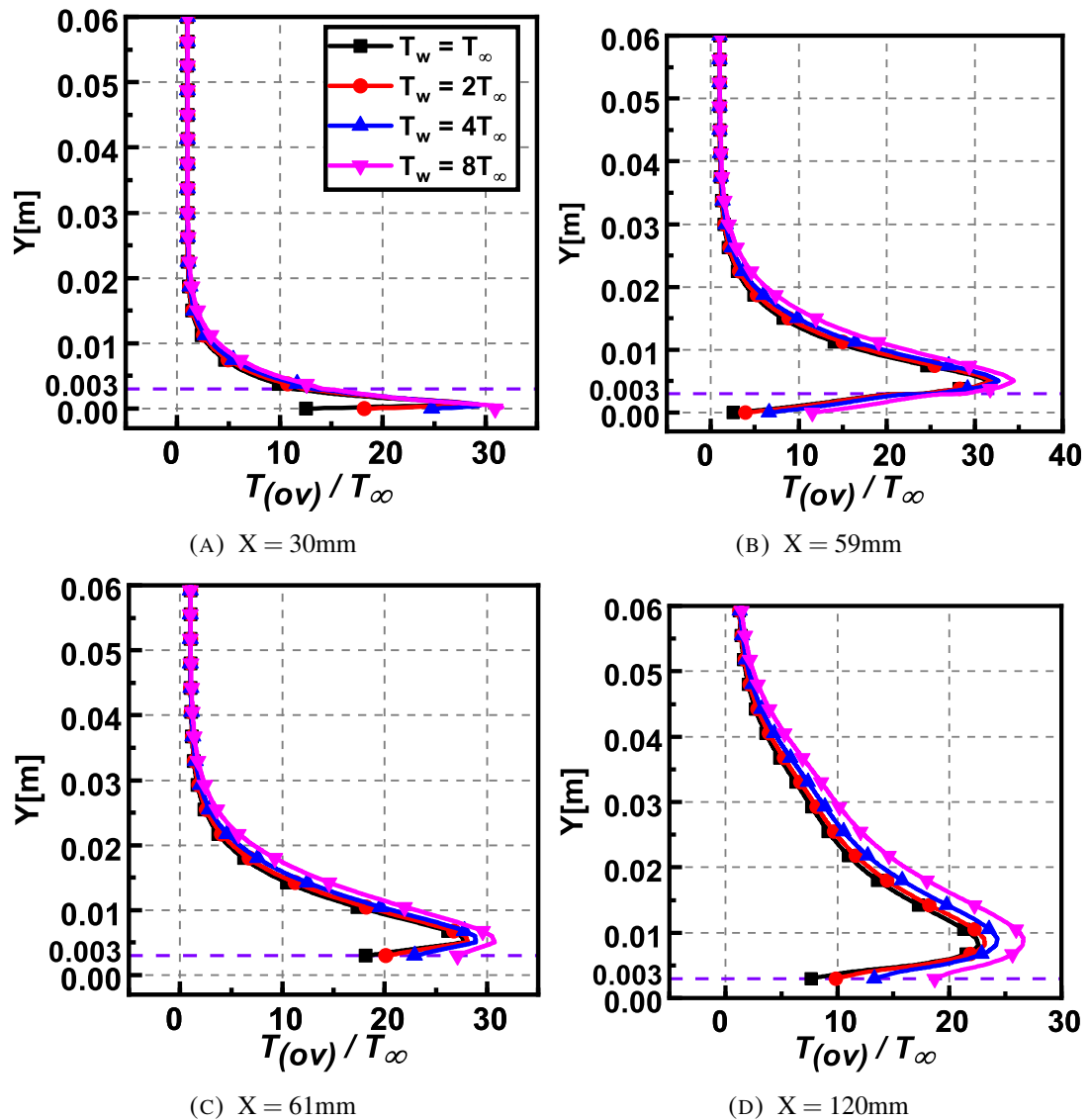


FIGURE 6.47: Variation of the non-dimensional temperature perpendicular to the surface of FFS for different T_w .

The distribution of pressure coefficient (C_p) along the upper and lower surfaces of the FFS for different T_w is shown in Figure 6.48. On the lower and upper surfaces, the variation in C_p is not significant as the pressure change is relatively less and the C_p values slightly increase with increasing wall temperature.

Skin friction coefficient:

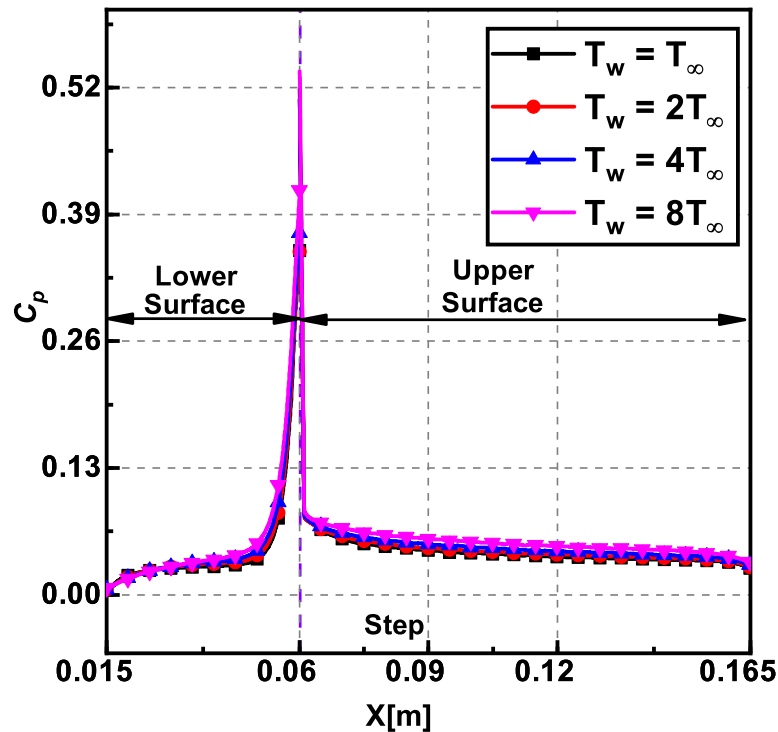


FIGURE 6.48: Variation of pressure coefficient C_p along the lower and upper surface of FFS for different T_w

The distribution of skin friction coefficient (C_f) along the upper and lower surfaces of the FFS for different T_w is shown in Figure 6.49. On the lower surface, the C_f values increase with wall temperature, whereas on the upper surface, the variation in C_f is slightly less. Also, the C_f magnitudes show an increase with an increase in wall temperature, which can be attributed to the viscous heating effects.

Heat transfer coefficient:

The distribution of heat transfer coefficient (C_h) along the upper and lower surfaces of the FFS for different T_w is shown in Figure 6.50. The profiles of C_h on both the lower and upper surfaces overlap and follow a similar trend. Thus, the change in wall temperature has no significant influence in the C_h magnitudes as the incoming fluid stream is of

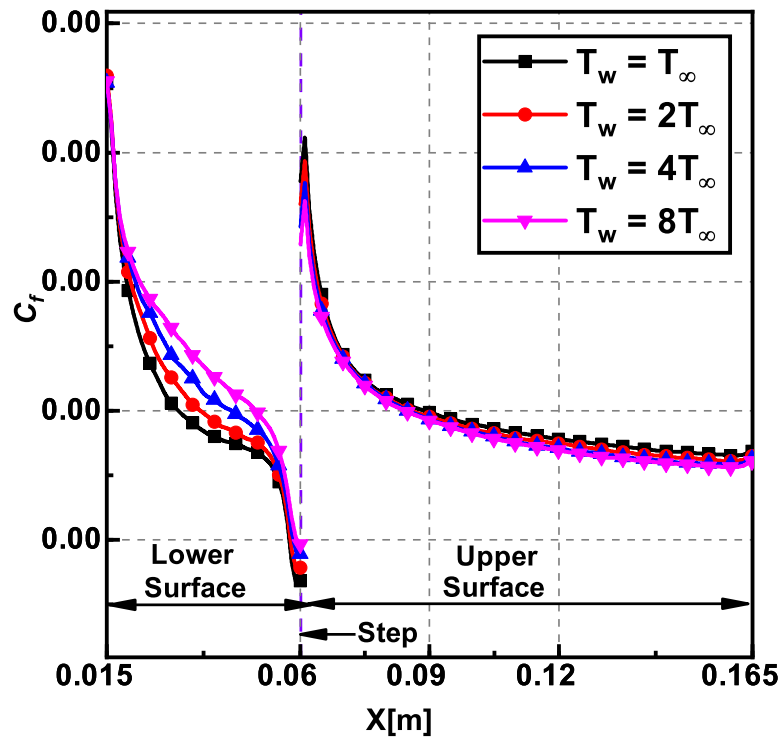


FIGURE 6.49: Variation of skin friction coefficient C_f along the lower and upper surfaces of FFS for different T_w

the same energy. Thus, the temperature changes are not substantial enough to cause a significant change in the heat transfer coefficient.

6.2.3 Influence of Knudsen number

This section describes the influence of Knudsen number (Kn) on the flow and surface properties over the FFS. The different Knudsen numbers studied are given in Table 6.2. For all the instances, the free-stream Mach number considered was 25, with a step height of ($h = 3$ mm), $H = 60$ mm, and $T_w = 4T_\infty$ is used. Initially the contours are presented, followed by the line plots.

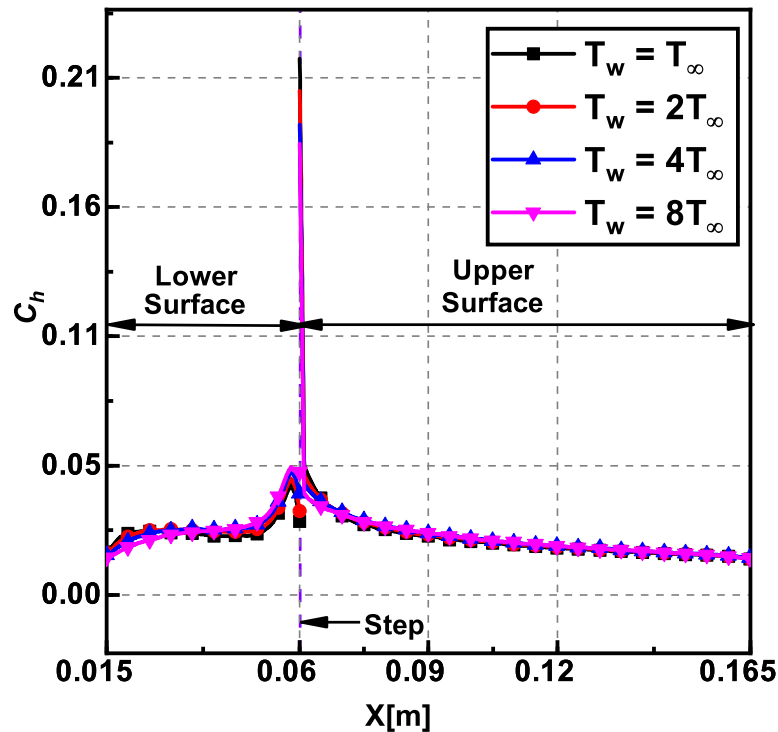


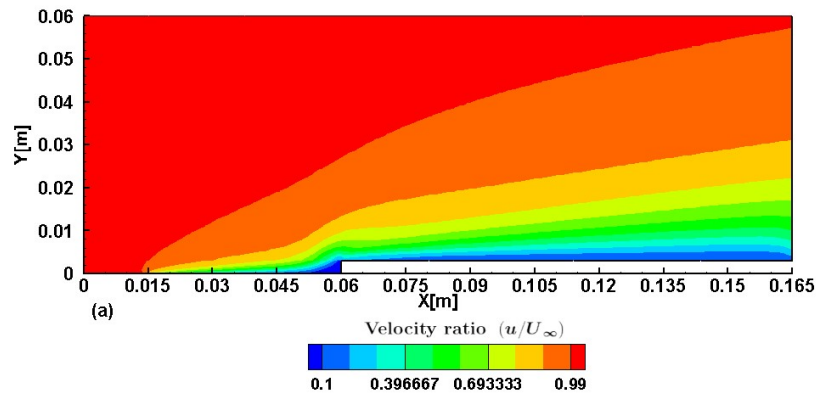
FIGURE 6.50: Variation of heat transfer coefficient C_h along the lower and upper surfaces of FFS for different T_w

For the case of $Kn = 1.06$, the contours of various flow properties are shown in Figure 6.51. The normalized velocity contour shows the hydrodynamic boundary layer, where the near-wall velocity is less and increases away from it to attain a free-stream magnitude. The presence of the step marginally influences the boundary layer development. The pressure changes in the upstream and downstream are more pronounced, with areas of higher pressure near the walls, which rapidly decreases away from the wall. Near the step, the compressibility effect causes high stagnation pressure leading to a substantial pressure surge. The wall temperature ratios are of the order of 10, which is much greater than the imposed wall temperature. This high temperature is due to the viscous dissipation effects, primarily seen in the near-wall region and the shear layer at the step height. The density contour follows a behavior similar to that of the pressure contour. A high-density ratio is observed in the shock wave, which originates from the lower

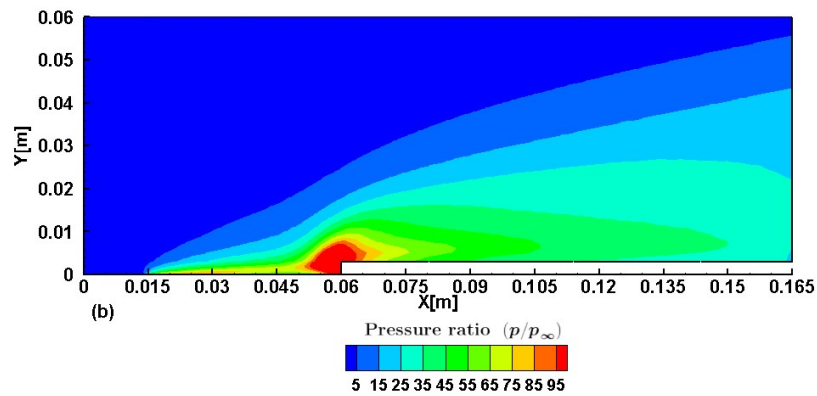
surface's leading-edge and expands towards the top surface.

Velocity field:

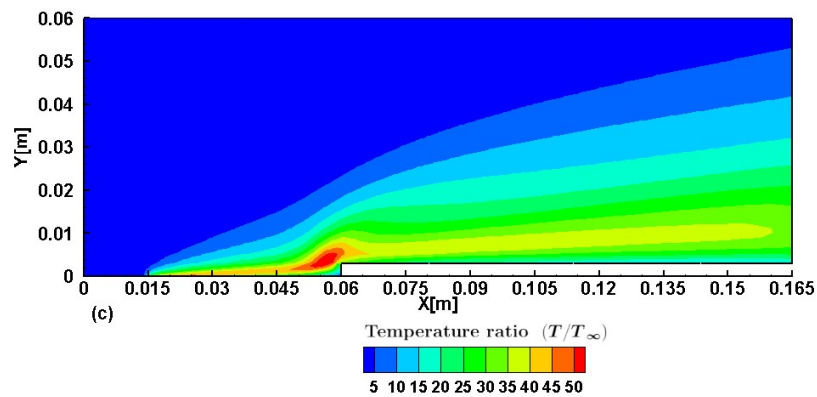
Figure 6.52 shows the streamwise velocity ratio (u/U_∞) distribution in the perpendicular direction for different Kn at various sections viz, $X = 30\text{mm}$, $X = 59\text{mm}$, $X = 61\text{mm}$, and $X = 120\text{mm}$ of the FFS. At the section $X = 30\text{mm}$, just before the step, the flow is undisturbed by the presence of the step, with similar behavior in the slip and transitional regimes. At the section $X = 59\text{mm}$, the velocity profiles for ($Kn = 0.05, 0.10, 1.06$) demonstrate adverse velocities just before the step, characterizing recirculation; a similar behavior was found in Camussi *et al.*'s [160] continuum regime study. At $X = 61\text{mm}$, $X = 120\text{mm}$, which are just after the step, the near-wall flow shows considerable slip, which increases with Kn and aligns with the findings by Ejtehadi *et al.* [161]. At all the sections, near-wall velocity is non-zero, which is in contrast to the zero velocity at the wall encountered in the continuum regime. With an increase in Kn , the boundary layer thickness increases, and the profiles tend to deviate from those in slip and transitional regimes. As the rarefaction increases, the collisions among molecules reduce, and the mean free path increases. Thus, the presence of the wall is felt to a larger distance away from it, hence decelerating the flow. For comparison, at the section $X = 59\text{mm}$, the velocity ratios at $Y = 0.03$ are 1.00, 0.99, 0.99, 0.85 and 0.77 for Kn 0.05, 0.1, 1.06, 10.33 and 21.33 respectively. Moreover, at this section it is worth noting that an increase in Kn from 0.05 to 21.1 results in the reduction of the velocity ratio by 23%. Further downstream at $X = 120\text{mm}$, the decrement is found to be 20%, suggesting flow expansion.



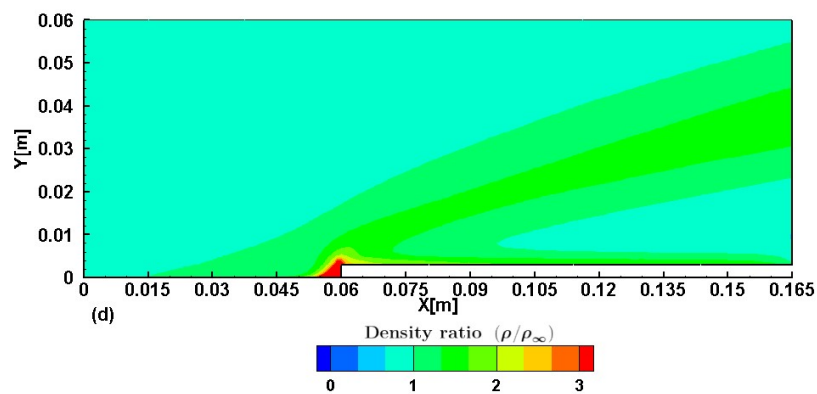
(A) Non-dimensional velocity.



(B) Non-dimensional pressure.



(C) Non-dimensional temperature.



(D) Non-dimensional density.

FIGURE 6.51: Contours of non-dimensional flow-field properties for $H = 60\text{mm}$, $Kn = 25$ and $Kn = 1.06$.

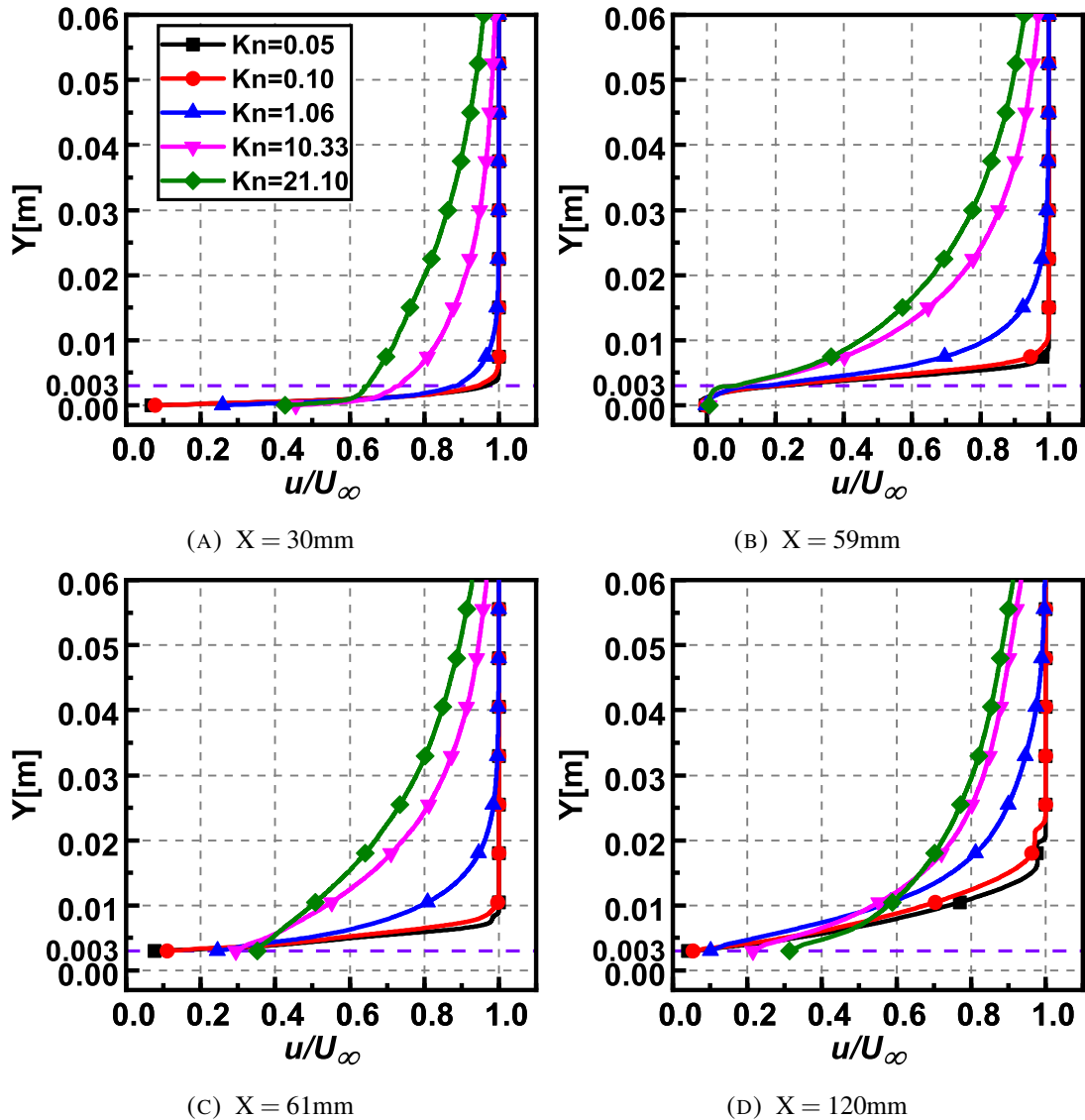


FIGURE 6.52: Variation of the non-dimensional velocity perpendicular to the surface of FFS for different Kn .

Figure 6.53 shows the streamwise velocity ratio (u/U_∞) distribution along the length of FFS for different Kn at various sections viz, $Y/H = 0$ (lower surface), $Y/H = 0.025$ (center of step), and $Y/H = 0.5$ (center of inlet). At the section $Y/H = 0$, the velocity is relatively linear up to the FFS's leading-edge owing to the symmetry boundary condition imposed. After that, it decreases non-linearly along the flow direction. The decelerating is quick for $Kn = 0.05$, whereas it is gradual in other cases. Furthermore, at the step,

the velocity ratio attains a negative value (except $Kn= 10.33, 21.1$), characterizing the recirculation. In the section $Y/H = 0.025$, the profiles again show a diminishing trend for all the cases. Furthermore, the velocity ratio at any specific position along the FFS length decreases with increasing Kn . Along the section $Y/H = 0.5$, at the center of the inlet, the flow is unaffected in the slip regime compared to other regimes. Upstream disturbance due to the presence of the step is found to increase with Kn where the velocity ratio decreases up to the step and remains reasonably constant downstream of the step. In contrast, for $Kn= 1.06$ (in the middle of the transitional regime), the velocity ratio decreases in the flow direction downstream of the step.

Figure 6.54 shows the velocity streamlines for different Kn . The Reynolds number (Re) are 783.11, 431.10, 46.61, 4.29, 2.08 for $Kn= 0.05, 0.1, 1.06, 10.33, 21.1$ respectively. The recirculation region occurs in the slip and early transitional regimes. In contrast, it is absent in the free-molecular regime, owing to the low flow velocity compared to the Knudsen number [162]. Table 6.11 shows the recirculation lengths for different cases, in which X_L and Y_L denote the axial extents of the recirculation region in x and y -directions respectively measured from the step corner (i.e., from $X = 60\text{mm}$). For estimating the recirculation lengths skin friction coefficient ($C_f = 0$) condition is adopted. Both X_L and Y_L decrease with Kn , which can be attributed to the decrease in Re and increase in Kn . With a decrease in Re , the viscous forces predominate inertial forces, consequently reducing the separation length. Similarly, as Kn increases, the velocity slip increases, reducing the chances of the flow adjacent to the wall to separate. Furthermore, the Knudsen layer formation also contributes to the reduction in recirculation lengths.

Pressure field:

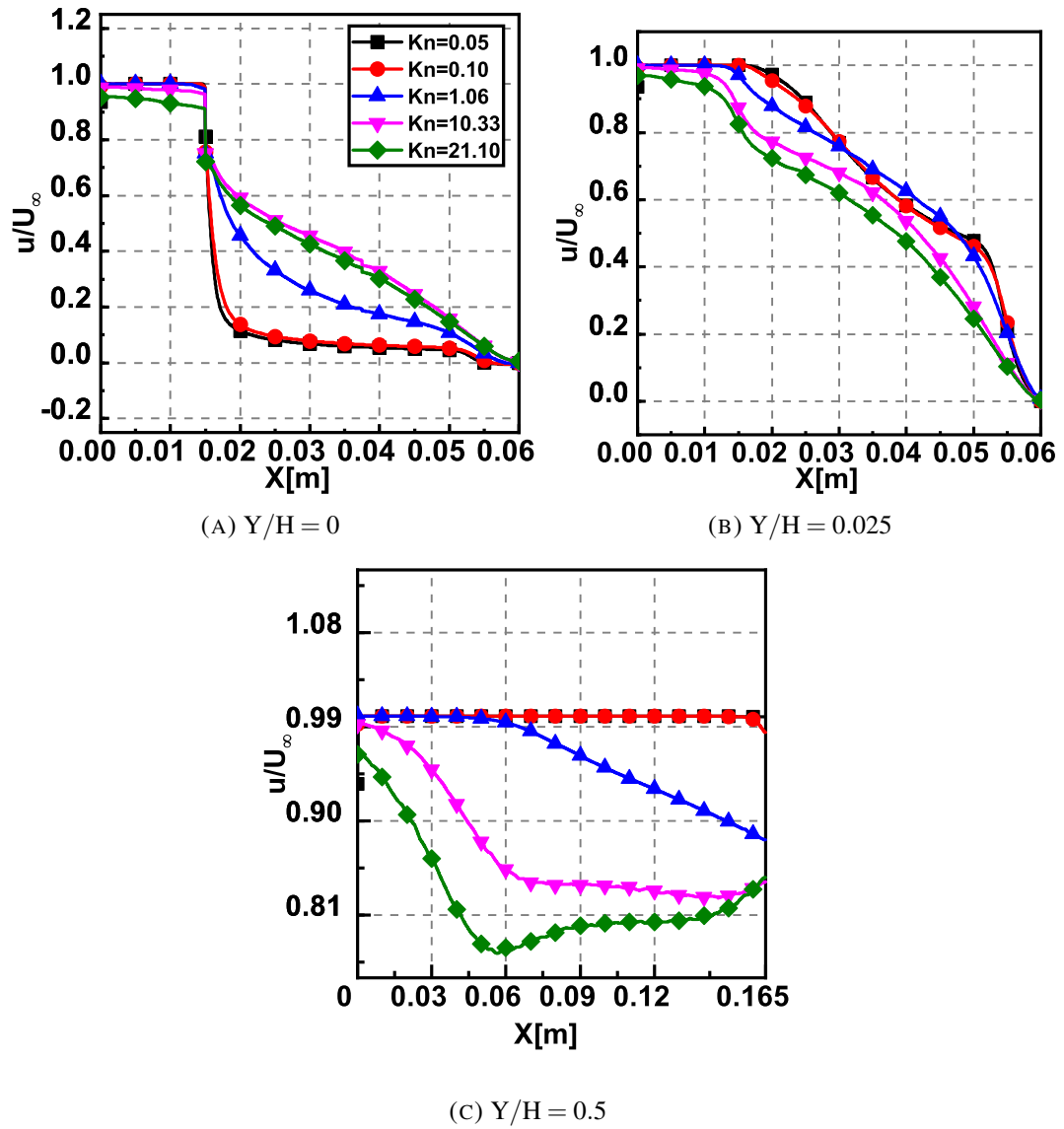


FIGURE 6.53: Variation of the non-dimensional velocity along the length of FFS for different Kn

TABLE 6.11: Recirculation lengths of FFS for different Kn .

Kn	0.05	0.1	1.06	10.33	21.10
X_L (mm)	4.80	3.85	2.10	-	-
Y_L (mm)	1.73	1.46	0.86	-	-

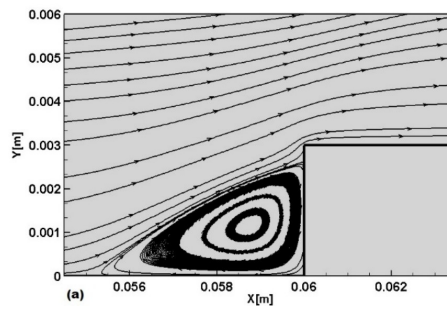
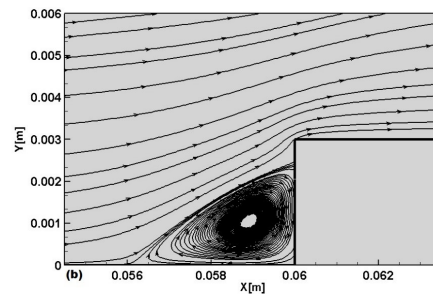
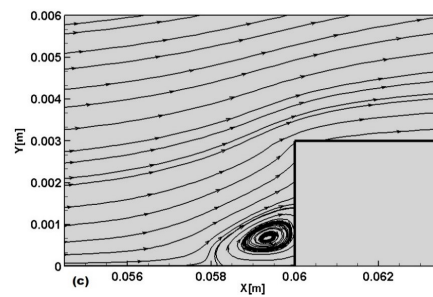
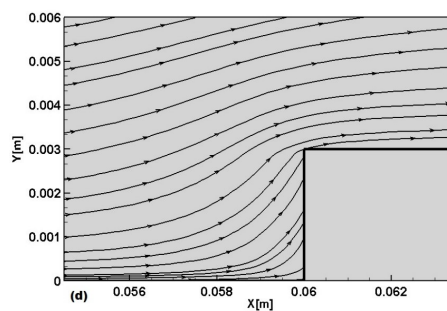
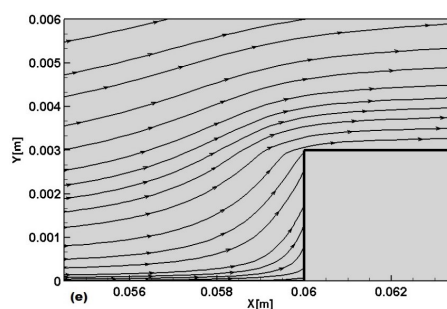
(A) $Kn=0.05$ (B) $Kn=0.1$ (C) $Kn=1.06$ (D) $Kn=10.33$ (E) $Kn=21.10$

FIGURE 6.54: Streamlines near the step of FFS for (a) $Kn=0.05$, (b) $Kn=0.1$, (c) $Kn=1.06$, (d) $Kn=10.33$, (e) $Kn=21.10$.

Figure 6.55 shows the pressure ratio (p/p_∞) distribution in the transverse direction to the flow for different Kn at various sections viz, $X = 30\text{mm}$, $X = 59\text{mm}$, $X = 61\text{mm}$, and $X = 120\text{mm}$ of the FFS. In these plots, the pressure ratio refers to the pressure p normalized by the free-stream pressure p_∞ . The pressure ratios near the step are an order of magnitude higher than the free-stream and increase with rarefaction. At section $X = 30\text{mm}$, the pressure ratio at a given X location reaches a free-stream magnitude more quickly in the slip regime when compared with the other regimes. In section $X = 59\text{mm}$, near the step, the near-wall pressure is different for various Kn . Also, peak pressure ratio occurs close to the face of the step due to compression of the incoming fluid stream, whereas (for $Y < 0.003$) and (for $Y > 0.003$) the pressure ratio decreases. At section $X = 61\text{mm}$, and $X = 120\text{mm}$, the pressure ratio profiles are similar to those in section $X = 59\text{mm}$, but of lower magnitude. For comparison at section $X = 59\text{mm}$, the maximum pressure ratios are 68.09, 85.67, 221.22, 339.72 and 340.88 for Kn 0.05, 0.1, 1.06, 10.33 and 21.33 respectively.

Figure 6.56 shows the pressure ratio (p/p_∞) distribution along the length of FFS for different Kn at various sections viz, $Y/H = 0$ (Bottom surface), $Y/H = 0.025$ (Center of step), and $Y/H = 0.5$ (Center of inlet). In all the profiles, the pressure ratio increases with rarefaction, also the maximum pressure ratio variation occurs in the center of the step. At the sections $Y/H = 0$ and $Y/H = 0.025$, the pressure ratio gradually increases along the length of the FFS. At the step ($X = 60\text{mm}$), the maximum pressure ratio occurs due to stagnation. In the section $Y/H = 0.5$, the pressure ratio is constant along the FFS length in the slip regime, whereas there is considerable pressure variation in other regimes, showing a non-linear trend. This non-linearity is due to the presence of the

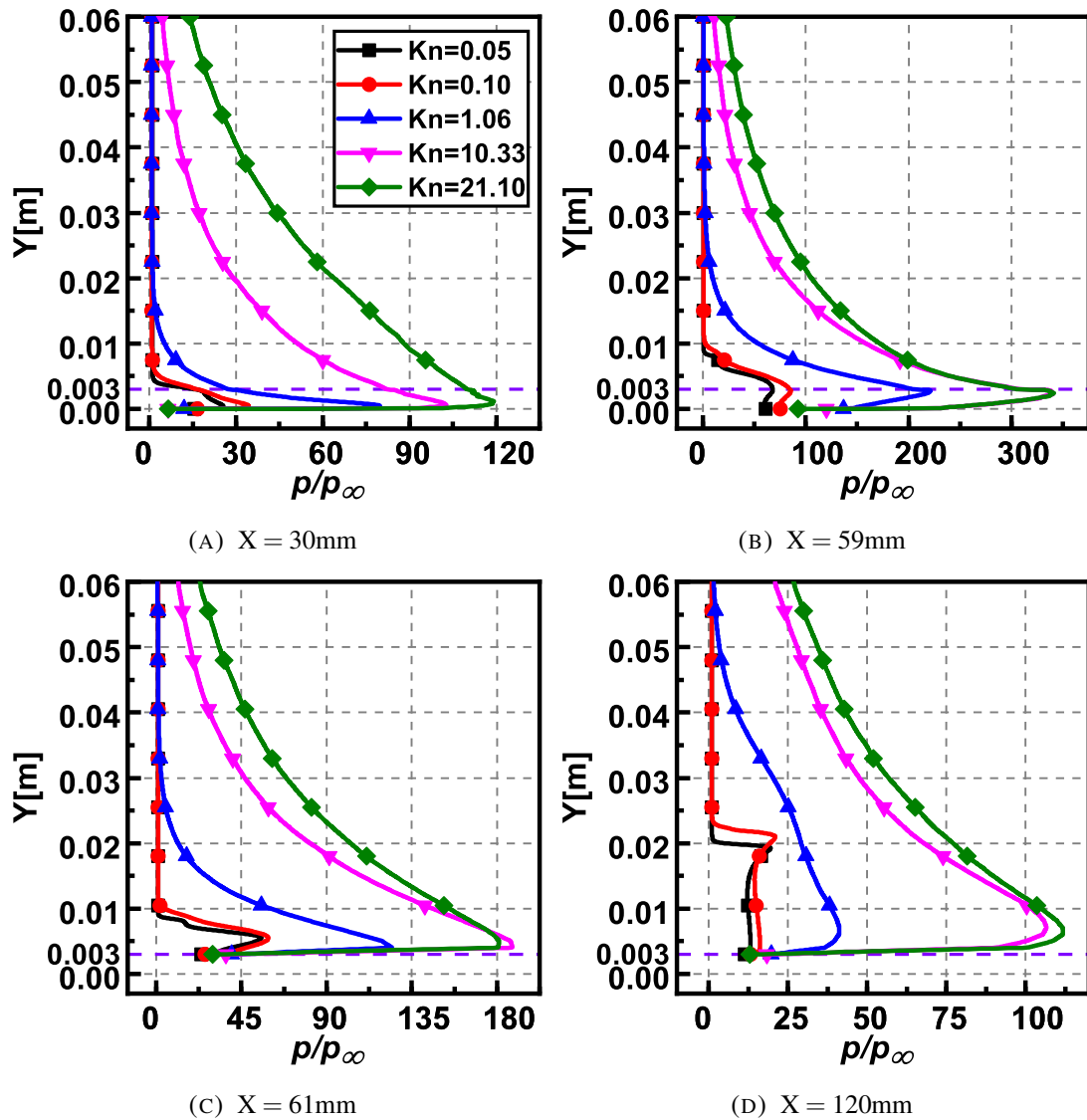


FIGURE 6.55: Variation of the non-dimensional pressure perpendicular to the surface of FFS for different Kn .

step. For the purpose of comparison at the section $Y/H = 0.025$, the maximum pressure ratios are 66.65, 86.87, 265.97, 646.97 and 709.89 for Kn 0.05, 0.1, 1.06, 10.33 and 21.33 respectively.

Temperature field:

Figure 6.57 shows the temperature ratio (T/T_∞) distribution in the transverse direction

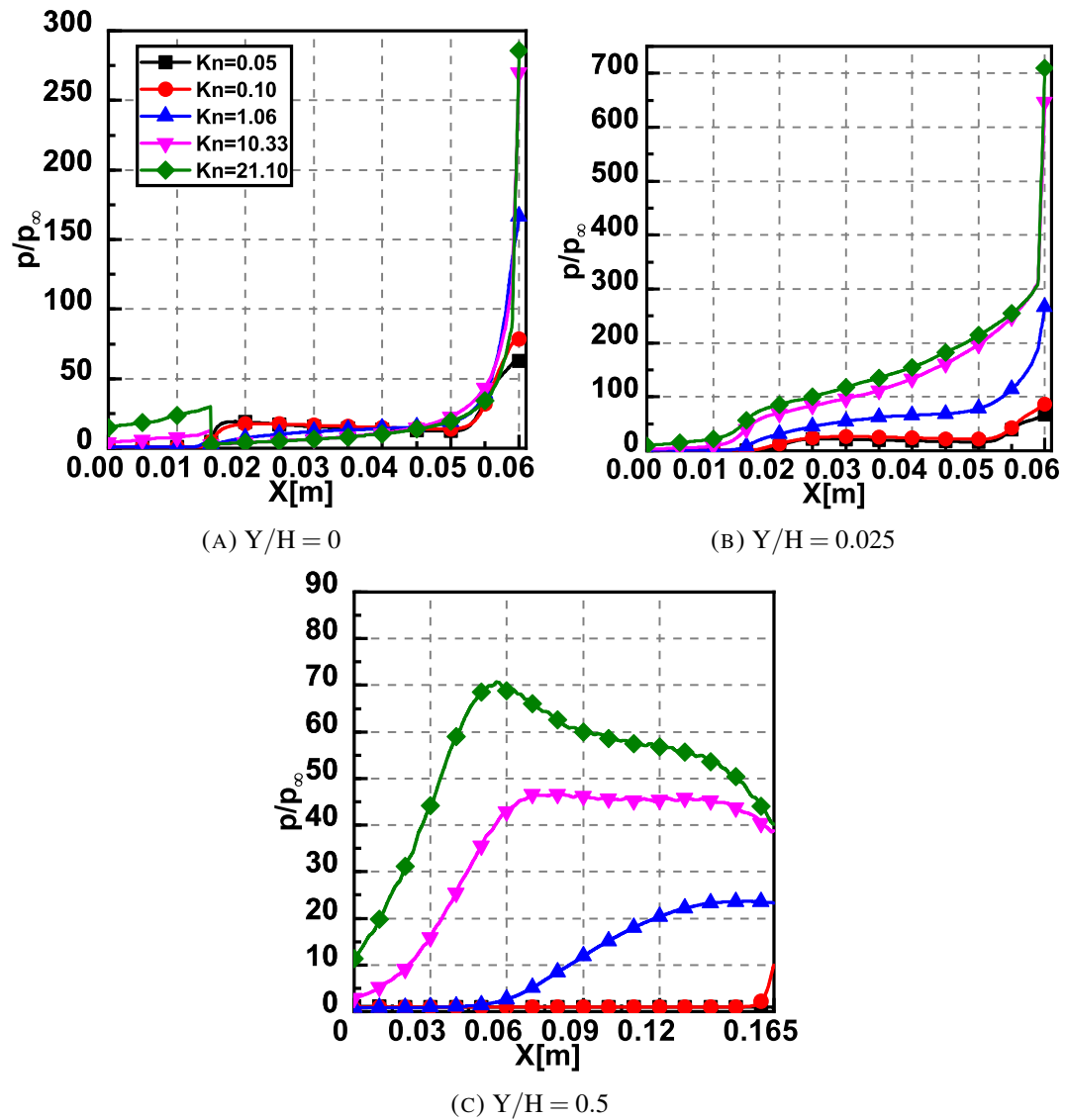


FIGURE 6.56: Variation of the non-dimensional pressure along the length of FFS for different Kn

to the flow for different Kn at various sections viz, $X = 30\text{mm}$, $X = 59\text{mm}$, $X = 61\text{mm}$, and $X = 120\text{mm}$ of the FFS. In these plots, the temperature ratio refers to the temperature T normalized by the free-stream temperature T_∞ . In all the profiles, the high incoming velocity of the fluid stream and velocity slip at the walls increases the viscous dissipation [163], leading to higher near-wall temperatures except, at $X = 59\text{mm}$, the near-wall temperatures are found to be close to the free-stream temperature. Also, the temperatures are an order of magnitude higher than the free-stream temperature. In the center of

the domain $Y = 0.03$, it is observed that (T/T_∞) ratios increase with rarefaction. This increase can be attributed to the distribution of the viscous dissipation in a smaller number of molecules leading to temperature rise. Whereas at lower Kn , the same viscous dissipation is distributed among a large number of molecules, which leads to lower temperature rise. For comparison, at the section $X = 59\text{mm}$, the temperature ratios at $Y = 0.03$ are 0.98, 0.99, 2.20, 24.52 and 33.15 Kn 0.05, 0.1, 1.06, 10.33 and 21.33 respectively.

Away from the wall in the Y direction, the temperature ratio increases rapidly, then reduces and gradually attains a free-stream magnitude. At the section $X = 59\text{mm}$, the maximum temperature ratios show a decreasing trend with rarefaction with their magnitudes being 50.23, 51.39, 50.46, 47.74, and 47.01 for Kn 0.05, 0.1, 1.06, 10.33 and 21.33 respectively. Overall, the temperature ratios have similar trends in all sections and have a peak just above the height of the step.

Figure 6.58 shows the temperature ratio (T/T_∞) distribution along the length of FFS for different Kn at various sections viz, $Y/H=0$ (Bottom surface), $Y/H=0.025$ (Center of step), and $Y/H=0.5$ (Center of inlet). At the section $Y/H = 0$, the temperature ratio increases up to the leading edge of FFS and then decreases. At the section $Y/H = 0.025$, there is a gradual increase in the temperature ratio due to the viscous dissipation effects, and the temperature ratio quickly drops near the vicinity of the step. At the center of the inlet, the temperature ratio is constant along the FFS length in the slip regime, whereas there is a considerable change in the other regimes. This trend is also similar to the trend of velocity and pressure ratios. It can be attributed to the fact that the local mean free

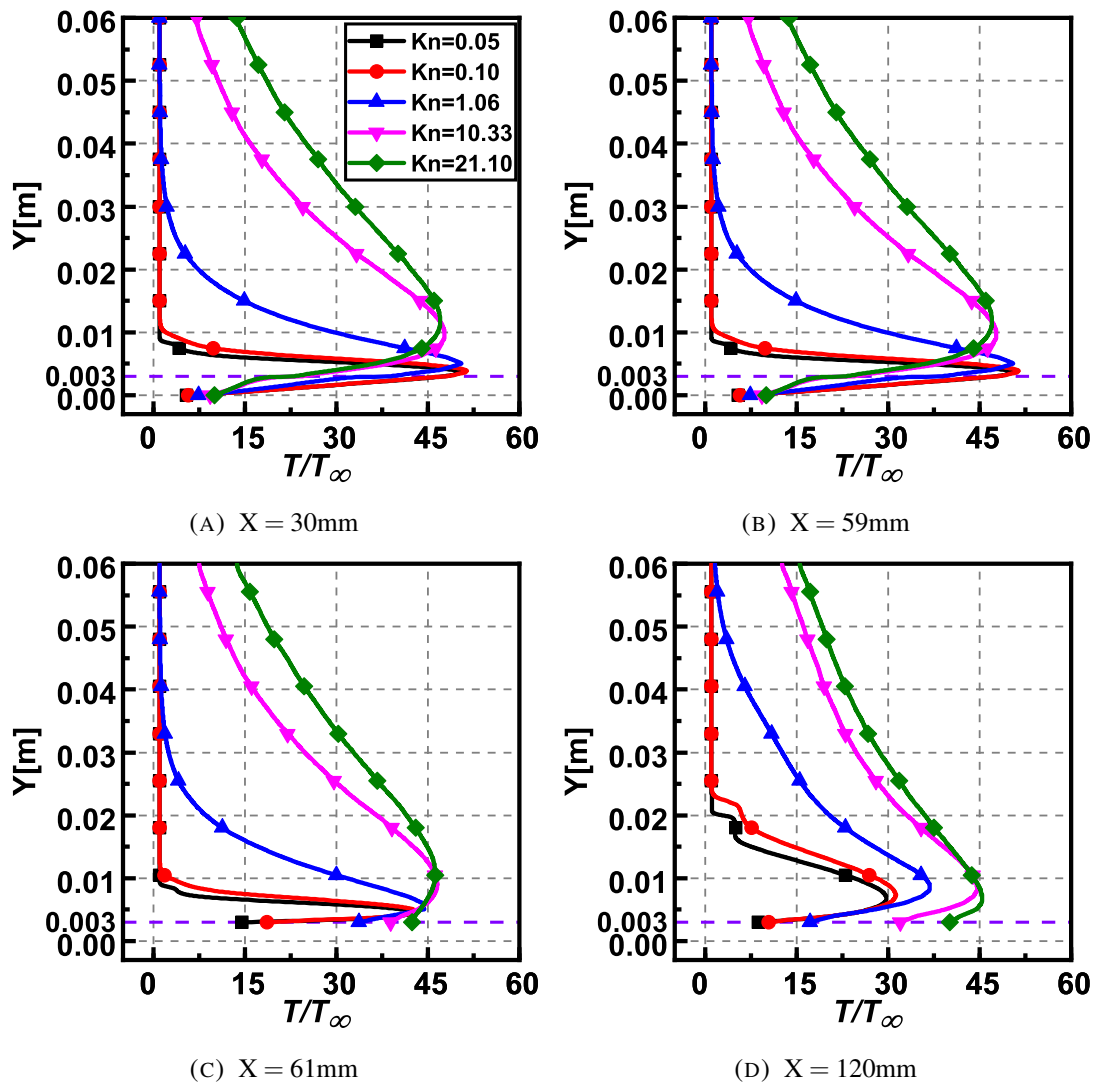


FIGURE 6.57: Variation of the non-dimensional temperature perpendicular to the surface of FFS for different Kn .

path increases with Kn , and hence the momentum/energy diffuses faster into the domain for larger Kn .

Pressure coefficient:

Figure 6.59 shows the distribution of the pressure coefficient (C_p) along the lower and upper surfaces of the FFS for different Kn . The profiles follow a similar trend for all Kn .

Along the lower surface the C_p gradually increases from the leading edge and reaches a

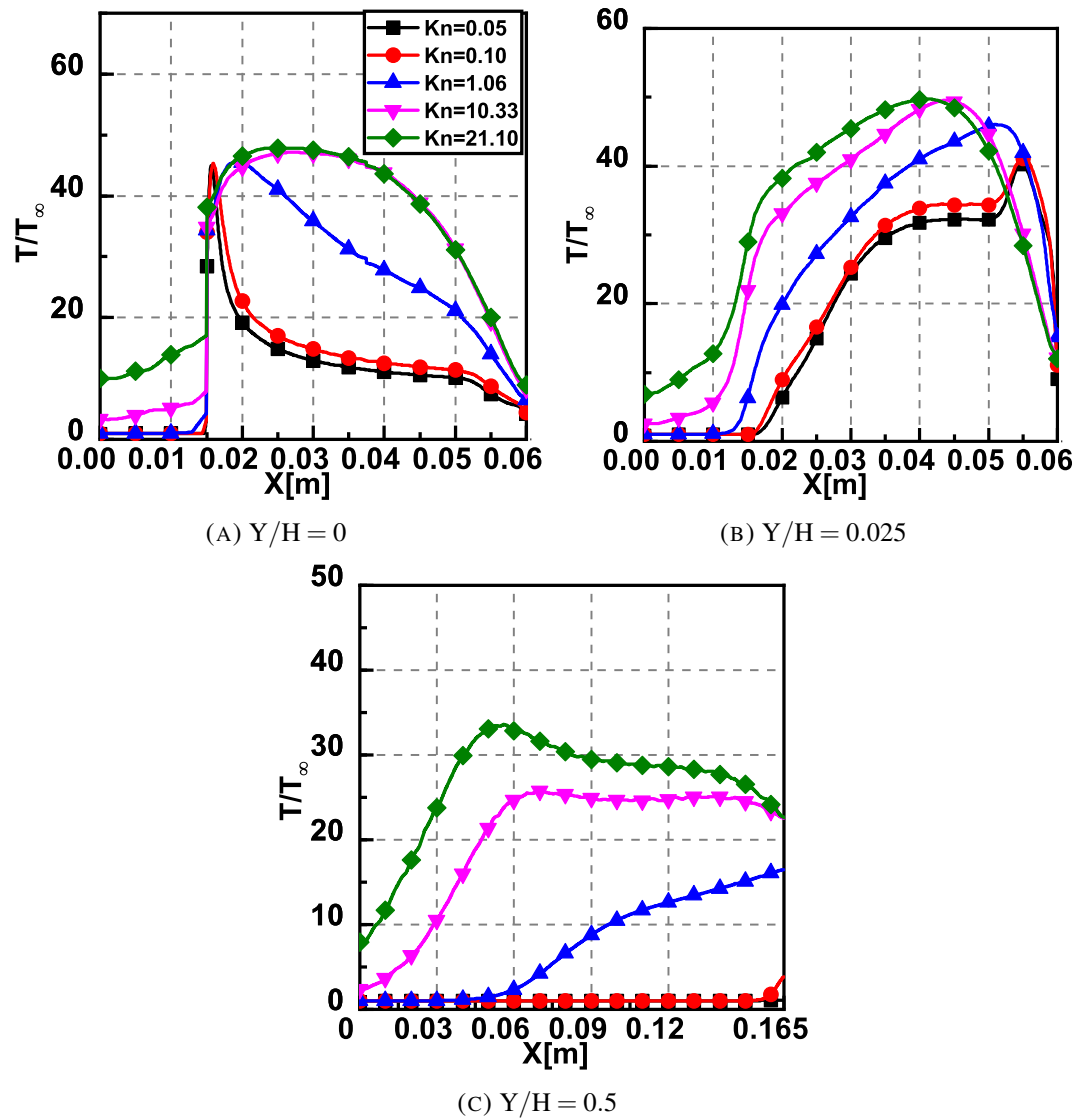


FIGURE 6.58: Variation of the non-dimensional temperature along the length of FFS for different Kn

peak near the step due to the stagnation pressure rise of the incoming fluid stream; this pressure rise increases with rarefaction. Downstream of the step on the upper surface, C_p shows a similar trend where it gradually reduces towards the outlet and is relatively similar for all Kn . At the outlet the C_p is positive, indicating that the wall pressure is of higher magnitude than the free-stream pressure. The peak C_p on the step is found to be 0.25, 0.19, 0.55, 0.94 and 0.99 for Kn 0.05, 0.1, 1.06, 10.33 and 21.33 respectively. It should be noted that C_p increases by almost four times in the free-molecular regime

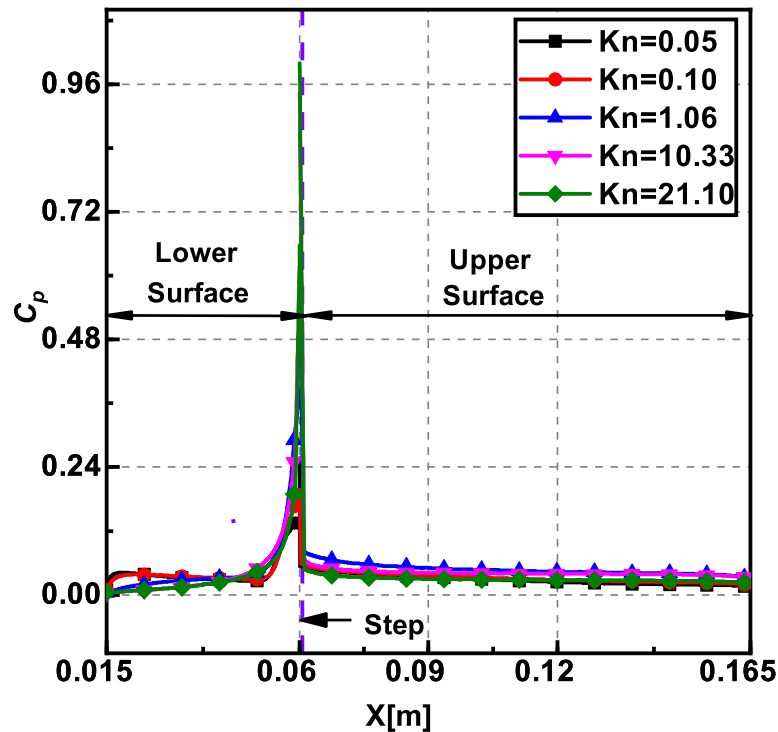


FIGURE 6.59: Variation of pressure coefficient C_p along the lower and upper surfaces of FFS for different Kn

when compared to the slip regime.

Along the frontal face of the step, the C_p gradually increases towards the top surface of the step. This increase can be attributed to the molecular collisions occurring on both the lower surface and on the frontal face, increasing their respective normal momentum. Furthermore, the increase in C_p is more significant in the transitional and free-molecular regimes, as the pressure ratio increases with rarefaction.

Skin friction coefficient:

Figure 6.60 shows the distribution of the skin friction coefficient (C_f) along the lower and upper surfaces of the FFS for different Kn . The magnitude of C_f is higher at the leading edge of FFS due to high near-wall velocity gradients; also, they increase with

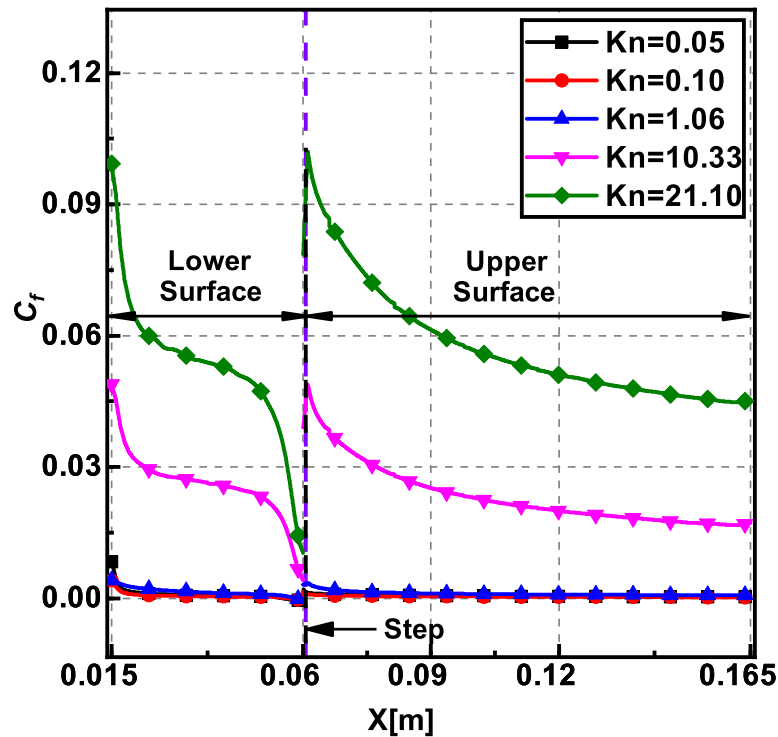


FIGURE 6.60: Variation of skin friction coefficient C_f along the lower and upper surfaces of FFS for different Kn

rarefaction. Similar to C_p the profiles for C_f follow similar trends concerning Kn . From the leading edge the C_f gradually reduces towards the step. In the slip and transitional regime, the C_f is negative near the step due to flow recirculation. On the upper surface, C_f rises sharply at the step and gradually decreases towards the outlet, with variation among different Kn . At the outlet C_f is significantly higher than the C_p signifying the dominance of tangential forces against the normal forces. The peak C_f on the step is found to be 2×10^{-3} , 1.4×10^{-3} , 3.3×10^{-3} , 4.4×10^{-2} and 9×10^{-2} for Kn 0.05, 0.1, 1.06, 10.33 and 21.33 respectively.

Heat transfer coefficient:

Figure 6.61 shows the distribution of the heat transfer coefficient (C_h) along the lower and upper surfaces of the FFS for different Kn . The profiles of C_h and C_p follow a similar

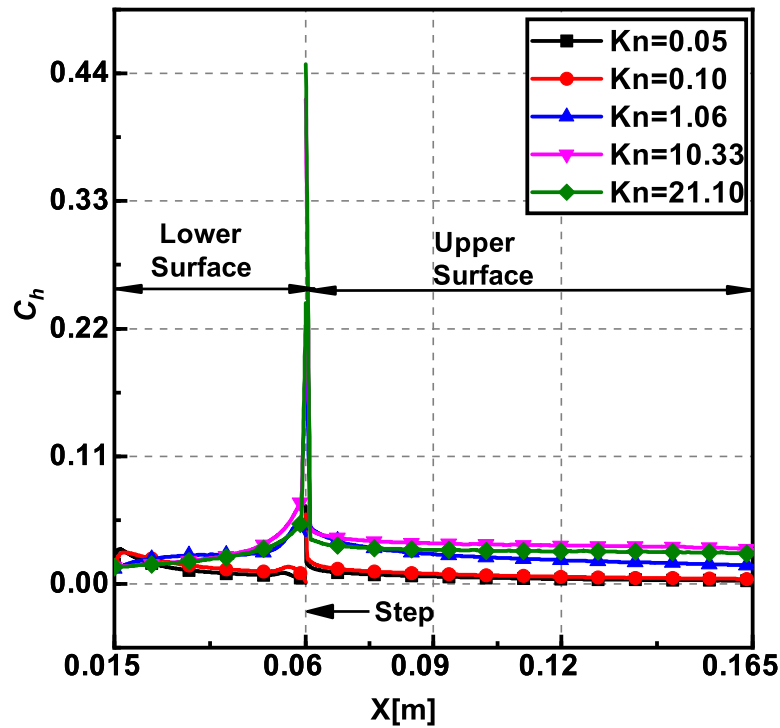


FIGURE 6.61: Variation of heat transfer coefficient C_h along the lower and upper surfaces of FFS for different Kn

trend. Along the lower surface in the slip and transitional regime C_h gradually increases reaches a peak close to the step, and finally decreases due to recirculation. Whereas, in the free-molecular regime C_h continually increases and reaches a peak at the step due to the absence of recirculation. The C_h in the free-molecular regime is one order higher than the slip regime. Along the upper surface, the peak C_h occurs at the step and gradually reduces towards the outlet. The peak C_h on the step is found to be 0.066, 0.06, 0.22, 0.41 and 0.44 for Kn 0.05, 0.1, 1.06, 10.33 and 21.33 respectively. Along the back face of the step, C_h gradually increases and reaches a maximum at the top surface of the step. For higher Kn , due to the higher mean free path of the molecules, the molecules from the center of the domain also contribute to the collisions with the frontal face, increasing the wall heat flux.

TABLE 6.12: Geometric parameters of the 2D open cavity.

Parameter	Value
Length at upstream	60mm
Cavity depth (h)	3mm
Cavity length (L)	3mm
Length at downstream	45mm
Cavity position	$X = 60\text{mm}$
Position of leading-edge of the lower surface	$X = 15\text{mm}$

TABLE 6.13: Boundary conditions for the 2D open cavity.

Surface	A	B	C	D	E
Boundary condition	Wall	Symmetry	Free-stream inlet	Free-stream inlet	Outlet

6.3 Analysis of rarefied flow over open cavity

In this section, the analysis of the rarefied flow past an open cavity is presented. The geometry, boundary conditions, and free-stream conditions are described initially and are followed by the analysis of the results.

Geometry and computational domain:

The schematic illustration of the 2D cavity is shown in Figure 6.62. The fluid movement occurs from left to right. The flow along the streamwise and transverse directions is depicted by the coordinates X and Y . The length (L) and depth of the cavity (h) was fixed to 3mm. The domain height at the outlet was set at $H = 60\text{mm}$ after conducting an influence study on the flow properties. The various parameters of the cavity are depicted in Table 6.12. The different boundary conditions applied on various surfaces are given in Table 6.13.

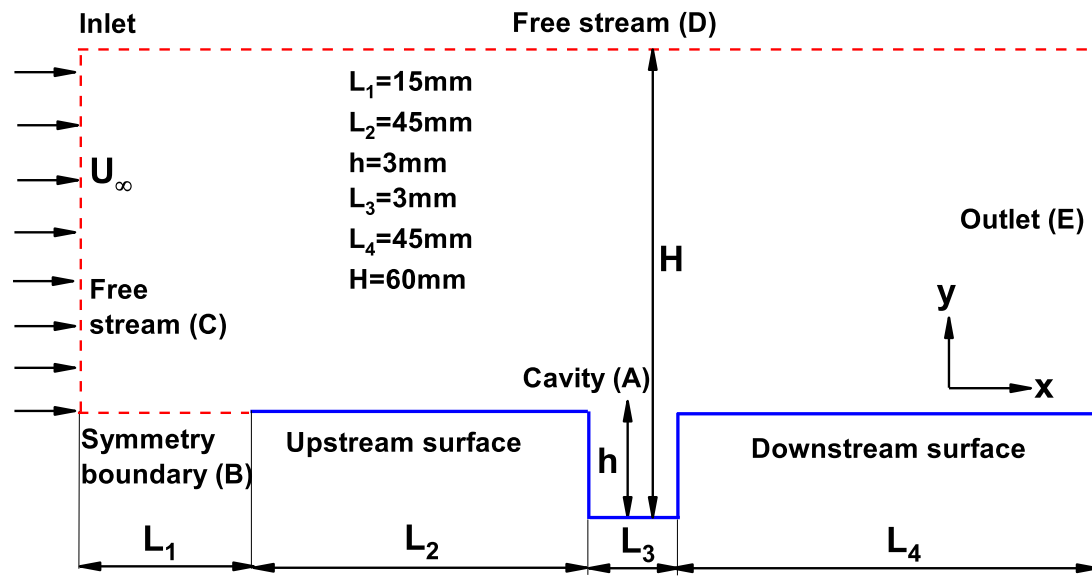


FIGURE 6.62: Schematic of the 2D open cavity.

Boundary conditions and mesh:

The computational domain is divided into several blocks and meshed in a structured manner, as shown in Figure 6.63. The cell widths in both X and Y directions were maintained below the mean free path, i.e., $\Delta x_{cell}, \Delta y_{cell} < 0.3\lambda_\infty$. The cell size was refined near the cavity. The total number of cells for the case of $Kn=1.06$ was about 40,548 cells. Also, the cell count varied for other cases depending on the corresponding mean free path. The flow conditions adopted are given in Table 6.2.

6.3.1 Influence of Mach number

This section describes the influence of Mach number (Ma) on the flow and surface properties over the open cavity. The different Mach numbers studied are $Ma=5$ (Supersonic), 10 (Hypersonic), 25 (High-Hypersonic), and 30 (Reentry speeds). For all instances in

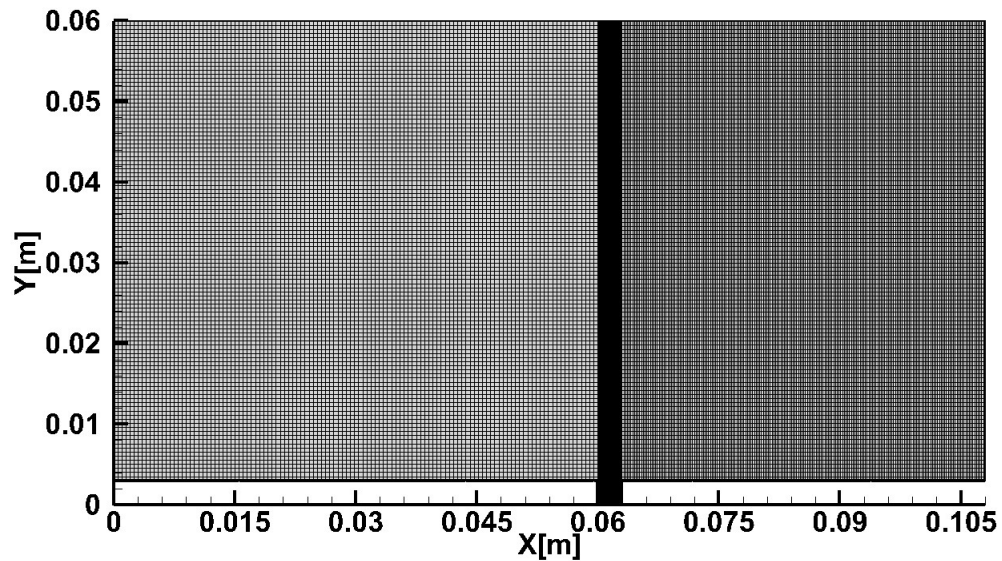


FIGURE 6.63: Meshed domain of the 2D open cavity.

this section, $H = 60\text{mm}$, $Kn = 1.06$ and $T_w = 4T_\infty$ is used. Henceforth, the variation of sampled results with Y are presented at the locations $X = 30\text{mm}$, 59 mm , 61mm and 93 mm respectively. Also inside the cavity the variations with X are presented for $Y/h=0.3,0.6,1$ respectively.

Velocity field:

Figure 6.64 shows the non-dimensional velocity (u/U_∞) in the perpendicular direction at sections $X = 30\text{mm}$, $X = 59\text{mm}$, $X = 61\text{mm}$, and $X = 93\text{mm}$ for different Ma . Y represents the perpendicular distance in y -direction above the surface of the cavity. The non-dimensional velocity profiles at $X = 30\text{mm}$ and $X = 59\text{mm}$, are found to be overlapping for different Ma away from the wall, depicting the flow is not influenced due to the presence of the cavity. Inside the cavity for $X = 61\text{mm}$, the non-dimensional velocities are negative, portraying flow recirculation. This observation aligns with the continuum results of Grotowsky and Ballmann [79] and that of Camussi *et al.* [160]

for comparative geometries. Also, the profiles overlap for different Ma up to the height of the cavity and deviate after that, signifying that the change in Ma has relatively less influence on the velocity field inside the cavity. At section $X = 93\text{mm}$, away from the bottom surface, the profiles look similar to the upstream profiles. Near-wall slip is observed at all the sections except inside the cavity where the recirculation takes place. Furthermore, the boundary layer thickness decreases with an increase in Ma as observed for continuum flows.

The non-dimensional velocity variation for different Ma at sections $Y/h = 0.3$, $Y/h = 0.6$ and $Y/h = 1$ is shown in Figure 6.65. At $Y/h = 0.3$, the non-dimensional velocity is negative due to the flow recirculation. Also, the decrease in the non-dimensional velocity is highest for the case of $Ma = 5$. This is due to the low inertia of the incoming fluid stream, whose momentum diffuses deeper into the cavity and causes the flow recirculation. As the Ma increases, the inertial effects of the flow are increased, and the fluid's momentum does not diffuse deeper into the cavity, which leads to lower magnitudes of the non-dimensional velocity compared with $Ma = 5$. A similar trend is observed for $Y/h = 0.6$, where the profiles are negative; however, the magnitudes are lower than $Y/h = 0.3$. At the top surface of the cavity for $Y/h = 1$, the profiles are positive as this fluid layer is a part of the freestream. Moreover, the profiles are not so wide apart from each other as compared to the other two sections.

Pressure field:

The non-dimensional pressure (p/p_∞) variation for different Ma at sections $X = 30\text{mm}$, $X = 59\text{mm}$, $X = 61\text{mm}$, and $X = 93\text{mm}$ is shown in Figure 6.66. Near the inlet of the

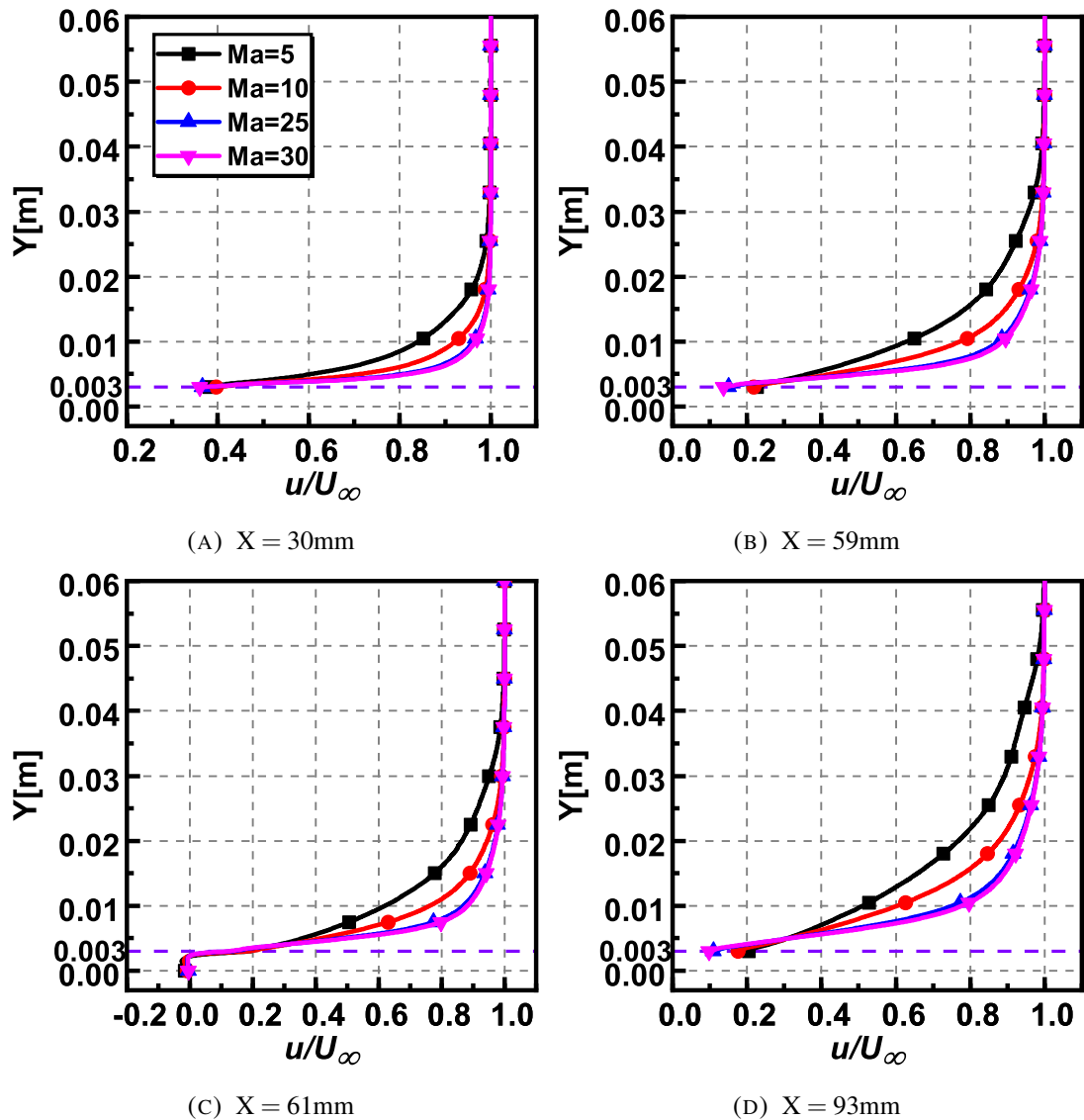


FIGURE 6.64: Variation of the non-dimensional velocity perpendicular to the surface of open cavity for different Ma .

domain at $X = 30\text{mm}$, the pressure magnitudes are higher and are two orders greater than the free-stream pressure. At $X = 59\text{mm}$, the pressure profiles are of lesser magnitudes and show deviation for different Ma . Inside the cavity at $X = 61\text{mm}$, the pressure magnitudes are lower due to the recirculation and expansion effects. Below the cavity depth (for $Y < 0.003$), the pressure reduces and attains the free-stream magnitudes, whereas, above the cavity (for $Y > 0.003$), the pressure magnitudes reach a peak shortly after that the

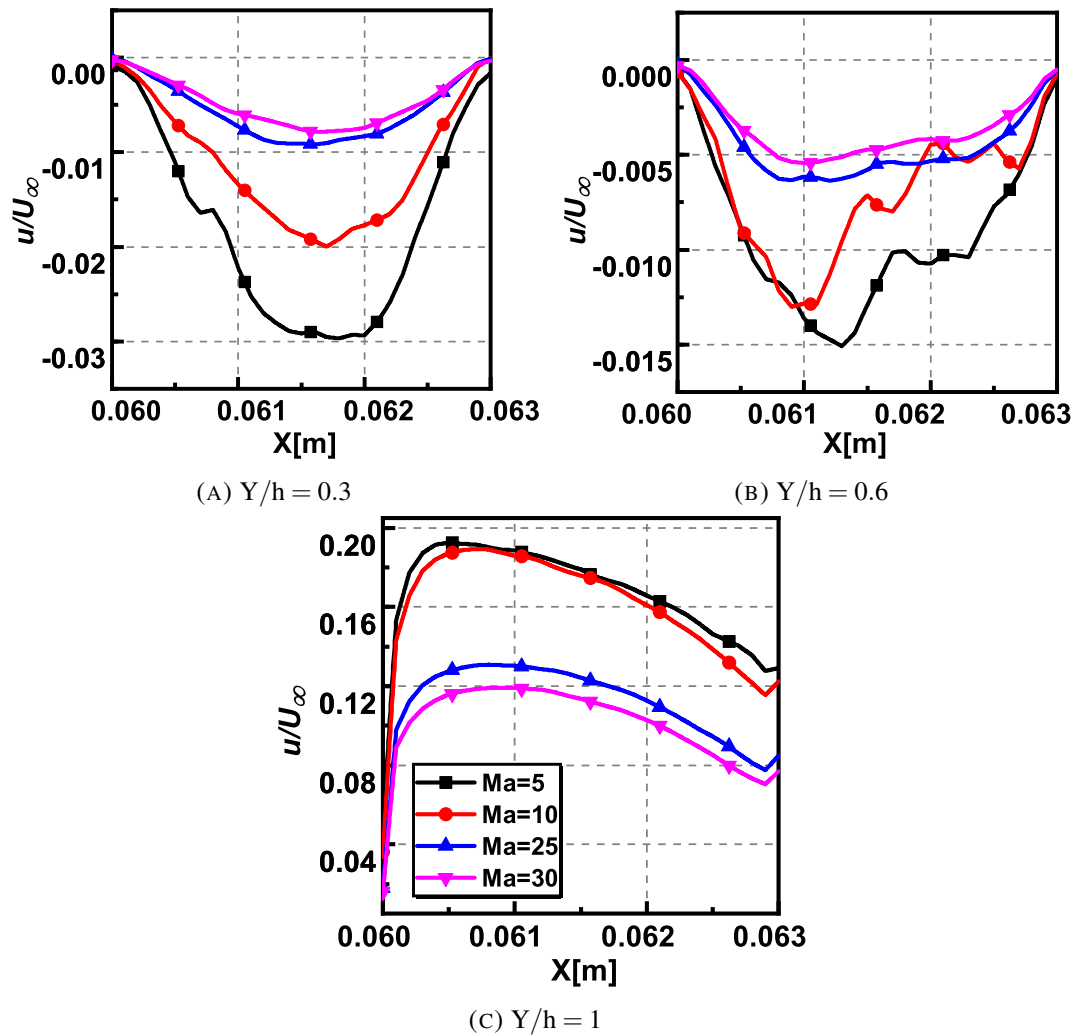


FIGURE 6.65: Variation of the non-dimensional velocity along the length of open cavity for different Ma

profiles overlap near the center of the domain. For reference, at section $X = 61$ mm, the peak pressure ratios are 3.41, 9.22, 58.57, and 87.03 for Mach numbers 5, 10, 25, and 30, respectively. Also, for different Ma , the near-wall pressure is relatively similar when compared to the other sections. The pressure magnitudes are lower downstream of the cavity, and the profiles show distinct variation for different Ma and attain free-stream magnitudes at a larger distance in the transverse direction. Thus, the non-dimensional pressure magnitudes are directly influenced by the Ma and increase with increasing Ma due to viscous heating.

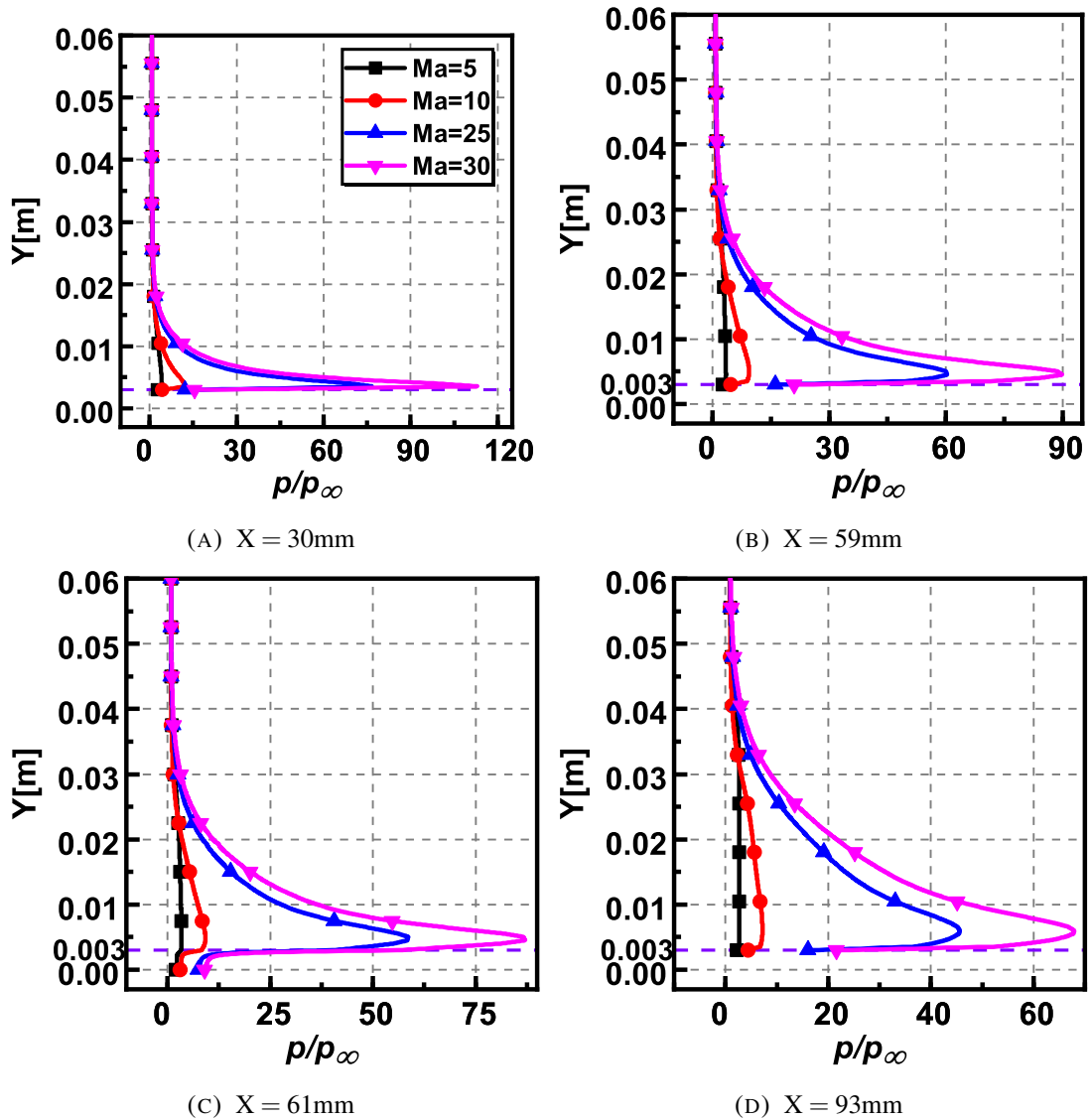


FIGURE 6.66: Variation of the non-dimensional pressure perpendicular to the surface of open cavity for different Ma .

The non-dimensional pressure variation for different Ma at sections $Y/h = 0.3$, $Y/h = 0.6$ and $Y/h = 1$ is shown in Figure 6.67. At $Y/h = 0$, the non-dimensional pressure shows lower magnitudes due to the recirculation effects. Whereas at $Y/h = 0.6$, the magnitudes are higher than $Y/h = 0$ (which are of an order of magnitude lower when compared against the free-stream values). Similarly, at the top surface of the cavity $Y/h = 1$, the pressure magnitudes are lower at the leading edge of the cavity and quickly increase along the cavity length as the flow stagnates at the right edge of the cavity entrance. Also,

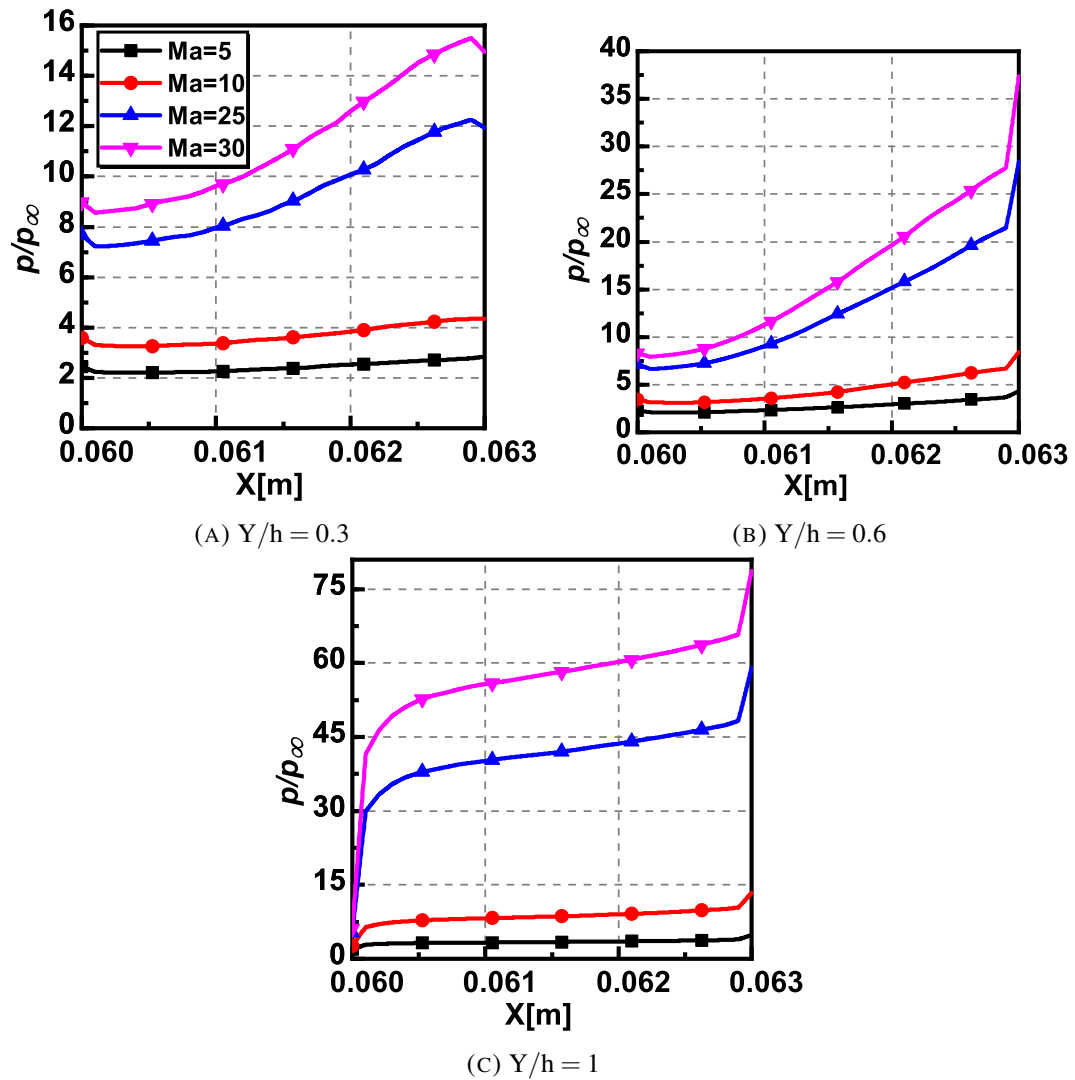


FIGURE 6.67: Variation of the non-dimensional pressure along the length of open cavity for different Ma

it is observed that at lower Ma , the pressure inside the cavity remains relatively constant. In contrast, at higher Ma there is a considerable pressure change, and the magnitudes increase along the cavity length.

Temperature field:

The non-dimensional temperature (T/T_∞) variation for different Ma at sections $X = 30$ mm, $X = 59$ mm, $X = 61$ mm, and $X = 93$ mm is shown in Figure 6.68. In $X = 30$ mm, the

temperatures near the wall are of higher magnitudes than the imposed wall temperature owing to viscous heating effects and soon overlap in the transverse direction. The profiles in section $X = 59\text{mm}$ are similar but take a longer distance in the transverse direction to coincide and attain temperature close to the free-stream magnitude. Inside the cavity at $X = 61\text{mm}$, identical to the pressure profiles, the near-wall temperatures for different Ma seem to be unaffected and are found to be relatively the same. This is due to the recirculation region, which causes the flow to stagnate and reduces the temperatures. For quantitative assessment at section $X = 61\text{mm}$, on the top face of the cavity, the peak temperature ratios are 4.39, 8.70, 42.50, and 60.44 for Mach numbers 5, 10, 25, and 30, respectively. Near the exit of the domain at $X = 93\text{mm}$, the profiles are similar but of a marginally lower magnitude. At the same level as the cavity entrance, the peak magnitudes of temperatures are observed in the shear layer. Thus, it is observed that similar to the pressure profiles, the temperatures are directly influenced by the change in Ma and show an increasing trend.

The non-dimensional temperature variation for different Ma at sections $Y/h = 0.3$, $Y/h = 0.6$ and $Y/h = 1$ is shown in Figure 6.69. At $Y/h = 0.3$, the non-dimensional temperature is of the same order as the imposed wall temperature. In section $Y/h = 0.6$, the profiles behave similarly with a marginal increase in magnitude. At the top surface of the cavity $Y/h = 1$, the temperatures are of considerably higher magnitude as it falls in the shear layer. The viscous dissipation causes this temperature rise. Along the cavity length, the profile for $Ma = 5$ is found to be constant, whereas variations are observed for the other Ma at all the sections. Also, similar to the pressure profiles, the temperature increase along the cavity length is observed, particularly at higher Mach numbers. The

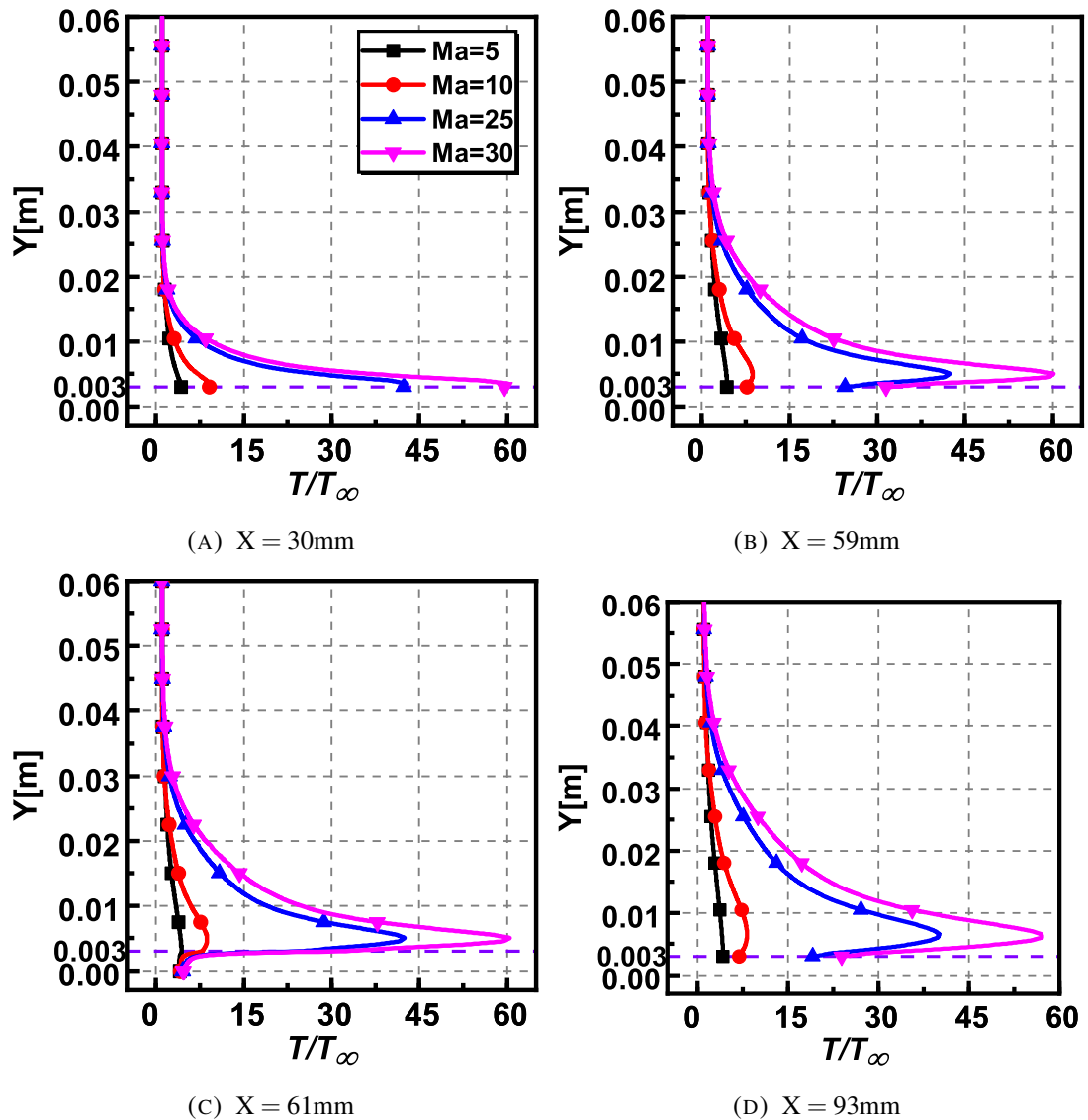


FIGURE 6.68: Variation of the non-dimensional temperature perpendicular to the surface of open cavity for different Ma .

peak temperatures along the cavity length are also observed towards the cavity's trailing edge due to flow stagnation.

Pressure coefficient:

Figure 6.70a shows that the pressure coefficient C_p is found to behave in a similar manner for different Ma , showing a nonlinear trend, resembling a parabolic profile. Along the

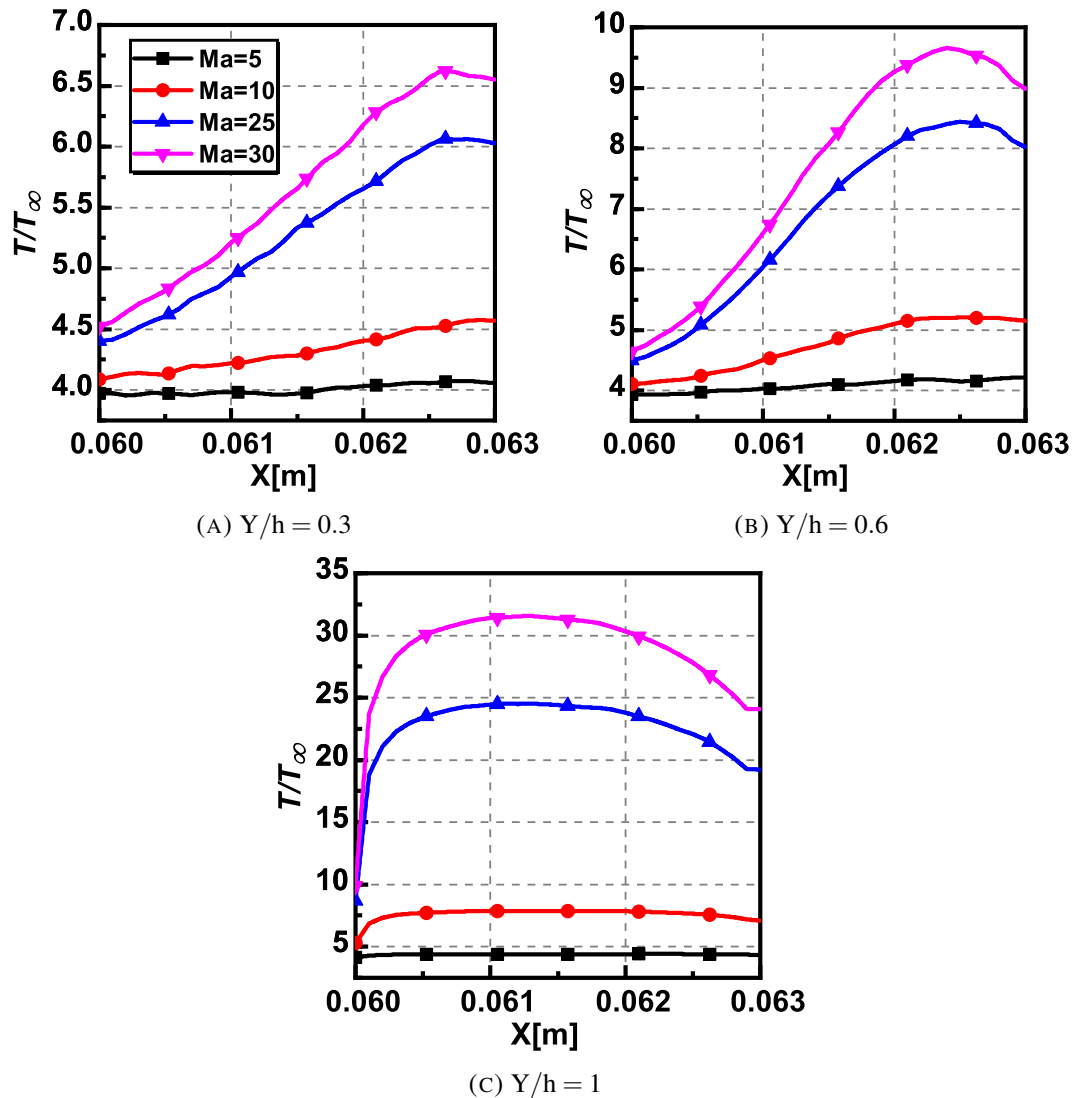


FIGURE 6.69: Variation of the non-dimensional temperature along the length of open cavity for different Ma

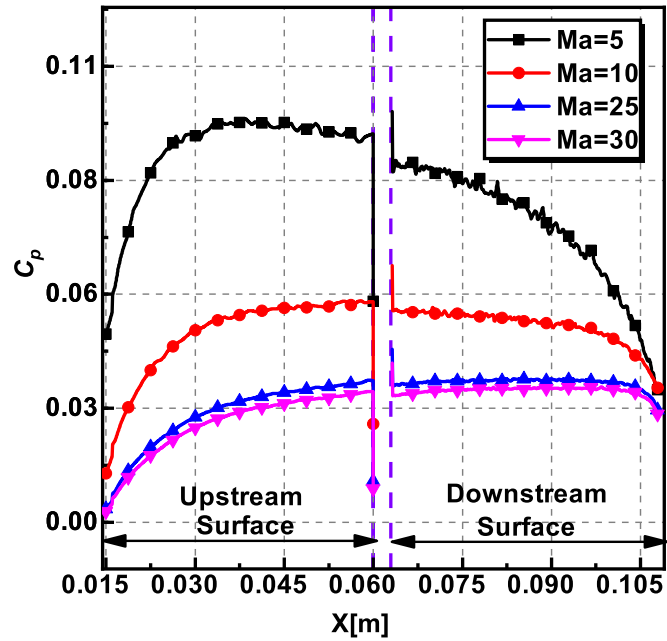
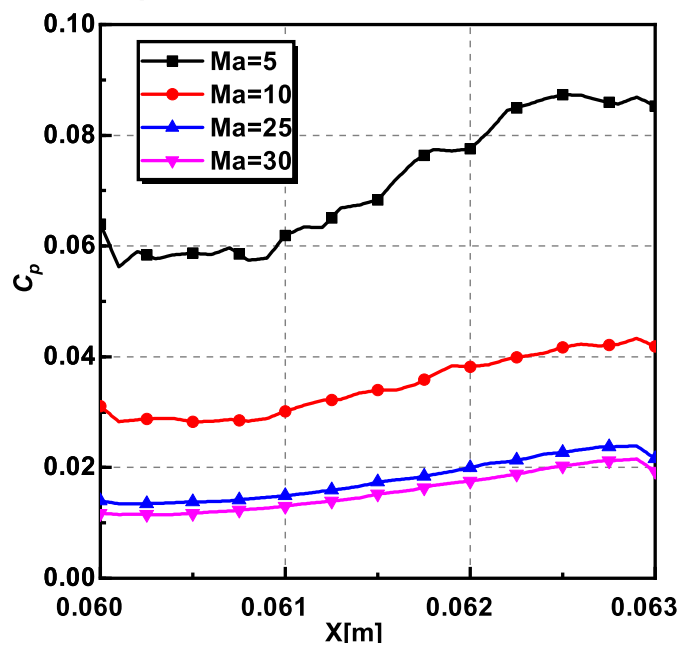
upstream surface, the magnitude of C_p gradually increases from the inlet. At the edge of the cavity the C_p reduces significantly. This can be attributed to the flow being expanded due to the increased area. Along the beginning of the downstream surface, stagnation pressure causes a surge in magnitudes of C_p . Subsequently the C_p shows a reducing trend towards the outlet. At the outlet, the magnitudes of C_p are greater than zero showing that the wall pressure is greater than the free-stream pressure. Inside the cavity, as shown in Figure 6.70b, the pressure coefficient C_p has a significantly lower magnitude due to

the flow recirculation which causes a reduction in pressure. Along the cavity the C_p gradually increases for the lowest case of $Ma = 5$, whereas it is reasonably constant for the other cases. Thus, to summarize, the increase in Ma causes a reduction in C_p . As the Mach number increases the free-stream velocity increases and the contribution of the inertial term $\frac{1}{2}\rho_\infty U_\infty^2$ in the equation 6.1 which causes a reduction in the magnitude of pressure coefficient.

Skin friction coefficient:

Figure 6.71a shows that the skin friction coefficient C_f which follows the pressure coefficient and behaves similarly for different Ma . Along the upstream surface, the magnitude of C_f is greater at the beginning due to the high-velocity gradients at the wall. This also causes the peak magnitudes of C_f near the upstream edge. From the upstream edge, C_f gradually decreases along X . Near the edge of the cavity C_f reduces significantly. Along the downstream surface, the magnitude of C_f surges quickly at a very short distance from the cavity and remains almost a constant towards the outlet. At the outlet, the magnitudes of C_f are again greater than zero as observed in the pressure coefficient. Inside the cavity (Figure 6.71b), C_f is found to be negative for all the cases due to the formation of the recirculation region. The reduction in the magnitude is highest for the case of lowest $Ma = 5$. Thus, similar to the pressure coefficient C_p , the increase in Ma causes a reduction in C_f . Also, the skin friction coefficient magnitudes are higher than the pressure coefficient, demonstrating tangential forces' dominance over the normal forces.

Heat transfer coefficient:

(A) C_p on the upstream and downstream surfaces.(B) C_p on the cavity base.FIGURE 6.70: Variation of pressure coefficient C_p for open cavity for different Ma .

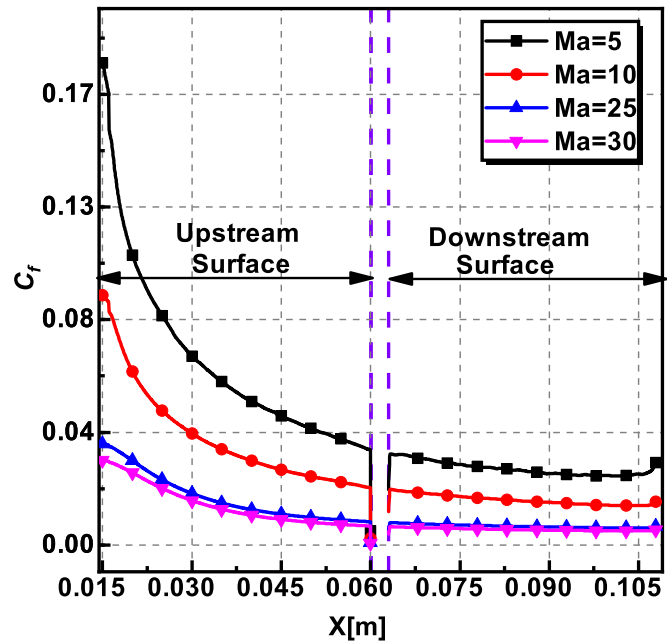
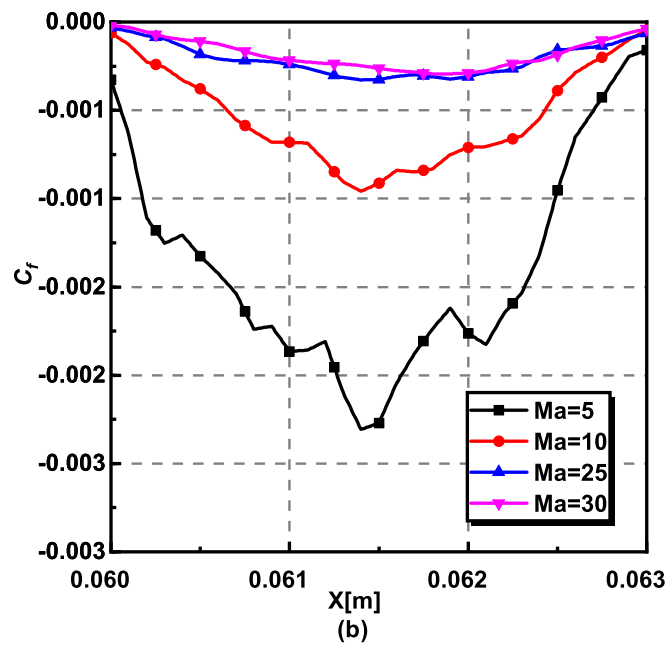
(A) C_f on the upstream and downstream surfaces.(B) C_f on the cavity base.FIGURE 6.71: Variation of skin friction coefficient C_f for open cavity for different Ma .

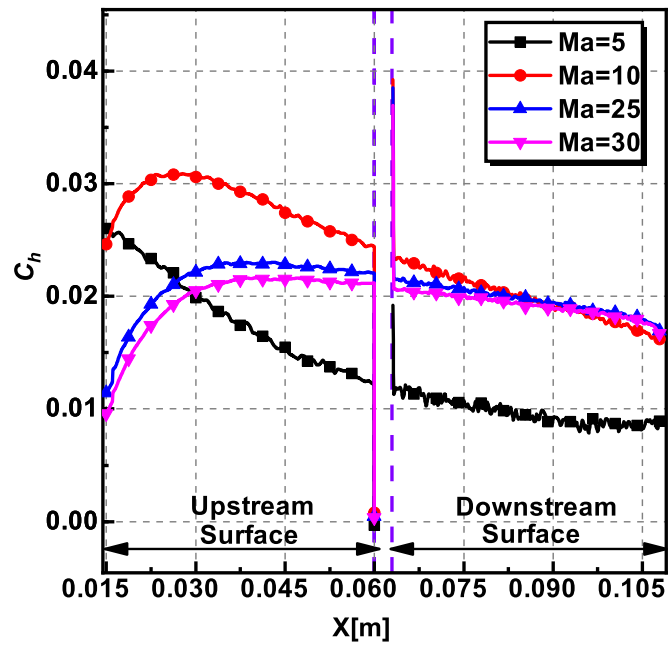
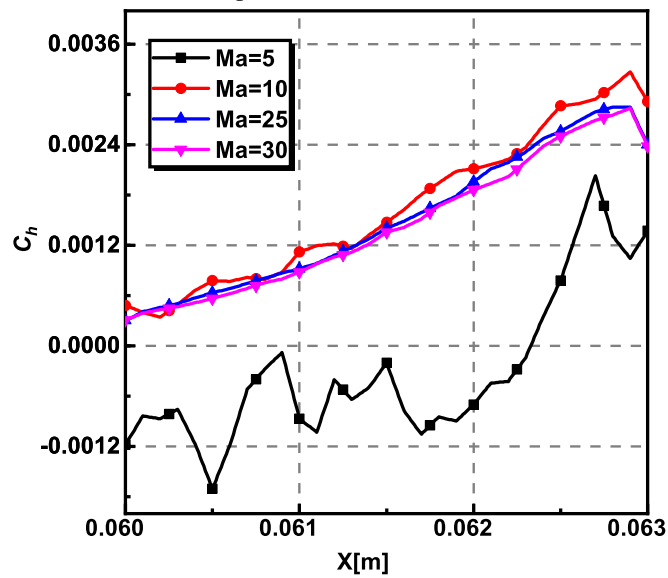
Figure 6.72a shows that the heat transfer coefficient C_h which shows contrasting trends for different Ma . Towards the upstream end, the magnitude of C_h is highest for $Ma=10$ in comparison with the other cases. Also, the profiles show a gradual decrease for the case of $Ma=5$, whereas for the other cases the C_h gradually increases and shows a decline after that. The varying boundary layer thickness possibly causes the differing profiles at the separation [155]. Along the downstream surface the C_h shows a declining trend for different Ma , though, the reduction in C_h is very minimal. Inside the cavity as shown in Figure 6.72a, the heat transfer coefficient C_h is found to be negative for $Ma=5$ for a considerable part of the cavity. However, towards the end of the cavity the C_h is found to recover and attain a positive value. For the other cases, the C_h values are fairly similar and are found to increase along the cavity length gradually. At the end of the cavity the C_h values are positive for all the cases due to viscous dissipation, which causes an increase in the wall heat flux and consequently the heat transfer coefficient.

6.3.2 Influence of Wall temperature

This section describes the influence of wall temperature (T_w) on the flow and surface properties over the open cavity. The wall temperature (T_w) was set to four different values, i.e., T_∞ , $2T_\infty$, $4T_\infty$ and $8T_\infty$ where, $T_\infty=204$ K. For all instances in this section, $H=60$ mm, $Kn=1.06$ and $Ma=25$ are used.

Velocity field:

The non-dimensional velocity variation for different T_w at sections $X=30$ mm, $X=59$ mm, $X=61$ mm, and $X=93$ mm is shown in Figure 6.73. There is a considerable velocity

(A) C_h on the upstream and downstream surfaces.(B) C_h on the cavity base.FIGURE 6.72: Variation of heat transfer coefficient C_h for open cavity for different Ma .

slip at the entrance of the domain for $X = 30\text{mm}$; however, the profiles are found to overlap and attain free-stream velocity quickly. At section $X = 59\text{mm}$, the profiles behave similar to $X = 30\text{mm}$ but with a reduced variation in the near-wall velocity slip. Inside the cavity at $X = 61\text{mm}$, the near-wall velocity for different T_w is found to be the same. This depicts that the imposed wall temperature has minimal effect on the velocity field inside the cavity. This can be attributed to the formation of the recirculation region inside the cavity for the prevailing flow conditions. At the exit of the flow domain at $X = 93\text{mm}$, the velocity profiles are similar to the upstream profiles; however, the flow field attains the free-stream magnitude after a considerable distance in the transverse direction. Also, the thickness of the boundary layer marginally increases with an increase in T_w .

The non-dimensional velocity variation for different T_w at sections $Y/h = 0.3$, $Y/h = 0.6$ and $Y/h = 1$ is shown in Figure 6.74. At $Y/h = 0.3$, the non-dimensional velocity is negative due to recirculation and is symmetric about the cavity mid-point. The velocity magnitude increases in the first half of the cavity and decreases to zero in the second half. In section $Y/h = 0.6$, the trends are similar; however, they are asymmetric about the cavity mid-point and relatively lower. At the top surface of the cavity for $Y/h = 1$, the velocity profiles are positive as the section is outside the recirculation region. The profiles resemble a parabola and show an increasing trend and then reduce along the cavity length. In all the sections, it is observed that the magnitudes of the velocity increase due to the rise in T_w . This is owing to the increased diffusion of the particles near the wall into the flow domain due to the increased wall temperature.

Pressure field:

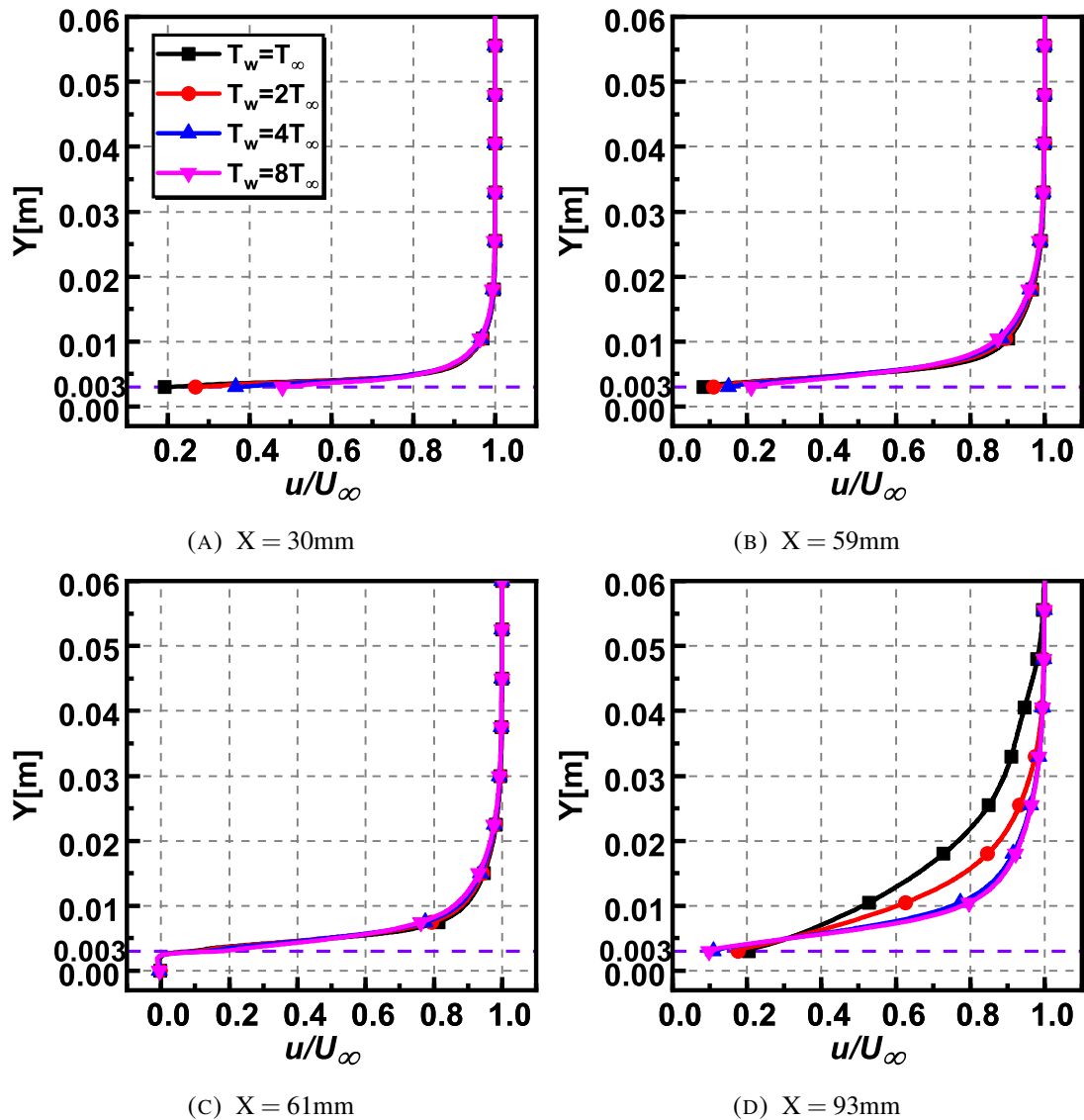


FIGURE 6.73: Variation of the non-dimensional velocity perpendicular to the surface of open cavity for different T_w .

The non-dimensional pressure variation for different T_w at sections $X = 30\text{mm}$, $X = 59\text{mm}$, $X = 61\text{mm}$, and $X = 93\text{mm}$ is shown in Figure 6.75. At section $X = 30\text{mm}$, the profiles overlap and are reasonably similar, demonstrating that the wall temperature effects are minimal at the inlet of the flow domain. At section $X = 59\text{mm}$, the profiles start showing differences, and it is observed that the magnitude of the velocities increase with an increase in T_w . At the outlet at $X = 93\text{mm}$, the profiles deviate substantially with

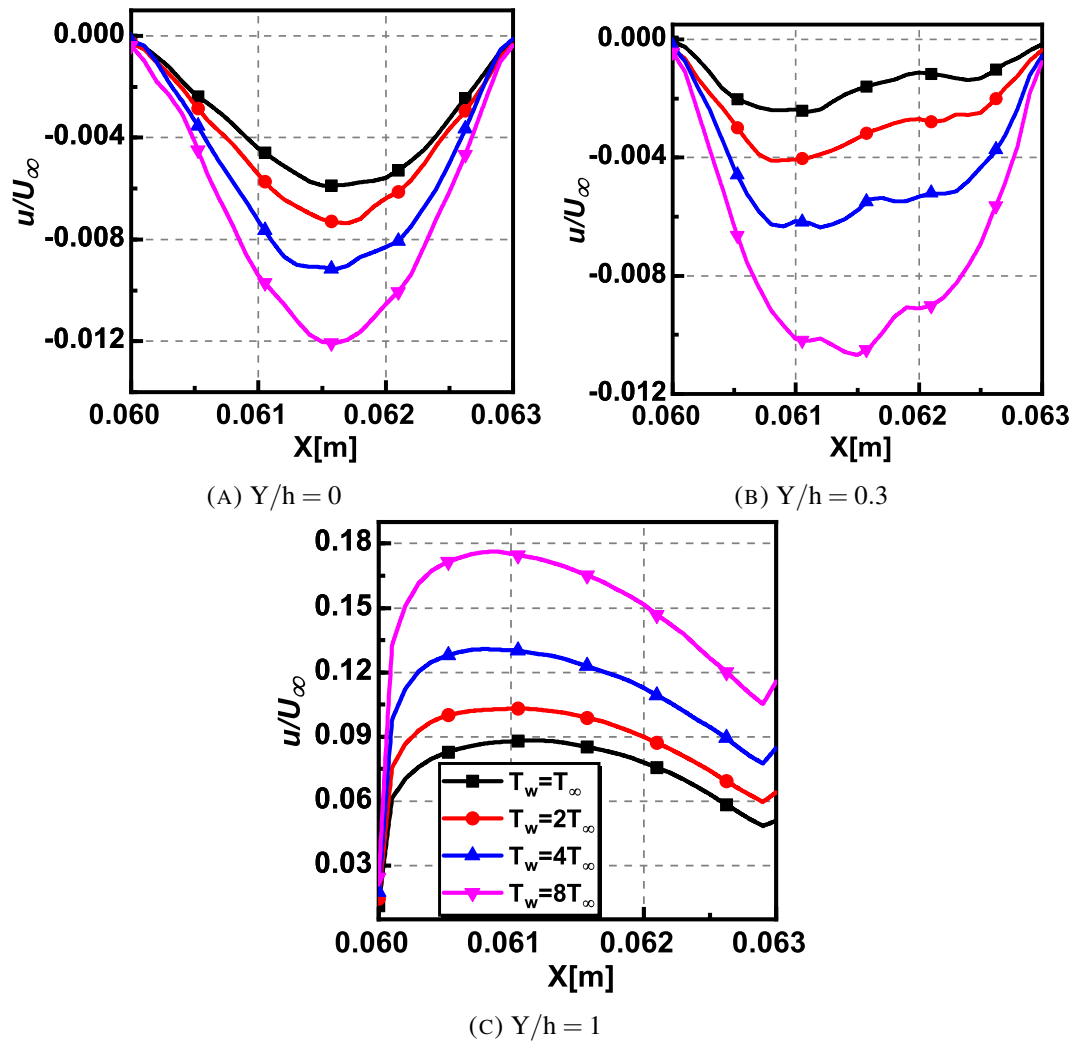


FIGURE 6.74: Variation of the non-dimensional velocity along the length of open cavity for different T_w

increasing T_w . For evaluation, in section $X = 93$ mm, the maximum pressure ratios are 38.27, 44.55, 45.68, and 56.60 for T_w/T_∞ 1, 2, 4, and 8, respectively. Thus, it can be observed that in all the cases, the magnitude of pressure increases as T_w increases. Also, as the flow progresses along X , the profiles overlap after a considerably larger distance in the transverse direction. The non-dimensional pressure variation for different T_w at sections $Y/h = 0.3$, $Y/h = 0.6$ and $Y/h = 1$ is shown in Figure 6.76. At $Y/h = 0.3$, the magnitude of non-dimensional pressure is lower due to the recirculation region, which reduces the near-wall pressure. In $Y/h = 0.6$, the magnitude of non-dimensional

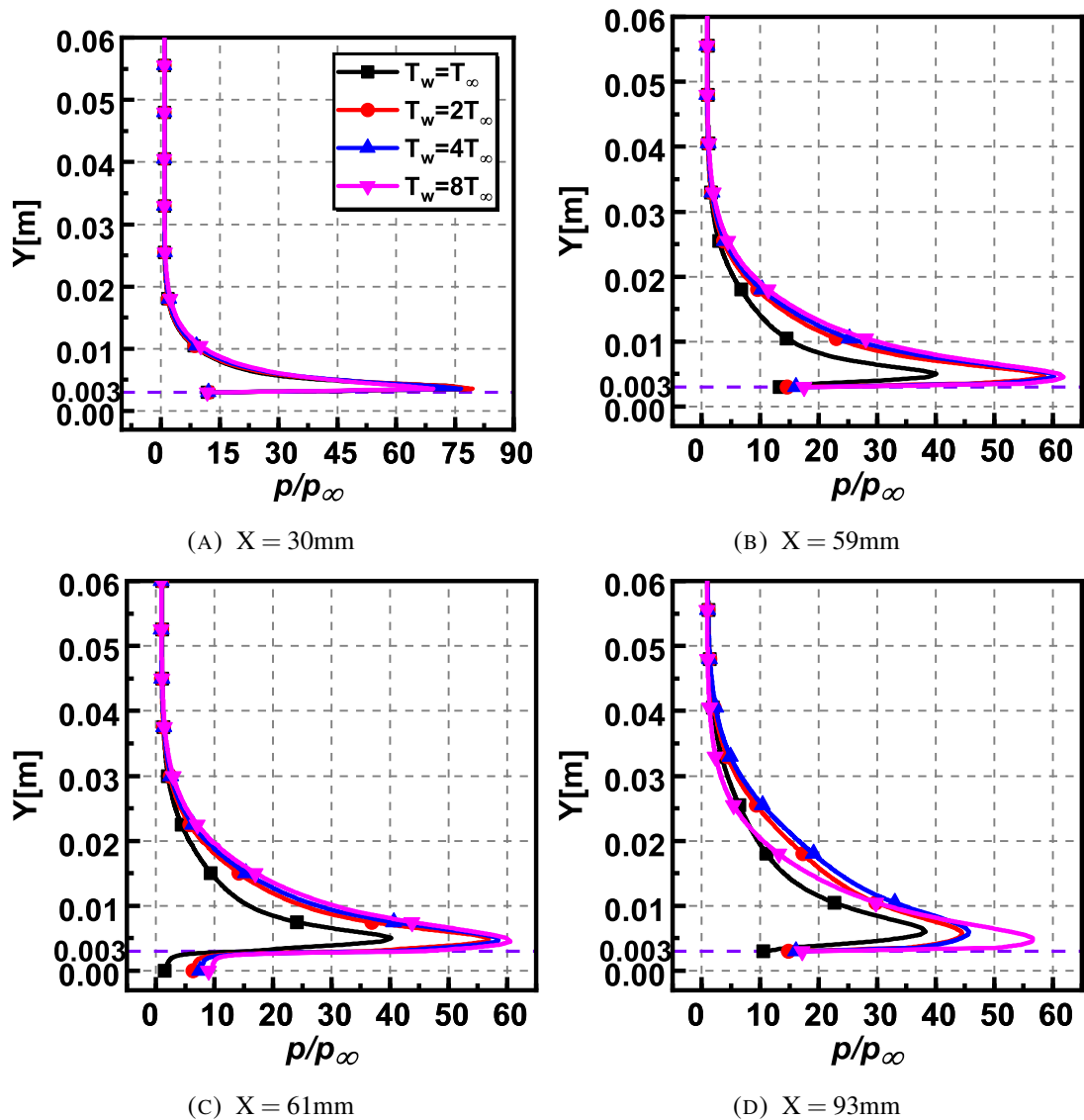


FIGURE 6.75: Variation of the non-dimensional pressure perpendicular to the surface of open cavity for different T_w .

pressure is marginally higher than at $Y/h = 0.3$, except for the $T_w = T_\infty$ case which remains the same. At the top surface of the cavity for $Y/h = 1$, the pressure magnitudes are almost two orders of magnitude higher than the free-stream pressure. The pressure profiles surge quickly near the cavity entrance and continue to increase all along the cavity length. Thus, the pressure inside the cavity shows a relatively increasing trend with T_w .

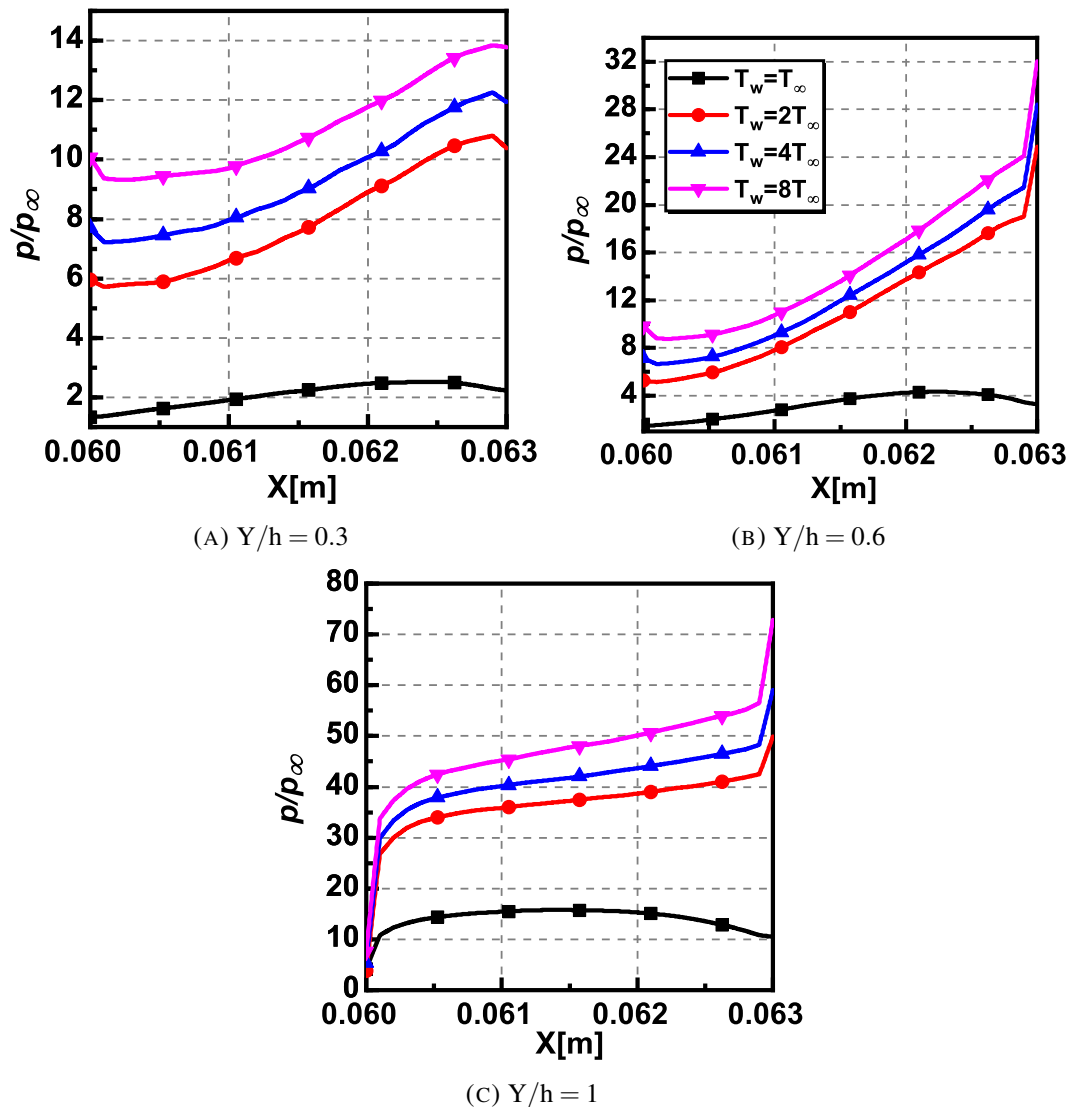


FIGURE 6.76: Variation of the non-dimensional pressure along the length of open cavity for different T_w

Temperature field:

The non-dimensional temperature variation for different T_w at sections $X = 30\text{mm}$, $X = 59\text{mm}$, $X = 61\text{mm}$, and $X = 93\text{mm}$ is shown in Figure 6.77. In all the sections, the magnitude of the temperature is one order greater than the free-stream temperature. Moreover, the near-wall temperature increases with T_w . But the profiles quickly overlap at a short distance from the wall. At section $X = 30\text{mm}$, the profiles are found to be overlapping, similar to the pressure profiles. From section $X = 59\text{mm}$ onwards, the

profiles for different T_w start deviating. Inside the cavity at $X = 61\text{mm}$, the profiles overlap up to a short distance above the height of the cavity and show a deviating trend after that. Near the outlet at $X = 93\text{mm}$, the profiles are similar as seen upstream but slightly different for different T_w . For quantitative evaluation in section $X = 93\text{mm}$, the maximum temperature ratios are 38.27, 38.78, 40.06, and 42.31 for T_w/T_∞ 1, 2, 4, and 8, respectively. Thus, it can be noted that the magnitude of change with an increase in T_w , is lesser in the temperature field in comparison to the pressure field. Also, the temperature variation is minimal as the flow progresses from the inlet, over the cavity, and towards the outlet. The non-dimensional temperature variation for different T_w at sections $Y/h = 0.3$, $Y/h = 0.6$ and $Y/h = 1$ is shown in Figure 6.78. Near the base of the cavity for $Y/h = 0.3$, the temperature magnitudes are of the same order as the free-stream temperature and show an increasing trend. The profiles near the center of the cavity for $Y/h = 0.6$ are also similar but with an increase in the magnitude of the temperature. At the top surface of the cavity for $Y/h = 1$, the temperatures quickly shoot up due to the viscous heating effects in the shear layer and cause the temperature to be an order of magnitude higher. Also, along the length of the cavity, the temperature gradually reduces.

Pressure coefficient:

The variation of pressure coefficient (C_p) for different T_w on the upstream, downstream, and the base surface of the cavity is shown in Figure 6.79. The pressure coefficient C_p shows a similar trend along X for different T_w . In contrast to the trends observed for different Ma , which showed a decrease in C_p with increasing Ma , the profiles of C_p for different T_w increase with increasing wall temperature. The Mach number for the cases

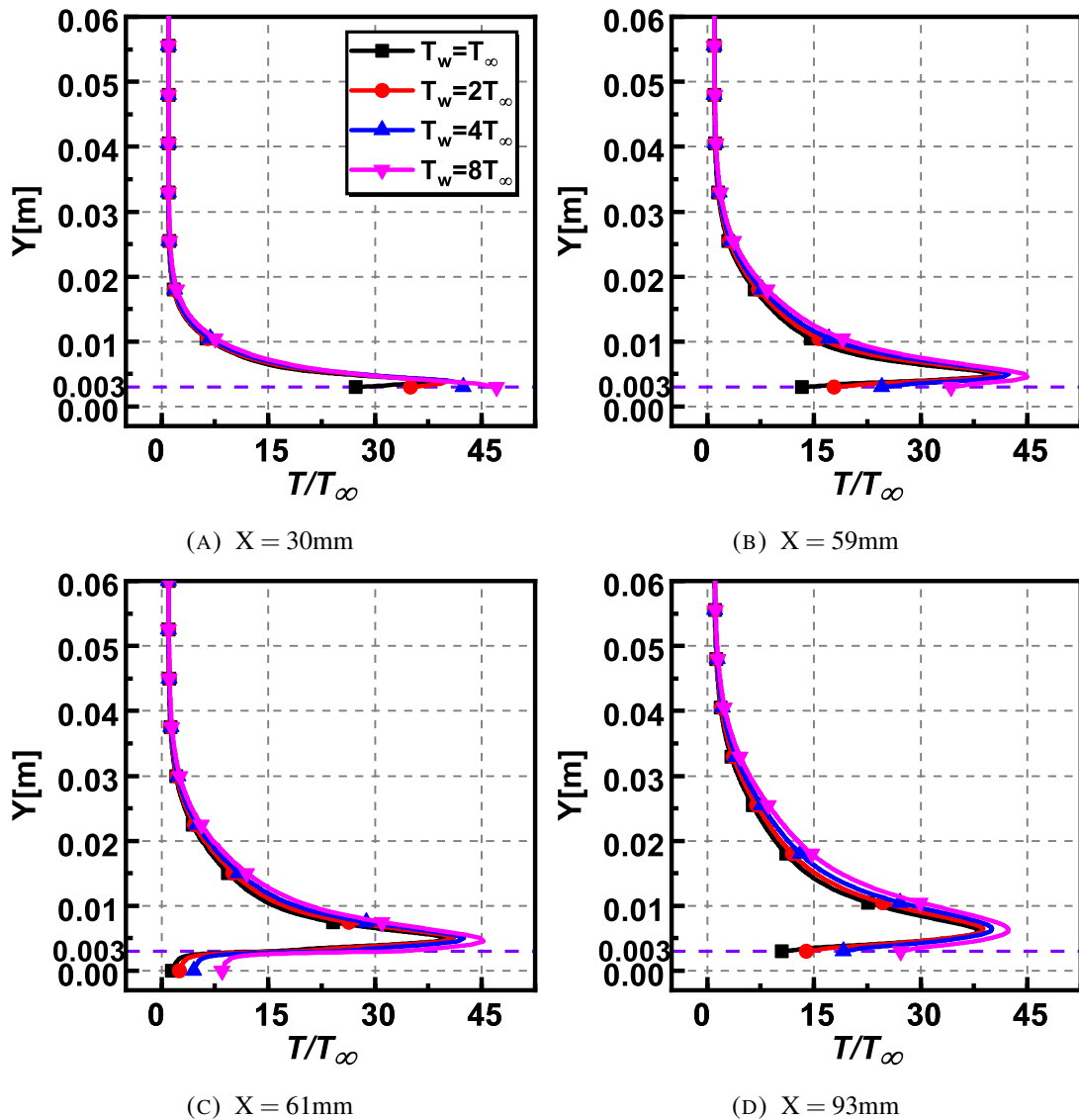


FIGURE 6.77: Variation of the non-dimensional temperature perpendicular to the surface of open cavity for different T_w .

is maintained constant, which reduces the contribution of the inertial term $\frac{1}{2}\rho_\infty U_\infty^2$ and the C_p is mainly dominated by the contribution from the wall pressure p_w . The increase in T_w causes an increase in the thermal velocity of the molecules, which in turn raises the magnitude of p_w and consequently the pressure coefficient. Along the upstream surface, the magnitude of C_p gradually increases from the inlet and shows a reduction near the edge of the cavity. Along the downstream surface, the magnitudes of C_p remain

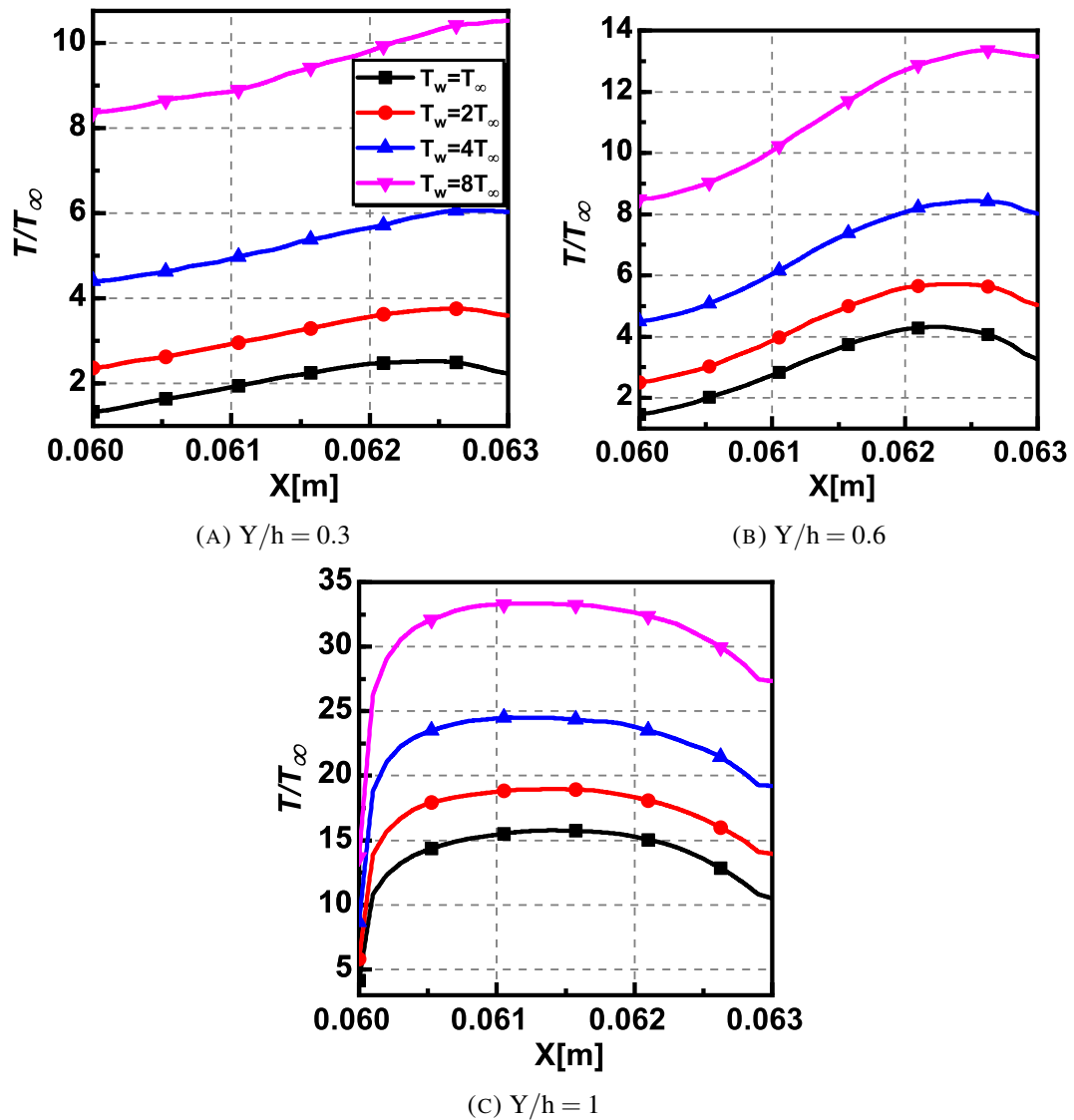
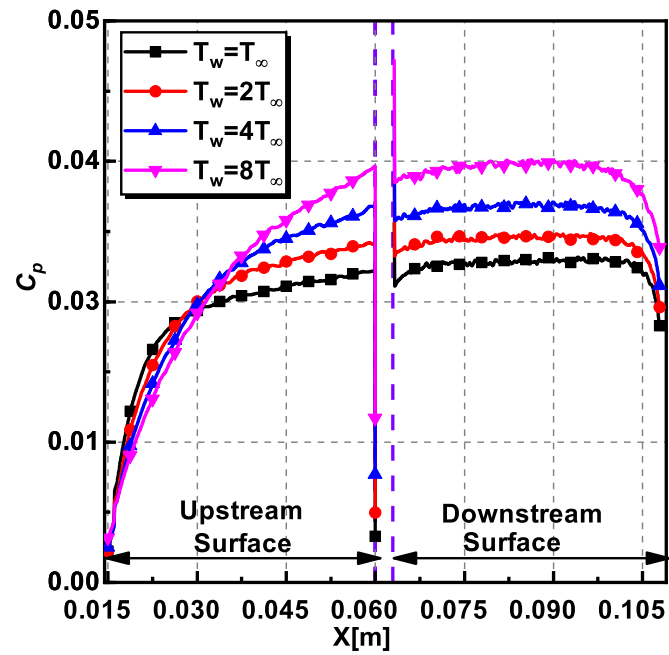
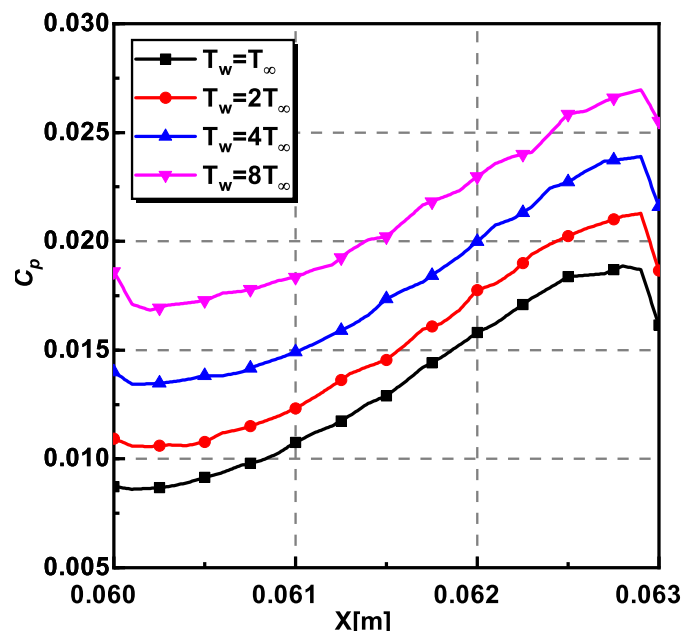


FIGURE 6.78: Variation of the non-dimensional temperature along the length of open cavity for different T_w

fairly constant till the outlet. Inside the cavity, the pressure coefficient C_p has a smaller magnitude and shows a gradually increasing trend along the cavity length, and have greater magnitudes for higher T_w .

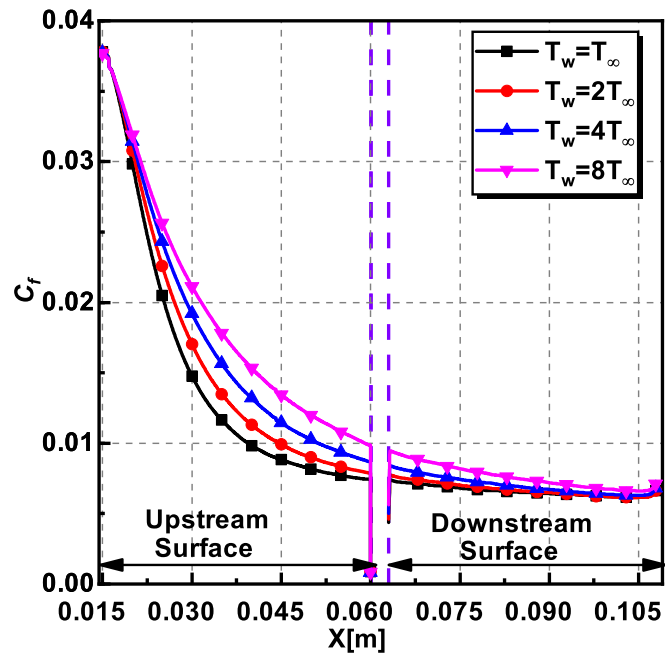
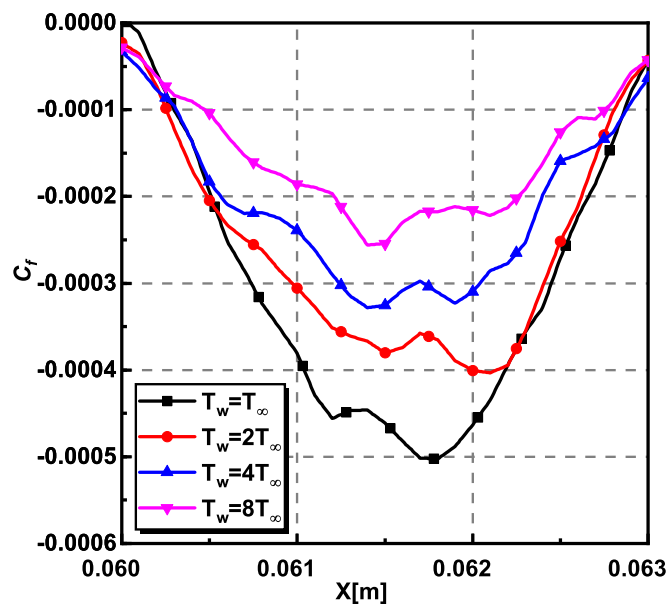
Skin friction coefficient:

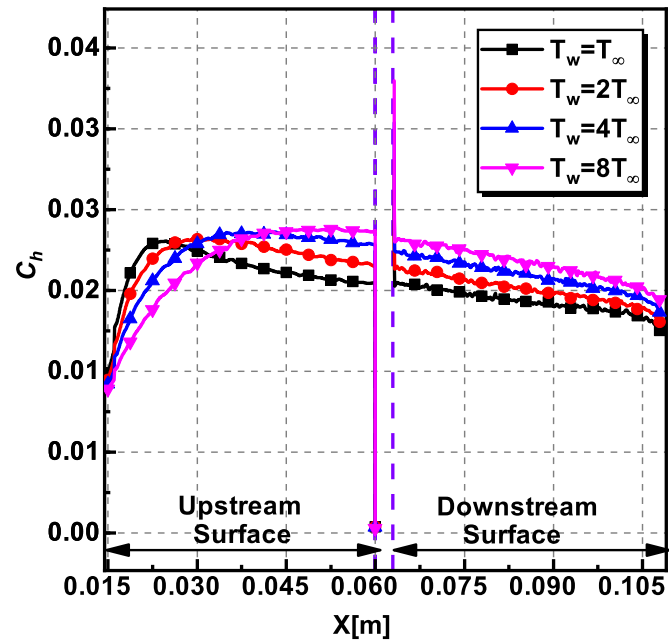
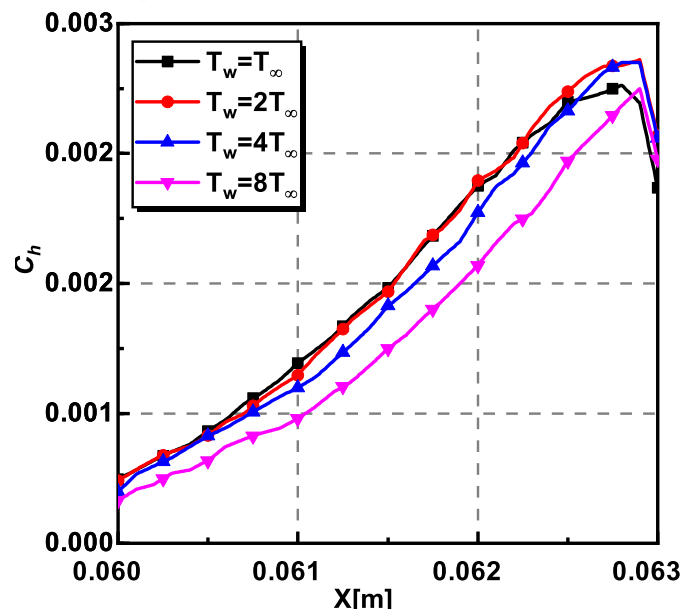
(A) C_p on the upstream and downstream surfaces.(B) C_p on the cavity base.FIGURE 6.79: Variation of pressure coefficient C_p for open cavity for different T_w .

The variation of skin friction coefficient (C_f) for different T_w on the upstream, downstream, and the base surface of the cavity is shown in Figure 6.80. Similar to C_p variation for different T_w , the magnitudes C_f increases with increasing wall temperature. As the wall temperature increases, the fluid's viscosity increases and contributes to a rise in the viscous forces. The increase in viscous forces leads to an overall rise in the C_f . Also, when compared against the skin friction magnitudes for different Ma , the magnitudes for different T_w are substantially lower. Along the upstream surface the C_f shows a diminishing trend similar to the one observed in the continuum regime for flat plate flows. Along the downstream surface, C_f shows a quick jump and then a marginal decrease towards the outlet. From eq. 6.5, it is found that the tangential mean flow velocity of the incident molecules influences the skin friction coefficient C_f . Along the flow direction on the lower surface, the change in skin friction coefficient C_f is marginal as the flow velocity is roughly constant. Inside the cavity, C_f is negative as expected for all the cases owing to the presence of a recirculation zone.

Heat transfer coefficient:

The variation of heat transfer coefficient (C_h) for different T_w on the upstream, downstream, and the base surface of the cavity is shown in Figure 6.81. Initially, it is found that the magnitude of C_h shows a peak whose distance from the inlet increases with T_w . However, the trend in variation with T_w is reversed as the flow progresses and the C_h values are greater for higher T_w . Along the downstream surface, the C_h follows a similar pattern for all the cases. The near-wall fluid heats up more for higher wall temperatures, resulting in a higher wall heat flux. Towards the outlet, the profiles show a declining trend. Inside the cavity, C_h again follows a similar trend, but its magnitudes are much

(A) C_f on the upstream and downstream surfaces.(B) C_f on the cavity base.FIGURE 6.80: Variation of skin friction coefficient C_f for open cavity for different T_w .

(A) C_p on the upstream and downstream surfaces.(B) C_p on the cavity base.FIGURE 6.81: Variation of heat transfer coefficient C_h for open cavity for different T_w .

lesser than those outside the cavity. The magnitude of C_h shows a steady increase as the flow traverses inside the cavity. Thus, by and large, the C_h magnitudes increase with increasing wall temperature due to higher levels of viscous heating effects.

6.3.3 Influence of Knudsen number

This section describes the influence of Knudsen number (Kn) on the flow and surface properties over the open cavity. The different Knudsen numbers studied are given in Table 6.2. For all the instances, the free-stream Mach number considered was 25, with a step height of ($h = 3$ mm), $H = 60$ mm, and $T_w = 4T_\infty$ is used.

Velocity field:

The non-dimensional velocity variation for different Kn at sections $X = 30$ mm, $X = 59$ mm, $X = 61$ mm, and $X = 93$ mm is shown in Figure 6.82. The non-dimensional velocity profiles are similar in appearance upstream of the cavity at $X = 30$ mm and $X = 59$ mm. Inside the cavity at $X = 61$ mm, the velocity magnitudes are negative due to the recirculation effects. This trend is also observed in the continuum study conducted by Camussi *et al.* [160]. Also, up to the cavity height, the velocity field is not influenced by the rarefaction effects as the profiles are relatively the same and are found to overlapping. However, above the cavity height, the rarefaction affects the velocity field, and the profiles show a deviation. At the exit of the domain at $X = 93$ mm, the profiles show resemblance to the ones observed upstream of the cavity. It is found that there is a substantial velocity slip at the walls at all sections, except inside the cavity where the velocity slip is relatively the same for different Kn . This velocity slip increases with rarefaction and falls in line with the results of Ejtehadi *et al.* [161].

Along the transverse direction, the non-dimensional velocity reduces with an increase in Kn . As Kn increases, the molecular mean free path increases substantially, resulting

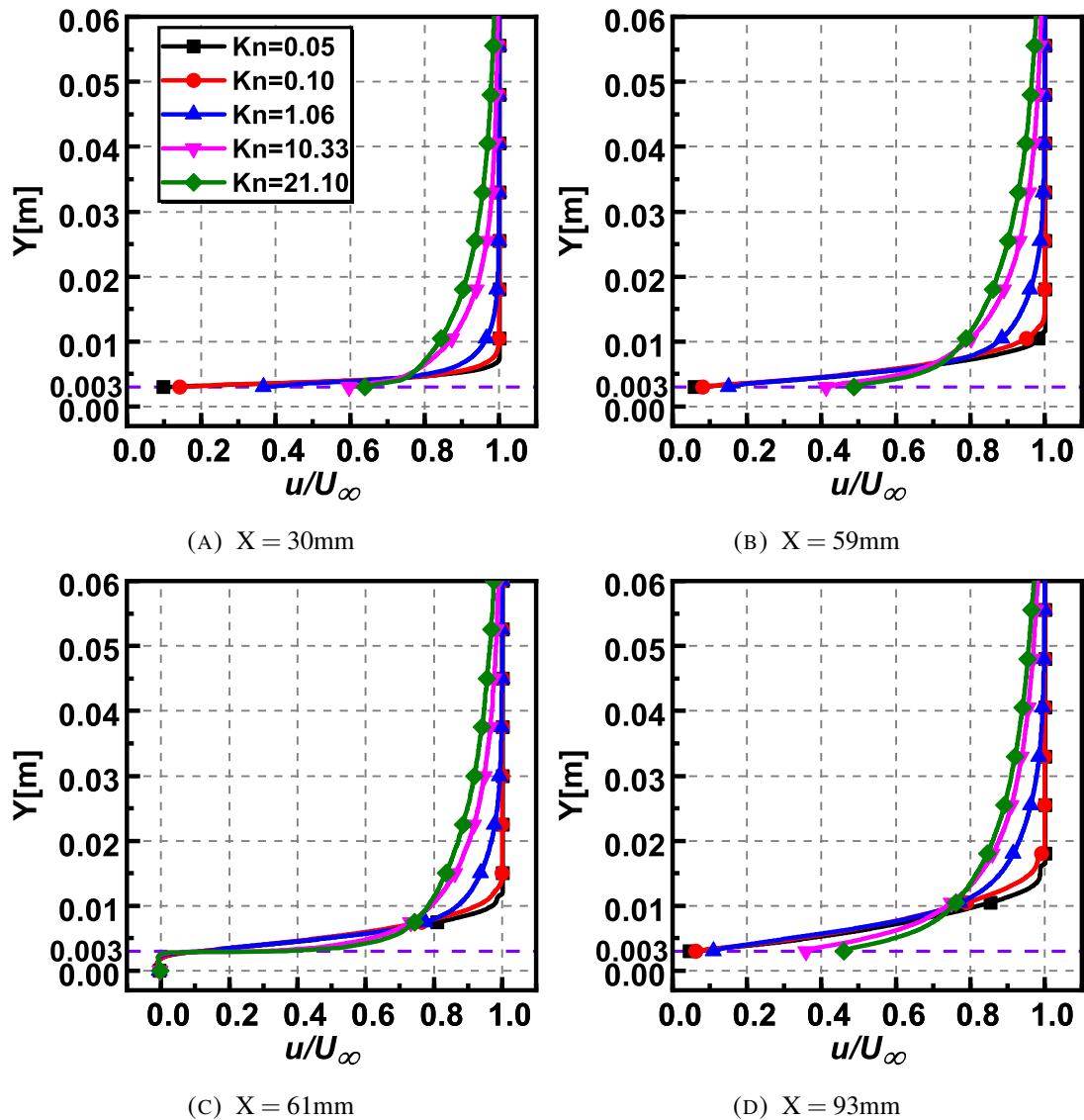


FIGURE 6.82: Variation of the non-dimensional velocity perpendicular to the surface of open cavity for different Kn .

in the more significant propagation of the wall effects into the flow domain. This is corroborated quantitatively by extracting the boundary layer thickness (δ). Here, the boundary layer thickness (δ) is calculated by considering $u/U_\infty = 0.99$. For the top surface location considered in the present study, the boundary layer is fully established for different Kn , except $Kn = 21.10$, which shows a developing trend. For a particular location of $X = 59\text{mm}$, (δ) and (δ/H) are given in Table 6.14.

TABLE 6.14: Boundary layer thickness (δ) at $X = 59\text{mm}$ of open cavity for different Kn .

Kn	0.05	0.10	1.06	10.33	21.10
$\delta(\text{mm})$	3.65	4.9	12.25	39.4	-
δ/h	1.21	1.63	4.08	13.13	-
δ/λ	24.1	16.3	3.84	1.27	-

The non-dimensional velocity variation for different Kn at sections $Y/h = 0.3$, $Y/h = 0.6$ and $Y/h = 1$ is shown in Figure 6.83. Near the base of the cavity for $Y/h = 0.3$, the non-dimensional velocity, as expected, is negative due to the flow recirculation. Also, the decrease in the velocity is highest for the lowest case of $Kn = 0.05$ in the slip regime. In contrast, in the transition and free molecular regime, the decrease in velocity is comparatively smaller. Interestingly, for $Y/h = 0.6$, the velocity magnitudes are positive in the slip regime and continue to show negative trends in the other regimes. This trend can be credited to the nature of the recirculation region found in the different regimes. At the top surface of the cavity for $Y/h = 1$, the profiles are positive as expected. Also, the velocity magnitudes increase with an increase in rarefaction due to the increased local mean free path, which displaces the molecules farther in the flow field.

The velocity streamlines for different Kn are depicted in Figure 6.84. It is observed that for all Kn , a recirculation region exists. Furthermore, streamlines of the free-molecular flow for the case of $Kn = 10.33, 21.10$ suggests that there exists a secondary smaller recirculation region. The vortex center shifts towards the top of the cavity as the rarefaction increases. The location of the primary vortex for different Kn is shown in Table 6.15.

Pressure field:

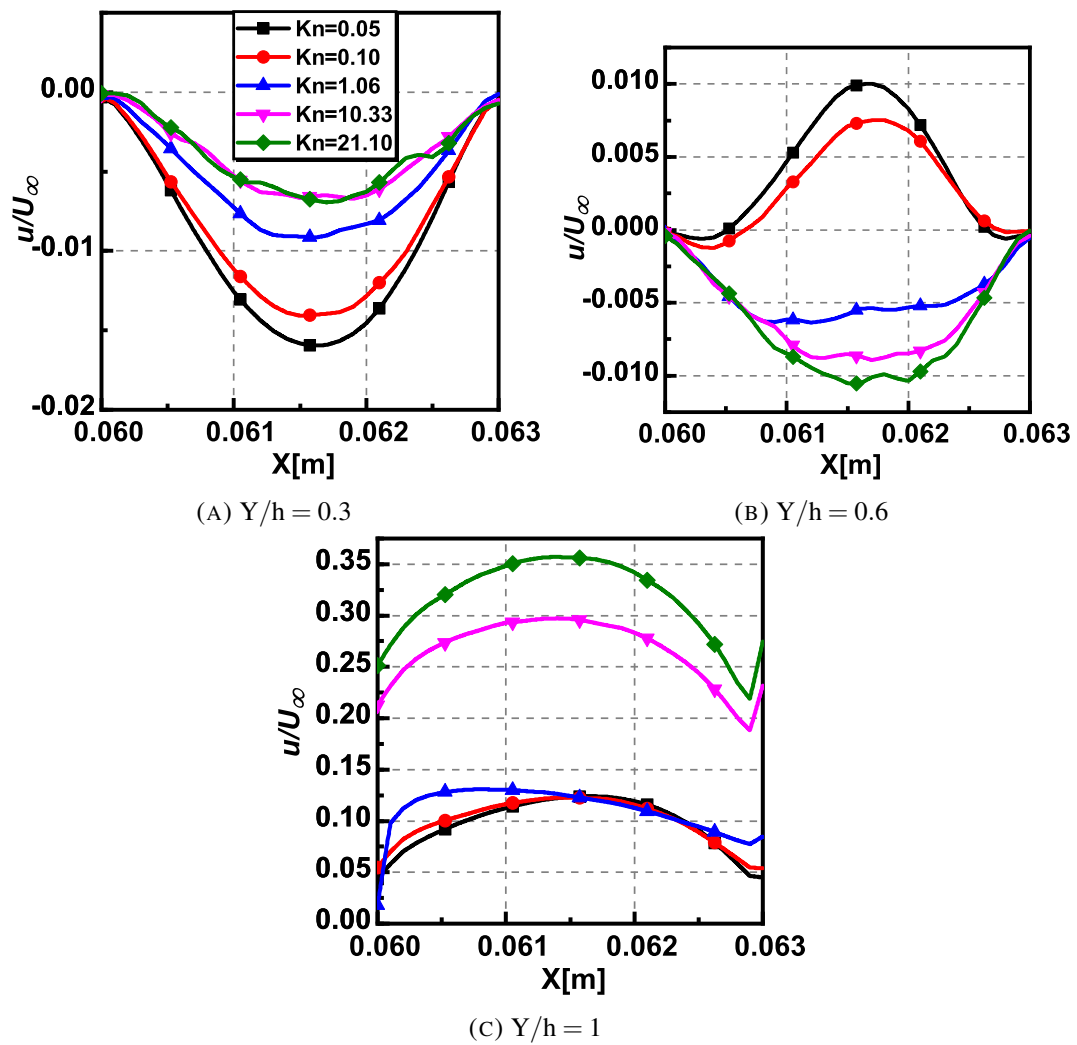


FIGURE 6.83: Variation of the non-dimensional velocity along the length of open cavity for different Kn

TABLE 6.15: Variation of the center of the primary vortex of open cavity for different Kn .

Knudsen number	Primary vortex location
	(X_c, Y_c) [mm]
$Kn = 0.05$	(1.6, 1.8)
$Kn = 0.1$	(1.7, 1.8)
$Kn = 1.06$	(1.8, 2.2)
$Kn = 10.33$	(1.9, 2.5)
$Kn = 21.10$	(2.3, 2.8)

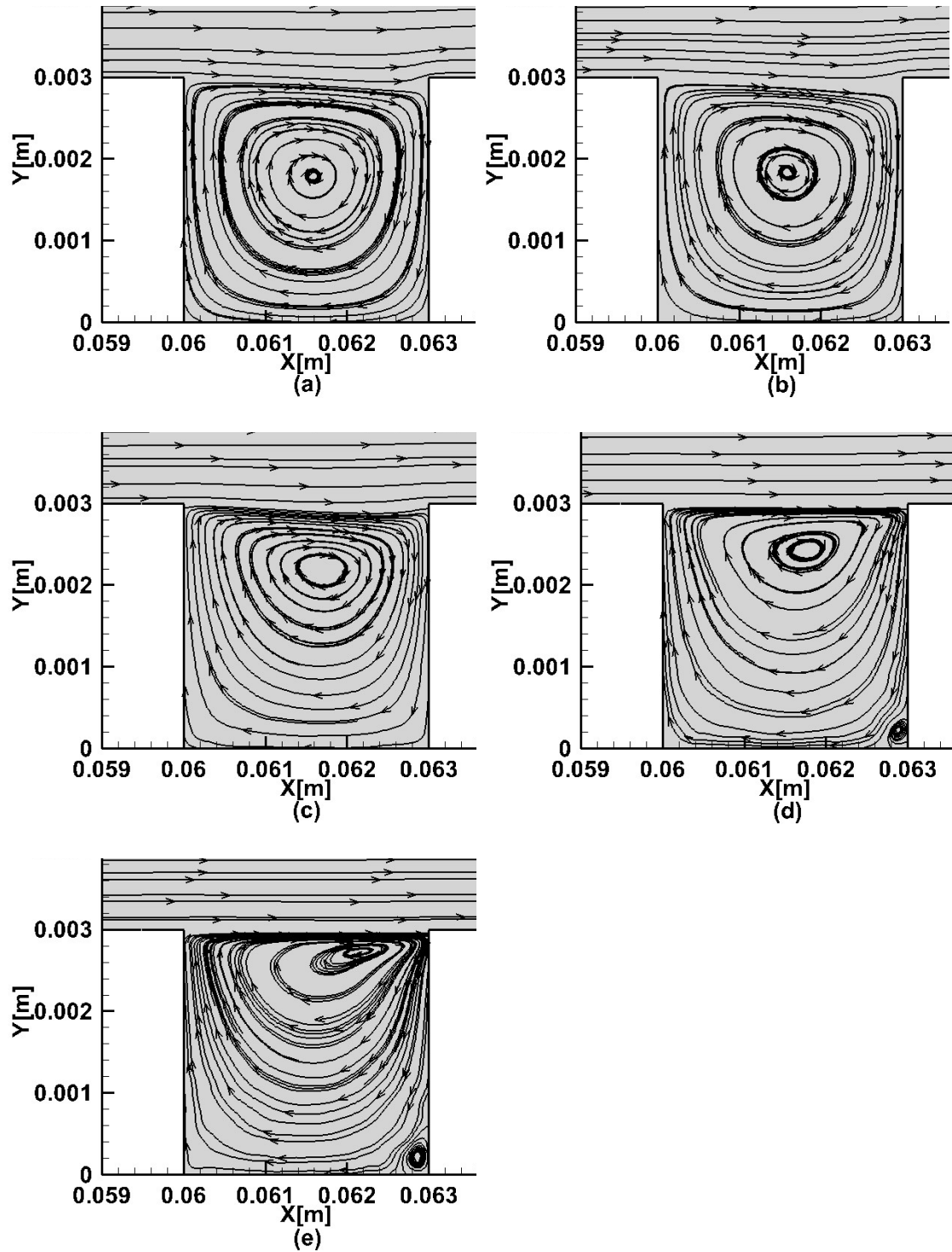


FIGURE 6.84: Streamlines inside the cavity for (a) $Kn=0.05$, (b) $Kn=0.1$, (c) $Kn=1.06$, (d) $Kn=10.33$, (e) $Kn=21.10$.

The non-dimensional pressure variation for different Kn at sections $X = 30\text{mm}$, $X = 59\text{mm}$, $X = 61\text{mm}$, and $X = 93\text{mm}$ is shown in Figure 6.85. The pressure profiles are found to behave similarly in all the sections; however, the magnitudes differ. The near-wall pressure in all the sections is higher than the corresponding free-stream pressure due to the stagnation effects. Also, in the transverse direction, pressure attains free-stream magnitude considerably quicker in the slip regime. Furthermore, the compressibility effects of the flow create a pressure surge just at the level of the cavity height. Inside the cavity at $X = 61\text{mm}$, the magnitudes of pressure are of the same order as that of the free-stream. In contrast, above the cavity (for $Y > 0.003$), the magnitudes attain a peak (owing to the presence of shock layer upstream) and gradually decrease and attain a free-stream value. For assessment, at section $X = 61\text{mm}$, the peak pressure ratios are 15.36, 18.96, 58.57, 99.08 and 90.73 for Kn 0.05, 0.1, 1.06, 10.33 and 21.10 respectively. Downstream of the cavity at $X = 93\text{mm}$, the pressure magnitudes are relatively lower.

The non-dimensional pressure variation for different Kn at sections $Y/h = 0.3$, $Y/h = 0.6$ and $Y/h = 1$ is shown in Figure 6.86. At $Y/h = 0.3$, the pressure magnitudes decrease with increasing Kn and show minimal variation along the cavity length. In section $Y/h = 0.6$, the profiles are similar as observed at the cavity base. However, there is a gradual rise in the pressure magnitudes along the cavity length. At the top surface of the cavity for $Y/h = 1$, the profiles show a contrasting behavior, and pressure magnitudes increase with increasing Kn and are several orders higher than the free-stream pressure. Due to the compressibility effects of the flow, the stagnation pressure increases, causing a surge in the pressure magnitudes. The pressure profiles show similar behavior in the slip and free molecular regime, and the magnitude of the non-dimensional pressure increases

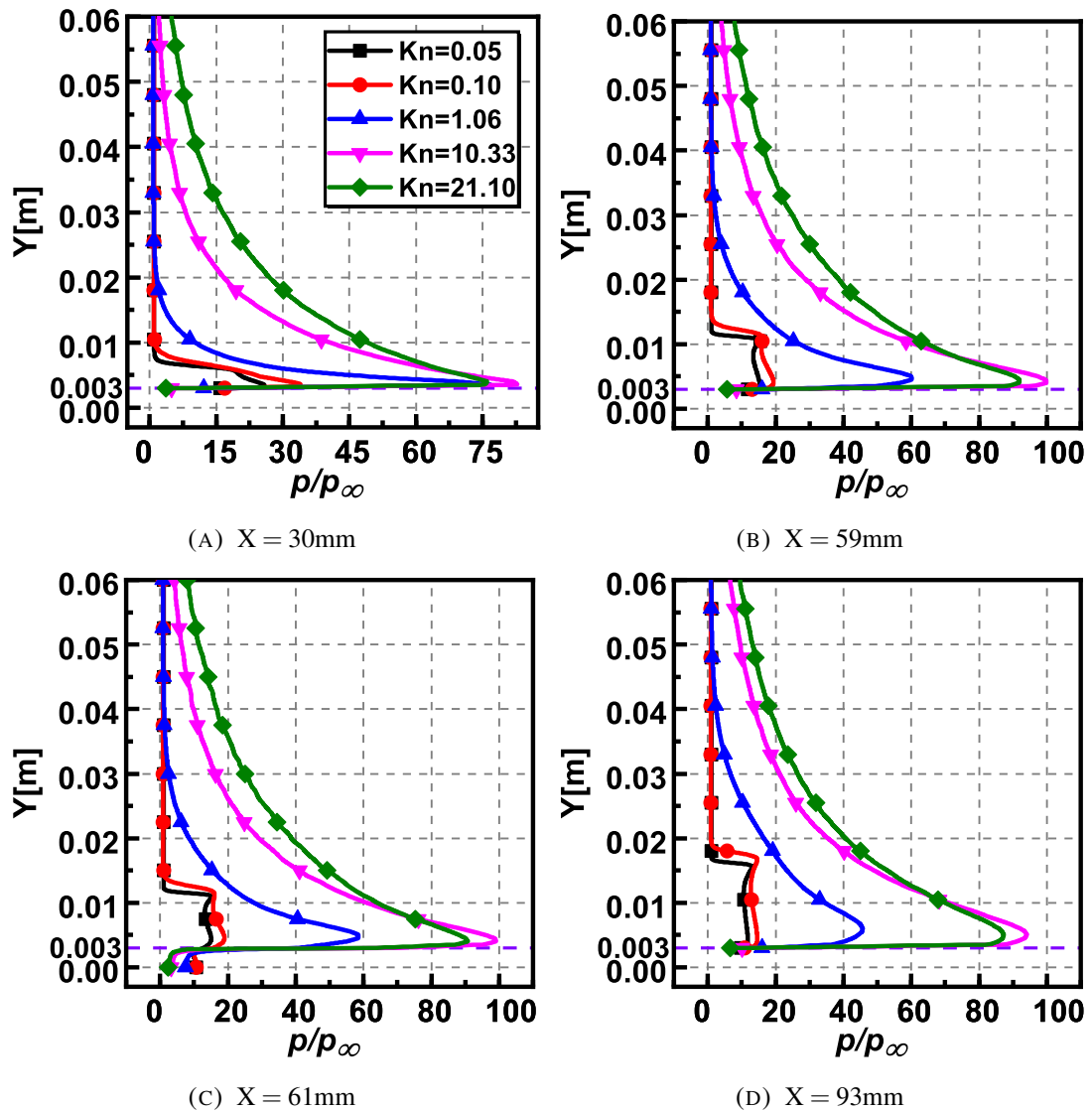


FIGURE 6.85: Variation of the non-dimensional pressure perpendicular to the surface of open cavity for different Kn .

along the cavity length.

Temperature field:

The non-dimensional temperature (T/T_∞) variation for different Kn at sections $X = 30\text{mm}$, $X = 59\text{mm}$, $X = 61\text{mm}$, and $X = 93\text{mm}$ is shown in Figure 6.87. The temperature profiles show a similar trend as the pressure profiles and the magnitudes of temperature

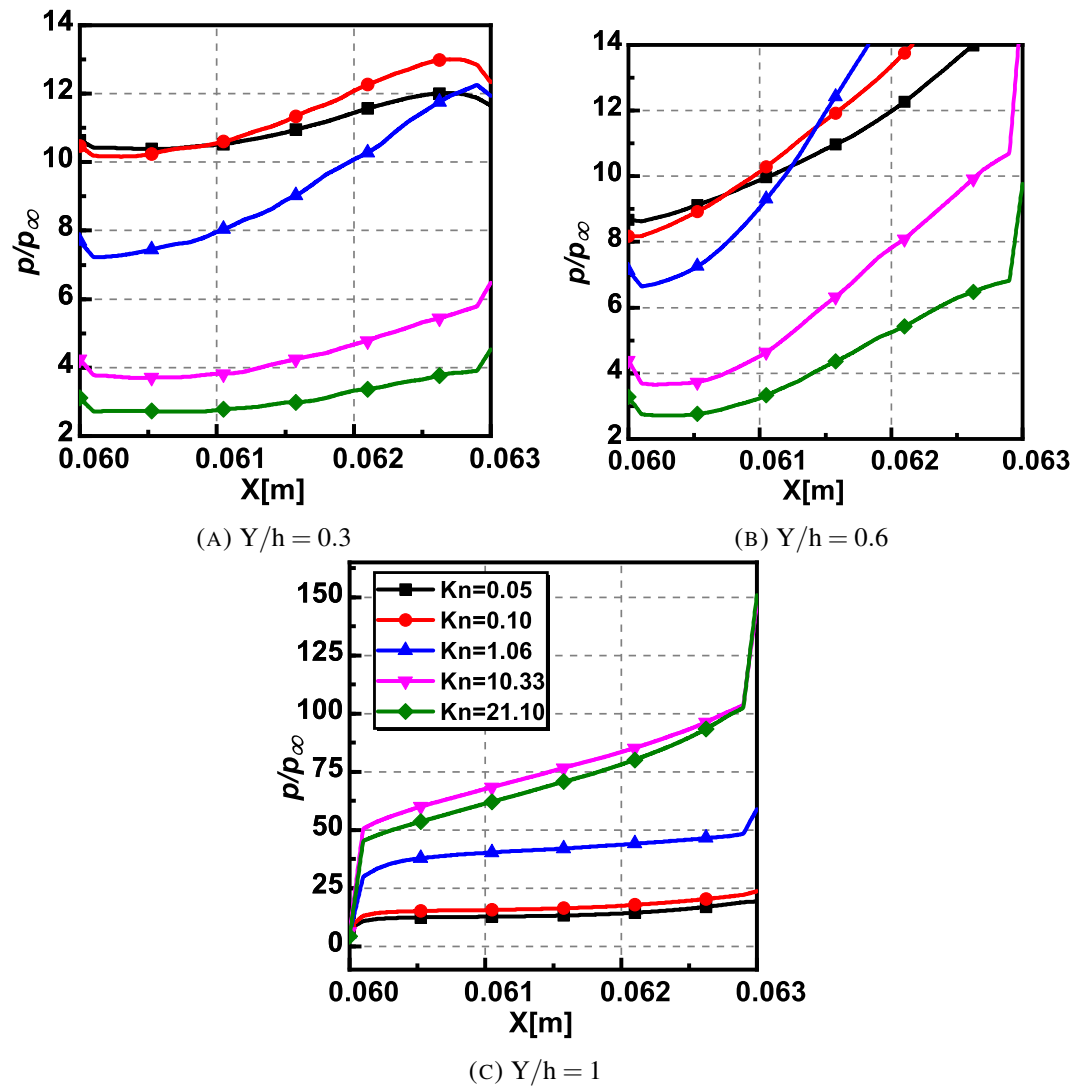


FIGURE 6.86: Variation of the non-dimensional pressure along the length of open cavity for different Kn

increase with increasing Kn . The compressible nature of the incoming flow leads to a significant rise in temperature at the walls. However, in contrast inside the cavity at $X = 61\text{mm}$, the near-wall temperature is similar for different Kn and is of the same order as the free-stream temperature.

In the transverse direction, the non-dimensional temperature surges near the cavity height level and then attains free-stream temperature. Also, at a given transverse location, it is found that the temperature increases with rarefaction. The number density of the

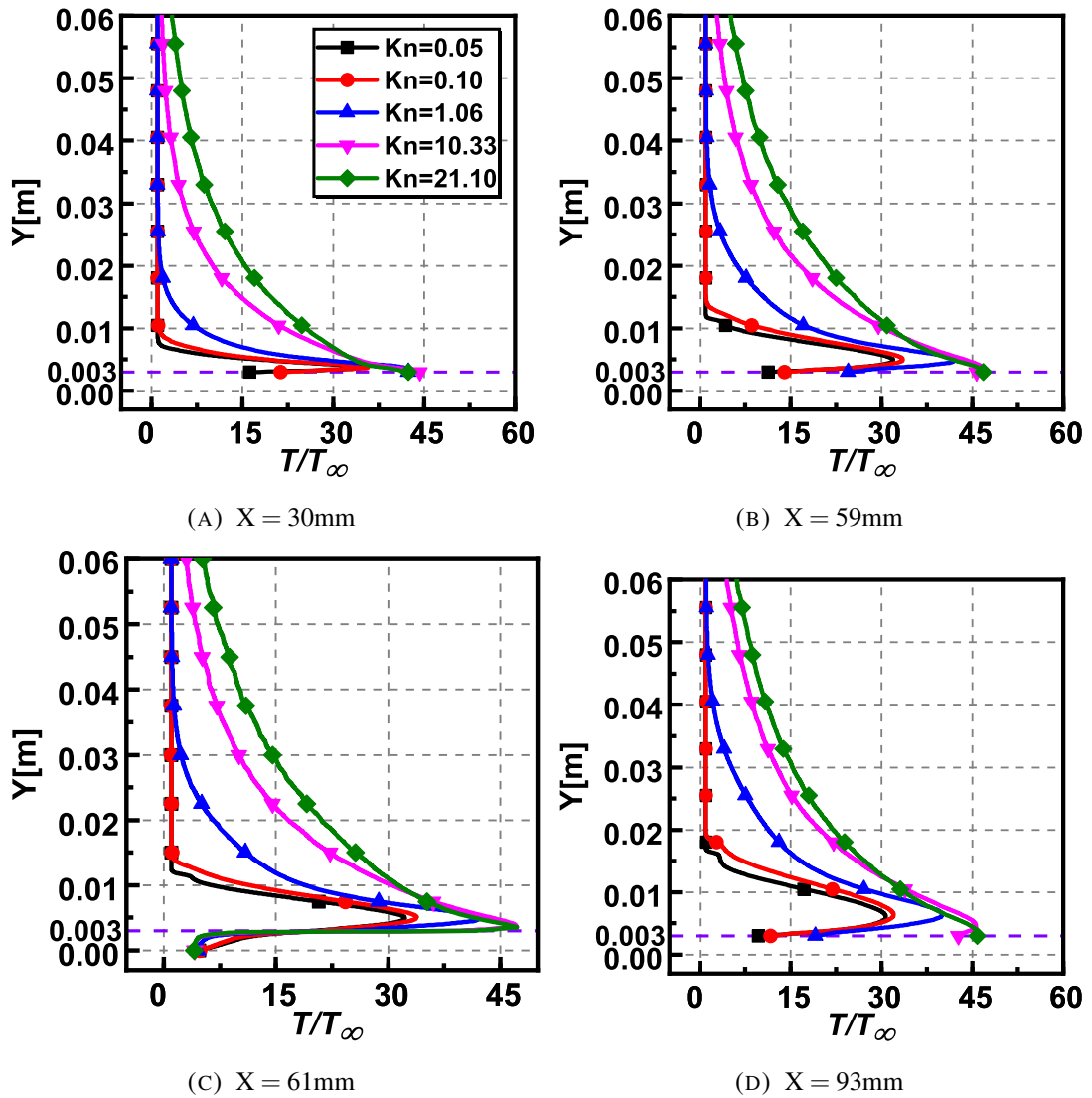


FIGURE 6.87: Variation of the non-dimensional temperature perpendicular to the surface of open cavity for different Kn .

molecules reduces with rarefaction; thereby, the viscous heating generated in the shear layer is distributed among lesser molecules causing a temperature rise. However, at lower levels of rarefactions where the molecules are significantly higher, the same intensity of viscous heating gets distributed among more molecules, inciting a reduced temperature gain. For quantitative assessment, at the section $X = 61\text{mm}$, the non-dimensional temperature at $Y = 0.03$ are 1.00, 0.99, 2.31, 10.02 and 14.53 for Kn 0.05, 0.1, 1.06, 10.33 and 21.10 respectively.

The non-dimensional temperature variation for different Kn at sections $Y/h = 0.3$, $Y/h = 0.6$ and $Y/h = 1$ is shown in Figure 6.88. For $Y/h = 0.3$, the temperature profiles show different trends in different rarefaction regimes. In the slip regime, the temperature increases, reaches a peak and then shows a decrease. Whereas in the other regimes, the temperature steadily increases. A similar trend is observed near the cavity center for $Y/h = 0.6$ but with higher peak magnitudes in the slip regime. At the top surface of the cavity for $Y/h = 1$, the profiles show opposing trends, and similar to pressure, the temperature magnitudes increase with increasing Kn . This trend is again due to the viscous heating in the shear layer.

Pressure coefficient:

The variation of pressure coefficient (C_p) for different Kn on the upstream, downstream, and the base surface of the cavity is shown in Figure 6.89. The C_p shows distinct trends in the slip regime where the profiles are similar for $Kn = 0.05, 0.10$. Also, in the transition and free-molecular regimes, the profiles behave similarly. On the upstream surface, the pressure coefficient C_p in the slip regime, attains a peak at a very short distance from the leading edge and then shows a gradually declining trend towards the edge of the cavity. The early peaks can probably be due to the relatively higher magnitude of near-wall pressure, as seen in Figure 6.85a. In contrast in the transition and free-molecular regime, the C_p gradually rises along the flow direction (X). The peak C_p on the upper surface is observed at X locations of 17.45mm, 20mm, 59mm, 59.40mm, and 59.45mm for Kn 0.05, 0.1, 1.06, 10.33, and 21.10, respectively. Along the downstream surface, the magnitudes of C_p are higher in the beginning and show a reduction towards the outlet for slip regime. For the other regimes, C_p attains a peak and then decreases. Inside the

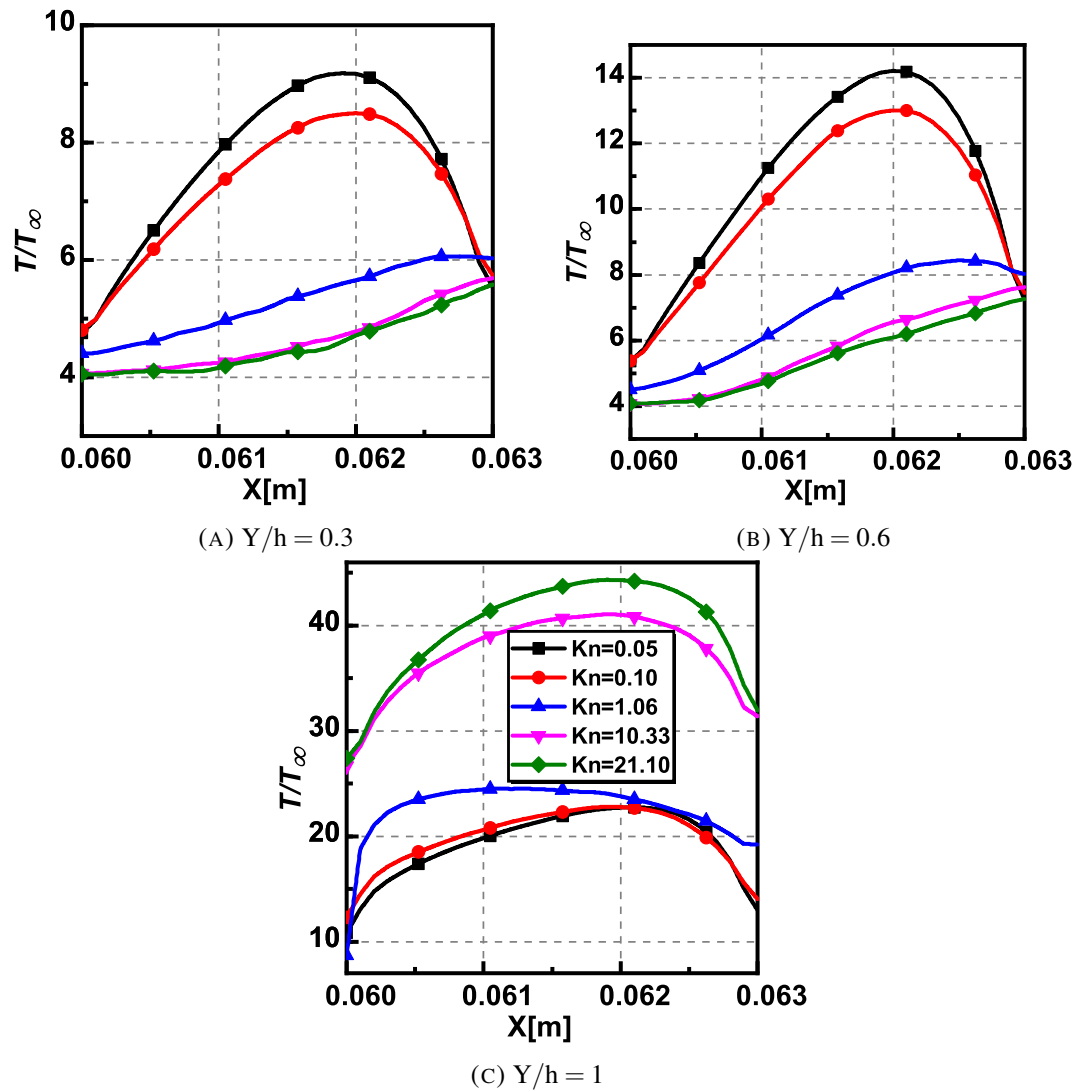
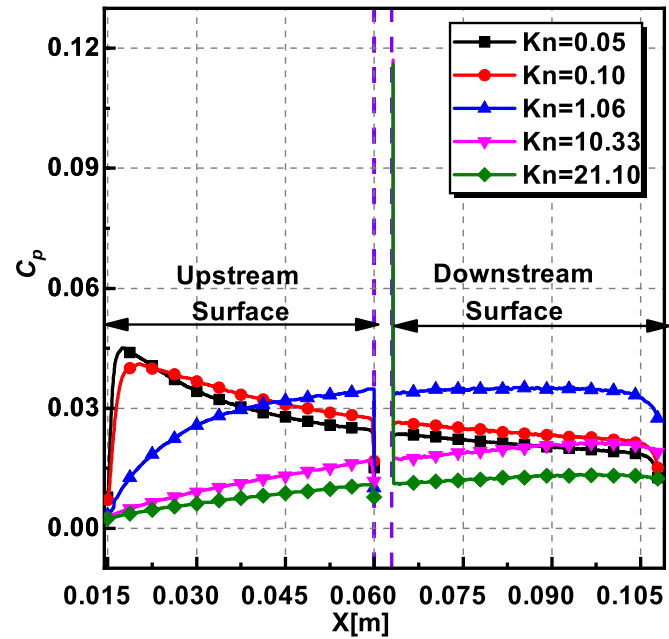
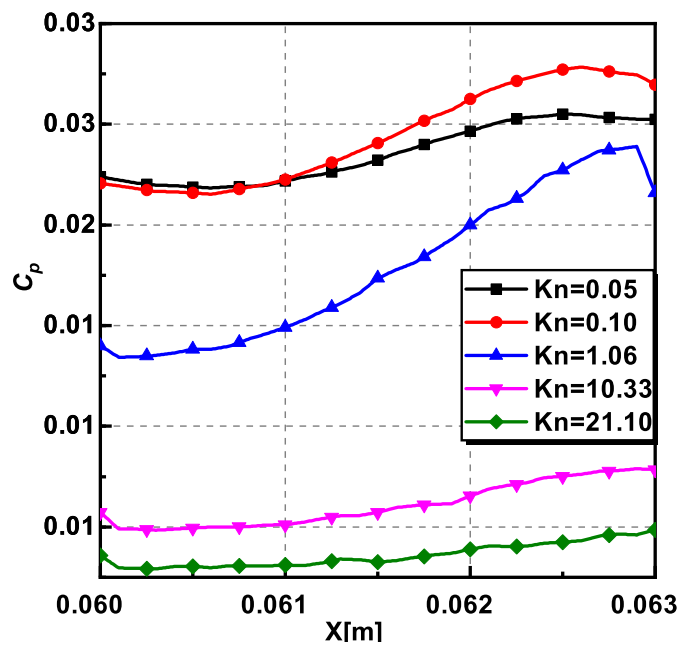


FIGURE 6.88: Variation of the non-dimensional temperature along the length of open cavity for different Kn

cavity, the spatial variation in the pressure coefficient C_p is nominal for different Kn and is found to be unaffected by the rarefaction effects.

Skin friction coefficient:

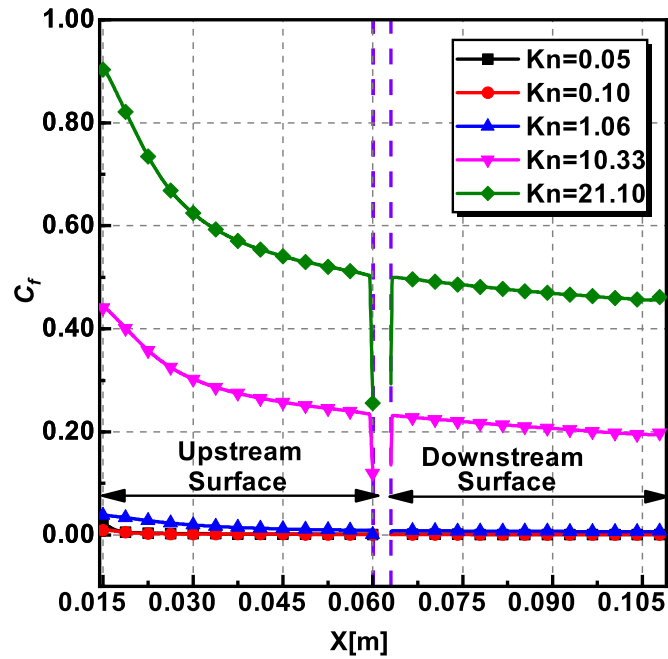
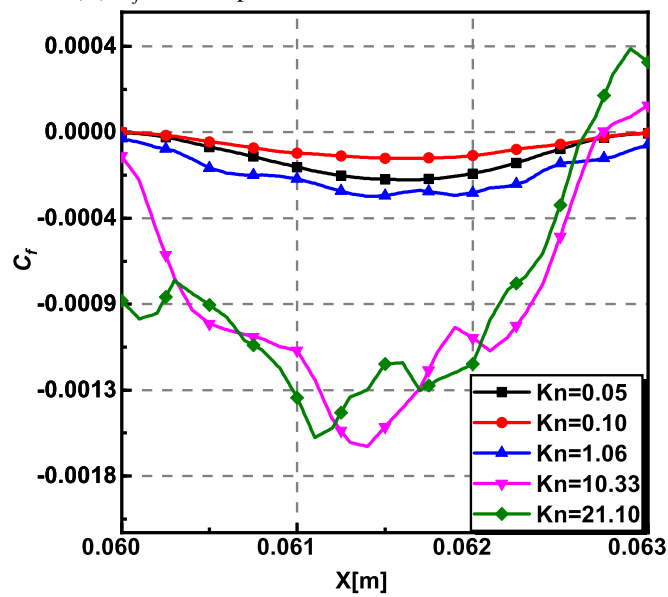
The variation of skin friction coefficient (C_f) for different Kn on the upstream, downstream, and the base surface of the cavity is shown in Figure 6.90. The skin friction

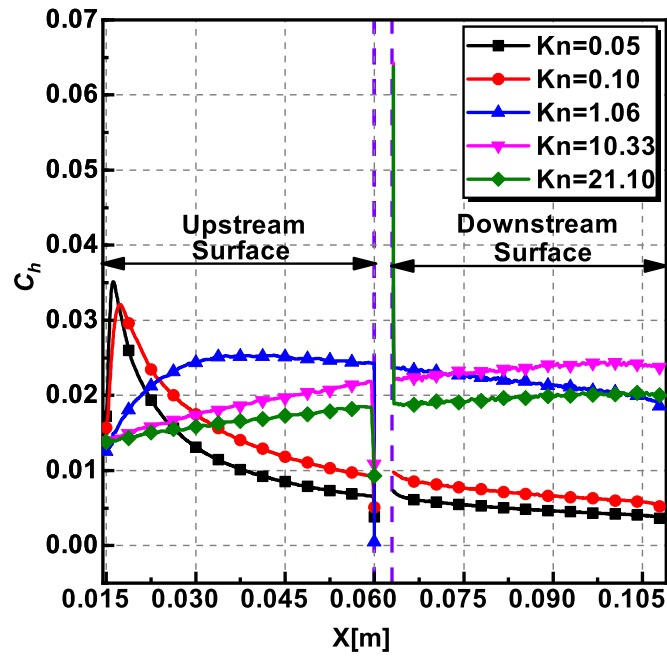
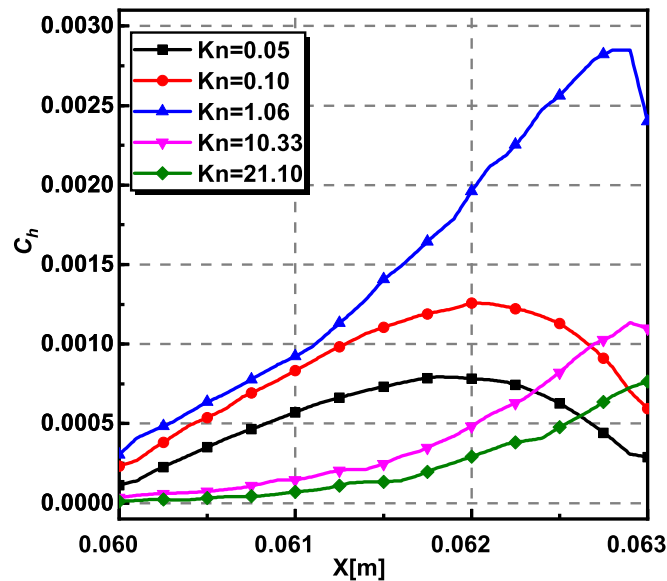
(A) C_p on the upstream and downstream surfaces.(B) C_p on the cavity base.FIGURE 6.89: Variation of pressure coefficient C_p for open cavity for different Kn .

coefficient C_f at a given location increases with increasing Kn . Due to the strong near-wall velocities at the leading edge of the inlet, the C_f is found to attain a peak value. Along the upstream surface, C_f shows a declining trend and attains a lower magnitude at the edge of the cavity. Further, as the flow begins to achieve a high degree of rarefaction, the magnitude of C tends to increase significantly. For instance, C_f at the inlet, increases by two folds on transitioning from $Kn = 10.33$ to $Kn = 21.10$. Along the downstream surface, the C_f decreases very marginally. Inside the cavity, the C_f is negative for all the cases due to recirculation observed in the streamline plot (see Figure 6.84). The decrease in C_f is higher in the free-molecular regime when compared to the other regimes. Also, in the free-molecular regime, the variation in C_f is significant due to the asymmetry of the vortex formed, whereas for $Kn \leq 1.06$, the C_f is fairly constant due to the symmetry in the vortex.

Heat transfer coefficient:

The variation of heat transfer coefficient (C_h) for different Kn on the upstream, downstream, and the base surface of the cavity is shown in Figure 6.91. The plots of C_h and C_p are similar in appearance. Also, on the upper surface, the profiles are dissimilar for different Kn . Along the upper surface of the cavity, near the leading edge, the heat transfer coefficient C_h show a sudden peak in the slip regime, whereas in the other regimes the C_h shows a gradually increasing trend. Near cavity base, flow expansion caused the temperature reducing, leading to a drop in the heat transfer coefficient C_h . Along the lower surface the C_h values are relatively constant in the slip regime, whereas they show a gradual increase in other regimes. As the rarefaction increases, particles

(A) C_f on the upstream and downstream surfaces.(B) C_f on the cavity base.FIGURE 6.90: Variation of skin friction coefficient C_f for open cavity for different Kn .

(A) C_h on the upstream and downstream surfaces.(B) C_h on the cavity base.FIGURE 6.91: Variation of heat transfer coefficient C_h for open cavity for different Kn .

from the middle of the computational domain participate in the collisions due to the increased mean free path, causing a rise in the heat transfer coefficient.

TABLE 6.16: Geometric parameters of the 2D wall-mounted cube.

Parameter	Value
Length at upstream	60mm
Cube depth (h)	3mm
Cube length (L_3)	3mm
Length at downstream	45mm
Cube position	$X = 60\text{mm}$
Position of leading-edge of the lower surface	$X = 15\text{mm}$

TABLE 6.17: Boundary conditions for the 2D wall-mounted cube.

Surface	A	B	C	D	E
Boundary condition	Wall	Symmetry	Free-stream inlet	Free-stream inlet	Outlet

6.4 Analysis of rarefied flow over wall-mounted cube

In this section, the study of the rarefied flow past a wall-mounted cube is presented. The geometry, boundary conditions, and free-stream conditions are described initially and are followed by the analysis of the results.

Geometry, boundary conditions, and grid:

The schematic illustration of the 2D cube is shown in Figure 6.92. The fluid movement occurs from left to right. The flow along the streamwise and transverse directions is depicted by the coordinates X and Y . The length (L) and depth of the cube (h) was fixed to 3mm. The domain height at the outlet was set at $H = 60\text{mm}$ after conducting an influence study on the flow properties. The various parameters of the cavity are depicted in 6.16. The different boundary conditions applied on various surfaces are given in Table 6.17. The flow conditions adopted are given in Table 6.2.

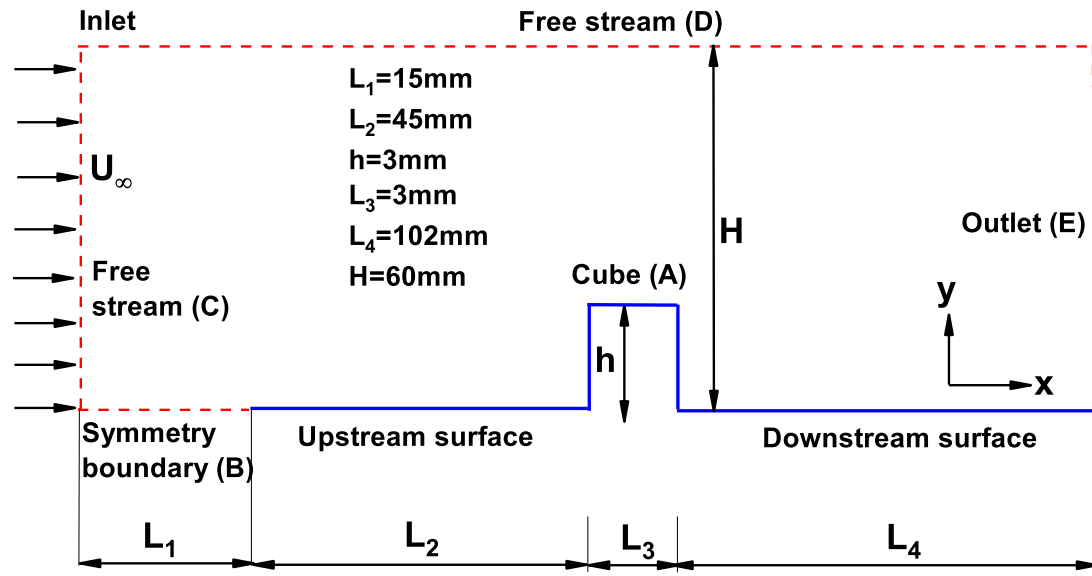


FIGURE 6.92: Schematic of the 2D wall-mounted cube.

The computational domain is divided into several blocks and meshed in a structured manner, as shown in Figure 6.93. The cell widths in both X and Y directions were maintained below the mean free path, i.e., $\Delta x_{cell}, \Delta y_{cell} < 0.3\lambda_\infty$. The cell size was refined near the cavity. The total number of cells for the case of $Kn=1.06$ was about 40,548 cells. Also, the cell count varied for other cases depending on the corresponding mean free path.

6.4.1 Influence of Mach number

This section describes the influence of Mach number (Ma) on the flow and surface properties over the wall-mounted cube. The different Mach numbers studied are $Ma=5$ (Supersonic), 10 (Hypersonic), 25 (High-Hypersonic), and 30 (Reentry speeds). For all instances in this section, $H=60\text{mm}$, $Kn=1.06$ and $T_w=4T_\infty$ is used.

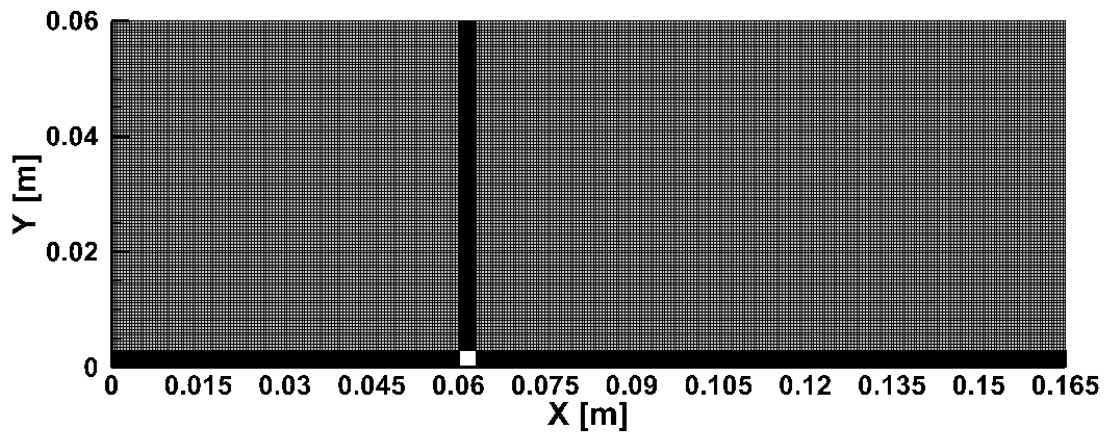


FIGURE 6.93: Meshed domain of the 2D wall-mounted cube.

Velocity field:

The non-dimensional velocity variation for different Ma at the upstream, cube top, and the downstream surface is shown in Figure 6.94. In all the sections, the profiles have higher magnitudes for lower Ma , which can be attributed to lower viscous dissipation. At the upstream surface, the non-dimensional velocity is greater at the inlet side and decreases towards the cube, and attains a negative value due to the flow recirculation on the upstream side of the cube. On the cube surface, the profiles for different Ma are found to follow a common trend and are relatively the same along the cube surface. On the downstream side, the profiles are again negative for a short distance due to recirculation and gradually increase towards the outlet.

Pressure field:

The non-dimensional pressure variation for different Ma at the upstream, cube top, and the downstream surface is shown in Figure 6.95. The non-dimensional pressure remains

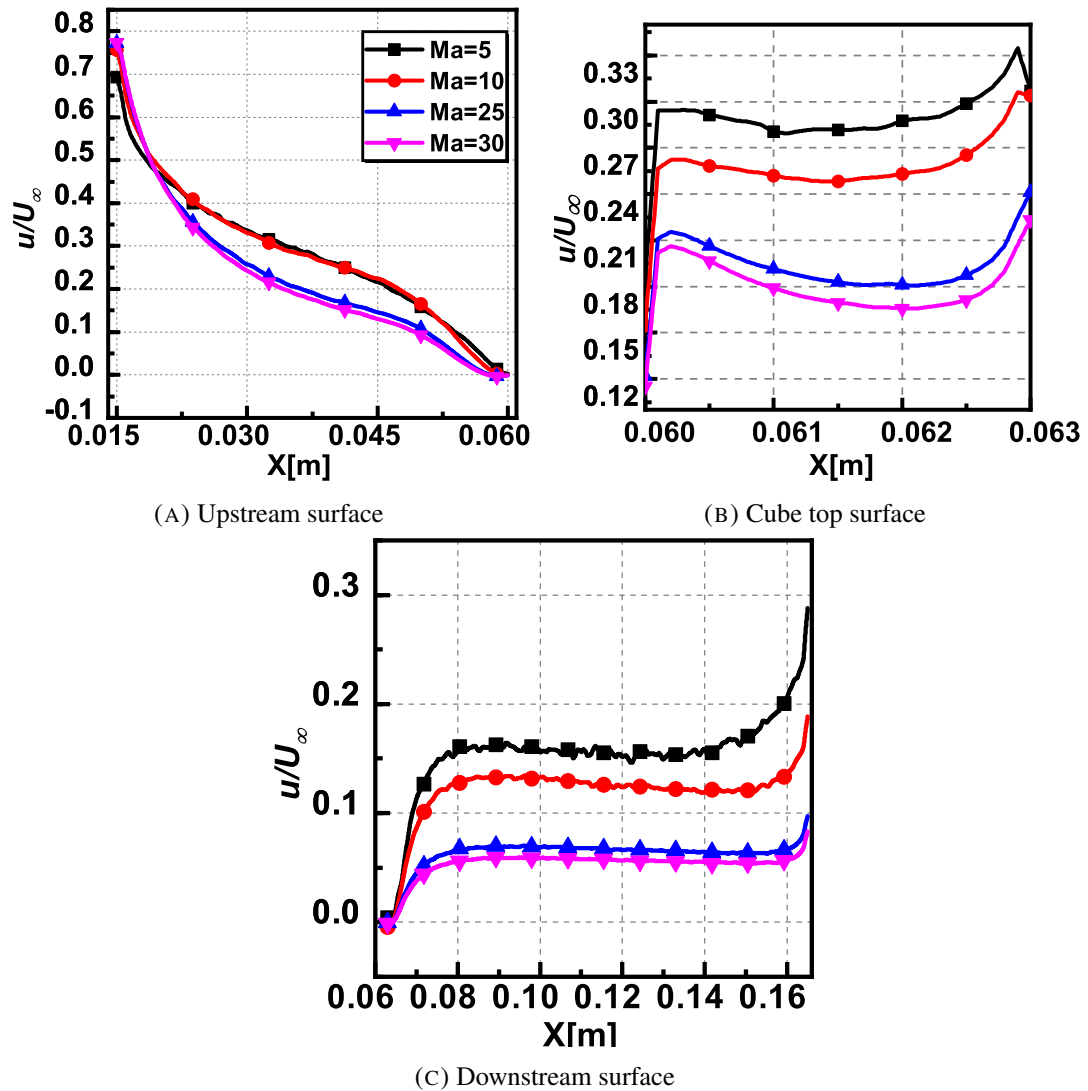


FIGURE 6.94: Variation of the non-dimensional velocity along the length of wall-mounted cube for different Ma

relatively constant along the upstream surface for most of the domain. It increases towards the cube due to the stagnation pressure rise caused by the incoming fluid stream. At lower Ma , the pressure rise is not significant when compared against the other cases. On the top surface of the cube, the pressure is relatively unaffected by the changes in Ma and the profiles are relatively constant along the cube length. On the downstream side, the pressure is low initially due to the recirculation effects and increases for a short distance and remains relatively constant after that. Thus, in all the cases, the pressure

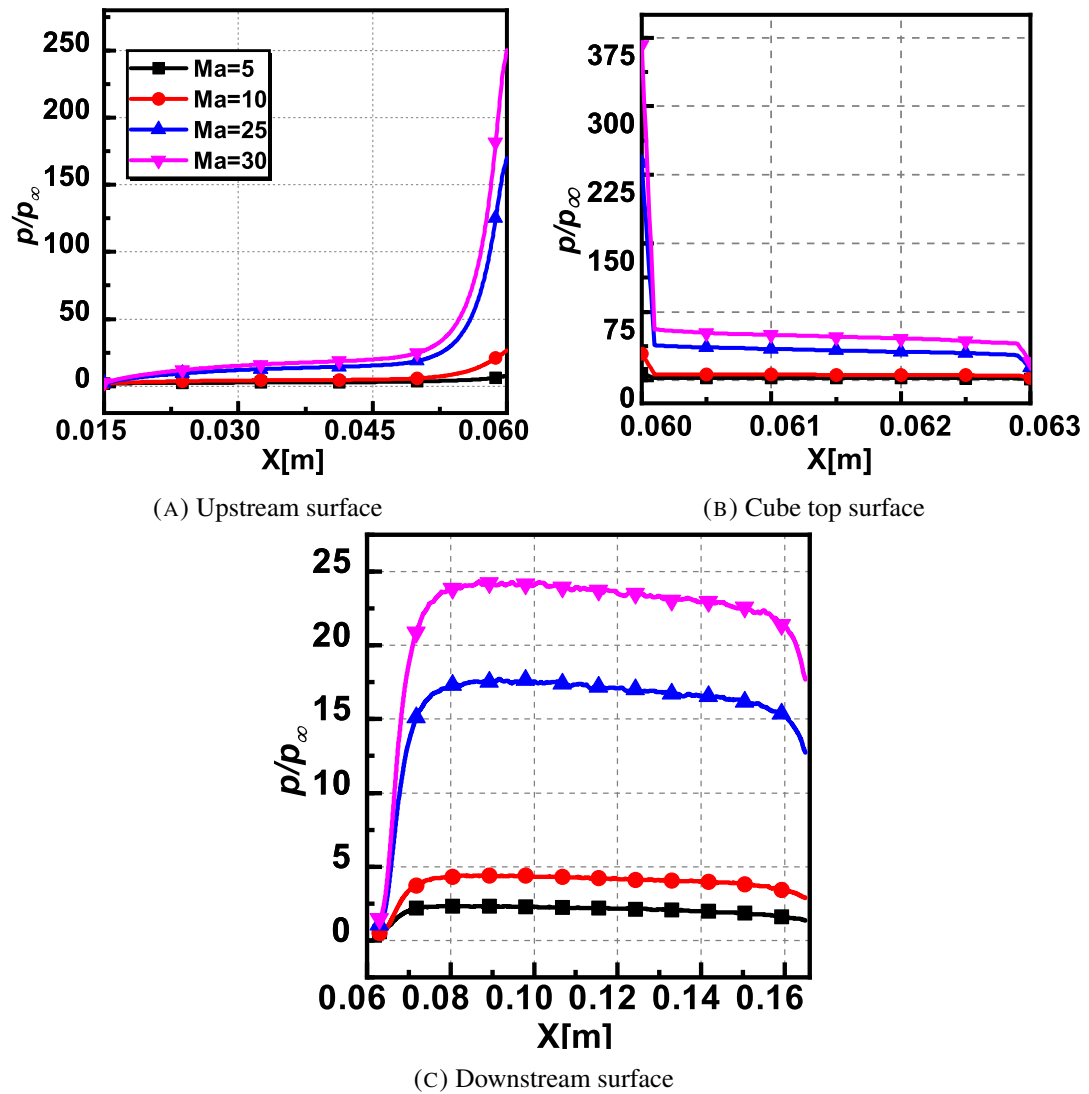


FIGURE 6.95: Variation of the non-dimensional pressure along the length of wall-mounted cube for different Ma

magnitudes are directly influenced by the Ma and show an increase with Ma .

Temperature field:

The non-dimensional temperature variation for different Ma at the upstream, cube top, and the downstream surface is shown in Figure 6.96. In all the sections, the temperature change is minimal for the lower Ma , whereas for $Ma \geq 25$, a significant change is observed. At the upstream surface, the temperature shows an initial peak for $Ma \geq 25$

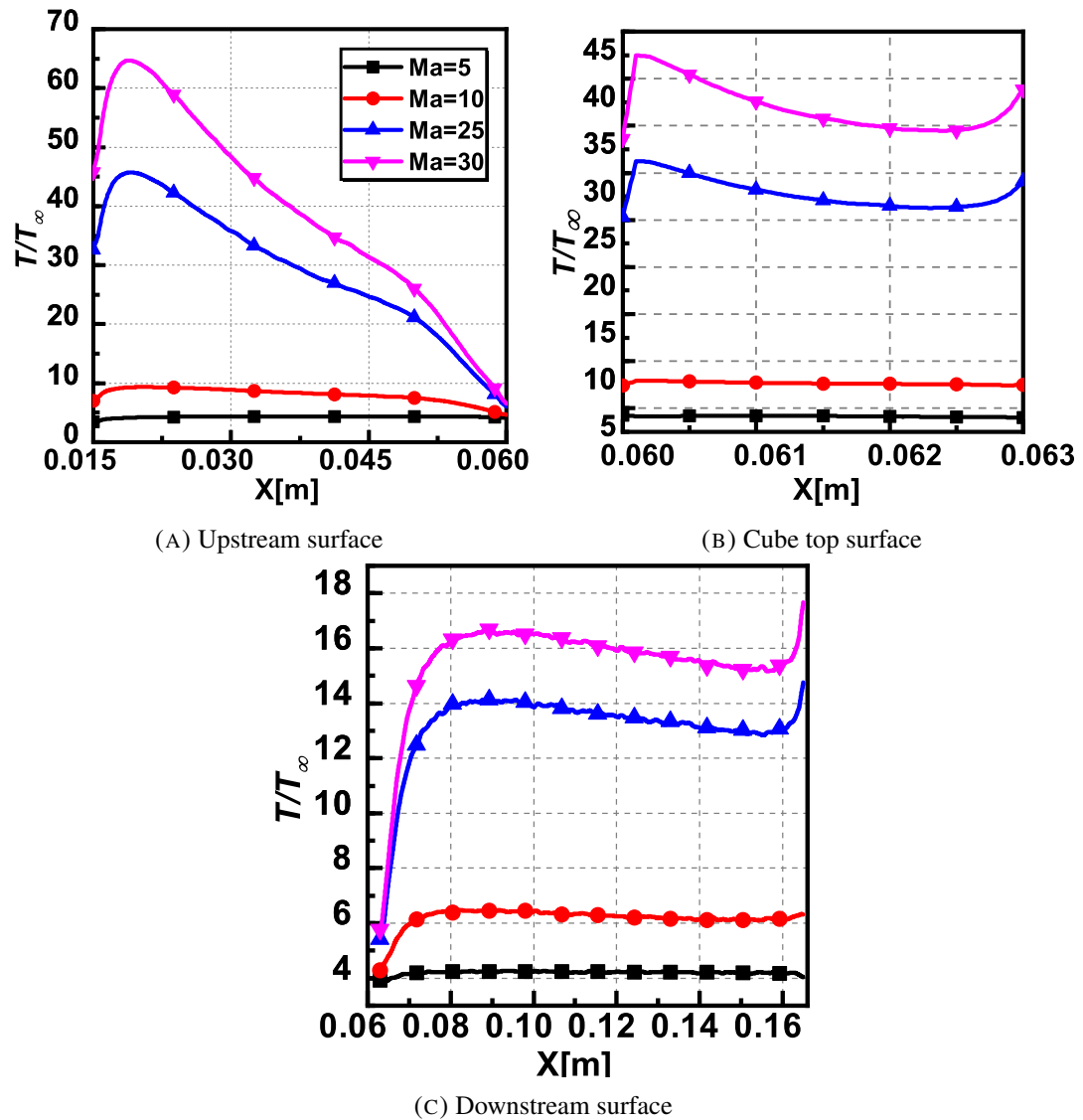


FIGURE 6.96: Variation of the non-dimensional temperature along the length of wall-mounted cube for different Ma

due to the viscous dissipation effects and continues to decline after that. On the top surface of the cube, the profiles are reasonably constant all along the cube length. On the downstream side, the profiles again show an initial peak and remain the same towards the outlet.

Pressure coefficient:

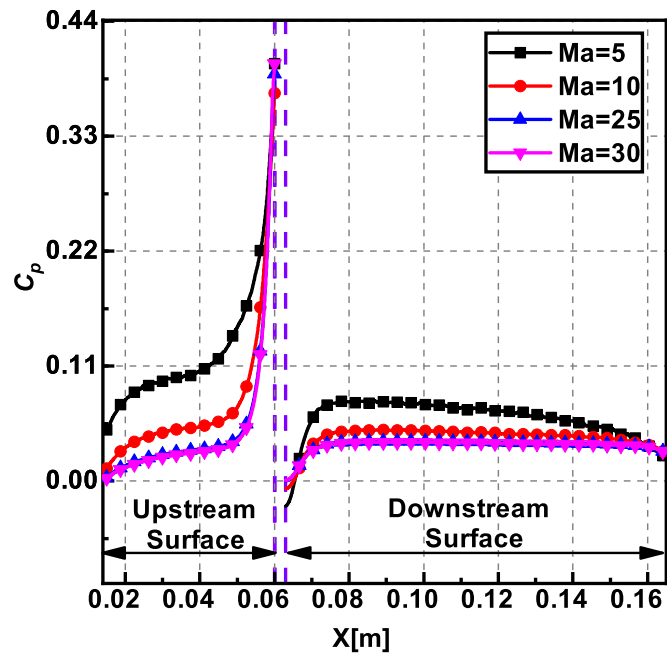
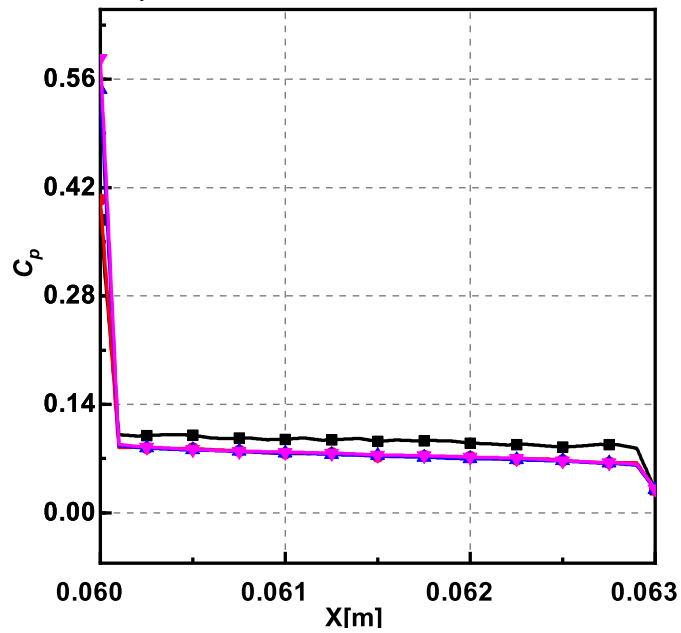
Figure 6.97a shows that the pressure coefficient C_p on the upstream and downstream surface for different Ma . The C_p magnitudes are low at the leading edge and show a gradual increase. Near the vicinity of the cube, the C surges many folds due to the stagnation pressure rise. On the downstream side, the C_p increases in the beginning for a short distance and then remains relatively constant towards the outlet. Also, the C_p magnitudes are found to decrease with increasing Ma . On the top surface of the cube, as shown in Figure 6.97b, the profiles are similar, depicting minimal influence of the compressibility effects on the magnitudes of C_p .

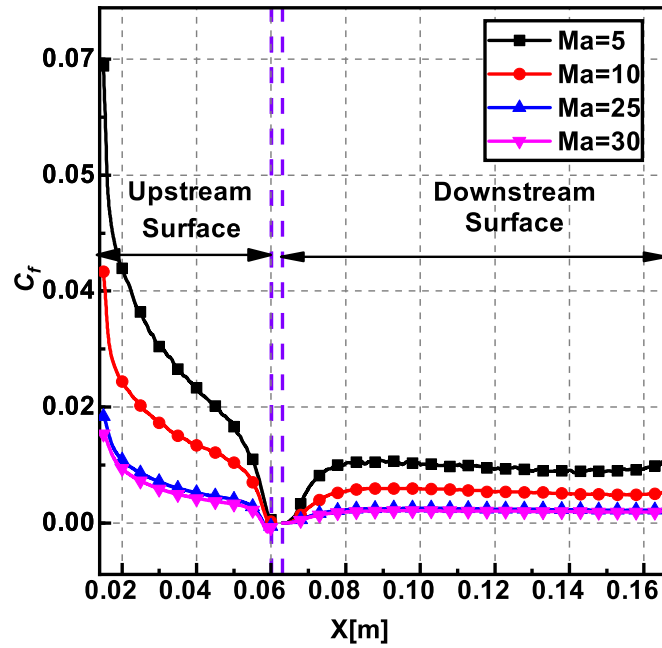
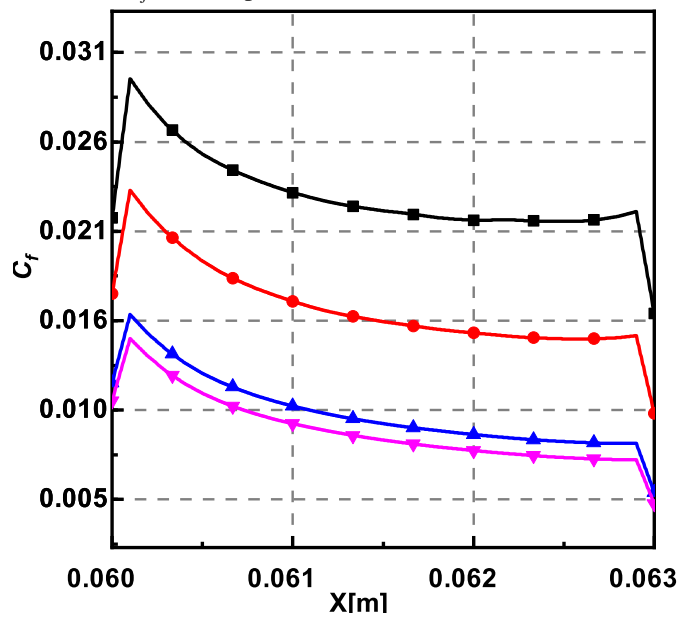
Skin friction coefficient:

Figure 6.98a shows that the skin friction coefficient C_f on the upstream and downstream surfaces for different Ma . The initial high magnitudes in C_f at the leading edge is due to the high-velocity gradients. The C_f magnitudes then show a declining trend and attain negative magnitudes near the cube owing to the flow recirculation. On the downstream surface, the C_f shows an initial increase and remains constant towards the outlet. The C_f profile on top surface of the cube shown in Figure 6.98b is found to decrease all along the cube length.

Heat transfer coefficient:

Figure 6.99 shows that the heat transfer coefficient C_h on the upstream and downstream surfaces for different Ma . On the upstream surface, the C_h shows a decrease for $Ma=5$, whereas, it follows a gradually increasing trend for the other cases. On the downstream side, the C_h increases initially and shows a gradual decline after that. However, the

(A) C_p on the upstream and downstream surfaces.(B) C_p on the cube top surface.FIGURE 6.97: Variation of pressure coefficient C_p for wall-mounted cube for different Ma .

(A) C_f on the upstream and downstream surfaces.(B) C_f on the cube top surface.FIGURE 6.98: Variation of skin friction coefficient C_f for wall-mounted cube for different Ma .

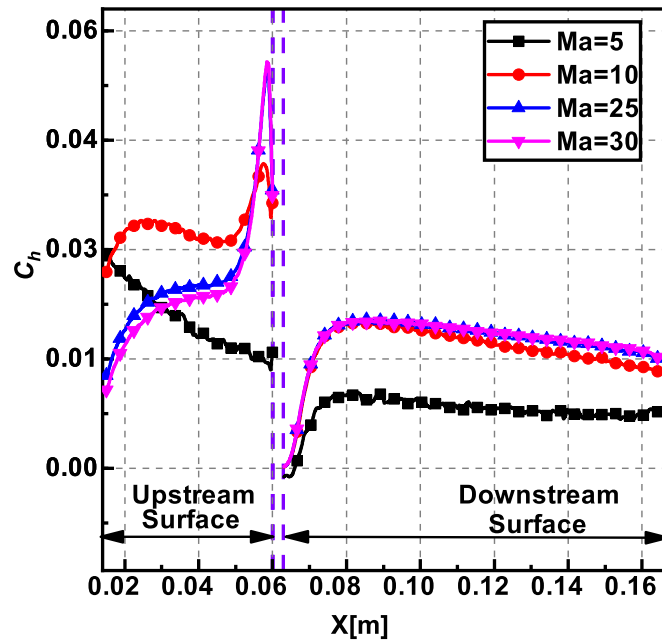
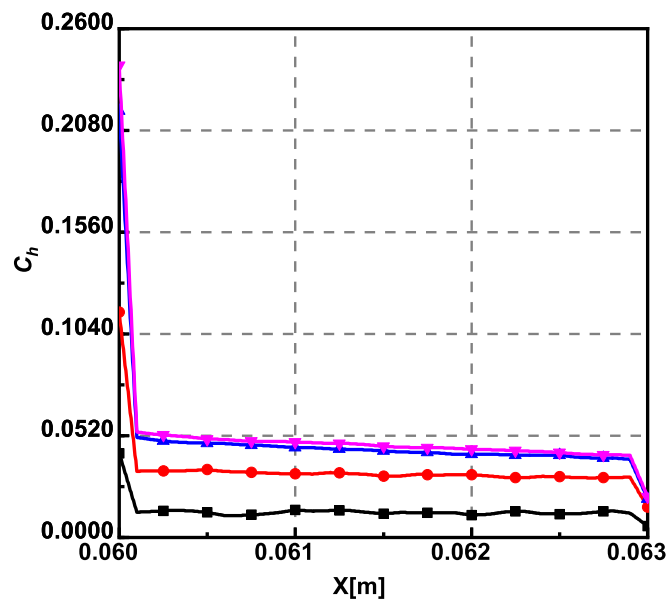
(A) C_h on the upstream and downstream surfaces.(B) C_h on the cube top surface.

FIGURE 6.99: Variation of heat transfer coefficient C_h for wall-mounted cube for different Ma .

magnitude of C_h is lower for $Ma=5$. On the cube's top surface the magnitudes of C_h remain fairly constant along the cube length.

6.4.2 Influence of Wall temperature

This section describes the influence of wall temperature (T_w) on the flow and surface properties over the wall-mounted cube. The wall temperature (T_w) was set to four different values, i.e., T_∞ , $2T_\infty$, $4T_\infty$ and $8T_\infty$ where, $T_\infty = 204$ K. For all instances in this section, $H = 60$ mm, $Kn = 1.06$ and $Ma = 25$ are used.

Velocity field:

The non-dimensional velocity variation for different T_w at the upstream, cube top, and the downstream surface is shown in Figure 6.100. The velocity profiles show an increase in magnitude with increasing T_w . As the wall temperature is increased, the molecules are dispersed at greater distances and increase the velocity. The velocity shows a declining trend along the flow direction and attain negative magnitudes towards the cube on the upstream side. On the cube's top surface, the profiles are similar in appearance for different cases and follow a similar trend. The profiles show a marginal increase at the downstream side of the cube as the flow progresses towards the outlet.

Pressure field:

The non-dimensional pressure variation for different T_w at the upstream, cube top, and the downstream surface is shown in Figure 6.101. The pressure profiles are similar and overlapping at the upstream and the top surface of the cube, however, of varying magnitudes. On the downstream side, the profiles show marginal variation for different

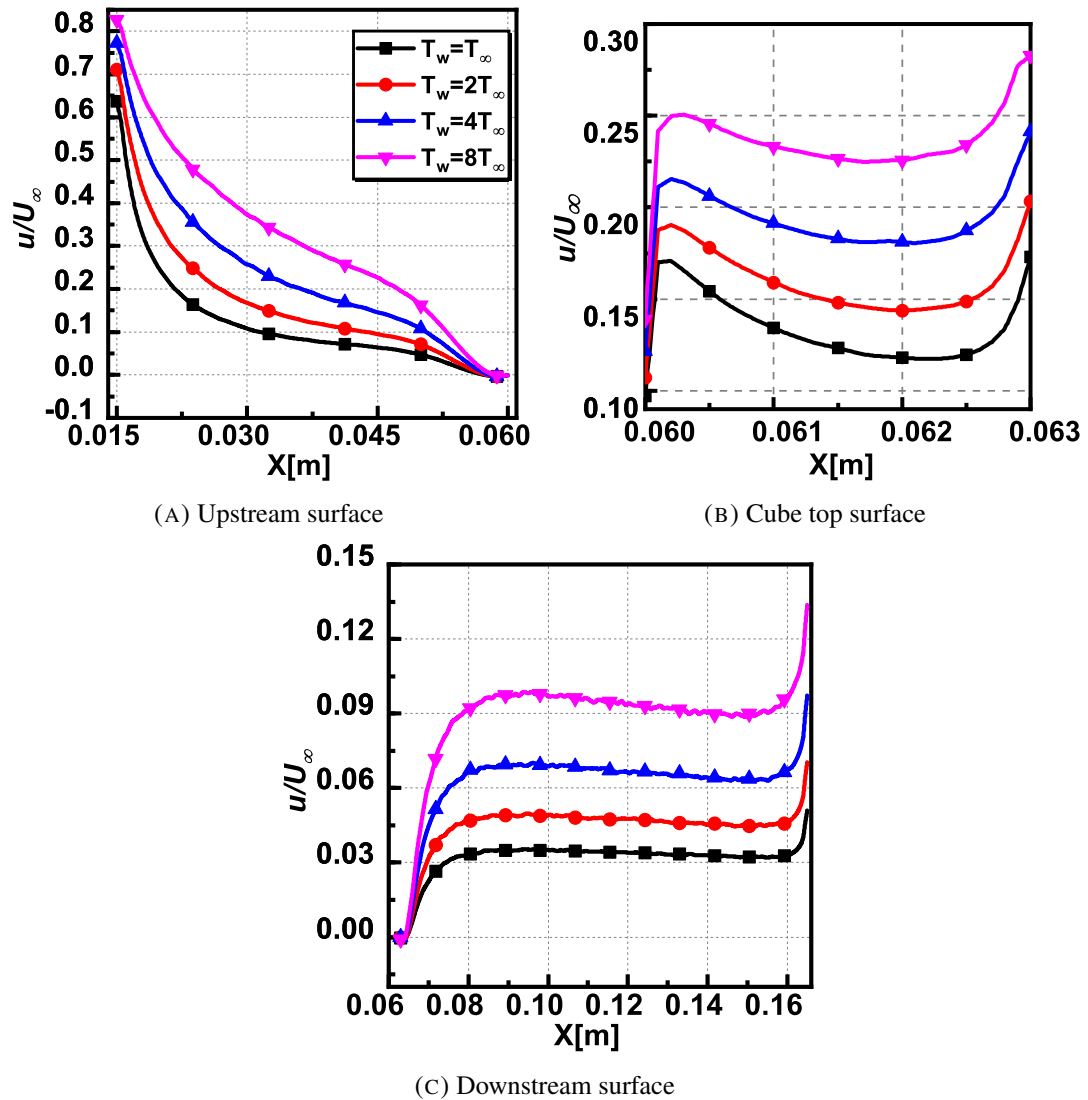


FIGURE 6.100: Variation of the non-dimensional velocity along the length of wall-mounted cube for different T_w

wall temperatures. Thus, it is observed that the pressure magnitudes are relatively unaffected by the change in wall temperature.

Temperature field:

The non-dimensional temperature variation for different T_w at the upstream, cube top, and the downstream surface is shown in Figure 6.102. The profiles show substantial deviation for the various cases studied. On the upstream side and on the top surface

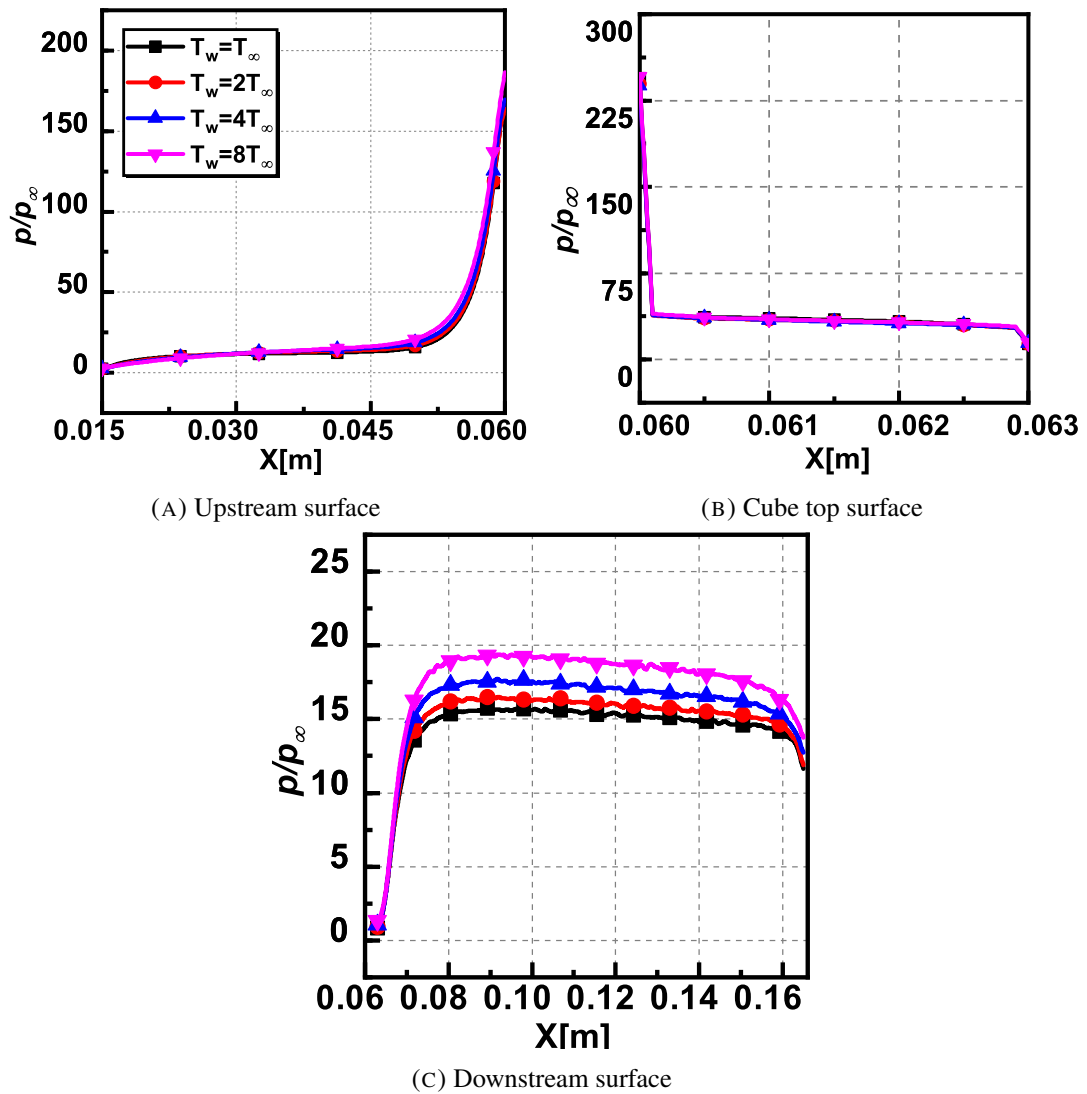


FIGURE 6.101: Variation of the non-dimensional pressure along the length of wall-mounted cube for different T_w

of the cube, the temperature magnitudes are higher when compared to the downstream side. In all the cases, the magnitudes show an increase with T_w . As the wall temperature increases, the viscous heating increases, which contributes to the temperature rise.

Pressure coefficient:

Figure 6.103 shows that the pressure coefficient C_p on the upstream and downstream surface for different T_w . The profiles on both the surfaces are found to be overlapping

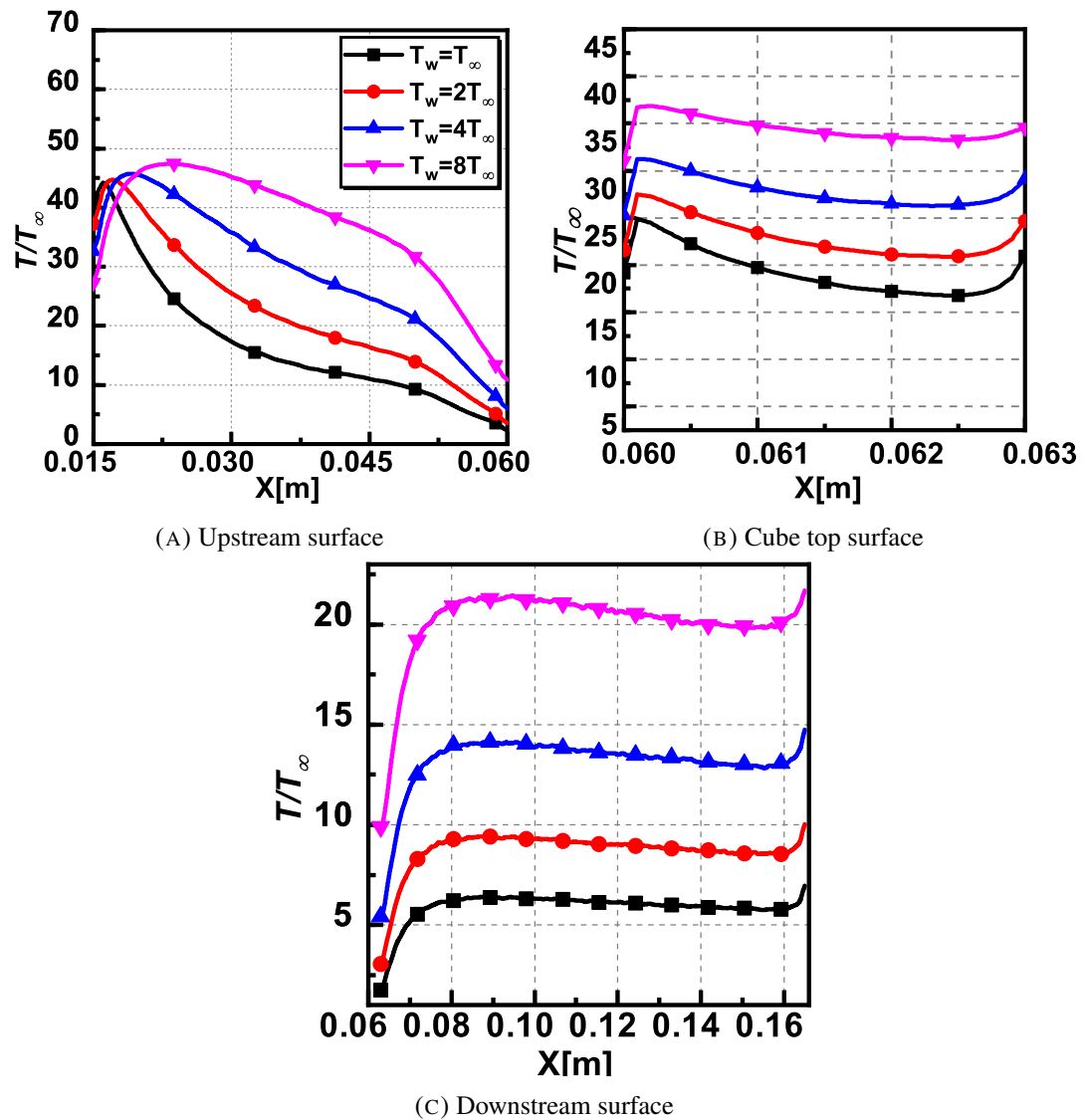
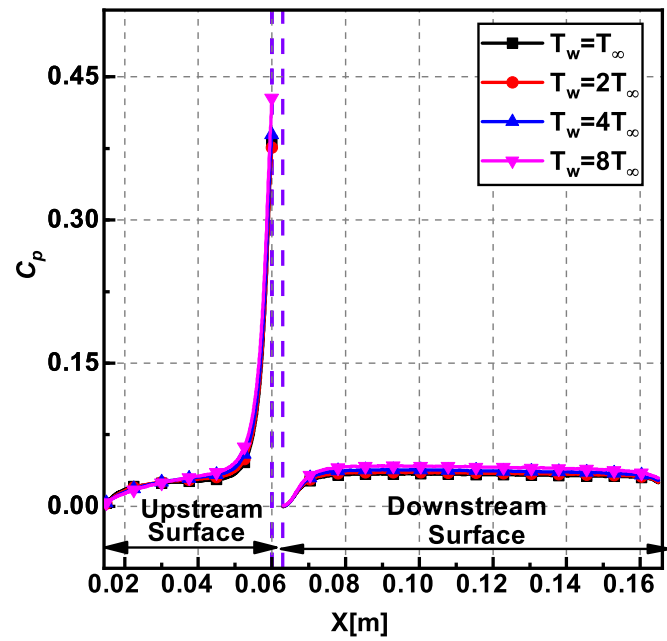
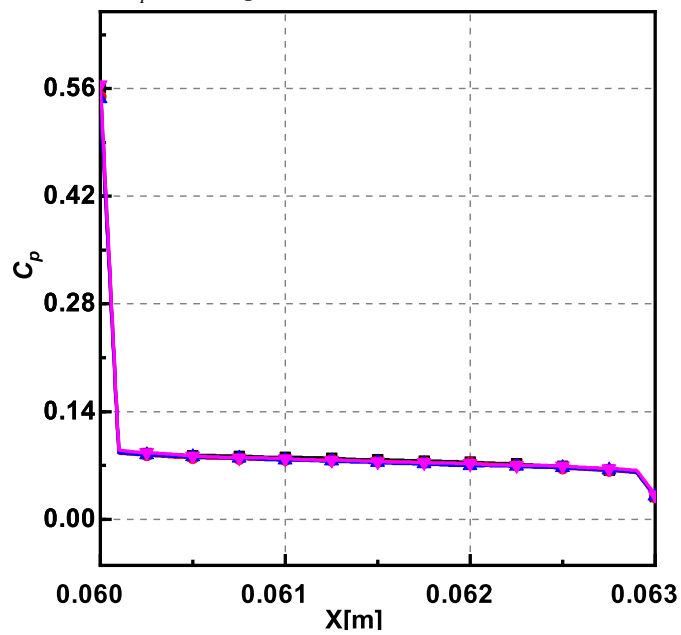


FIGURE 6.102: Variation of the non-dimensional temperature along the length of wall-mounted cube for different T_w

for all the cases with a negligible variation. On the top surface of the cube depicted in a similar overlapping trend is observed. Thus, it demonstrates that the wall temperature effects have minimal influence on the pressure coefficient.

Skin friction coefficient:

Figure 6.104 shows that the skin friction coefficient C_f on the upstream and downstream

(A) C_p on the upstream and downstream surfaces.(B) C_p on the cube top surface.FIGURE 6.103: Variation of pressure coefficient C_p for wall-mounted cube for different T_w .

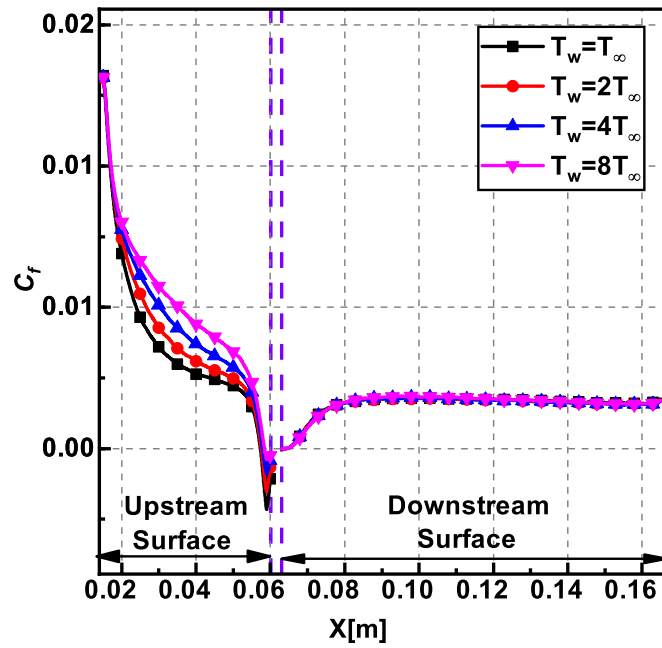
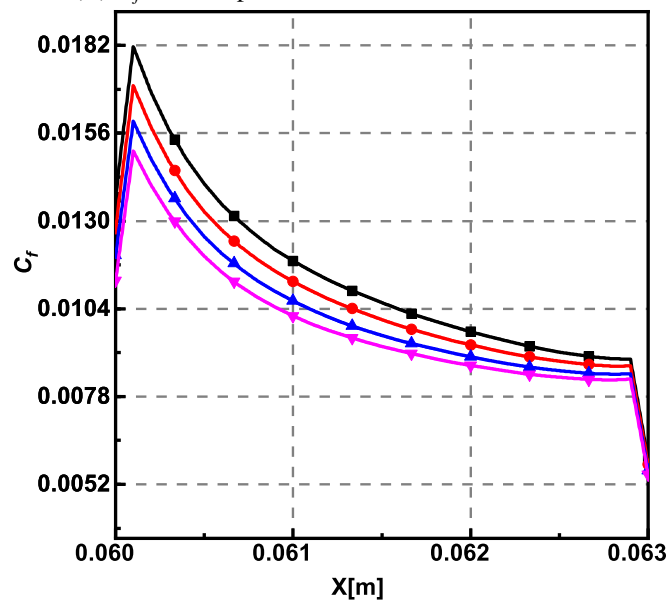
surface for different T_w . On the upstream surface the C_f magnitudes are high and found to overlap for a short distance. After that, a variation is observed among the profiles for a considerable distance, and they once again overlap towards the vicinity of the cube. On the downstream side, the profiles overlap all along the length towards the outlet. On the cube's top surface, the magnitudes show a gradual decline as the flow traverses over the cube surface.

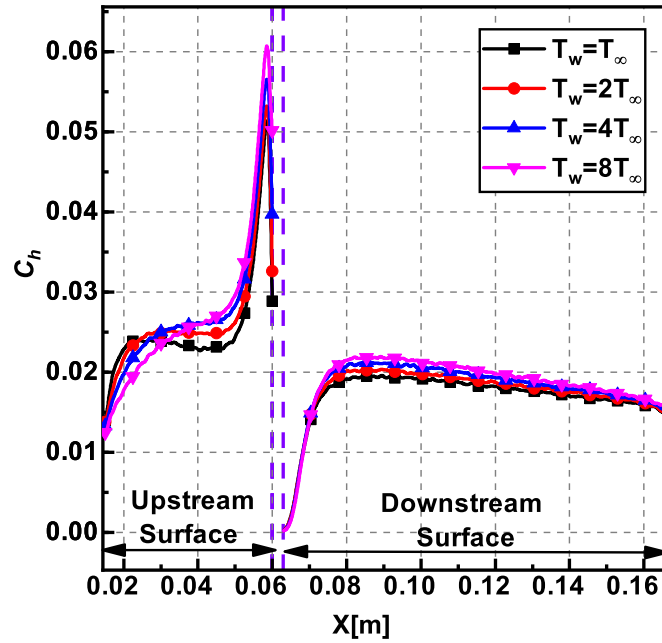
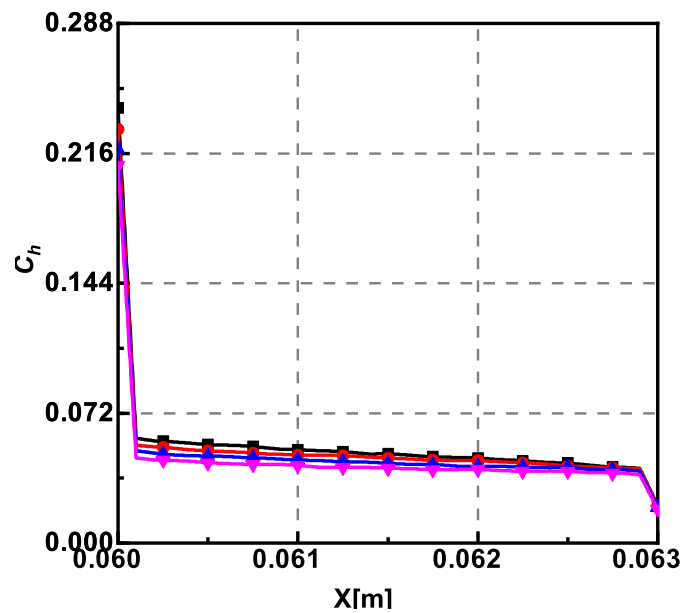
Heat transfer coefficient:

Figure 6.105 shows the heat transfer coefficient (C_h) on the upstream and downstream surface for different T_w . The C_h on the upstream surface increases initially, remains steady for a short distance, and then again increases towards the edge of the cube. The difference in the profiles for different cases is not significant. The profiles increase with overlapping trends for a short distance and then show a gradual decline on the downstream side. A similar trend of gradual decline in the magnitudes is observed on the top surface of the cube.

6.4.3 Influence of Knudsen number

This section describes the influence of Knudsen number (Kn) on the flow and surface properties over the wall-mounted cube. The different Knudsen numbers studied are given in Table 6.2. For all the instances, the free-stream Mach number considered was 25, with a step height of ($h = 3$ mm), $H = 60$ mm, and $T_w = 4T_\infty$ is used. Initially the contours are presented, followed by the line plots.

(A) C_f on the upstream and downstream surfaces.(B) C_f on the cube top surface.FIGURE 6.104: Variation of skin friction coefficient C_f for wall-mounted cube for different T_w .

(A) C_h on the upstream and downstream surfaces.(B) C_h on the cavity base.FIGURE 6.105: Variation of heat transfer coefficient C_h for wall-mounted cube for different T_w .

Velocity field:

The non-dimensional velocity variation for different Kn at the upstream, cube top, and the downstream surface is shown in Figure 6.106. At the upstream side of the domain, the velocity magnitudes are high at the leading edge and soon continue to reduce towards the cube. At the cube's top surface, the velocity profiles do not show any appreciable change and are relatively constant. The profiles are constant in the slip and transition regime at the downstream side, whereas they gradually increase in the free-molecular regime. In all the cases, the velocity magnitudes are directly dictated by the Knudsen number, which can be attributed to the rise in mean free path causing greater dispersion of the molecules in the flow domain.

Pressure field:

The non-dimensional pressure variation for different Kn at the upstream, cube top, and the downstream surface is shown in Figure 6.107. At the upstream side and on the cube's top surface, the pressure magnitudes, by and large, remain the same without any significant deviation for different rarefaction regimes. In contrast, there is no definitive trend observed on the downstream side. Also, the pressure magnitudes show a decrease as the flow traverses from the inlet towards the outlet.

Temperature field:

The non-dimensional temperature variation for different Kn at the upstream, cube top, and the downstream surface is shown in Figure 6.108. On the upstream side, the temperature magnitudes are initially high and show a decline after that. At the cube's top surface,

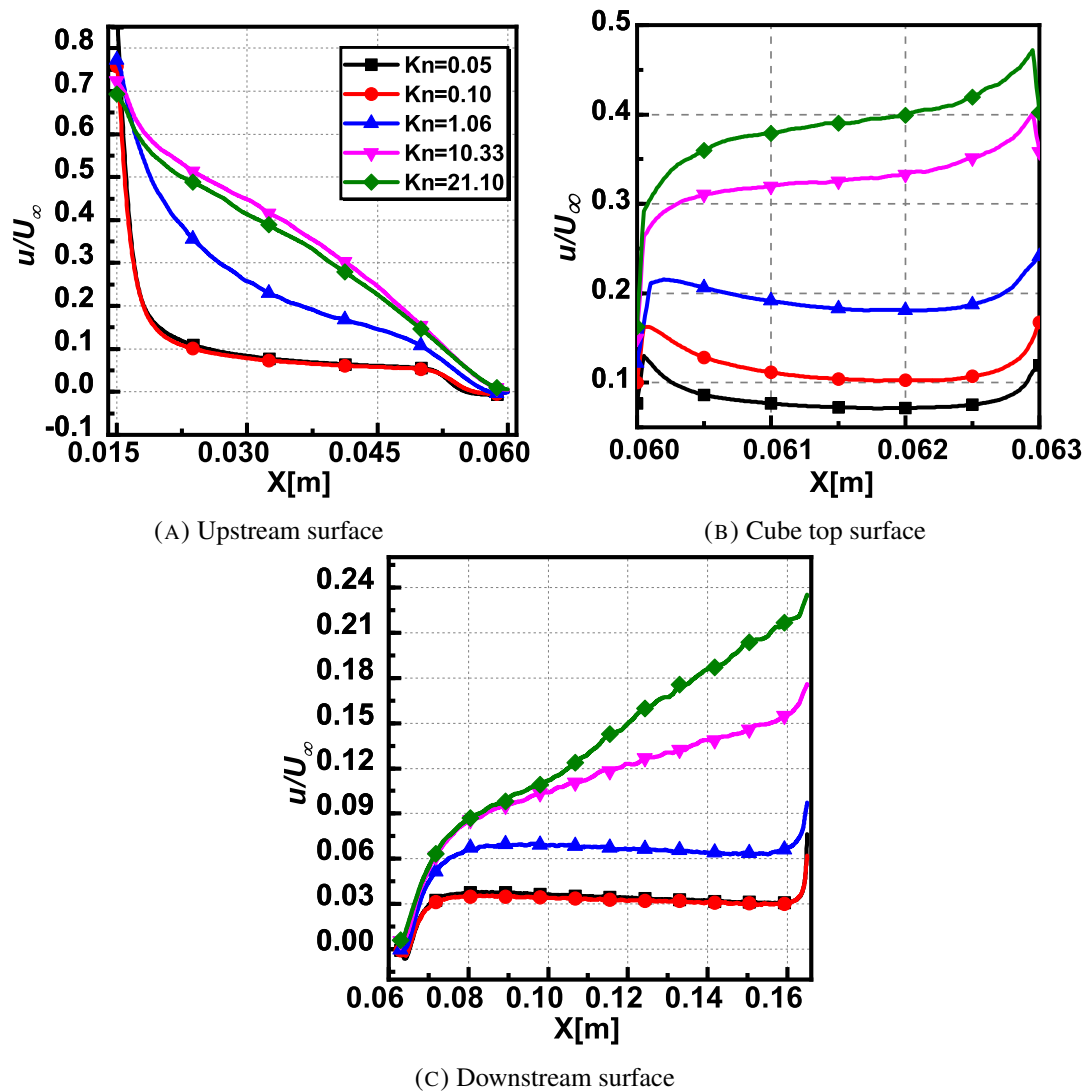


FIGURE 6.106: Variation of the non-dimensional velocity along the length of wall-mounted cube for different Kn

the profiles remain fairly constant all along the length. There is a gradual temperature rise at higher levels of rarefaction on the downstream side, whereas, at lower levels of rarefaction, the profiles are reasonably constant.

Pressure coefficient:

Figure 6.109a shows that the pressure coefficient C_p on the upstream and downstream surface for different Kn . On the upstream surface the C_p increases gradually and reaches

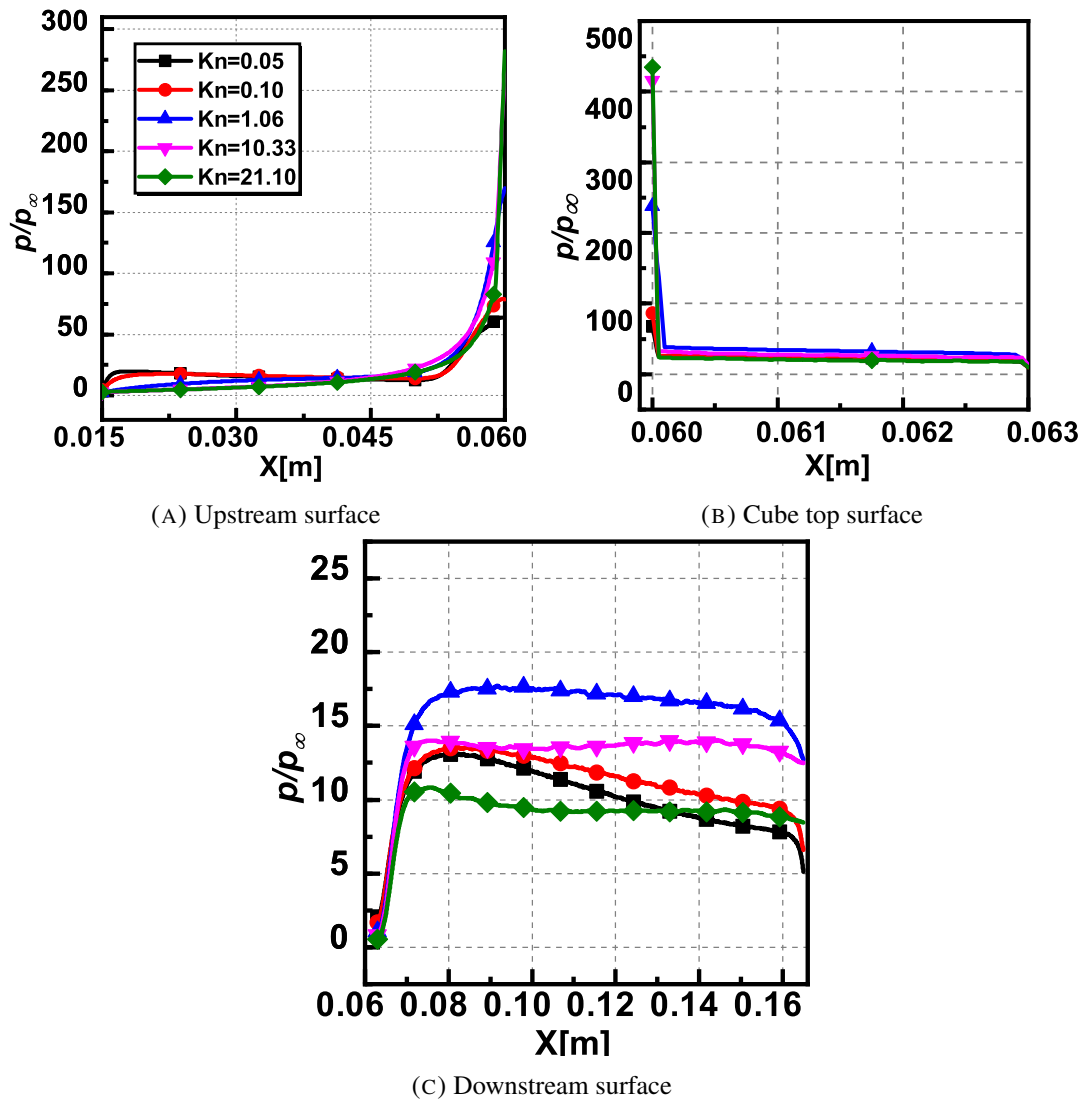


FIGURE 6.107: Variation of the non-dimensional pressure along the length of wall-mounted cube for different Kn

a peak near the edge of the cube due to stagnation pressure rise. Also, the magnitudes of C_p increase with rarefaction. On the downstream side, the C_p shows a minimal increase initially and then continues to remain reasonably constant, with no influence of rarefaction. The magnitudes of C_p on the top surface of the cube, Figure 6.109b is found to be constant along the cube length with higher magnitudes at higher levels of rarefaction.

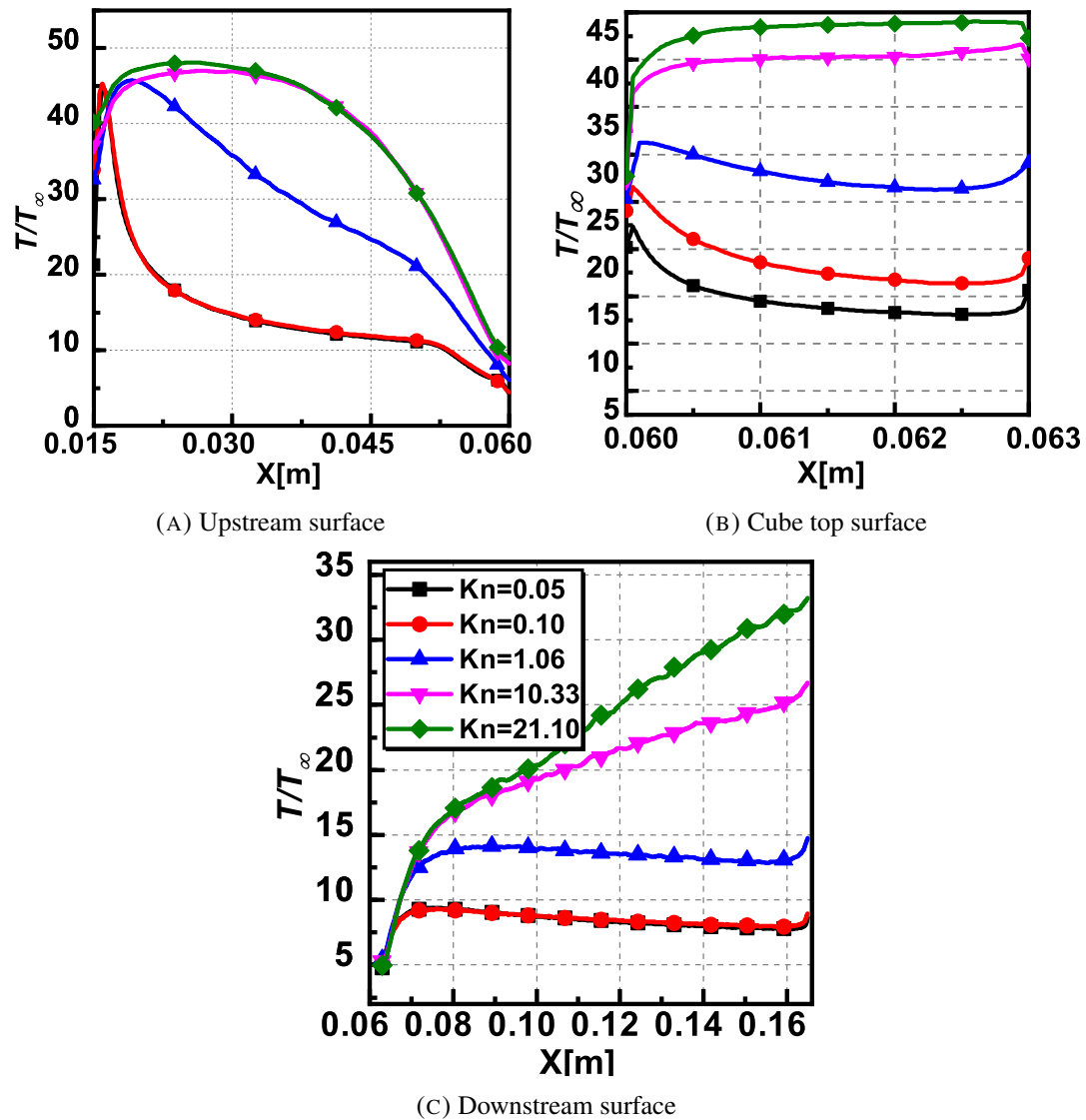
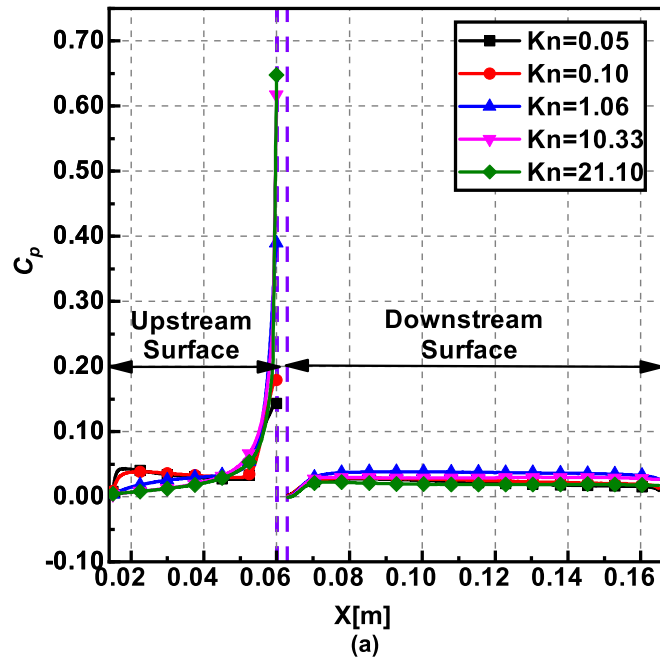
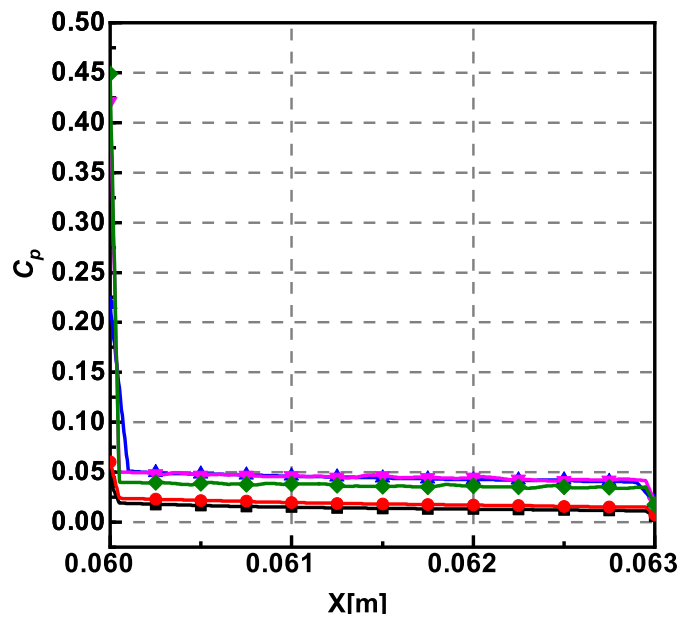
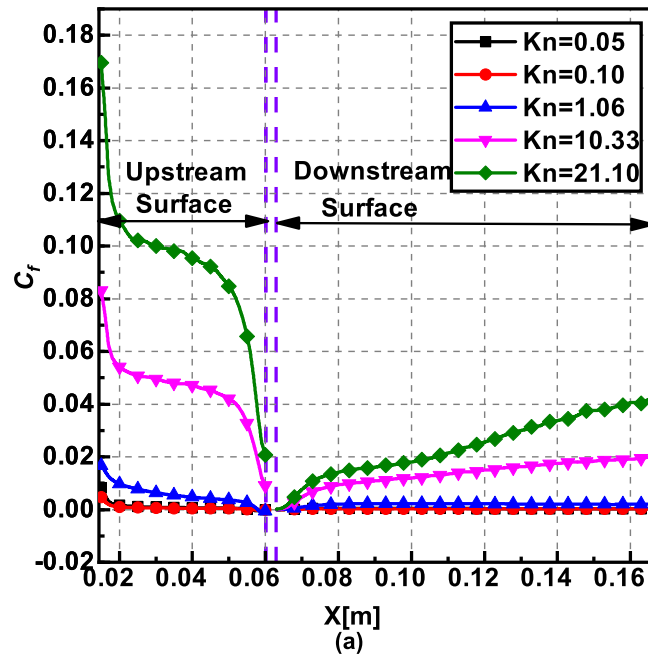
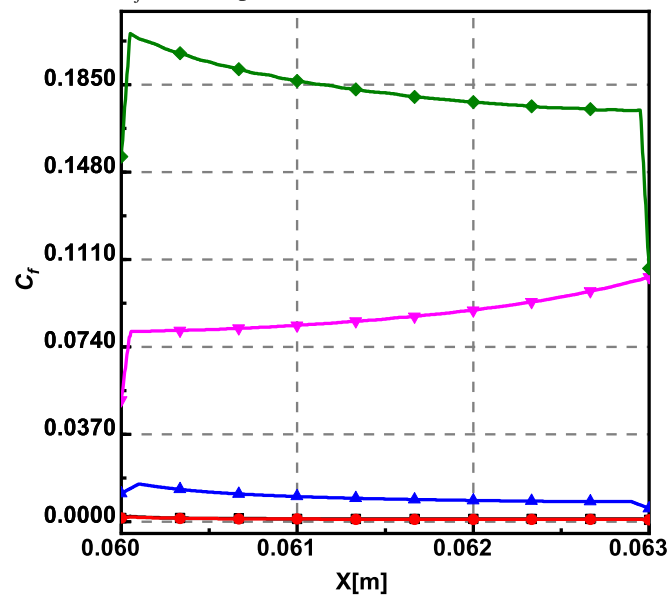


FIGURE 6.108: Variation of the non-dimensional temperature along the length of wall-mounted cube for different Kn

Skin friction coefficient:

Figure 6.110 shows that the skin friction coefficient C_f on the upstream and downstream surfaces for different Kn . On the upstream, the C_f profiles show substantial deviation for different Kn , except in the slip regime and increase in magnitude at high degrees of rarefaction. Also, the peak is observed at the beginning, and then the C_f show a continuous decrease. On the downstream side the C_f remains constant in the slip and

(A) C_p on the upstream and downstream surfaces.(B) C_p on the cube top surface.FIGURE 6.109: Variation of pressure coefficient C_p for wall-mounted cube for different Kn .

(A) C_f on the upstream and downstream surfaces.(B) C_f on the cube top surface.FIGURE 6.110: Variation of skin friction coefficient C_f for wall-mounted cube for different Kn .

transition regime and shows an increase in the other regime, though the increase is minimal. A similar trend is observed on the cube's surface, where the magnitudes are higher at higher Kn and along the length they remain reasonably identical.

Heat transfer coefficient:

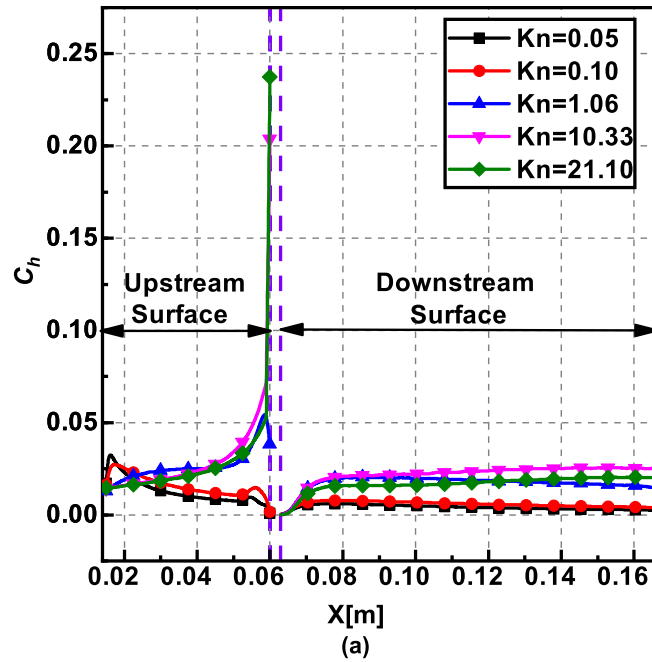
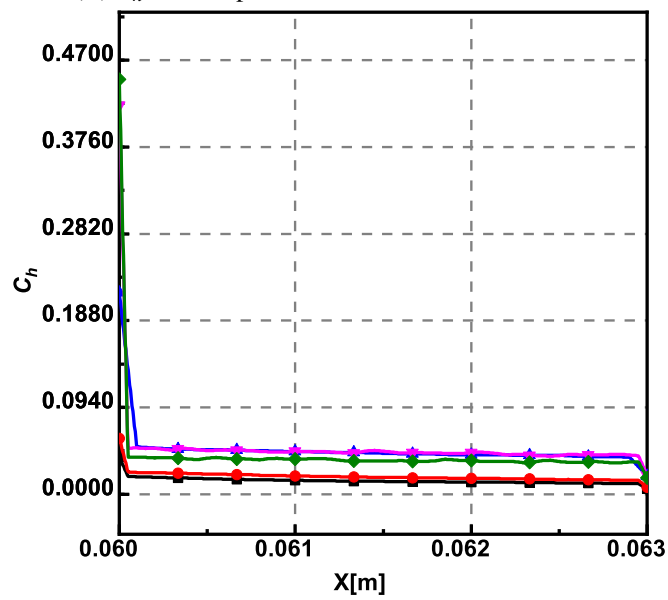
Figure 6.111 shows that the heat transfer coefficient C_h on the upstream and downstream surfaces for different Kn . The C_h shows different trends at different regimes. On the upstream side, the C_h shows a reducing trend in the slip regime, whereas, in the other regimes, it shows an increase. On the downstream side, the C_h profiles remain constant along the outlet. On the top surface of the cube, the C_h behaves similarly for different Kn with no significant difference among the different regimes.

6.5 Comparison with chemical reacting flows

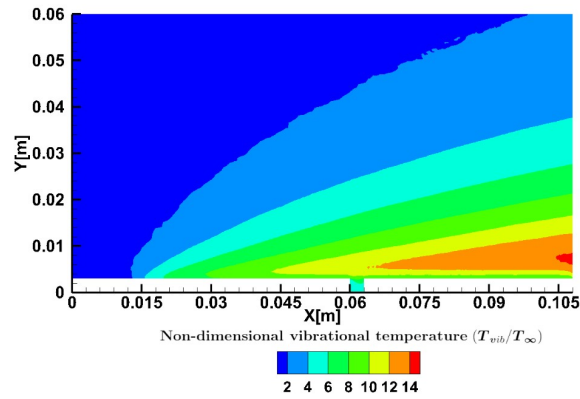
The present study involves hypersonic flow conditions, resulting in an energized system where the vibrational modes of the gas are activated, and chemical reactions occur. Therefore, the influence of these vibrational excitations on the flow properties needs to be studied.

For a comparison between chemically reacting and non-reacting flow, the hypersonic flow condition with $Ma = 25$ was studied for different Kn . When chemical reactions were considered and compared against the non-reacting flows, the flow-field properties such as velocity, pressure, and density showed no marked difference. Hence, the discussion will be limited to only the temperature field. Figure 6.112 shows the non-dimensional temperature contours for different components of the temperature $Kn = 1.06$.

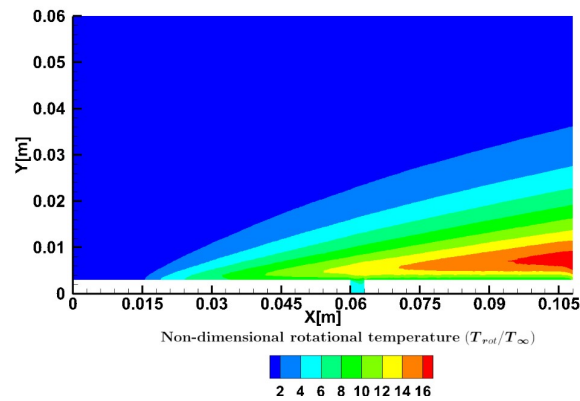
The vibrational component of the temperature in Figure 6.112a is relatively lower in magnitude than the other components. The vibrational excitations appear not to affect the cavity, and as a result, the vibrational temperature shows no marked difference.

(A) C_h on the upstream and downstream surfaces.FIGURE 6.111: Variation of heat transfer coefficient C_h for wall-mounted cube for different Kn .

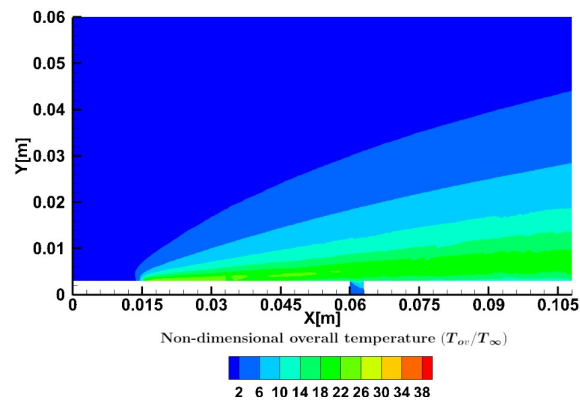
However, a temperature surge is observed towards the outlet. The rotational component of the temperature is shown in Figure 6.112b. Its order of magnitude is the same as that of the vibrational component with only marginally higher values. Similarly, the overall and translational components are shown in Figure 6.112c and 6.112d, respectively. The contours show that near the wall, the translational temperature has a much larger magnitude (of about 10^3K). This surge can be attributed to the viscous heating effects observed in the shear layer at the top of the cavity and near the wall. The rotational and vibrational temperatures show similar behavior as well. This entire effect is reflected in the contours of overall temperature in Figure 6.112c. Rapid flow expansion is observed just upstream of the cavity and results in expansion cooling inside the cavity. This expansion cooling is the reason for the observed colder region and lower magnitudes of the translational temperature inside the cavity. Expansion cooling also affects the translational temperature downstream near the outlet, resulting in lower translational temperature values. Diffusion, advection, and reduced shear rates profoundly affect the high translational temperature in the shear layer just downstream of the gap. As the flow reaches the outlet, these effects result in a considerable decrease in the magnitude of the translational temperature. Contrasting to this behavior, an increase in the rotational and vibrational temperatures near the outlet is visible, as shown in Figure 6.112a and 6.112b, respectively, which can be due to the non-equilibrium effects. Figure 6.112d shows that the combined effect of increased rotational and vibrational temperature is compensated by the decreased translational temperature downstream of the cavity. As a result, a relatively uniform overall temperature variation is observed downstream of the gap.



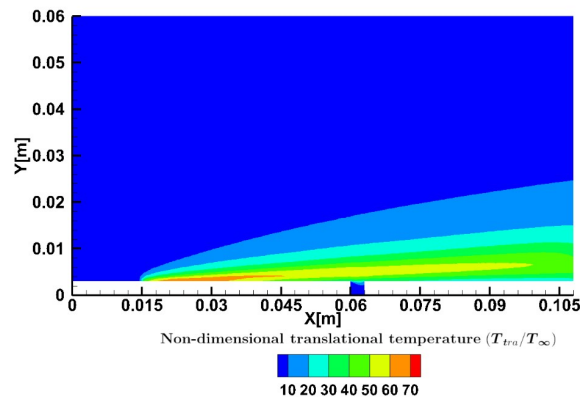
(A) Non-dimensional vibrational temperature.



(B) Non-dimensional rotational temperature.



(C) Non-dimensional overall temperature.



(D) Non-dimensional translational temperature.

FIGURE 6.112: Contours of different temperature components of open cavity for $H = 60\text{mm}$, $Kn = 25$ and $Kn = 1.06$.

The non-dimensional temperature variation for different Kn at sections $X = 30\text{mm}$, $X = 59\text{mm}$, $X = 61\text{mm}$, and $X = 93\text{mm}$ is shown in Figure 6.113. The temperature profiles for both chemically reacting flow as well as non-reacting flow are compared with each other. In comparison, it is observed that both follow the same trends for different Kn . However, a considerable difference in the predicted value is observed. The maximum temperature in the shear layer is calculated, and the relative change is measured with respect to the non-reacting flow for various locations. At $X = 30\text{ mm}$ the maximum temperature ratio values predicted by non-reacting flow, differ with chemically reacting flow by roughly 66.52%, 80.12%, 49.78%, 6.76% and 0.79% for $Kn = 0.05 - 21.10$ respectively. At $X = 59\text{ mm}$, the percentage change is 46.47%, 56.35%, 92.3%, 21.27%, and 14.03% for $Kn = 0.05 - 21.10$, respectively. Similarly, inside the cavity at $X = 61\text{ mm}$, the change in the maximum temperature is greater than 35% for all Kn . Finally, downstream at $X = 93\text{ mm}$ the errors are 39.13%, 46.36%, 98.1%, 30%, and 15.72% for $Kn = 0.05 - 21.10$, respectively.

The non-dimensional temperature variation for different Kn at sections $Y/h = 0.3$, $Y/h = 0.6$ and $Y/h = 1$ is shown in Figure 6.114. At all the Y locations, on average, the non-reacting flow over-predicts the temperature ratios (as the chemical reactions result in absorption of the energy by the fluid). The average over prediction of the temperature ratio value by the non-reacting flow is under 11% and 17% for all Kn along the bottom and middle of the cavity. At $Y/h = 1$, along the top of the cavity, the shear effects are more prominent, and the average over prediction of temperature ratios for a non-reacting flow is approximately 38.65%, 44.64%, 57.37%, 40.96%, and 35.97% for $Kn = 0.05 - 21.10$, respectively. Thus, it can be observed that there is substantial

variation in the temperature field when the chemical reactions are considered.

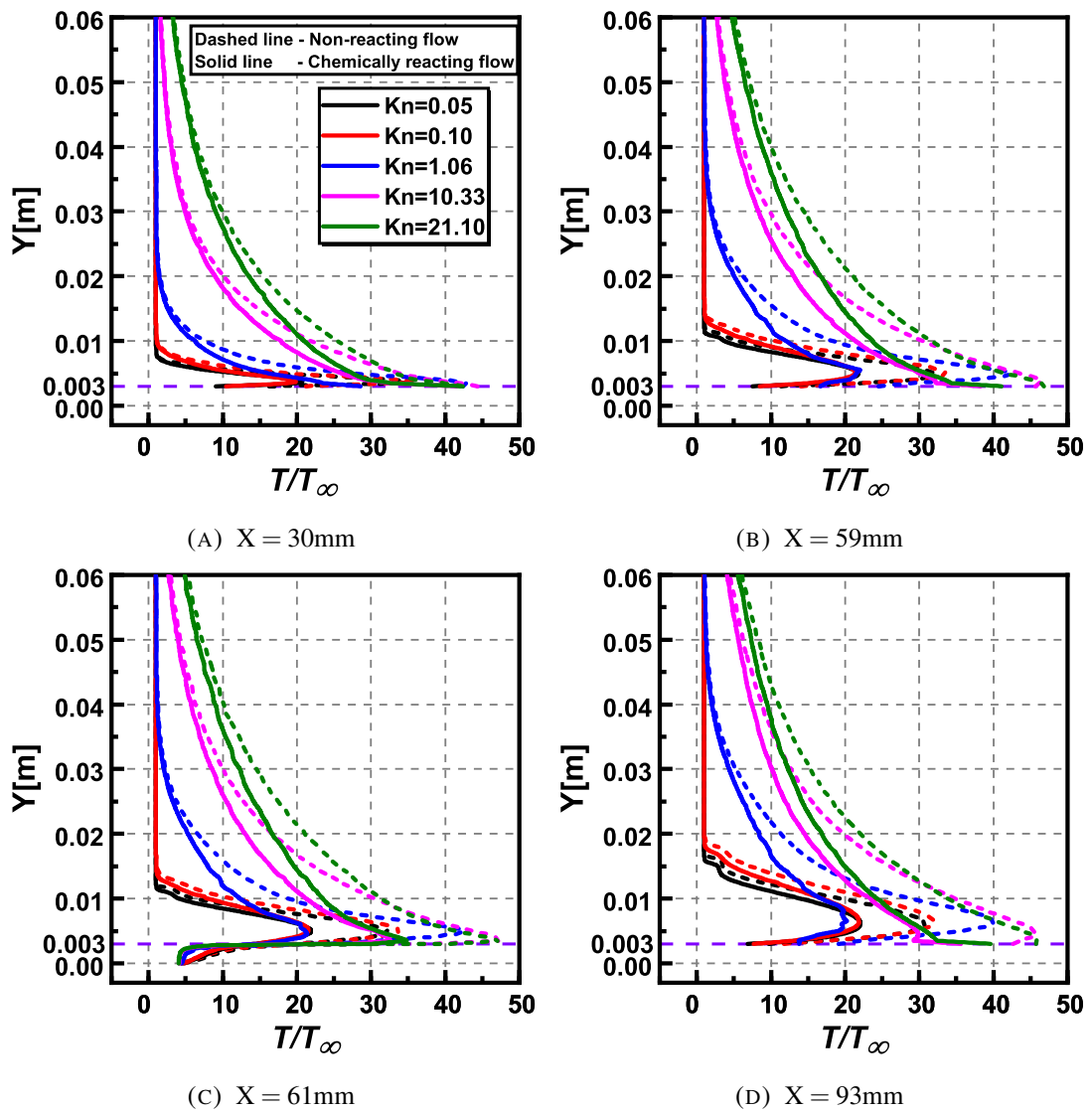


FIGURE 6.113: Comparison of for reacting and non-reacting cases of open cavity for different Kn .

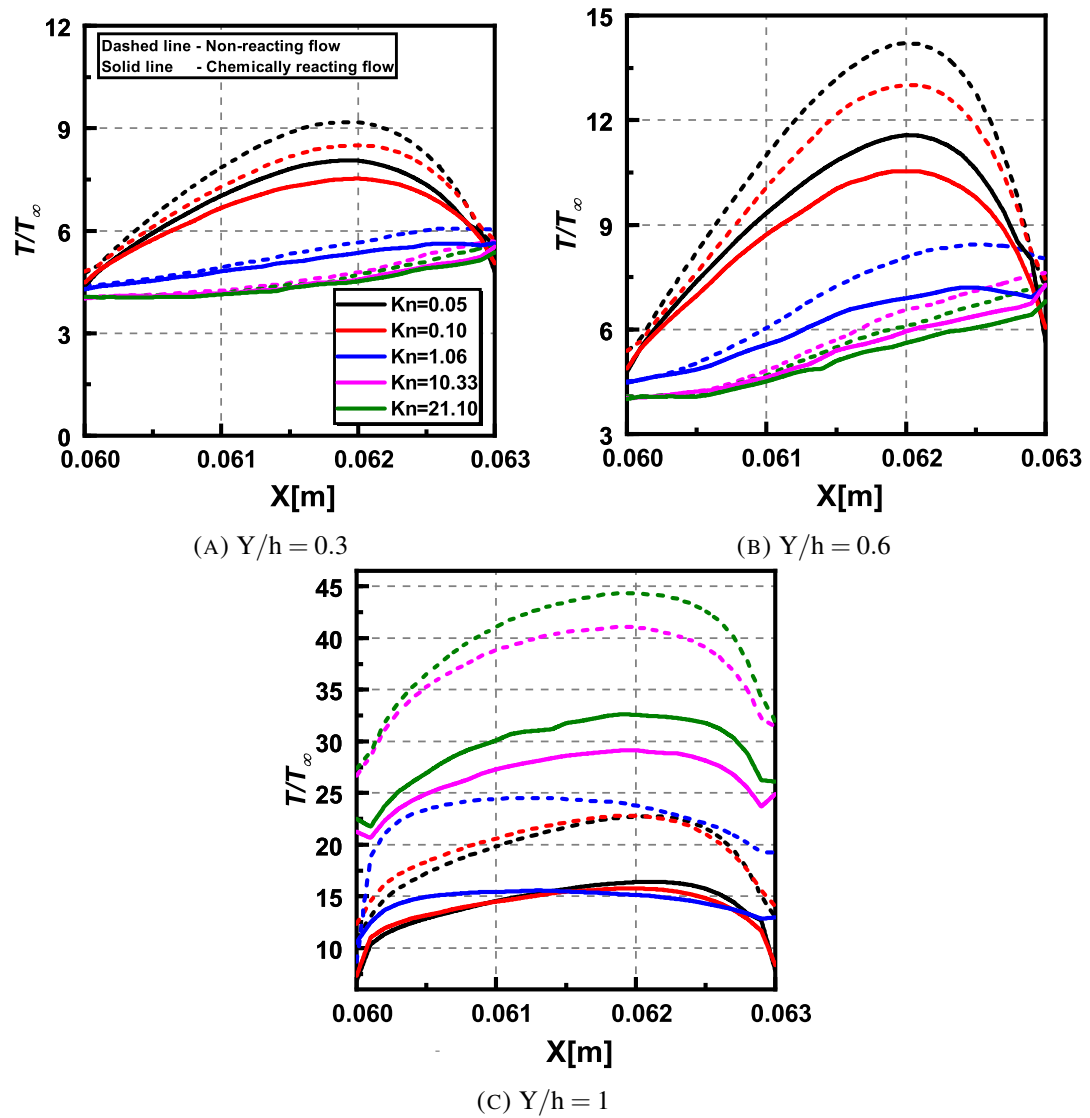


FIGURE 6.114: Comparison of the non-dimensional overall temperature along the length of the open cavity for different Kn .

Chapter 7

Conclusion and future scope

In this chapter, the concluding remarks are presented. This chapter begins with a summary and conclusions of the research conducted. It is followed by the specific contributions that are made to the research domain. Furthermore, the study's usefulness from a practical viewpoint is also given along with some limitations, and finally, the future scope is presented.

7.1 Summary and primary conclusions

The most significant findings and observations established from each chapter are as follows:

Chapter 1:

The motivation behind the research work was initially discussed. The classification of flow regimes based on the Knudsen number was then presented along with the various approaches to model a fluid flow problem. A brief overview of the DSMC method was

mentioned, along with various flow configurations that will be examined, and the outline of the thesis work was presented.

Chapter 2:

The various studies reported in the literature were presented in this chapter. The different flow configurations involving both internal and external flows studied in the literature were explained in detail. From the literature review, some of the main conclusions are outlined below:

- For the internal bounded flows involving the driven cavity, it was observed that several studies were reported using various numerical techniques. However, the studies mainly focused on the continuum regime analysis, while few works reported the flow physics in the slip regime. Very few works focused on analyzing the higher rarefaction regimes where the flow is complex in nature.
- Moreover, for the internal flows, most studies focused on examining the flow behavior for a single-lid-driven cavity. In contrast, very few studies focused on exploring the flow physics for a double-sided and four-sided lid-driven case whose flow behavior is helpful in various industrial applications.
- The comprehensive analysis of the rarefied flow behavior that investigated different rarefaction regimes for internally bounded flows is limited in the literature.

In the second part of the literature, the different flow configurations that occur on the surfaces of hypersonic vehicles reported in the literature were presented. These included both experimental and computational studies on different configurations such

as backward-facing step, forward-facing step, open cavity, and wall-mounted cube. The main observations were:

- The literature review showed that although many works were reported for different flow configurations, most of the studies focussed on analyzing the flow physics in the lower rarefaction regimes.
- The majority of the studies were at lower velocities falling in the subsonic range, and scarce studies were found in the hypersonic or re-entry speeds.

Thus from the literature study, it was found that minimal studies have been carried out at higher rarefaction regimes, particularly the free molecular regime. This research aims to bridge the gap and explores the flow-field and aerodynamic properties for various flow configurations. The study mainly focuses on examining the influence of the Mach number, different wall temperatures, and Knudsen number on the flow field and aerodynamic characteristics.

Chapter 3:

This chapter presented the computational methodology adopted in the present research. The specifics of the DSMC method were explained in detail. Also, some of the limitations of the computational technique were mentioned.

Chapter 4:

This chapter presented the various validation studies conducted to ascertain the accuracy of the results. In the first part, the independence studies were presented to select optimal

parameters for grid size, time step, and particles per cell. This was followed by the validation studies. In this, a benchmark case of the lid-driven cavity was validated. After that, the validations were performed for the flow over a flat plate, BFS, and cavity. The validation studies showed good agreement with results from the literature.

Chapter 5:

This chapter provided the simulation studies of the rarefied flow for internal flows. The main conclusions that can be drawn are described below:

- With rarefaction, the flow properties do not vary much.
- The peak near-wall velocity of the fluid was roughly one-fourth of the driving wall velocity for the anti-parallel case and about one-half for the parallel case. This may be attributed to increased friction in the flow for the anti-parallel case where there are four symmetrical vortices instead of two (as found in the parallel case).
- The magnitude of wall heat flux was found to increase with Ma as more kinetic energy is imparted to the fluid by the driving walls. In contrast, the heat flux decreases with Kn .
- The non-equilibrium effects on the flow are relatively less for the different cases considered as the flows were subsonic.
- Different results illustrated in this study display an interplay of viscous dissipation, compressibility, and rarefaction effects.
- The results from NSF equations and DSMC agree well in the slip regime.

Chapter 6:

The rarefied flow investigations for various external configurations were studied in this chapter. In a representative range of parameters, the effects of Mach number, wall temperature, and Knudsen number were investigated for the main flow properties like velocity, pressure, temperature, density, and surface properties like pressure coefficient, skin friction coefficient, and heat transfer coefficient. The following principal conclusions can be drawn from the study conducted: The first part of the chapter 6 involved the rarefied flow past BFS. The analysis showed the following salient conclusions:

- The magnitudes of the flow properties attain the freestream values far away from the wall in the transverse direction. The properties (other than velocity) are higher in the shear layers near the wall and after the step.
- Significant variation is observed among the flow properties for different Ma primarily due to viscous dissipation and compressibility, whereas, for different T_w , the variation is minimal. For different Kn the flow properties by and large showed an increasing trend.
- The recirculation length of the vortex in the wake of the step is reasonably independent of both free stream Mach number and wall temperature, whereas it decreases with Knudsen number.
- The surface properties are found to decrease with Ma and increase with T_w . Whereas for different Kn the aerodynamic surface properties C_p and C_h by and large followed a similar trend, with peak magnitudes located upstream. The skin

friction coefficient C_f on the other hand, showed a consistent increase with Kn all along the lower and upper surfaces.

The second part of the chapter 6 involved the rarefied flow past FFS. The study indicated the following conclusions:

- The near-wall flow properties increased with increasing Ma , Kn and T_w .
- The surface properties, along the lower and upper surfaces, C_p and C_f were found to decrease with increasing Ma , whereas C_h showed an increase. For different Kn , the surface properties C_p , C_f and C_h were found to increase with Kn , with peak magnitudes located on the upstream and frontal face of the step.
- The change in T_w had a minimal influence on the surface properties.
- The recirculation lengths increase with Ma ; contrastingly, they were found to decrease with increasing T_w .
- For the free-stream and flow conditions employed in the current study, recirculation and separation occurred in the slip and transitional regime, whereas it was absent in the free-molecular regime; moreover, the recirculation lengths decreased with rarefaction. This decrease is attributed to the formation of the Knudsen layer and the dominance of viscous forces over inertial forces.

The third part of the chapter 6 involved the rarefied flow past an open cavity, whose results are summarized below:

- The near-wall flow field properties showed an increasing trend. Inside the cavity, the trends were similar except for the velocity field that showed a contrasting trend.

- The wall temperature also directly influenced the flow properties and caused a rise in their magnitudes. A similar pattern was observed inside the cavity, except for the density field, which showed an opposite trend. Furthermore, the overall rise in magnitude was less than the increase due to the Mach number.
- Rarefaction of the flow caused a reduction in the velocity due to the increased boundary layer thickness. The pressure field and temperature field increased with increasing Knudsen number, whereas the density remained uninfluenced. Inside the cavity, no definitive trend was observed.
- The presence of the cavity was felt by the flow field only in the immediate vicinity of it, and trends in the variation of the flow properties far away from it are mostly unaffected.
- Inside the cavity, flow recirculation was observed in all regimes. The recirculation was symmetric in the slip regime and asymmetric in other regimes. Secondary vortices set in for the free-molecular flows.
- Magnitude of the aerodynamic coefficients (i) decrease with Ma , both inside the cavity and on its upstream and downstream surfaces (ii) increase with the wall temperature; only C_f and C_h show an opposing trend inside the cavity (iii) show more complex trends with an increase in Kn both inside and outside the cavity. They increase in the slip regime and decrease in the transitional and free-molecular regimes, whereas, only C_f shows an opposing variation.

The fourth part of the chapter 6 involved the rarefied flow past a wall-mounted cube. The primary conclusions from the simulations are given below:

- The flow-field properties such as velocity, pressure, and density followed a similar trend as the open cavity.
- The surface properties on the cube top surface showed no marked difference for different Ma , T_w and Kn .

In the final part of chapter 6 a comparison was made for the reacting and non-reacting flows by considering the open cavity as the configuration. The flow-field properties such as velocity, pressure, and density showed no marked difference when compared against the non-reacting flows. In contrast, considerable difference was observed in the temperature field as the chemical reactions result in absorption of the energy by the fluid. The temperature differences were substantial, particularly in the shear layer.

Thus, the rarefied flow behavior for internal and external flow configurations was investigated using the DSMC approach. The influence of Mach number, wall temperature, and Knudsen number on the flow-field and surface properties were thoroughly analyzed at various sections. The properties were mainly affected due to the compressibility and viscous dissipation effects. Based on the aforementioned results and facts, it is observed that the existence of discontinuity in the form of steps, gaps cannot be overlooked. For the conditions investigated, it is observed the thermal and aerodynamic loads on the surface of the step significantly increased, thus demanding better aerodynamic thermal protection.

7.2 Specific contributions to research

Through this thesis work the following contributions have been made towards the research of aerothermodynamics:

- Analysis of the rarefied flow behavior of internally bounded flows for both double-sided and four-sided cavities involving parallel and anti-parallel wall movements is investigated for all rarefaction levels.
- Investigation of the impacts of compressibility and rarefaction on the different surface imperfections.
- Determination of the thermal and aerodynamic loads on the surfaces of the simplified geometries for a range of Knudsen numbers, Mach numbers and different wall temperatures that mimic the reentry vehicle's path while entering back to the earth's atmosphere.

7.3 The usefulness of the research

- Understanding the flow physics around the configurations studied in this research helps us gain insight into the flow around more complicated geometries. Hence, this study forms the basis for a better design with improved safety features in an atmospheric re-entry vehicle.
- Experimental studies on re-entry vehicles in the outer atmosphere are difficult to carry out given the wide range of flow regimes encountered. The atmospheric

conditions on other planets like Mars are even harder to replicate to simulate vehicles landing on them. These challenges can be addressed much more easily using numerical studies.

- Agencies like ISRO and DRDO closely work on launch vehicles and ballistic missiles. These technologies are based on sound knowledge of the rarefied gas flow behavior.
- The proposed studies are carried out for a range of non-dimensional parameters like Re and Kn . Therefore, these results can also be extended, for the most part, to the micro flows. This will help in a better design of MEMS/NEMS devices which have numerous applications outlined in the section.

7.4 Limitations of the current study

- The present analysis considered only 2D configurations, whereas 3D models can give better understanding of the flow physics.
- Investigation of the effects of surface ablation can be incorporated in the analysis.

7.5 Future scope of work

The following are some suggestions for improving this study:

- The effect of surface ablation can be incorporated and explored.
- The influence of the angle of attack on flow physics can be examined.

-
- The influence of gas-surface interaction on flow physics can be studied.
 - The Neural network techniques can be utilized to predict the flow and surface properties.
 - Current studies form a foundation for studying more complicated geometries; moreover, these results might be useful as a benchmark, mainly where the results for higher rarefaction are unavailable.

Bibliography

- [1] I. B. Sebastião and W. F. Santos, “Numerical simulation of heat transfer and pressure distributions in micronozzles with surface discontinuities on the divergent contour,” *Computers & Fluids*, vol. 92, pp. 125–137, Mar. 2014.
- [2] G. Guo and Q. Luo, “Flowfield structure characteristics of the hypersonic flow over a cavity: From the continuum to the transition flow regimes,” *Acta Astronautica*, vol. 161, pp. 87–100, 2019, publisher: Elsevier.
- [3] M. A. Gallis, R. B. Bond, and J. R. Torczynski, “A kinetic-theory approach for computing chemical-reaction rates in upper-atmosphere hypersonic flows,” *The Journal of chemical physics*, vol. 131, no. 12, p. 124311, 2009, publisher: American Institute of Physics.
- [4] F. Martin, *Legacy of the Space Shuttle From an Aerodynamic and Aerothermodynamic Perspective*. AIAA, 2011. [Online]. Available: <https://arc.aiaa.org/doi/abs/10.2514/6.2011-7122>
- [5] T. Horvath, “Experimental aerothermodynamics in support of the Columbia accident investigation,” in *42nd AIAA Aerospace Sciences Meeting and Exhibit*, 2004, p. 1387.

- [6] K. Bibb and R. Prabhu, "Computational Aerodynamics of Shuttle Orbiter Damage Scenarios in Support of the Columbia Accident Investigation," in *37th AIAA Thermophysics Conference*, 2004, p. 2279.
- [7] J. Everhart, K. Bey, W. Wood, and M. Pulsonetti, "Experimental and Computational Investigation of Cavity Flow Simulating Debris Damage to Thermal Protection System Tiles," in *JANNAF 27th Airbreathing Propulsion Subcommittee Meeting, Colorado Springs, CO*, 2003.
- [8] G. Bird, "Sophisticated DSMC Short Course," in *Direct Simulation Monte Carlo Theory, Methods & Applications conference, hosted by Sandia National Laboratory*, 2007.
- [9] G. Bird, M. Gallis, J. Torczynski, and D. Rader, "Accuracy and efficiency of the sophisticated direct simulation Monte Carlo algorithm for simulating noncontinuum gas flows," *Physics of Fluids*, vol. 21, no. 1, p. 017103, 2009, publisher: American Institute of Physics.
- [10] A. Mohammadzadeh, E. Roohi, H. Niazmand, S. Stefanov, and R. S. Myong, "Thermal and second-law analysis of a micro- or nanocavity using direct-simulation Monte Carlo," *Phys Rev E Stat Nonlin Soft Matter Phys*, vol. 85, no. 5 Pt 2, p. 056310, May 2012.
- [11] M. Gad-el Hak, "The Fluid Mechanics of Microdevices—The Freeman Scholar Lecture," *J. Fluids Eng*, vol. 121, no. 1, pp. 5–33, Mar. 1999. [Online]. Available: <http://dx.doi.org/10.1115/1.2822013>

- [12] E. Roohi and M. Darbandi, “Extending the Navier–Stokes solutions to transition regime in two-dimensional micro- and nanochannel flows using information preservation scheme,” *Physics of Fluids*, vol. 21, no. 8, p. 082001, Aug. 2009. [Online]. Available: <http://aip.scitation.org/doi/10.1063/1.3177351>
- [13] D. C. Rapaport, “The Art of Molecular Dynamics Simulation by D. C. Rapaport,” Apr. 2004.
- [14] G. Bird, “Molecular gas dynamics and the direct simulation monte carlo of gas flows,” *Clarendon, Oxford*, vol. 508, p. 128, 1994.
- [15] C. Cercignani, *The Boltzmann Equation and Its Applications*, ser. Applied Mathematical Sciences. New York: Springer-Verlag, 1988. [Online]. Available: [//www.springer.com/in/book/9780387966373](http://www.springer.com/in/book/9780387966373)
- [16] H. Aminfar and M. Mohammadpourfard, “Lattice Boltzmann BGK model for gas flow in a microchannel,” *Proceedings of the Institution of Mechanical Engineers, Part C: Journal of Mechanical Engineering Science*, vol. 222, no. 9, pp. 1855–1860, Sep. 2008. [Online]. Available: <http://journals.sagepub.com/doi/10.1243/09544062JMES809>
- [17] P. Lopez, “Thermal Lattice Boltzmann Simulation for Rarefied Flow in Microchannels,” PhD Thesis, Rice University, 2014.
- [18] G. A. Bird, *Molecular Gas Dynamics and the Direct Simulation of Gas Flows*, ser. Oxford Engineering Science Series. New York: Oxford University Press, May 1994.

- [19] H. C. Kuhlmann, M. Wanschura, and H. J. Rath, "Flow in two-sided lid-driven cavities: non-uniqueness, instabilities, and cellular structures," *Journal of Fluid Mechanics*, vol. 336, pp. 267–299, Apr. 1997.
- [20] D. Arumuga Perumal and A. K. Dass, "Multiplicity of steady solutions in two-dimensional lid-driven cavity flows by Lattice Boltzmann Method," *Computers & Mathematics with Applications*, vol. 61, no. 12, pp. 3711–3721, Jun. 2011. [Online]. Available: <http://www.sciencedirect.com/science/article/pii/S0898122110002427>
- [21] A. B. Cortes and J. D. Miller, "Numerical experiments with the lid driven cavity flow problem," *Computers & Fluids*, vol. 23, no. 8, pp. 1005–1027, Nov. 1994. [Online]. Available: <http://www.sciencedirect.com/science/article/pii/0045793094900027>
- [22] M. Cheng and K. C. Hung, "Vortex structure of steady flow in a rectangular cavity," *Computers & Fluids*, vol. 35, no. 10, pp. 1046–1062, Dec. 2006. [Online]. Available: <http://www.sciencedirect.com/science/article/pii/S0045793005001222>
- [23] R. Iwatsu, J. M. Hyun, and K. Kuwahara, "Numerical Simulation of Flows Driven by a Torsionally Oscillating Lid in a Square Cavity," *J. Fluids Eng*, vol. 114, no. 2, pp. 143–151, Jun. 1992. [Online]. Available: <http://dx.doi.org/10.1115/1.2910008>
- [24] C.-L. Chen and C.-H. Cheng, "Numerical simulation of periodic mixed convective heat transfer in a rectangular cavity with a vibrating lid," *Applied Thermal Engineering*, vol. 29, no. 14, pp. 2855–2862, Oct. 2009. [Online]. Available: <http://www.sciencedirect.com/science/article/pii/S135943110900057X>

- [25] D. Auld and Y. Lan, "Simulation of lid-driven cavity flow by parallel DSMC method," in *24th AIAA Applied Aerodynamics Conference*, 2006, p. 3328.
- [26] A. Mohammadzadeh, E. Roohi, and H. Niazmand, "A Parallel DSMC Investigation of Monatomic/Diatomic Gas Flows in a Micro/Nano Cavity," *Numerical Heat Transfer, Part A: Applications*, vol. 63, no. 4, pp. 305–325, Jan. 2013. [Online]. Available: <https://doi.org/10.1080/10407782.2013.730463>
- [27] H. Liu, M. Wang, J. Wang, G. Zhang, H. Liao, R. Huang, and X. Zhang, "Monte Carlo simulations of gas flow and heat transfer in vacuum packaged MEMS devices," *Applied Thermal Engineering*, vol. 27, no. 2, pp. 323–329, Feb. 2007. [Online]. Available: <http://www.sciencedirect.com/science/article/pii/S1359431106002808>
- [28] C. Cai, "Heat transfer in vacuum packaged microelectromechanical system devices," *Physics of Fluids*, vol. 20, no. 1, p. 017103, Jan. 2008. [Online]. Available: <http://aip.scitation.org/doi/10.1063/1.2832777>
- [29] A. Rana, M. Torrilhon, and H. Struchtrup, "A robust numerical method for the R13 equations of rarefied gas dynamics: Application to lid driven cavity," *Journal of Computational Physics*, vol. 236, pp. 169–186, Mar. 2013. [Online]. Available: <http://linkinghub.elsevier.com/retrieve/pii/S0021999112007036>
- [30] E. Y. Moghadam, E. Roohi, and J. A. Esfahani, "Heat transfer and fluid characteristics of rarefied flow in thermal cavities," *Vacuum*, vol. 109, pp. 333–340, Nov. 2014. [Online]. Available: <http://linkinghub.elsevier.com/retrieve/pii/S0042207X1400205X>

- [31] M. Eskandari and S. Nourazar, "On the time relaxed Monte Carlo computations for the lid-driven micro cavity flow," *Journal of Computational Physics*, vol. 343, pp. 355–367, Aug. 2017. [Online]. Available: <https://linkinghub.elsevier.com/retrieve/pii/S0021999117302048>
- [32] B. John, X.-J. Gu, and D. R. Emerson, "Investigation of Heat and Mass Transfer in a Lid-Driven Cavity Under Nonequilibrium Flow Conditions," *Numerical Heat Transfer, Part B: Fundamentals*, vol. 58, no. 5, pp. 287–303, Nov. 2010. [Online]. Available: <https://www.tandfonline.com/doi/abs/10.1080/10407790.2010.528737>
- [33] B. John, "Effects of incomplete surface accommodation on non-equilibrium heat transfer in cavity flow: A parallel dsmc study," *Computers & Fluids*, vol. 45, no. 1, pp. 197–201, 2011, 22nd International Conference on Parallel Computational Fluid Dynamics (ParCFD 2010). [Online]. Available: <https://www.sciencedirect.com/science/article/pii/S004579301100051X>
- [34] S. Naris and D. Valougeorgis, "The driven cavity flow over the whole range of the Knudsen number," *Physics of Fluids*, vol. 17, no. 9, p. 097106, Sep. 2005. [Online]. Available: <https://aip.scitation.org/doi/abs/10.1063/1.2047549>
- [35] K. Aoki, S. Takata, H. Aikawa, and F. Golse, "A rarefied gas flow caused by a discontinuous wall temperature," *Physics of Fluids*, vol. 13, no. 9, pp. 2645–2661, Sep. 2001. [Online]. Available: <http://aip.scitation.org/doi/10.1063/1.1389283>
- [36] J.-C. Huang, K. Xu, and P. Yu, "A Unified Gas-Kinetic Scheme for Continuum and Rarefied Flows II: Multi-Dimensional Cases," *Communications in Computational Physics*, vol. 12, no. 3, pp. 662–690, Sep. 2012.

- [37] V. Venugopal and S. S. Girimaji, "Unified Gas Kinetic Scheme and Direct Simulation Monte Carlo Computations of High-Speed Lid-Driven Microcavity Flows," *Communications in Computational Physics*, vol. 17, no. 05, pp. 1127–1150, May 2015. [Online]. Available: http://www.journals.cambridge.org/abstract_S1815240615000365
- [38] L. Wu, J. Reese, and Y. Zhang, "Oscillatory rarefied gas flow inside rectangular cavities," *Journal of Fluid Mechanics*, vol. 748, pp. 350–367, Jun. 2014. [Online]. Available: http://www.journals.cambridge.org/abstract_S0022112014001839
- [39] P. Wang, W. Su, L. Zhu, and Y. Zhang, "Heat and mass transfer of oscillatory lid-driven cavity flow in the continuum, transition and free molecular flow regimes," *International Journal of Heat and Mass Transfer*, vol. 131, pp. 291–300, Mar. 2019. [Online]. Available: <https://linkinghub.elsevier.com/retrieve/pii/S0017931018343618>
- [40] S. B. R., D. A. Perumal, and A. K. Yadav, "Computation of fluid flow in double sided cross-shaped lid-driven cavities using Lattice Boltzmann method," *European Journal of Mechanics - B/Fluids*, vol. 70, pp. 46–72, Jul. 2018. [Online]. Available: <http://www.sciencedirect.com/science/article/pii/S0997754616303417>
- [41] E. Wahba, "Multiplicity of states for two-sided and four-sided lid driven cavity flows," *Computers & Fluids*, vol. 38, no. 2, pp. 247–253, Feb. 2009. [Online]. Available: <https://linkinghub.elsevier.com/retrieve/pii/S0045793008000303>
- [42] J. Arrington, M. Bertram, A. Cary Jr, and L. Weinstein, "Heat transfer to wavy wall in hypersonic flow." *AIAA Journal*, vol. 5, no. 10, pp. 1760–1767, 1967.

- [43] A. Mazaheri and W. A. Wood, "Heating augmentation for short hypersonic protuberances," *Journal of Spacecraft and Rockets*, vol. 46, no. 2, pp. 284–291, 2009.
- [44] D. Estruch, D. G. MacManus, J. L. Stollery, N. J. Lawson, and K. P. Garry, "Hypersonic interference heating in the vicinity of surface protuberances," *Experiments in Fluids*, vol. 49, no. 3, pp. 683–699, Sep. 2010. [Online]. Available: <http://link.springer.com/10.1007/s00348-010-0844-x>
- [45] R. D. Neumann and D. C. Freeman, "Experimental Measurement of Aerodynamic Heating About Complex Shapes at Supersonic Mach Numbers," *Journal of Spacecraft and Rockets*, vol. 49, no. 6, pp. 1080–1087, Nov. 2012. [Online]. Available: <https://arc.aiaa.org/doi/10.2514/1.A32201>
- [46] A. F. Charwat, "Separation of a supersonic accelerated flow over notches," *AIAA Journal*, vol. 9, no. 8, pp. 1656–1657, Aug. 1971. [Online]. Available: <https://arc.aiaa.org/doi/10.2514/3.6413>
- [47] R. H. Howell and H. H. Korst, "Separation controlled transonic drag-rise modification for V-shaped notches," *AIAA Journal*, vol. 9, no. 10, pp. 2051–2057, Oct. 1971. [Online]. Available: <https://arc.aiaa.org/doi/10.2514/3.6460>
- [48] F. Pan and A. Acrivos, "Steady flows in rectangular cavities," *Journal of Fluid Mechanics*, vol. 28, no. 4, pp. 643–655, 1967.
- [49] A. Morgenstern and N. Chokani, "Hypersonic flow past open cavities," *AIAA journal*, vol. 32, no. 12, pp. 2387–2393, 1994.

- [50] A. P. Jackson, R. Hillier, and S. Soltani, “Experimental and computational study of laminar cavity flows at hypersonic speeds,” *J. Fluid Mech.*, vol. 427, pp. 329–358, Jan. 2001. [Online]. Available: https://www.cambridge.org/core/product/identifier/S0022112000002433/type/journal_article
- [51] J. L. Everhart, “Supersonic/Hypersonic Laminar Heating Correlations for Rectangular and Impact-Induced Open and Closed Cavities,” *Journal of Spacecraft and Rockets*, vol. 46, no. 3, pp. 545–560, May 2009. [Online]. Available: <https://arc.aiaa.org/doi/10.2514/1.36830>
- [52] J. Bertin and W. Goodrich, “Aerodynamic heating for gaps in laminar and transitional boundary layers,” in *18th Aerospace Sciences Meeting*. Pasadena, CA, U.S.A.: American Institute of Aeronautics and Astronautics, Jan. 1980. [Online]. Available: <http://arc.aiaa.org/doi/10.2514/6.1980-287>
- [53] D. Petley, D. Smith, C. Edwards, A. Carlson, and H. Hamilton, “Surface step induced gap heating in the shuttle thermal protection system,” *Journal of Spacecraft and Rockets*, vol. 21, no. 2, pp. 156–161, 1984.
- [54] M. Hinderks, A. Gülhan, and R. Radespiel, “Simulation of Hypersonic Gap Flow with Consideration of Fluid Structure Interaction,” in *34th AIAA Fluid Dynamics Conference and Exhibit*. Portland, Oregon: American Institute of Aeronautics and Astronautics, Jun. 2004. [Online]. Available: <http://arc.aiaa.org/doi/10.2514/6.2004-2238>
- [55] H. Le, P. Moin, and J. Kim, “Direct numerical simulation of turbulent flow over a backward-facing step,” *Journal of Fluid Mechanics*, vol. 330, pp.

- 349–374, Jan. 1997. [Online]. Available: http://www.journals.cambridge.org/abstract_S0022112096003941
- [56] A. Liakos and N. A. Malamataris, “Topological study of steady state, three dimensional flow over a backward facing step,” *Computers & Fluids*, vol. 118, pp. 1–18, Sep. 2015. [Online]. Available: <https://linkinghub.elsevier.com/retrieve/pii/S0045793015001747>
- [57] G.R. Inger, “Supersonic Laminar Flow Past a Small Rear-Facing Step,” *AIAA Journal*, vol. 12, no. 6, pp. 739–740, Jun. 1974. [Online]. Available: <http://arc.aiaa.org/doi/abs/10.2514/3.49343>
- [58] E. Baum, “An interaction model of a supersonic laminar boundary layer on sharp and rounded backward facing steps.” *AIAA Journal*, vol. 6, no. 3, pp. 440–447, Mar. 1968. [Online]. Available: <http://arc.aiaa.org/doi/10.2514/3.4518>
- [59] S. L. Gai and M. J. Hayne, “Heat Transfer Behind a Step in High-Enthalpy Laminar Hypersonic Flow,” *Journal of Thermophysics and Heat Transfer*, vol. 24, no. 4, pp. 839–841, Oct. 2010. [Online]. Available: <http://arc.aiaa.org/doi/10.2514/1.49300>
- [60] S. L. Gai, “Separated high enthalpy dissociated laminar hypersonic flow behind a step - Pressure measurements,” *AIAA Journal*, vol. 30, no. 7, pp. 1915–1918, Jul. 1992. [Online]. Available: <http://arc.aiaa.org/doi/10.2514/3.11155>
- [61] H.-i. Choi, D.-h. Lee, and D. Lee, “Complex Microscale Flow Simulations Using Langmuir Slip Condition,” *Numerical Heat Transfer, Part A:*

- Applications*, vol. 48, no. 5, pp. 407–425, Sep. 2005. [Online]. Available: <http://www.tandfonline.com/doi/abs/10.1080/10407780590957206>
- [62] T.-Y. Hsieh, Z.-C. Hong, and Y.-C. Pan, “Flow Characteristics of Three-Dimensional Microscale Backward-Facing Step Flows,” *Numerical Heat Transfer, Part A: Applications*, vol. 57, no. 5, pp. 331–345, Mar. 2010. [Online]. Available: <http://www.tandfonline.com/doi/abs/10.1080/10407780903582992>
- [63] A. Beskok, “Validation of a new velocity-slip model for separated gas microflows,” *Numerical Heat Transfer, Part B: Fundamentals*, vol. 40, no. 6, pp. 451–471, Dec. 2001. [Online]. Available: <https://www.tandfonline.com/doi/full/10.1080/104077901753306593>
- [64] B. Celik and F. O. Edis, “Computational Investigation of Micro Backward-Facing Step Duct Flow in Slip Regime,” *Nanoscale and Microscale Thermophysical Engineering*, vol. 11, no. 3-4, pp. 319–331, Dec. 2007. [Online]. Available: <http://www.tandfonline.com/doi/abs/10.1080/15567260701715438>
- [65] J. Rached and N. Daher, “Numerical prediction of slip flow and heat transfer in microchannels,” in *Proceedings of the 6th Annual Engineering Students Conference-American University of Beirut*. Citeseer, 2007, pp. 109–114.
- [66] O. Baysal, N. Erbas, and M. Koklu, “Control of separated flow past a backward facing step in a microchannel,” *Microfluidics and Nanofluidics*, vol. 1, no. 1, pp. 86–92, Nov. 2004. [Online]. Available: <http://link.springer.com/10.1007/s10404-004-0003-x>

- [67] H. Xue and S. Chen, "Dsmc simulation of microscale backward facing step flow," *Microscale Thermophysical Engineering*, vol. 7, no. 1, pp. 69–86, Jan. 2003. [Online]. Available: <http://www.tandfonline.com/doi/abs/10.1080/10893950390150449>
- [68] H. Xue, B. Xu, Y. Wei, and J. Wu, "Unique behaviors of a backward-facing step flow at microscale," *Numerical Heat Transfer, Part A: Applications*, vol. 47, no. 3, pp. 251–268, Jan. 2005. [Online]. Available: <http://www.tandfonline.com/doi/abs/10.1080/10407780590889121>
- [69] U. Kursun and J. Kapat, "Modeling of Microscale Gas Flows in Transition Regime Part I: Flow over Backward Facing Steps," *Nanoscale and Microscale Thermophysical Engineering*, vol. 11, no. 1-2, pp. 15–30, May 2007. [Online]. Available: <http://www.tandfonline.com/doi/abs/10.1080/15567260701333372>
- [70] F.-b. Bao and J.-z. Lin, "Continuum Simulation of the Microscale Backward-Facing Step Flow in a Transition Regime," *Numerical Heat Transfer, Part A: Applications*, vol. 59, no. 8, pp. 616–632, Apr. 2011. [Online]. Available: <https://doi.org/10.1080/10407782.2011.561073>
- [71] M. Darbandi and E. Roohi, "DSMC simulation of subsonic flow through nanochannels and micro/nano backward-facing steps," *International Communications in Heat and Mass Transfer*, vol. 38, no. 10, pp. 1443–1448, Dec. 2011. [Online]. Available: <https://linkinghub.elsevier.com/retrieve/pii/S0735193311001746>
- [72] A.-M. Mahdavi, N. T. P. Le, E. Roohi, and C. White, "Thermal Rarefied Gas Flow Investigations Through Micro-/Nano-Backward-Facing

- Step: Comparison of DSMC and CFD Subject to Hybrid Slip and Jump Boundary Conditions,” *Numerical Heat Transfer, Part A: Applications*, vol. 66, no. 7, pp. 733–755, Oct. 2014. [Online]. Available: <http://www.tandfonline.com/doi/abs/10.1080/10407782.2014.892349>
- [73] A. Gavasane, A. Agrawal, and U. Bhandarkar, “Study of rarefied gas flows in backward facing micro-step using Direct Simulation Monte Carlo,” *Vacuum*, vol. 155, pp. 249–259, Sep. 2018. [Online]. Available: <https://linkinghub.elsevier.com/retrieve/pii/S0042207X18303841>
- [74] P. H. M. Leite and W. F. N. Santos, “Computational Analysis of a Rarefied Hypersonic Flow over Backward-Facing Steps,” *Journal of Thermophysics and Heat Transfer*, pp. 1–13, Feb. 2019. [Online]. Available: <https://arc.aiaa.org/doi/10.2514/1.T5486>
- [75] S. M. Bogdonoff and C. E. Kepler, “Separation of a Supersonic Turbulent Boundary Layer,” *Journal of the Aeronautical Sciences*, vol. 22, no. 6, pp. 414–430, Jun. 1955. [Online]. Available: <https://arc.aiaa.org/doi/10.2514/8.3358>
- [76] E. Rogers and C. Berry, “Research at the NPL on the influence at supersonic speeds and low Reynolds numbers of thick laminar boundary layers,” in *Rarefied Gas Dynamics, Volume 1*, 1965, p. 574.
- [77] R. T. Driftmyer, *A forward facing step study: the step height less than the boundary-layer thickness*. United States Naval Ordnance Laboratory, 1973, vol. 73.

- [78] D. I. Pullin and J. K. Harvey, "Direct simulation calculations of the rarefied flow past a forward-facing step," *AIAA Journal*, vol. 15, no. 1, pp. 124–126, Jan. 1977. [Online]. Available: <http://arc.aiaa.org/doi/10.2514/3.7310>
- [79] I. Grotowsky and J. Ballmann, "Numerical investigation of hypersonic step-flows," *Shock Waves*, vol. 10, no. 1, pp. 57–72, Mar. 2000. [Online]. Available: <https://doi.org/10.1007/s001930050179>
- [80] P. Leite and W. Santos, "Computational analysis of the flow field structure of a non-reacting hypersonic flow over forward-facing steps," *Journal of Fluid Mechanics*, vol. 763, pp. 460–499, Jan. 2015. [Online]. Available: http://www.journals.cambridge.org/abstract_S0022112014006776
- [81] A. F. Charwat, C. F. Dewey, J. N. Roos, and J. A. Hitz, "An Investigation of Separated Flows- Part II : Flow in the Cavity and Heat Transfer," *Journal of the Aerospace Sciences*, vol. 28, no. 7, pp. 513–527, Jul. 1961. [Online]. Available: <https://arc.aiaa.org/doi/10.2514/8.9099>
- [82] M. H. Bertram and M. M. Wiggs, "Effect of surface distortions on the heat transfer to a wing at hypersonic speeds," *AIAA Journal*, vol. 1, no. 6, pp. 1313–1319, Jun. 1963. [Online]. Available: <https://arc.aiaa.org/doi/10.2514/3.1786>
- [83] Nestler, D. E.; Saydah, A. R., "Heat transfer to steps and cavities in hypersonic turbulent flow." *AIAA Journal*, vol. 7, no. 7, pp. 1368–1370, Jul. 1969. [Online]. Available: <http://arc.aiaa.org/doi/abs/10.2514/3.5351>
- [84] D. E. Nestler, "An experimental study of hypersonic cavity flow," *Journal of Spacecraft and Rockets*, vol. 19, no. 3, pp. 195–196, 1982.

- [85] J. Everhart, S. Alter, R. Merski, W. Wood, and R. Prabhu, "Pressure Gradient Effects on Hypersonic Cavity Flow Heating," in *44th AIAA Aerospace Sciences Meeting and Exhibit*. Reno, Nevada: American Institute of Aeronautics and Astronautics, Jan. 2006. [Online]. Available: <http://arc.aiaa.org/doi/10.2514/6.2006-185>
- [86] S. Creighton and R. Hillier, "Experimental and computational study of unsteady hypersonic cavity flows," *The Aeronautical Journal*, vol. 111, no. 1125, pp. 673–688, 2007, publisher: Cambridge University Press.
- [87] R. C. Palharini, T. J. Scanlon, and J. M. Reese, "Aerothermodynamic Comparison of Two- and Three-Dimensional Rarefied Hypersonic Cavity Flows," *Journal of Spacecraft and Rockets*, vol. 51, no. 5, pp. 1619–1630, Sep. 2014. [Online]. Available: <https://arc.aiaa.org/doi/10.2514/1.A32746>
- [88] L. T. L. C. Paolicchi and W. F. N. Santos, "Length-to-Depth Ratio Effects on Aerodynamic Surface Quantities of a Hypersonic Gap Flow," *AIAA Journal*, vol. 56, no. 2, pp. 780–792, Feb. 2018. [Online]. Available: <https://arc.aiaa.org/doi/10.2514/1.J055826>
- [89] G. Guo and Q. Luo, "DSMC investigation on flow characteristics of rarefied hypersonic flow over a cavity with different geometric shapes," *International Journal of Mechanical Sciences*, vol. 148, pp. 496–509, Nov. 2018. [Online]. Available: <https://linkinghub.elsevier.com/retrieve/pii/S0020740318314437>
- [90] R. C. Palharini, T. J. Scanlon, and C. White, "Chemically reacting hypersonic flows over 3D cavities: Flowfield structure characterisation,"

- Computers & Fluids*, vol. 165, pp. 173–187, Mar. 2018. [Online]. Available: <https://linkinghub.elsevier.com/retrieve/pii/S0045793018300355>
- [91] R. C. Palharini and W. F. Santos, “The impact of the length-to-depth ratio on aerodynamic surface quantities of a rarefied hypersonic cavity flow,” *Aerospace Science and Technology*, vol. 88, pp. 110–125, 2019, publisher: Elsevier.
- [92] X. Jin, B. Wang, X. Cheng, Q. Wang, and F. Huang, “The effects of Maxwellian accommodation coefficient and free-stream Knudsen number on rarefied hypersonic cavity flows,” *Aerospace Science and Technology*, vol. 97, p. 105577, Feb. 2020. [Online]. Available: <https://linkinghub.elsevier.com/retrieve/pii/S1270963819320346>
- [93] I. Castro and A. Robins, “The flow around a surface-mounted cube in uniform and turbulent streams,” *Journal of fluid Mechanics*, vol. 79, no. 2, pp. 307–335, 1977.
- [94] R. P. Hoxey, P. J. Richards, and J. L. Short, “A 6 m cube in an atmospheric boundary layer flow -Part 1. Full-scale and wind-tunnel results,” *Wind and Structures*, vol. 5, no. 2_3_4, pp. 165–176, 2002. [Online]. Available: <http://koreascience.or.kr/article/JAKO200221349897950.page>
- [95] J. Sousa, “Turbulent flow around a surface-mounted obstacle using 2D-3C DPIV,” *Experiments in Fluids*, vol. 33, no. 6, pp. 854–862, Dec. 2002. [Online]. Available: <http://link.springer.com/10.1007/s00348-002-0497-5>
- [96] H. Nakamura, T. Igarashi, and T. Tsutsui, “Local heat transfer around a wall-mounted cube in the turbulent boundary layer,” *International Journal of Heat*

- and Mass Transfer*, vol. 44, no. 18, pp. 3385–3395, Sep. 2001. [Online]. Available: <http://www.sciencedirect.com/science/article/pii/S0017931001000096>
- [97] A. Yakhot, H. Liu, and N. Nikitin, “Turbulent flow around a wall-mounted cube: A direct numerical simulation,” *International Journal of Heat and Fluid Flow*, vol. 27, no. 6, pp. 994–1009, Dec. 2006. [Online]. Available: <http://www.sciencedirect.com/science/article/pii/S0142727X06000476>
- [98] H. C. Lim, T. G. Thomas, and I. P. Castro, “Flow around a cube in a turbulent boundary layer: LES and experiment,” *Journal of Wind Engineering and Industrial Aerodynamics*, vol. 97, no. 2, pp. 96–109, Feb. 2009. [Online]. Available: <http://www.sciencedirect.com/science/article/pii/S0167610509000117>
- [99] S. Murakami and A. Mochida, “On turbulent vortex shedding flow past 2D square cylinder predicted by CFD,” *Journal of Wind Engineering and Industrial Aerodynamics*, vol. 54-55, pp. 191–211, Feb. 1995. [Online]. Available: <http://www.sciencedirect.com/science/article/pii/016761059400043D>
- [100] W. Ren, H. Liu, and S. Jin, “An asymptotic-preserving Monte Carlo method for the Boltzmann equation,” *Journal of Computational Physics*, vol. 276, pp. 380–404, Nov. 2014. [Online]. Available: <http://www.sciencedirect.com/science/article/pii/S0021999114005221>
- [101] B. Zhang, H. Liu, and S. Jin, “An asymptotic preserving Monte Carlo method for the multispecies Boltzmann equation,” *Journal of Computational Physics*, vol. 305, pp. 575–588, 2016, publisher: Elsevier.

- [102] E. Lekzian, A. Ebrahimi, and H. Parhizkar, "Performance analysis of microelectromechanical thrusters using a direct simulation Monte Carlo solver," *Proceedings of the Institution of Mechanical Engineers, Part G: Journal of Aerospace Engineering*, vol. 232, no. 7, pp. 1212–1222, Jun. 2018. [Online]. Available: <http://journals.sagepub.com/doi/10.1177/0954410017691066>
- [103] K. S. Myo, W. Zhou, K. L. Lee, S. Yu, and W. Hua, "Direct Monte Carlo simulation of nanoscale mixed gas bearings," *Advances in Mechanical Engineering*, vol. 7, no. 6, p. 168781401558952, Jun. 2015. [Online]. Available: <http://journals.sagepub.com/doi/10.1177/1687814015589528>
- [104] D. Gladkov, J.-J. Tapia, S. Alberts, and R. M. D'Souza, "Graphics processing unit based direct simulation Monte Carlo," *SIMULATION*, vol. 88, no. 6, pp. 680–693, Jun. 2012. [Online]. Available: <http://journals.sagepub.com/doi/10.1177/0037549711418787>
- [105] G. Zuppari, G. Visone, R. Votta, and A. Schettino, "Analysis of Aerodynamic Performances of Experimental Flying Test Bed in High-Altitude Flight," *Proceedings of the Institution of Mechanical Engineers, Part G: Journal of Aerospace Engineering*, vol. 225, no. 3, pp. 247–258, Mar. 2011. [Online]. Available: <http://journals.sagepub.com/doi/10.1243/09544100JAERO873>
- [106] M. Nourmohammadzadeh, M. Rahnama, S. Jafari, and A. Akhgar, "Microchannel flow simulation in transition regime using lattice Boltzmann method," *Proceedings of the Institution of Mechanical Engineers, Part C: Journal of Mechanical Engineering Science*, vol. 226, no. 2, pp. 552–562, Feb. 2012. [Online]. Available: <http://pic.sagepub.com/lookup/doi/10.1177/0954406211413959>

- [107] G. Zuppari and D. Paterna, "Influence of rarefaction on the computation of aerodynamic parameters in hypersonic flow," *Proceedings of the Institution of Mechanical Engineers, Part G: Journal of Aerospace Engineering*, vol. 216, no. 6, pp. 277–290, Jun. 2002. [Online]. Available: <http://journals.sagepub.com/doi/10.1243/095441002321029026>
- [108] Y. H. Sun, W. K. Chan, and N. Y. Liu, "A slip model for gas lubrication based on an effective viscosity concept," *Proceedings of the Institution of Mechanical Engineers, Part J: Journal of Engineering Tribology*, vol. 217, no. 3, pp. 187–195, Mar. 2003. [Online]. Available: <http://journals.sagepub.com/doi/10.1243/135065003765714836>
- [109] A.-S. Yang, "Plume impingement investigation using Monte-Carlo computations," *Proceedings of the Institution of Mechanical Engineers, Part G: Journal of Aerospace Engineering*, vol. 220, no. 5, pp. 365–373, Oct. 2006. [Online]. Available: <http://journals.sagepub.com/doi/10.1243/09544100JAERO84>
- [110] F. J. Alexander, A. L. Garcia, and B. J. Alder, "Cell size dependence of transport coefficients in stochastic particle algorithms," *Physics of Fluids*, vol. 10, no. 6, pp. 1540–1542, May 1998. [Online]. Available: <https://aip.scitation.org/doi/10.1063/1.869674>
- [111] F. J., A. L. Garcia, Alexander, and B. J. Alder, "Erratum: "cell size dependence of transport coefficients in stochastic particle algorithms"[phys. fluids 10, 1540 (1998)]," *Physics of Fluids*, vol. 12, no. 3, pp. 731–731, 2000.

- [112] N. G. Hadjiconstantinou, “Analysis of discretization in the direct simulation Monte Carlo,” *Physics of Fluids*, vol. 12, no. 10, pp. 2634–2638, Sep. 2000. [Online]. Available: <https://aip.scitation.org/doi/10.1063/1.1289393>
- [113] D. Zhou, A. T. J. Kadaksham, M. D. Murthy Peri, I. Varghese, and C. Cetinkaya, “Nanoparticle Detachment Using Shock Waves,” *Proceedings of the Institution of Mechanical Engineers, Part N: Journal of Nanoengineering and Nanosystems*, vol. 219, no. 3, pp. 91–102, Sep. 2005. [Online]. Available: <http://journals.sagepub.com/doi/10.1243/17403499JNN45>
- [114] Z.-X. Sun, Z. Tang, Y.-L. He, and W.-Q. Tao, “Proper cell dimension and number of particles per cell for DSMC,” *Computers & Fluids*, vol. 50, no. 1, pp. 1–9, Nov. 2011. [Online]. Available: <https://linkinghub.elsevier.com/retrieve/pii/S0045793011001472>
- [115] T. Abe, “Generalized scheme of the no-time-counter scheme for the DSMC in rarefied gas flow analysis,” *Computers & Fluids*, vol. 22, no. 2, pp. 253–257, Mar. 1993. [Online]. Available: <http://www.sciencedirect.com/science/article/pii/S004579309390057G>
- [116] E. Roohi, S. Stefanov, A. Shoja-Sani, and H. Ejraei, “A generalized form of the Bernoulli Trial collision scheme in DSMC: Derivation and evaluation,” *Journal of Computational Physics*, vol. 354, pp. 476–492, Feb. 2018. [Online]. Available: <http://www.sciencedirect.com/science/article/pii/S0021999117307921>

- [117] S. K. Stefanov, "On DSMC Calculations of Rarefied Gas Flows with Small Number of Particles in Cells," *SIAM J. Sci. Comput.*, vol. 33, no. 2, pp. 677–702, Jan. 2011. [Online]. Available: <https://epubs.siam.org/doi/10.1137/090751864>
- [118] B. Goshayeshi, E. Roohi, and S. Stefanov, "DSMC simulation of hypersonic flows using an improved SBT-TAS technique," *Journal of Computational Physics*, vol. 303, pp. 28–44, Dec. 2015. [Online]. Available: <https://linkinghub.elsevier.com/retrieve/pii/S0021999115006208>
- [119] G. B. Roohi Ehsan and S. Stefan, "A novel simplified bernoulli trials collision scheme in the direct simulation monte carlo with intelligence over particle distances," *Physics of Fluids*, vol. 27, no. 10, p. 107104, 2015.
- [120] S. A. Saadati and E. Roohi, "Detailed investigation of flow and thermal field in micro/nano nozzles using Simplified Bernoulli Trial (SBT) collision scheme in DSMC," *Aerospace Science and Technology*, vol. 46, pp. 236–255, Oct. 2015. [Online]. Available: <http://www.sciencedirect.com/science/article/pii/S1270963815002205>
- [121] E. Taheri, E. Roohi, and S. Stefanov, "On the convergence of the simplified Bernoulli trial collision scheme in rarefied Fourier flow," *Physics of Fluids*, vol. 29, no. 6, p. 062003, Jun. 2017. [Online]. Available: <https://aip.scitation.org/doi/abs/10.1063/1.4985712>
- [122] P. Prasanth and J. K. Kakkassery, "Direct simulation Monte Carlo (DSMC): A numerical method for transition-regime flows-A review," *Journal of the Indian Institute of Science*, vol. 86, no. 3, pp. 169–192, 2013.

- [123] J. K. Kakkassery and P. Prasanth, "Molecular models for simulation of rarefied gas flows using direct simulation monte carlo method," *Fluid dynamics research*, vol. 40, no. 4, p. 233, 2008.
- [124] C. Borgnakke and P. S. Larsen, "Statistical collision model for Monte Carlo simulation of polyatomic gas mixture," *Journal of Computational Physics*, vol. 18, no. 4, pp. 405–420, Aug. 1975. [Online]. Available: <http://www.sciencedirect.com/science/article/pii/0021999175900947>
- [125] E. Gabriel, G. E. Fagg, G. Bosilca, T. Angskun, J. J. Dongarra, J. M. Squyres, V. Sahay, P. Kambadur, B. Barrett, A. Lumsdaine, and others, "Open MPI: Goals, concept, and design of a next generation MPI implementation," in *European Parallel Virtual Machine/Message Passing Interface Users' Group Meeting*. Springer, 2004, pp. 97–104.
- [126] T. J. Scanlon, C. White, M. K. Borg, R. C. Palharini, E. Farbar, I. D. Boyd, J. M. Reese, and R. E. Brown, "Open-source direct simulation monte carlo chemistry modeling for hypersonic flows," *AIAA journal*, vol. 53, no. 6, pp. 1670–1680, 2015, publisher: The American Institute of Aeronautics and Astronautics.
- [127] H. Jasak, A. Jemcov, Z. Tukovic, and others, "OpenFOAM: A C++ library for complex physics simulations," in *International workshop on coupled methods in numerical dynamics*, vol. 1000. IUC Dubrovnik Croatia, 2007, pp. 1–20.
- [128] G. Bird, "The QK model for gas-phase chemical reaction rates," *Physics of Fluids*, vol. 23, no. 10, p. 106101, 2011, publisher: American Institute of Physics.

- [129] C. White, M. K. Borg, T. J. Scanlon, S. M. Longshaw, B. John, D. R. Emerson, and J. M. Reese, “dsmcfoam+: An openfoam based direct simulation monte carlo solver,” *Computer Physics Communications*, vol. 224, pp. 22–43, 2018.
- [130] E. Oran, C. Oh, and B. Cybyk, “Direct simulation monte carlo: Recent Advances and Applications,” *Annual Review of Fluid Mechanics*, vol. 30, no. 1, pp. 403–441, Jan. 1998. [Online]. Available: <http://www.annualreviews.org/doi/10.1146/annurev.fluid.30.1.403>
- [131] M. Gad-el Hak, “Molecular-based microfluidic simulation models,” in *The MEMS Handbook-3 Volume Set*. CRC Press, 2019, pp. 116–142.
- [132] A. Karchani and O. Ejtehadi, “A review and perspective on a convergence analysis of the direct simulation Monte Carlo and solution verification,” *Physics of Fluids*, vol. 31, no. 6, p. 066101, Jun. 2019. [Online]. Available: <http://aip.scitation.org/doi/10.1063/1.5093746>
- [133] M. Becker, F. Robben, and R. Cattolicai, “Velocity Distribution Functions Near the Leading Edge of a Flat Plate,” *AIAA Journal*, vol. 12, no. 9, pp. 1247–1253, Sep. 1974. [Online]. Available: <http://arc.aiaa.org/doi/10.2514/3.49461>
- [134] W. L. Hermina, “Monte Carlo simulation of rarefied flow along a flat plate,” *Journal of Thermophysics and Heat Transfer*, vol. 3, no. 1, pp. 7–12, Jan. 1989. [Online]. Available: <http://arc.aiaa.org/doi/10.2514/3.118>
- [135] G.-m. Guo, H. Liu, and B. Zhang, “Numerical study of active flow control over a hypersonic backward-facing step using supersonic jet in near space,”

- Acta Astronautica*, vol. 132, pp. 256–267, Mar. 2017. [Online]. Available: <https://linkinghub.elsevier.com/retrieve/pii/S0094576516311432>
- [136] A. Y. Gelfgat, “Linear instability of the lid-driven flow in a cubic cavity,” *Theoretical and Computational Fluid Dynamics*, vol. 33, no. 1, pp. 59–82, Feb. 2019. [Online]. Available: <http://link.springer.com/10.1007/s00162-019-00483-1>
- [137] C.-H. Bruneau and M. Saad, “The 2D lid-driven cavity problem revisited,” *Computers & Fluids*, vol. 35, no. 3, pp. 326–348, Mar. 2006. [Online]. Available: <http://www.sciencedirect.com/science/article/pii/S0045793005000368>
- [138] U. Ghia, K. N. Ghia, and C. T. Shin, “High-Re solutions for incompressible flow using the Navier-Stokes equations and a multigrid method,” *Journal of Computational Physics*, vol. 48, no. 3, pp. 387–411, Dec. 1982. [Online]. Available: <http://www.sciencedirect.com/science/article/pii/0021999182900584>
- [139] P. N. Shankar and M. D. Deshpande, “Fluid Mechanics in the Driven Cavity,” *Annual Review of Fluid Mechanics*, vol. 32, no. 1, pp. 93–136, 2000. [Online]. Available: <https://doi.org/10.1146/annurev.fluid.32.1.93>
- [140] M. Balaj, H. Akhlaghi, and E. Roohi, “Rarefied gas flow behavior in micro/nanochannels under specified wall heat flux,” *International Journal of Modern Physics C*, vol. 26, no. 08, p. 1550087, Aug. 2015. [Online]. Available: <https://www.worldscientific.com/doi/abs/10.1142/S0129183115500874>
- [141] Y. Sone, *Molecular gas dynamics: theory, techniques, and applications*. Springer Science & Business Media, 2007.

- [142] E. Roohi, V. Shahabi, and A. Bagherzadeh, "On the vortical characteristics and cold-to-hot transfer of rarefied gas flow in a lid driven isosceles orthogonal triangular cavity with isothermal walls," *International Journal of Thermal Sciences*, vol. 125, pp. 381–394, Mar. 2018. [Online]. Available: <http://www.sciencedirect.com/science/article/pii/S1290072917310141>
- [143] A. Bhagat, H. Gijare, and N. Dongari, "Implementation of Knudsen Layer Phenomena in Rarefied High-Speed Gas Flows," *Journal of Aerospace Engineering*, vol. 32, no. 6, p. 04019100, Nov. 2019. [Online]. Available: <http://ascelibrary.org/doi/10.1061/%28ASCE%29AS.1943-5525.0001097>
- [144] A. Kurganov, S. Noelle, and G. Petrova, "Semidiscrete central-upwind schemes for hyperbolic conservation laws and hamilton–jacobi equations," *SIAM Journal on Scientific Computing*, vol. 23, no. 3, pp. 707–740, 2001.
- [145] C. J. Greenshields, H. G. Weller, L. Gasparini, and J. M. Reese, "Implementation of semi-discrete, non-staggered central schemes in a colocated, polyhedral, finite volume framework, for high-speed viscous flows," *International journal for numerical methods in fluids*, vol. 63, no. 1, pp. 1–21, 2010.
- [146] N. T. Le and E. Roohi, "A new form of the second-order temperature jump boundary condition for the low-speed nanoscale and hypersonic rarefied gas flow simulations," *International Journal of Thermal Sciences*, vol. 98, pp. 51–59, 2015.
- [147] E. Roohi and S. Stefanov, "Collision partner selection schemes in DSMC: From micro/nano flows to hypersonic flows," *Physics Reports*, vol. 656, pp. 1–38,

- Oct. 2016. [Online]. Available: <http://www.sciencedirect.com/science/article/pii/S0370157316302344>
- [148] U. S. Atmosphere, *US standard atmosphere*. National Oceanic and Atmospheric Administration, 1976.
- [149] F. Schäfer, M. Breuer, and F. Durst, “The dynamics of the transitional flow over a backward-facing step,” *Journal of Fluid Mechanics*, vol. 623, p. 85, Mar. 2009. [Online]. Available: http://www.journals.cambridge.org/abstract_S0022112008005235
- [150] M. Ji and M. Wang, “Sound generation by turbulent boundary-layer flow over small steps,” *Journal of Fluid Mechanics*, vol. 654, pp. 161–193, Jul. 2010. [Online]. Available: http://www.journals.cambridge.org/abstract_S0022112010000467
- [151] M. Wang and M. Ji, “Surface pressure fluctuations on steps immersed in turbulent boundary layers,” *Journal of Fluid Mechanics*, vol. 712, pp. 471–504, Dec. 2012. [Online]. Available: http://www.journals.cambridge.org/abstract_S0022112012004338
- [152] N. Deepak, S. Gai, and A. Neely, “A computational study of high enthalpy flow over a rearward facing step,” in *48th AIAA Aerospace Sciences Meeting Including the New Horizons Forum and Aerospace Exposition, Orlando, FL, AIAA Paper*, vol. 444, 2010.
- [153] R. Cassineli Palharini and T. Scanlon, “Atmospheric reentry modelling using an open source DSMC code,” PhD Thesis, University of Strathclyde, 2014.

- [154] H.-i. Choi, D.-h. Lee, and D. Lee, "Complex microscale flow simulations using langmuir slip condition," *Numerical Heat Transfer, Part A: Applications*, vol. 48, no. 5, pp. 407–425, 2005.
- [155] J. Rom and A. Seginer, "Laminar heat transfer to a two-dimensional backward facing step from the high-enthalpy supersonic flow in the shock tube," *AIAA Journal*, vol. 2, no. 2, pp. 251–255, Feb. 1964. [Online]. Available: <https://arc.aiaa.org/doi/10.2514/3.2295>
- [156] R. Gupta, C. Scott, and J. Moss, "Surface-slip equations for low-Reynolds-number multicomponent gas flows," in *19th Thermophysics Conference*, 1984, p. 1732.
- [157] S. A. Rooholghdos and E. Roohi, "Extension of a second order velocity slip/temperature jump boundary condition to simulate high speed micro/nanoflows," *Computers & Mathematics with Applications*, vol. 67, no. 11, pp. 2029–2040, Jun. 2014. [Online]. Available: <https://linkinghub.elsevier.com/retrieve/pii/S0898122114001850>
- [158] H. Akhlaghi, M. Balaj, and E. Roohi, "Direct simulation Monte Carlo investigation of mixed supersonic–subsonic flow through micro-/nano-scale channels," *Physica Scripta*, vol. 88, no. 1, p. 015401, 2013, publisher: IOP Publishing.
- [159] K. Guo and G. Liaw, "A Review-Boundary conditions for the DSMC method," in *35th AIAA Thermophysics Conference*, 2001, p. 2953.
- [160] R. Camussi, M. Felli, F. Pereira, G. Aloisio, and A. Di Marco, "Statistical properties of wall pressure fluctuations over a forward-facing step," *Physics*

- of Fluids*, vol. 20, no. 7, p. 075113, Jul. 2008. [Online]. Available: <http://aip.scitation.org/doi/10.1063/1.2959172>
- [161] O. Ejtehadi, E. Roohi, and J. A. Esfahani, "Detailed investigation of hydrodynamics and thermal behavior of nano/micro shear driven flow using DSMC," *Scientia Iranica*, p. 13, 2013.
- [162] E. K. Ahangar, M. B. Ayani, and J. A. Esfahani, "Simulation of rarefied gas flow in a microchannel with backward facing step by two relaxation times using Lattice Boltzmann method—Slip and transient flow regimes," *International Journal of Mechanical Sciences*, vol. 157, pp. 802–815, 2019, publisher: Elsevier.
- [163] C. Hong and Y. Asako, "Some considerations on thermal boundary condition of slip flow," *International Journal of Heat and Mass Transfer*, vol. 53, no. 15-16, pp. 3075–3079, 2010, publisher: Elsevier.

Scientific publications from the present research work

International Journals

- (1) **Deepak Nabapure**, Ram Chandra Murthy K, “DSMC Investigation of Rarefied Gas Flow in a Four-Sided Lid Driven Cavity: Effect of Rarefaction and Lid Velocities ”, *Journal of Computational Science*.
<https://doi.org/10.1016/j.jocs.2020.101276>
- (2) **Deepak Nabapure**, Ram Chandra Murthy K, “DSMC investigation of rarefied gas flow over a 2D forward-facing step: Effect of Knudsen number”, *Acta Astronautica*, vol. 178, pp. 89–109, Jan. 2021.
<https://doi.org/10.1016/j.actaastro.2020.08.030>
- (3) **Deepak Nabapure**, Ram Chandra Murthy K, “DSMC simulation of rarefied gas flow over a 2D backward-facing step in the transitional flow regime: Effect of Mach number and wall temperature”, *Proceedings of the Institution of Mechanical Engineers, Part G: Journal of Aerospace Engineering, SAGE Publications*, vol. online first, pp. 0954410020959872, Sep. 2020.
<https://doi.org/10.1177/0954410020959872>
- (4) **Deepak Nabapure**, Ram Chandra Murthy K, “Simulation of flow in single and double-sided lid driven square cavities by direct simulation Monte Carlo method”,

Thermal Science, vol. 24, pp. 3031-3045, June. 2020.

<https://doi.org/10.2298/TSCI180906066N>

- (5) **Deepak Nabapure**, Arjun Singh, Ram Chandra Murthy K, “ Investigation of rarefied flow over backward-facing step in different rarefaction regimes using direct simulation Monte Carlo”, *The Aeronautical Journal*, 1-28,2021.
<https://doi.org/10.1017/aer.2021.88>
- (6) **Deepak Nabapure**, Ram Chandra Murthy K, “Effect of Aspect Ratio on the Rarefied Flow of Argon in a Four-Sided Lid-Driven Cavity using Direct Simulation Monte Carlo Method”, (under review).
- (7) **Deepak Nabapure**, Ram Chandra Murthy K, “Investigation of rarefied flow over an open cavity using DSMC”, (under review).

Conference Proceedings

- (1) **Deepak Nabapure**, Jayesh Sanwal, Sreeram Rajesh, K Ram Chandra Murthy, “Investigation of Subsonic and Hypersonic Rarefied Gas Flow over a Backward Facing Step”, *Journal of Physics: Conference Series*, vol. 1276, pp. 012007, Aug. 2019.
<https://iopscience.iop.org/article/10.1088/1742-6596/1276/1/012007/meta>
- (2) **Deepak Nabapure**, Ram Chandra Murthy K, “DSMC Simulation of Rarefied Gas Flow Over a Forward-Facing Step”, *ICTEA: International Conference on Thermal Engineering*, vol. 2019, pp. 1, July. 2019.
<https://journals.library.ryerson.ca/index.php/ictea/article/download/1223/1176>
- (3) **Deepak Nabapure**, Arjun Singh, Ram Chandra Murthy K, “Effect of Mach Number on the Rarefied Gas Flow over a Forward- Facing Step”, *Lecture Notes in Mechanical Engineering (LNME)*, Volume 1: Theoretical, Computational, and Experimental Solutions to Thermo-Fluid Systems- Select Proceedings of ICITFES

2020, January 31, 2021.

<https://www.springer.com/gp/book/9789813341647>.

- (4) **Deepak Nabapure**, Ram Chandra Murthy K, “DSMC simulation of rarefied gas flow over a forward-facing step: Effect of expansion ratio”, *AIP Conference Proceedings*, Volume 2316, pp 030032, Feb 2021.
<https://aip.scitation.org/doi/abs/10.1063/5.0036427>.

Book Chapters

- (1) **Deepak Nabapure**, Ram Chandra Murthy K, “DSMC Simulation of Rarefied Gas Flow Over a Wall Mounted Cube”, *American Society of Mechanical Engineers*, vol. 59032, pp. V002T02A071, July. 2019.
<https://doi.org/10.1115/AJKFluids2019-5447>

International Conferences

- (1) **Deepak Nabapure**, Ram Chandra Murthy K, “DSMC investigation of rarefied flow over a wall-mounted cube”, *30th International Conference on Discrete Simulation of Fluid Dynamics, (DSFD-2021) University of Tuscia, Viterbo, Italy*, Sep 13 – Ep 17, 2021.
- (2) **Deepak Nabapure**, Ram Chandra Murthy K, “DSMC Investigation of rarefied cavity flows in all rarefaction regimes”, *2020 Division of Fluid Dynamics 73rd Annual Meeting, (APS-DFD-2020) Illinois, Chicago, USA*, November 22 – November 24, 2020.
- (3) **Deepak Nabapure**, Ram Chandra Murthy K, “Investigation of Rarefied Open Cavity Flows in all Rarefaction Regimes using DSMC Method”, *29th International Conference on Discrete Simulation of Fluid Dynamics, (DSFD-2020) University of Tuscia, Viterbo, Italy*, July 13 – July 17, 2020.

- (4) **Deepak Nabapure**, Ram Chandra Murthy K, “Effect of Mach Number on the Rarefied Gas Flow over a Forward-Facing Step ”,*International Conference On Innovations In Thermo-Fluid Engineering And Sciences (ICITFES-2020) NIT Rourkela,Rourkela,India*, February 10 - February 12, 2020.
- (5) **Deepak Nabapure**, Ram Chandra Murthy K, “Investigation of Rarefied Gas Flow over a Backward-Facing Step : Effect of Channel Height ”,*25th National and 3rd International ISHMT-ASTFE Heat and Mass Transfer Conference (IHMTTC-2019)*, *IIT-Roorkee, Roorkee, India*, December 28 - December 31, 2019.
- (6) **Deepak Nabapure**, Ram Chandra Murthy K, “DSMC Simulation of Rarefied Gas Flow over a Forward-Facing Step: Effect of Expansion ratio”,*International Conference on Advanced Trends in Mechanical and Aerospace Engineering (ATMA-2019)*, *Dayananda Sagar University, School of Engineering,Bengaluru India*, November 07 - November 09, 2019.
- (7) **Deepak Nabapure**, Ram Chandra Murthy K, “DSMC Simulation of four-sided lid-driven cavity flow problem”,*28th International Conference on Discrete Simulation of Fluid Dynamics,Jawaharlal Nehru Centre for Advanced Scientific Research,Bengaluru,India*, July 22– July 26, 2019.
- (8) **Deepak Nabapure**, Ram Chandra Murthy K, “DSMC Simulation of Rarefied Gas Flow over a Wall Mounted Cube ”,*ASME-JSME-KSME Joint Fluids Engineering Conference,(AJK Fluids) Hyatt Regency San Francisco, CA, USA*, July 28 – August 1, 2019.
- (9) **Deepak Nabapure**, Ram Chandra Murthy K, “Investigation of Subsonic and Hypersonic Rarefied Gas Flow over a Forward-Facing Step ”,*12th International Conference on Thermal Engineering: Theory and Applications,(ICTEA)*, *Pandit Deendayal Petroleum University Gandhinagar, India in collaboration with Ryerson University Toronto, Canada*, February 22 - February 26, 2019.
- (10) **Deepak Nabapure**, Jayesh Sanwal, Sreeram Rajesh, Ram Chandra Murthy K, “Investigation of Subsonic and Hypersonic Rarefied Gas Flow over a Backward

Facing Step”, *International Conference on Recent Advances in Fluid and Thermal Sciences, (iCRAFT), BITS Dubai*, December 5 - December 7, 2018.

- (11) **Deepak Nabapure**, Jayesh Sanwal, Sreeram Rajesh, Ram Chandra Murthy K, “DSMC Simulation of Rarefied Gas Flow in a Single-sided and Double-sided Lid-Driven Cavity”, *7th International and 45th National Conference on Fluid Mechanics and Fluid Power, (FMFP) IIT Bombay, India*, December 10 - December 12, 2018.
- (12) Arjun Singh, **Deepak Nabapure**, Ram Chandra Murthy K, “Chemically reacting rarefied hypersonic flow over a Backward-Facing Step”, *AIAA Aviation Forum and Exposition, (AIAA-2021)*, August 02-August 06 2021.

Brief Biography of the Candidate

Deepak Nabapure (author) is presently Research Scholar at the Department of Mechanical Engineering, Birla Institute of Technology and Science, Pilani (BITS Pilani), Hyderabad Campus. He obtained his B.E in Mechanical Engineering from Visvesvaraya Technological University, Belagavi in 2013 with university second rank to the state. Thereafter he obtained M.E in Mechanical Engineering (with specialization in Thermal engineering) from BITS-Pilani in 2017. Prior to joining Ph.D in BITS-Pilani, Hyderabad he has professional work experience of 2 years. His research interest includes Rarefied gas dynamics, CFD and Microfluidics.

Brief Biography of the Supervisor

Dr. Ram Chandra Murthy K is presently an Assistant Professor at the Department of Mechanical Engineering, Birla Institute of Technology and Science, Pilani (BITS Pilani), Hyderabad Campus. He obtained his B.Tech. in Mechanical Engineering from Indian Institute of Technology, Madras in the year 2006. Thereafter he moved to US to complete his M.S. and Ph.D in Mechanical Engineering from Rutgers, The State University of New Jersey, in the year 2011. He then returned back to India and worked as a CFD Specialist at Altair Engineering, Bangalore for a period of 4 years. His teaching and research interests include Computational Fluid Dynamics, Fluid-Structure Interaction and Rarefied Gas Dynamics. He has published around 15 papers in reputed international journals, and presented more than 20 research works in National and International Conferences. Dr. Ram Chandra Murthy K is presently guiding 02 Ph.D. and guided/guiding several graduate and undergraduate students.